

Daniel Fjæstad

Transverse displacements of buried pipelines subjected to external loading

Graduate thesis in Civil and Environmental Engineering

Supervisor: Dr. Arnfinn Emdal (NTNU/IBM)

External Supervisor: Dr. Assaf-Avraham Klar (DTU/GEO)

June 2019



Daniel Fjæstad

Transverse displacements of buried pipelines subjected to external loading

Graduate thesis in Civil and Environmental Engineering

Supervisor: Dr. Arnfinn Emdal (NTNU/IBM)

External Supervisor: Dr. Assaf-Avraham Klar (DTU/GEO)

June 2019

Norwegian University of Science and Technology

Faculty of Engineering

Department of Civil and Environmental Engineering



Norwegian University of
Science and Technology

Abstract

This thesis investigates the effects of an external load on buried pipelines. The focus is on transverse, vertical displacements of the pipeline itself. Experimental and numerical studies the pipeline response and compares the results to a new analytical solution developed by the supervisor of this thesis. Several prediction models for transverse displacements of pipelines have been developed; most of them concern the response to tunnel induced displacements. Therefore, the literature review in this thesis presents the history of tunnel induced pipeline displacements before tying it in with general external loads. In 2018, Klar (2018) presented an elastic continuum solution using Fourier expansion. This allows the input of tunneling-induced Greenfield displacements or any arbitrary load. The pipeline response can ultimately be described using a spatial frequency-dependent stiffness rather than a constant stiffness seen in the commonly used Winkler-model.

In this thesis, a point load is applied to the pipelines. This caused uplift and transverse displacements of the pipeline, which has been measured using particle image velocimetry. The experiments are effectively attempting to pull the pipeline out of the soil, but images are taken continuously to get the response with increasing loads. In addition to the continuum solution, prediction formulas for the pullout response of pipes are investigated. Pullout capacity and maximum mobilization distance the experiments are compared to the predicted values. All of these formulas assume a perfectly rigid pipe, but the point load situation and transverse deflection profile of this pipe commonly occur in the field. The tests establish the validity of current practices for estimating the pullout response of a pipe. The numerical study only concerns linear elastic strains as the elastic continuum solution works in the linear-elastic range of the soil. A spatial frequency dependency for the stiffness was established from the numerical studies, and the values are in good agreement with the elastic continuum solution. This shows that the stiffness in the commonly used Winkler-model is missing information on the soil-structure response. Measurements from the experiments with strains exceeding the linear threshold indicate that the spatial frequency-dependent stiffness reverts to a constant and is in the same range as the Winkler-model. More tests are needed to confirm this.

A new experimental set up was designed for this thesis. The model is intended for centrifuge experiments, but three out of four experiments are not carried out during flight. The 1g experiments are both intended as a proof of concept, but the results are also analyzed. The design of the centrifuge model is documented in this thesis. Future projects can refer to this document if the setup or one of its components are used. The pilot tests show that the model had some issues during flight. Necessary improvements to the set up are also given.

Preface

This master's thesis is submitted in partial fulfillment of the requirements for the Degree of Master of Science in Civil and Environmental Engineering, at the Norwegian University of Science and Technology (NTNU) in Trondheim. The thesis is written under the Geotechnical division at NTNU in collaboration with the Geotechnical group and the Department of Civil Engineering at Denmark Technical University (DTU). The work was carried out during fall and spring 2018/2019. My supervisors during this semester have been professor Arnfinn Emdal at NTNU and professor Assaf-Avraham Klar at DTU. The topic was proposed by professor Klar.

Acknowledgments

First of all, I would like to thank my external supervisor and professor at DTU Assaf-Avraham Klar for his help and support during this project. His knowledge on the topic and unparalleled enthusiasm inspired me, and I learned a great deal from working with him.

Special thanks to my internal supervisor Arnfinn Emdal and professor Varvara Zania for help, support and guidance on the thesis. Dr. Zania helped me with the centrifuge-specific tasks and Dr. Emdal gave me general feedback and advice along the way.

I would also like to thank the lab technicians at DTU, whose work and advice I heavily relied on. Special thanks to engineering assistant John C. Troelsen for helping me with the installation of the centrifuge strongbox.

Last but not least, I would like to thank my wife and mom to my newborn child for support and patience throughout the project. My little girl Saga was born in the middle of the project and I was literally bicycling from the hospital to the centrifuge lab only a few days after birth. This was by far my least favourite moment of this project and I am lucky to have a very understanding wife.

For financial support, I would like to thank the Erasmus+ programme of the European Union.

Sammendrag på norsk

Denne hovedoppgaven undersøker effektene av en ekstern last på nedgravede rør. Fokuset er på forskyvninger på langs av røret. Numeriske og eksperimentelle forsøk er utført, og resultatene er sammenlignet med en ny analytisk løsning laget av oppgavens eksterne veileder. En rekke beregningsmodeller er tilgjengelig i vitenskapelig litteratur, men de involverer hovedsakelig forskyvninger som følge av tunnelutbygging. Literaturstudiet i denne oppgaven introduserer derfor de viktigste beregningsmodellene for forskyvninger over en tunnel og laster generelt. I 2018 utledet Klar en elastisk kontinuum løsning med Fourier serier. Denne løsningen tillater både forskyvninger som følge av tunnelutbygging eller en hvilken som helst tilfeldig last. Rørledningens respons kan til slutt beskrives med en romlig frekvens avhengig stivhet istedenfor den konstante stivhetskoeffisienten man typisk fra den mye brukte Winkler-modellen.

Rørledningene blir påført en punklast i denne oppgaven. Dette førte til oppløfting og en variabel forskyvningsprofil på langs med røret som ble målt med Particle Image Velocimetry (PIV). Eksperimentelle forsøk prøver å dra rørledningene ut av grunnen og bilder er tatt kontinuerlig med økende last. I tillegg til å undersøke den elastiske kontinuum løsningen, blir resultatene også sammenlignet med en rekke beregningsformler for uttrekning av rør og den maksimale mobiliseringsdistansen. Samtlige beregningsformler antar at røret er ubøyelige i lengderetning, men situasjonen med en punklast og en variabel forskyvningsprofil forekommer ofte i felten. Testene indikerer hvor godt beregningsformlene fungerer for et rør som ikke har variabel forskyvning i lengderetning. Den numeriske studien dreier seg kun om elastiske deformasjoner i løsmassen fordi dette er nødvendig i den elastiske kontinuerlige løsningen. En romlig frekvens avhengighet ble etablert basert på de numeriske modellene og verdiene var i overensstemmelse med teoretisk-analytiske beregninger. Dette viser at Winkler-modellen mister informasjon når stivheten blir bestemt. Målinger fra eksperimentelle forsøk med tøyninger som overstiger terskelen for lineær oppførsel i løsmasser viser at stivheten blir konstant med romlig frekvens og er i samme størrelsesorden som Winkler-modellen.

Et nytt eksperimentelt oppsett ble designet som en del av hovedoppgaven. Modellen er laget for eksperimenter i sentrifugen men de fleste eksperimentene ble utført uten at sentrifugen ble akselerert. Eksperimentene i 1g er ment som konseptbevis, men resultatene er analysert fra disse. Designet av sentrifugemodellen er dokumentert i denne oppgaven. Fremtidige prosjekter kan henvise til dette dokumentet hvis hele modellen eller deler av komponentene brukes. Pilottester viste at modellen har enkelte problemer i sentrifugen. Nødvendige forbedringer til modellen er gitt i slutten av oppgaven.

Table of contents

Abstract	i
Preface	ii
Acknowledgments.....	ii
Sammendrag på norsk	iii
Table of contents	iv
List of symbols.....	vii
List of figures.....	x
List of tables	xiii
1 Introduction	1
1.1 Background.....	1
1.2 Problem Formulation	1
1.3 Thesis outline	2
2 Literature review.....	3
2.1 Transverse displacement of a pipeline	3
2.1.1 Ground displacements caused by tunnelling	3
2.1.2 Transverse settlements of a pipeline	4
2.1.3 Winkler-based interaction problem	7
2.3 Elastic continuum solutions (Klar et al 2005).....	9
2.4 Elastic continuum solution using Fourier expansion (Klar, 2018).....	11
2.5 Uplift mechanisms of pipelines buried in sand	15
2.6 Soil stiffness modelling.....	19
2.7 Centrifuge modelling.....	22
2.7.1 Scaling effects	22
2.7.2 Particle size limitations	25
2.8 Particle image velocimetry (PIV)	25
3 Methodology	28
3.1 Theoretical framework.....	28
3.1.1 The Fourier series expansion of a function	28
3.1.2 Elastic continuum solution for a point load using Fourier expansion.....	32
3.2 DTU geotechnical centrifuge	36

3.3 Design of the centrifuge model.....	36
3.2.1 The model assembly	37
3.2.2 The strongbox.....	41
3.2.3 The pipe	42
3.2.4 The wire	47
3.2.5 The separation wall	49
3.2.6 The camera mount	54
3.2.7 The camera	55
3.4 Rotational speed	55
3.5 Calibration of load cells	56
3.6 Centrifuge counterweight	56
3.7 Model preparation	57
3.7.1 Fontainebleau sand	57
3.7.2 Sand pouring method	57
3.8 Test procedure	59
3.9 GeoPIV	62
3.10 Accuracy and precision of the GeoPIV	65
3.11 Fibre optics	66
3.12 Verification of the elastic continuum solution.....	67
3.12.1 Computed displacements with the elastic continuum solution	67
3.12.2 Verification of elastic continuum solution with measured values	70
4 Evaluation of elastic continuum solution with numerical models	71
4.1 Modelling approach	71
4.1.1 The finite element model	72
4.2 FEM results.....	75
4.3 Comparison of analytical and numerical solutions	78
4.4 Sensitivity test a-values.....	80
4.5 Summary	81
5 Pullout test results.....	82
5.1 PVC pipe in 1G (test 1 and test 2)	82
5.1.1 Pipeline uplift response	82
5.1.2 Displacement field of the surrounding soil	86
5.1.3 Engineering shear strain in overlying soil.....	91

5.1.4 Volumetric strain	95
5.1.5 Deflection shape of the pipeline	97
5.1.6 Ground displacement profile.....	102
5.1.7 Fiber optics data	104
5.1.8 Load-displacement curves derived from the fibre optics moment and PIV displacements.....	108
5.1.9 Comparison of fibre optics and PIV data	111
5.2 Aluminium pipe with fixed ends in 1G (test 3).....	114
5.3 Centrifuge test results (test 4)	117
5.4 Evaluation of elastic continuum solution and experimental results	118
5.5 Summary	121
6 Conclusions and recommendations	123
6.1 Conclusions.....	123
6.2 Validity of the results	125
6.3 Recommended improvements to the Centrifuge model.....	125
6.4 Further Research	126
7 Bibliography.....	128

List of symbols

Latin

A	Area
A_ω	Harmonic amplitude of a point load
C	Cover, measured from surface of soil to the top of the pipe
D_{50}	Average grain diameter
G	elastic shear modulus
D	Diameter of the pipe
E	Young's modulus
E_p	Young's modulus of the pipe
E_s	Young's modulus of the soil
EA	Axial stiffness
EI	Bending stiffness
EI_{pipe}	Bending stiffness of the pipe
F	Point load/force
I	Second moment of area
H	Frame height for images
K	Earth pressure coefficient
K	Trough width parameter
K_0	Passive earth pressure coefficient
K_0 / K_1	Bessel functions of first and second order
K_{eff}	Effective subgrade reaction modulus
K_∞	Subgrade reaction modulus for an infinitely long pipe
L	Length of the pipe (Note: A period of 2L is often used for one pipe length).
L	Patch size in GeoPIV
L_w	Length of weld
M	Moment
P	Load/force
$N_{w,Ed}$	Force on weld
$N_{w,Rd}$	Weld capacity
S_v	Vertical displacement of soil (Greenfield)
R	Relative rigidity
R_e	Centrifuge radius at a reference location
RD	Relative density
U_{gf}	Periodic amplitude of Greenfield soil displacements
V	Volume
V_s	Volume of solid
V_v	Volume of voids
W	Frame width for images
W	Width of the centrifuge box

a	Width of the gaussian Error function (a = one standard deviation)
a	Weld throat thickness
d	Pipe diameter
g	Gravity [9.81 m/s_2]
e	Void ratio
e_{\min}	Minimum void ratio
e_{\max}	Maximum void ratio
h_m	Height of the soil in the centrifuge model
i	Inflection point of the fitted soil displacements (horizontal distance x)
i_p	Inflection point of the fitted pipe displacements (horizontal distance x)
$k_\omega, k_\omega(\omega)$	Spatial frequency-dependent stiffness.
$k_{\omega,vv}$	Spatial frequency-dependent stiffness vertical displacements component.
$k_{\omega,v\theta}/k_{\omega,v\theta}$	Spatial frequency-dependent stiffness accounting for rotation of the element
m	Power law coefficient
n	Shape parameter used in a modified Gaussian curve
n	Centrifuge acceleration [$n \cdot 9.81 \text{ m/s}_2$] and scaling factor
n_m	Acceleration at a point in the middle taking into account non-linearity of gravity
p'	Effective confining pressure
p_{ref}	Reference confining pressure, usually 100 kPa
q	Distributed load on a beam
r	Radius
r_o	Outer pipe radius
r_i	Inner pipe radius
t	Wall thickness
u	Displacement
u_p, v	Vertical pipe displacement
u_{gf}	Greenfield displacements of the soil
u^{CAT}	Greenfield soil displacements at pipe level
x	Horizontal coordinate, point load is applied at $x = 0$
z	Vertical coordinate, reference level ($z=0$) is at the surface
z_p	Depth of the pipe axis

Greek

δ	Deflection of the pipe during pullout
δ	Friction angle between soil and pile shaft
ϵ	Strain
ϵ_v	Volumetric strain
$\epsilon_{xx}, \epsilon_{zz},$	In-plane strain components
ϵ_{xz}	
ϕ'	Effective friction angle
ϕ_{\max}	Maximum friction angle
ϕ_{crit}	Critical friction angle
γ	Unit weight
γ	Engineering shear strain

γ_{dry}	Dry weight of soil
γ_{tl}	The linear threshold strain
γ_{tv}	The volumetric threshold strain
λ	Soil stiffness parameter
ν	Poisson's ratio of soil
ν, ν_s	Poisson's ratio of soil
ρ	Density of soil
σ	Stress
σ, σ_m	Stress in model scale
σ_p	Stress in prototype scale
σ_v	Vertical stress
σ_h	Horizontal stress
ψ	Dilation angle
ω	Wave number
ω	Angular velocity

Abbreviations

FEM = Finite Element Method

PIV = Particle Image Velocimetry

List of figures

Figure 1: Transverse displacements of a pipeline due to an external load, for example frost heave.	2
Figure 2: Pipeline displacement due to tunnelling induced Greenfield displacements.	3
Figure 3: The Greenfield displacements over a tunnel.	5
Figure 4a: The experimental set up of a centrifuge model by Marshall, Klar and Mair (2010).	6
Figure 4b: Typical results from Marshall, Klar and Mair (2010)	7
Figure 5: A Winkler-based model of a buried pipeline	7
Figure 6: The Gaussian greenfield function as the superposition of cosine functions	12
Figure 7: A sinusoidal, periodic barell load..	12
Figure 8a: Spatial frequency-dependent stiffness for a pipeline at infinite depth.....	14
Figure 8b: Spatial frequency-dependent stiffness for different burial depths to pipe radius ratios ...	14
Figure 9: Different pullout mechanisms	16
Figure 10a: Typical uplift response of a buried pipeline. After Wang, Shi and Ng, (2011).	18
Figure 10b: A simplified trilinear curve after DNV-RP-F110 design recommendations	18
Figure 11: Three idealized soil models.....	20
Figure 12: Typical stiffness degradation with increasing strains. After (Mair, 1993).	20
Figure 13: Comparison of stress in the centrifuge and the corresponding prototype	24
Figure 14: Correlation algorithm for the GeoPIV software. From White and Take, (2002).	26
Figure 15: The square wave function as a Fourier series with an increasing number of harmonics. ...	30
Figure 16: Forces in a beam element as a response to a load $f(x)$	32
Figure 17: A simplified drawing of the experimental set up seen from the side.....	42
Figure 18: The PVC half-pipe.....	44
Figure 19: The wire-pipe attachment	45
Figure 20: Typical design for a counterfort wall.	49
Figure 21a/b: Horizontal force experienced by the welds of the separation wall.	51
Figure 22: Von Mises stress in the separation wall with 0.5 m of sand at 50g.....	53
Figure 23: Displacement of the separation wall with 0.5 m of sand at 50g.	54
Figure 24: Potential travelling loops with the sand pouring hopper. After Zhao et al. (2006).....	58
Figure 25: A typical mesh from the GeoPIV.....	62
Figure 26: Example of an input file for GeoPIV-RG.....	63
Figure 27a: The mesh is located under the pipe in an area with negligible displacements	64
Figure 27b: The displacements vectors are skewed by a significant amount	64

Figure 28: Typical microstrains recorded for a loaded pipe in test 1 and test 2.	67
Figure 29: Pipeline periodic displacements. The continuum solution requires that u_p is continuous, therefore the deflection angle must be zero at each period.....	68
Figure 30: Values for $k\omega$ replotted after the continuum solution. The input here is also based on the continuum solution and therefore a perfect match.	69
Figure 31: The buried pipeline model consists of two solid elements: a pipeline with and the surrounding material	73
Figure 32: A narrow Gaussian surface load was applied as a point load cannot exist in a 3D space. ..	74
Figure 33: Typical finite element mesh.....	75
Figure 34: Pipeline displacement profile for two different pipeline radii.	76
Figure 35: Pipeline displacement profile for three different pipe radii and the same z_p/r_0 ratio.	76
Figure 36: Pipeline displacement for three different z_p/r_0 ratios and the same pipe radius.	77
Figure 37a: Spatial frequency-dependent stiffness for $r_0 = 5$ mm at different depths.....	78
Figure 37b: Spatial frequency-dependent stiffness for $r_0 = 10$ mm at different depths	79
Figure 37c: Spatial frequency-dependent stiffness for $r_0 = 15$ mm at different depths	79
Figure 38: Spatial frequency-dependent stiffness for different a -values, where a controls the width of the Gaussian function.	81
Figure 39a: Load-displacements curves for test 1, based on maximum displacement.....	83
Figure 39b: Load-displacements curves for test 2, based on maximum displacement	84
Figure 40: Rotation of the pipe arrested the pullout of the pipe during test 1.....	86
Figure 41a-f: Total displacement field at different loads for test 2.....	87
Figure 42a-f: Total displacement field at different loads for test 2.....	89
Figure 43a-f: Engineering strain field at different loads for test 1.	92
Figure 44a-f: Engineering strain field at different loads for test 2.	93
Figure 45a: Contour plot of volumetric strains at 34 N for test 1.....	96
Figure 45b: Contour plot of volumetric strains at 78 N for test 1.....	96
Figure 45c: Contour plot of volumetric strains at 29 N for test 1.....	97
Figure 45d: Contour plot of volumetric strains at 44 N for test 1.....	91
Figure 46: Mesh used to obtain the displacements at pipe level in test 1	98
Figure 47: Displacement profile of the pipe in test 1	98
Figure 48: Mesh used to obtain the displacements at pipe level in test 1	99
Figure 49: Displacement profile of the pipe in test 2	99

Figure 50: Typical Gaussian fitted to measured data in test 1	101
Figure 51: Typical Gaussian fitted to measured data in test 2	102
Figure 52a: Mesh used to get soil heave profile.....	103
Figure 52b: Soil heave profile	103
Figure 53: Inflection point of the Gaussian best fit with depth	104
Figure 54a: Moment derived from fiber optics strains in test 1.....	106
Figure 54b: Moment derived from fiber optics strains in test 2.....	107
Figure 55a: Load on the pipe from the surrounding soil in test 1	107
Figure 55b: Load on the pipe from the surrounding soil in test 2	109
Figure 56: Soil load-displacement curves from test 1.....	109
Figure 57a-c: Comparison on moments based on fibre optics and PIV measurements for test 1.....	112
Figure 58a-c: Comparison on moments based on fibre optics and PIV measurements for test 2.....	113
Figure 59: Mesh used to obtain displacements of the pipe in test 3	114
Figure 60: Typical results from the PIV analysis in test 3.....	114
Figure 61: Pipeline deflection at the last image taken before failure.	115
Figure 62: The end of the pipe after test 3.	116
Figure 63: Load displacement curve for test 3.	116
Figure 64: Estimated soil resistance vs maximum displacement of the pipe	117
Figure 65: Displacement profile at pipe level during test 4.....	118
Figure 66a: Spatial frequency-dependent stiffness at different loads from test 1.	119
Figure 66b: Spatial frequency-dependent stiffness at different loads from test 2	119

List of tables

Table 1: Pullout capacity prediction formulas.	19
Table 2: Effect of different parameters on small-strain stiffness. After (Hardin and Drnevich, 1972) and Benz (2007).	21
Table 3: Scaling laws in the centrifuge.....	23
Table 4: Relevant Fourier transforms in this thesis	31
Table 5: A summary of the centrifuge model components including the SOLIDWORKS drawings. ...	37
Table 6: Properties of the four pipes made for this project	43
Table 7: Recommended and minimum pipeline lengths.	46
Table 8: Predicted pullout capacity for a depths of 100 mm and 200 mm and a 10 mm pipe radius.	47
Table 9: Predicted wire friction for representative 1g and 50g experiments.....	48
Table 10a: Properties of the Fontainebleau sand.....	57
Table 10b: Sand properties based on installed density cups from test 1.....	59
Table 10b: Sand properties based on installed density cups from test 2.....	59
Table 11: Test number and conditions for each test	59
Table 12: Comparison of model and prototype stress for the centrifuge test (test 4)	61
Table 13: Typical results from the error analysis.....	64
Table 14: Calibration results for fibre optics location.....	66
Table 15: Parameters of every FEM simulation carried out	74
Table 16: Test number and conditions for each experimental test.....	82
Table 17: Predicted and measured pullout capacity for the halfpipe in test 1 and test 2.	85
Table 18: Maximum shear strain observed in test 1 and test 2.	91
Table 19: Gaussian Best Fit to the Pipeline Displacement in test 1.....	100
Table 20: Gaussian Best Fit to the Pipeline Displacement in test 2.....	101
Table 21: Estimated spring coefficient at different points of the pipe in test 1	110
Table 22: Estimated spring coefficient at different points of the pipe in test 1.....	111
Table 23: Estimated Young's modulus compared to predicted initial Young's modulus	121

1 Introduction

1.1 Background

The high rate of urbanization all over the world requires optimal utilization of underground space for transportation and utility systems. The underground space is congested with pipelines, some of them decades old, and other structures. One of the major questions is how construction, as well as natural as the natural events, will affect existing pipelines. Tunneling induced ground movements, for instance, causes ground movements which affect overlying structures and pipelines. External loads causing such as swelling, ground heave, fault or even adjacent bursting pipelines can also cause major displacements. Hence, it is important to understand the effects of different external loads on buried pipelines.

1.2 Problem Formulation

This thesis investigates displacements of a continuous pipeline buried in sand and the resulting ground movements. The scope is limited to transverse displacements of the pipe. An elastic continuum solution by Klar (2018) describes the response of a buried pipeline to a known load but has not yet been verified with numerical or experimental studies. In this thesis, buried pipelines are subjected to a point load (figure 1). This case will be used to verify the elastic continuum solution.

The specific research goals are as follows:

- 1a) Design a new experimental setup for both 1G and centrifuge experiments. A half-pipe is buried next in a strongbox with a window view and pulled vertically with a wire.
- 1b) Measure the pulling force.
- 1c) Use particle image velocimetry (GeoPIV) to obtain soil and pipeline displacements.
- 2) Evaluate the response of a buried pipeline and analyse the displacements in the frequency domain with the elastic continuum solution by Klar (2018).
- 3) Investigate the behaviour of the surrounding soil.
- 4) Examine different burial depths and pipe bending stiffnesses.

Also considered is finite element analyses performed using COMSOL Multiphysics.

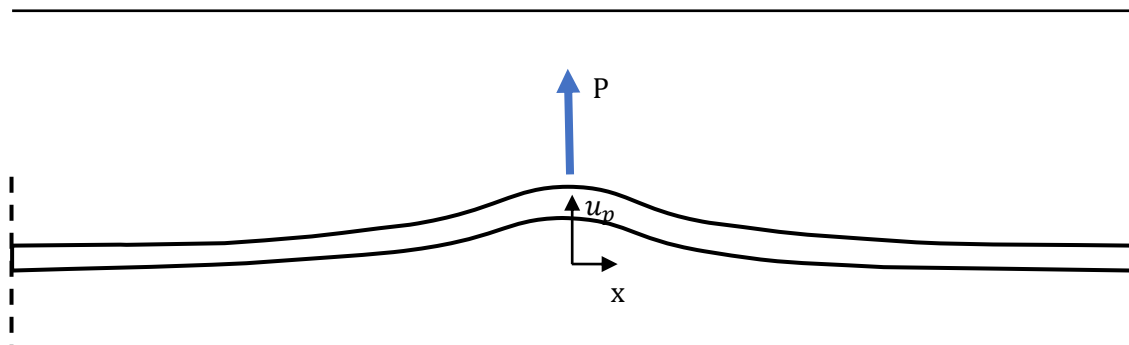


Figure 1: Transverse displacements of a pipeline due to an external load, for example frost heave.

1.3 Thesis outline

This thesis is divided into seven chapter with the following structuring:

Chapter 2 first presents existing literature on the specific topic of transverse pipeline displacements. The transverse displacements of a pipeline due to tunnel induced ground movements are included since this is what most previous studies have looked into. This is later tied into the point load case with the elastic continuum model. This chapter also contains relevant theory for the models in this thesis.

Chapter 3 provides an elastic continuum solution for specifically for a point load and is an extension of the work of (Klar, 2018). This chapter also presents the centrifuge model that was made as a part of this thesis. Lastly, this chapter goes through the Wolfram Mathematica scripts that are used to evaluate the results.

Chapter 4 contains finite element analysis of buried pipelines. The pipeline response is evaluated and compared to the elastic continuum solution.

Chapter 5 includes four experimental tests, three in 1g and one at 50g in the centrifuge. The results of the first two tests in 1g are investigated further. Soil movements, pipeline deflection and fibre optics measurements are analysed. The pipeline displacements are used as input in the elastic continuum solution at the end of the chapter.

Chapter 6 first gives a conclusion and recommendations for further research. Recommended improvements to the centrifuge set up are also given, as the performance of the model was not the best. Future studies should be able to use the model with good results after these relatively simple improvements.

2 Literature review

2.1 Transverse displacement of a pipeline

Current understanding of transverse deformations of pipelines primarily comes from studies on the effect of tunnelling beneath existing pipes. Figure 2 shows the problem. Greenfield displacements u_{gf} refer to the settlements in soil without structure interaction. Soft ground tunnel excavation causes ground loss and stress relief, which results in ground movements of the surrounding soil. The gap formation above the tunnel leads to a loss of bearing pressure. This causes vertical displacement of the pipeline above the tunnel axis. The pipeline displacement u_p is governed by the pipeline stiffness, soil stiffness, and the soil-pipe interaction.

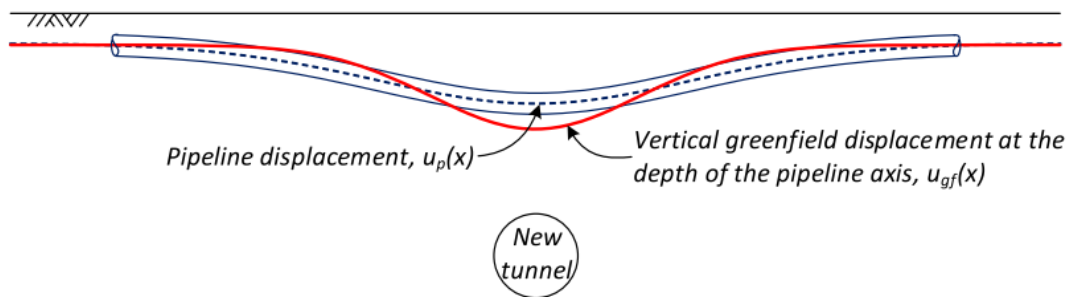


Figure 2: Pipeline displacement due to tunnelling induced Greenfield displacements. The elastic continuum solution solves the pipeline displacements with Greenfield displacement as input. From Klar (2018).

In this thesis, the load imposed directly on the pipeline as a point load and Greenfield displacements are not present (Figure 1). However, this research is still important as the main historical background for the research in this thesis. The elastic continuum solution by (Klar, 2018) is a continuation of research on tunnel induced pipeline deformation. As the continuum solution allows any arbitrary load as input, experimentally verification with a point load will also validate the Greenfield input. No one has attempted to experimentally verify this solution.

2.1.1 Ground displacements caused by tunnelling

Several studies have investigated the failure modes and resulting soil displacement at the tunnel face during construction. Centrifuge tests by Atkinson and Potts (1977) in sand show a chimney-like failure mechanism, propagating almost perfectly vertically.

2.1.2 Transverse settlements of a pipeline

Peck (1969) and Schmidt (1969) observed from case studies of tunnel collapse that the transverse settlement trough over a tunnel follows the shape of a Gaussian curve. Peck (1969) proposed the following surface settlement, S_v , with distance from the centreline:

$$S_v = S_{v,max} * \exp\left(-\frac{x^2}{2i^2}\right) \quad (1)$$

Where,

$S_{v,max}$ is the maximum settlement at the centre,

x is the distance to the centreline, and

i is the inflection point.

Figure 3 shows the Greenfield settlement trough over a tunnel, which is a Gaussian, and the pipeline response. S_v and u_{gf} will be used interchangeably for the rest of this thesis. The maximum Greenfield settlement is at the centreline ($x = 0$), and the value at the inflection point is (Marshall, 2009):

$$S_v(x = i) = S_{v,max} * \exp\left(-\frac{x^2}{2i^2}\right) = 0.61S_{v,max} \quad (2)$$

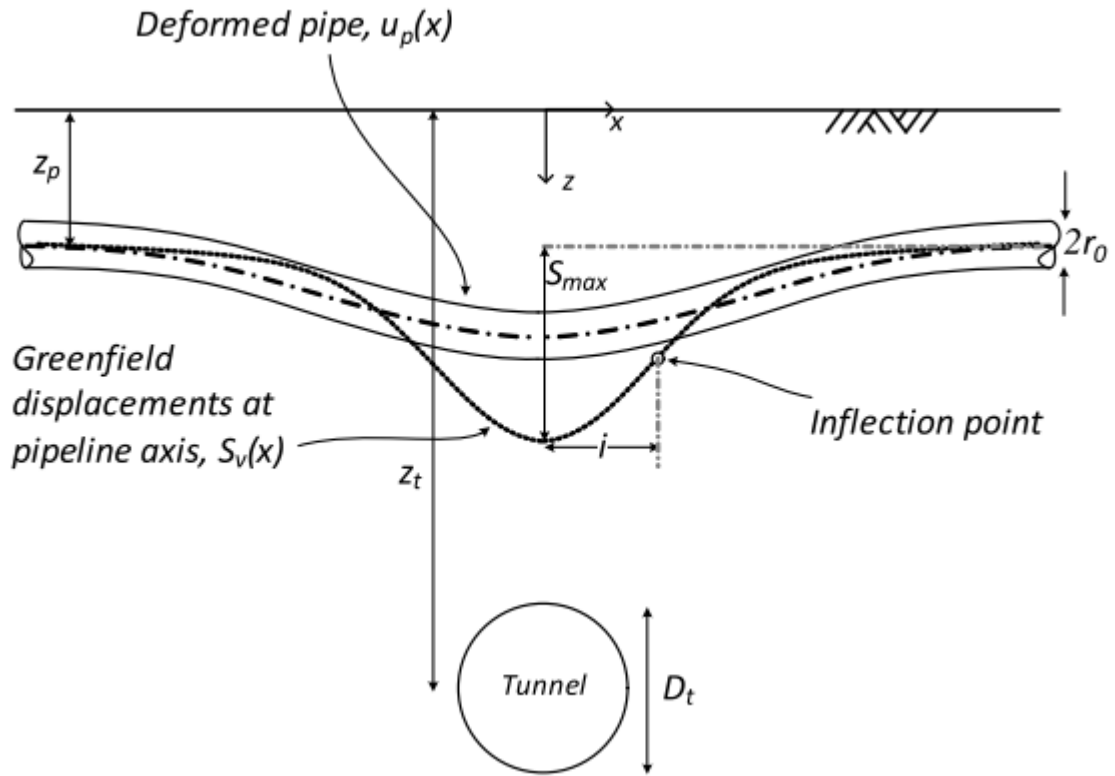


Figure 3: The Greenfield displacements over a tunnel takes the shape of the Gaussian error function. From Klar, Elkayam and Marshall (2016).

O'reilly and New (1982) showed that the inflection point is approximately a linear function of depth. For simplicity, O'reilly and New (1982) suggest using the simplified formula:

$$i = K * z_T \quad (3)$$

Where K is a trough width parameter. They recommended a value of 0.5 for tunnels in clay and 0.25 for tunnels in sand or gravel. Mair and Taylor (1996) propose K values of 0.25-0.45 for granular soils. In actuality, the trough width parameter K changes with depth too, but the simplification is usually sufficient (Mair, Taylor and Bracegirdle, 1993).

The Gaussian settlement trough is accurate for undrained clays but does not accurately describe settlement trough in sand. Vorster (2006) ran centrifuge experiments with sand to investigate settlements caused by tunnelling and suggested a modified Gaussian settlement trough:

$$S_v = S_{v,max} * \frac{n}{(n-1) + \exp\left(\alpha * \frac{x^2}{i^2}\right)}; \quad n = e^{\alpha \frac{2\alpha-1}{2\alpha+1}} + 1 \quad (4)$$

The parameter α provides another degree of freedom and allows greater flexibility of the Gaussian curve to match the settlement trough, for example in sands. For $\alpha = 0.5$, formula 4 reverts back to the standard Gaussian curve, whereas values of $\alpha > 0.5$ (or $n > 1$)

result in a narrower profile. Sands are expected to be described by formula 4 for some value $\alpha > 0.5$ due to their chimney-like failure.

Vorster *et al.* (2006) also ran a series of centrifuge tests on pipelines buried in sand. The study tested an acrylic pipe with diameter 16 mm and two aluminium pipes with diameters of 15.9 mm and 34.9 mm, all with a length of 700 mm, at 75g. Several observations were made from measured soil stress, moment of the pipe and the relative movement of pipeline and soil. Gap formation occurred around the point of maximum settlement which means that only the overlying soil has an effect on the pipe. It was also observed that the soil is sagging in the centre, where the soil moves more than the pipeline, and hogging elsewhere.

Figure 4a shows the experimental set up of Marshall, Klar and Mair (2010). The set up incorporates a half-sectioned pipeline and low-friction boundary to effectively model half of the prototype with a symmetry plane. Displacements are obtained at the window surface with image analysis using particle image velocimetry PIV. The moment obtained from strain gauge data and PIV displacement data showed good agreement. Marshall, Klar and Mair (2010) concluded that PIV measurements can safely be used as the only method of displacement measurements in this setup.

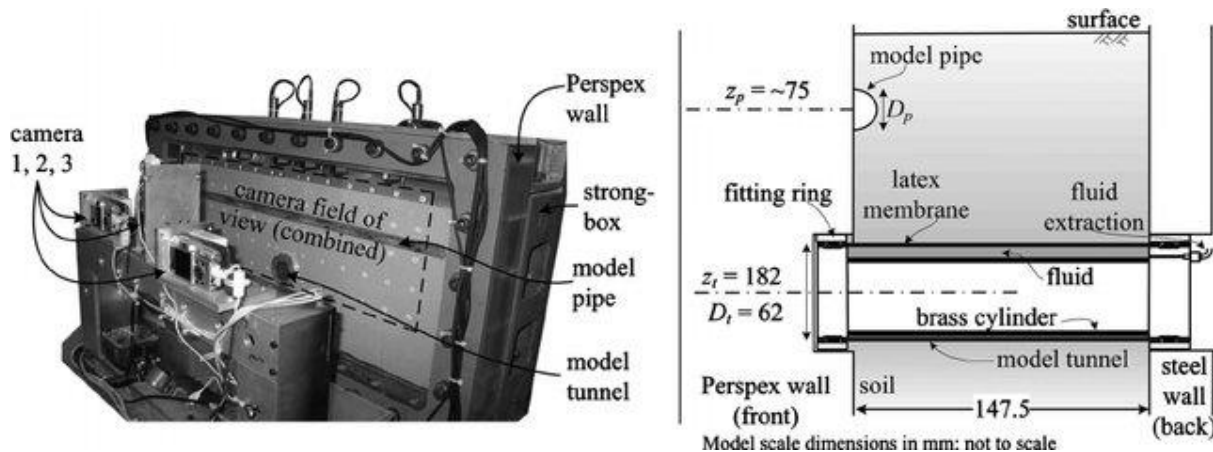


Figure 4a: The experimental set up of a centrifuge model by Marshall, Klar and Mair (2010). The set up places a half-pipe at the window to give a view of the pipe and soil displacements. From Marshall, Klar and Mair (2010).

Marshall, Klar and Mair (2010) investigated three 700 mm pipes at 75 g. Pipe diameters range from 16 to 20 mm and bending stiffness of 6.44 N/m², 238.5 N/m² and 809.6 N/m², respectively. Figure 4b shows the results from the medium stiff pipeline buried at a depth of 65 mm, or a radius to pipeline depth ratio $r/z_p \approx 7$. The distance from the pipeline to the tunnel is approximately 180 mm. A relative pullout of the soil occurs in the middle where the soil moves more than the pipe, similar to observations by Vorster *et al.* (2006). Marshall, Klar and Mair (2010) observed from the PIV data that the maximum moment of a rigid pipe increases with volume loss until the maximum pullout resistance has been reached. For high volume losses, the pipeline bending movement was more or less constant. The effect was not observed for the flexible pipeline.

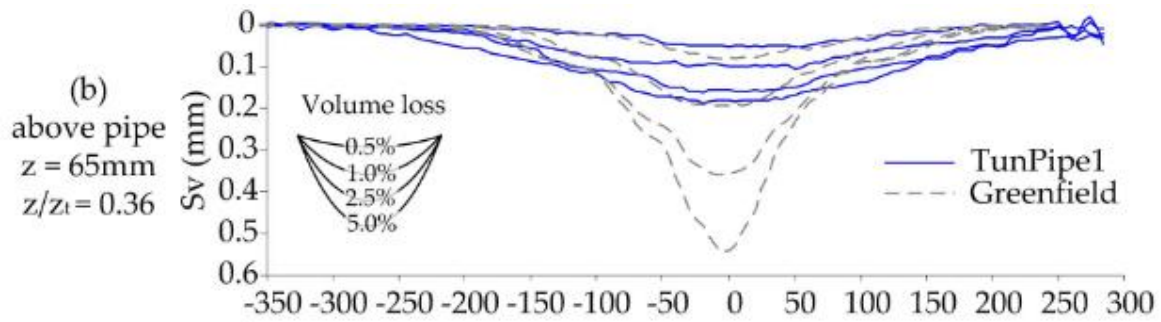


Figure 4b: Typical results from Marshall, Klar and Mair (2010). Soil displacements are measured with particle image velocimetry (PIV). From Marshall, Klar and Mair (2010).

Klar (2018) later showed that a pipeline's response to a Gaussian load is also a Gaussian, but with a lower maximum displacement and larger inflection point i_p .

2.1.3 Winkler-based interaction problem

This chapter describes on of the subgrade reaction analysis by Attewell, Yeates and Selby (1986). They modeled the tunnel-induced soil-pipeline interaction as an infinite Winkler (1867) beam. Figure 5 illustrates a Winkler model of a buried pipeline.

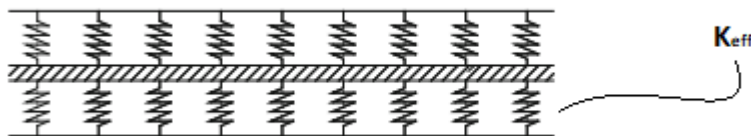


Figure 5: A Winkler-based model of a buried pipeline

Attewell's model assumes the following conditions:

1. The pipe is linear elastic and isotropic
2. The soil is linear elastic, homogeneous and isotropic
3. The pipe is always in contact with the soil

Additionally, the model is only valid for pipelines that are long enough to act as if the length is infinite. This requires a length of at least $1/\lambda$ but ideally more than $2.5/\lambda$ (Attewell, Yeates and Selby, 1986), where the soil-pipe stiffness parameter λ has dimensions L^{-1} .

Attewell, Yeates and Selby (1986) discovered that the pipe deformation depends on several factors. The most important factors are the stiffness, grain size and load history for the soil, and the bending stiffness – and to some degree, axial stiffness, of the pipe. However, the soil and pipeline settlements are affected by the coupled interaction of the soil and the pipe. Stiffer pipelines will exhibit a larger resistance to movement which in turn affects the soil behaviour. The pipe joints also influence the stiffness and pipeline response, but is

outside the scope of this thesis. Pipeline coating affects the interface shear between the pipe and the soil.

Attewell, Yeates and Selby (1986) also provided a Winkler-based analytical solution using an empirical Greenfield condition. The pipeline settlements can be estimated by the soil-pipe stiffness parameter λ and Greenfield settlement according to the following equation:

$$\frac{\partial^4 u}{\partial x^4} + 4\lambda^4 u = 4\lambda^4 S_v(x) \quad (5)$$

Where,

$$\lambda = \sqrt[4]{\frac{K_{eff}}{4E_p I_p}} \quad (6)$$

And the effective subgrade reaction modulus K_{eff} for a buried pipeline is equal to

$$K_{eff} = 2K_\infty \quad (7)$$

Attewell suggested using the subgrade modulus the K_∞ proposed by Vesic's (1961). The effective subgrade modulus based on buried at infinite depth in incompressible soil (Poisson's ratio $\nu = 0.5$) according to Vesic (1961) is:

$$K_\infty = 0.65 \sqrt[12]{\frac{E_s D_p^4}{E_p I_p}} * \frac{E_s}{1 - \nu_s^2} \quad (8)$$

The s and p subscripts here denote the soil and pipeline properties, respectively.

Attewell, Yeates and Selby (1986) made several observations from the Winkler based problem. Some of the findings include: Soil yielding decreases stress and movement of the pipe compared the linear elastic analysis. Pipe yielding decreases stress but increases movement of the pipe compared to linear elastic analysis. Furthermore, stiffer soil increases pipe stress and strain while a higher pipe Young's modulus increases stress and decreases strain.

For a point load F, the pipeline deflection according to the Winkler model is is

$$u_p(x) = \frac{F\lambda e^{-\lambda x}(\cos\lambda x + \sin\lambda x)}{2K_{eff}} \quad (9)$$

2.3 Elastic continuum solutions (Klar et al 2005)

This chapter describes important findings made by Klar *et al.* (2005) and Vorster *et al.* (2005).

The subgrade reaction analysis by Attewell used a numerical approach to solve the Winkler problem. Klar *et al.* (2005) later used this to provide a closed-form solution to the Winkler problem.

A concentrated point load on an infinite Winkler beam gives the following moment:

$$M = \frac{P}{4\lambda} \exp(-\lambda t) [\cos(\lambda t) - \sin(\lambda t)] \quad (10)$$

By replacing the point load with an infinite number of infinitesimal concentrated loads $dP(x)$ and inserting this into the equation above, Klar et al. 2005 obtained the following relationship for the maximum sagging moment:

$$\frac{M_{max} i^2}{E_p I_p S_{max}} = 2\lambda^3 i^2 * \int_0^\infty \exp \left[-\lambda x - 0.5 \left(\frac{x}{i} \right)^2 \right] * [\cos(\lambda x) - \sin(\lambda x)] dx \quad (11)$$

The closed-form solution to the equation above is

$$\frac{M_{max} i^2}{E_p I_p S_{max}} = \sqrt{2\pi} \xi^3 \left\{ \cos(\xi^2) \left(1 - 2C \left(\frac{2\xi}{\sqrt{2\pi}} \right) \right) + \sin(\xi^2) \left(1 - 2S \left(\frac{2\xi}{\sqrt{2\pi}} \right) \right) \right\} \quad (12a)$$

$$C(u) \equiv \int_0^u \cos \left(\frac{\pi t^2}{2} \right) dt; S(u) \equiv \int_0^u \sin \left(\frac{\pi t^2}{2} \right) dt \quad (12b)$$

Where $\xi = \lambda i$.

General agreement was found between the numerical solution by Attewell 1986 and the closed-form solution by Klar *et al.* (2005). However, the validation analysis also showed that Vesic's expression (equation 8) is not necessarily adequate. Additionally, the expression may not be conservative. It is recommended to use the closed form solution since this is always conservative. Based on a finite element analysis of the elastic continuum solution, Klar *et al.* (2005) proposed a new subgrade modulus for the Winkler model:

$$K = \frac{12E_s r_0}{i} \quad (13)$$

Klar *et al.* (2005) used the elastic continuum soil model to describe the behavior of pipe-soil interaction. Assuming small strains, the elastic continuum solution to the response of pipelines of a tunnel is expressed by the following equation (Klar *et al.*, 2005):

$$[S] + [K^*] + [K^*][\lambda_s^*][S]\{u\} = [K^*]\{u^{CAT}\} \quad (14)$$

Where $[S]$ is the stiffness matrix of the pipe, $\{u\}$ is the pipe displacements, $[\lambda_s^*]$ and $[K^*]$ is related to the soil stiffness, $\{u^{CAT}\}$ is the Greenfield settlement trough. $[K^*]$ and $[\lambda_s^*]$ can be obtained from Mindlin's solution for deformations under a point load (Mindlin, 1936).

In addition to the aforementioned requirements for Attewells model, the following assumptions were made:

- 1) The pipe does not affect the tunnel,
- 2) The soil responds as if the if the tunnel does not exist at pipe level;
- 3) The contact between pipeline and the soil is continuous.

In his paper, Klar used the Gaussian curve (Peck, 1969) to describe the Greenfield settlements.

Vorster *et al.* (2005) studied the effect of pipe stiffness on pipeline response using the elastic continuum solution by Klar *et al.*, (2005). A normalized expression for soil and pipe properties, termed relative rigidity, was defined:

$$R = \frac{E_p I_p}{E_s D_t i^3} \quad (15)$$

Where D_t is the diameter of the tunnel.

Based on the value of the relative rigidity, Vorster divided the soil-pipeline interaction into three different categories:

$R < 0.1$: The pipeline behaves flexibly and follows the soil, hence soil-pipeline interaction need not be considered. The displacements can be estimated by Greenfield conditions alone.

$0.1 < R < 5$: The pipeline exhibits resistance to the soil movement, but the Greenfield settlements have a big influence on the displacements.

$R > 5$: The pipeline resistance is large enough that local mechanisms must be considered and pipe-soil interaction analysis is required. Global Greenfield settlements is not a good prediction of the pipeline displacements.

Furthermore, the normalized hogging and sagging moment in pipelines is a function of the rigidity factor.

Klar and Marshall (2015) identified the volume loss equality as a constraint in the elastic continuum solution by Klar *et al.* (2005). Volume loss equality requires that $\int_{-\infty}^{\infty} u^{gf}(x) dx = \int_{-\infty}^{\infty} u(x) dx$. Based on this, they suggested using one set of parameters to describe the greenfield Gaussian and another set of parameters for the function of the pipeline deflection:

$$u_p(x) = u_{max} * \exp\left(-\frac{x^2}{2i_p^2}\right) \quad (16)$$

The two Gaussian curves can be related using the volume loss constraint, which requires that $s_{max} * i = u_{max} * i_p$. The pipe moment is found by using the second-order differential equation of the deflection curve:

$$M(x) = -\frac{EI d^2 u(x)}{dx^2} \quad (17)$$

$$M(x) = -\frac{EI u_{max}}{i_p^2} \exp\left(-\frac{x^2}{2i_p^2}\right) \left(1 - \frac{x^2}{i_p^2}\right) \quad (18)$$

2.4 Elastic continuum solution using Fourier expansion (Klar, 2018)

The work of Klar et al. (2005) and later papers involved continuum solutions as matrix formulations, which required discretization or approximation of the pipeline deflection profile. Klar (2018) incorporated a Fourier transform in a new solution which does not involve any discretization or approximation along the pipeline. The Fourier based elastic continuum solution is described in this section.

Klar (2018) used the Greenfield displacements, represented by the Gaussian function, as a part of the elastic continuum solution. The solution is later extended to allow any arbitrary load (section 3.1.2). The function is the same as equation 1 in section 2.1.2. This identity is then rewritten as a Fourier integral expansion:

$$u_{gf}(x) = \sqrt{\frac{2}{\pi}} \int_0^\infty U_{gf}(\omega) \cos(\omega x) d\omega \quad (19)$$

Where U_{gf} is the Fourier transform $\mathcal{F}_x[S_{v,max} * \exp(-\frac{1}{2} \frac{x^2}{i^2})](\omega)$ and ω is the wave number with unit $[L^{-1}]$. The result of the Fourier transform is a new Gaussian function in the spatial frequency domain:

$$U_{gf} = S_{v,max} * i * \exp\left(-\frac{1}{2} i^2 \omega^2\right) \quad (20)$$

Where $S_{v,max}$ is the maximum soil displacement and i is the inflection point.

The settlement trough is now expressed as the superposition of cosine functions, as illustrated by figure 6. A finite number of cosine functions gives a reasonable

representation. When the wave number becomes high, the Fourier series becomes the settlement trough.

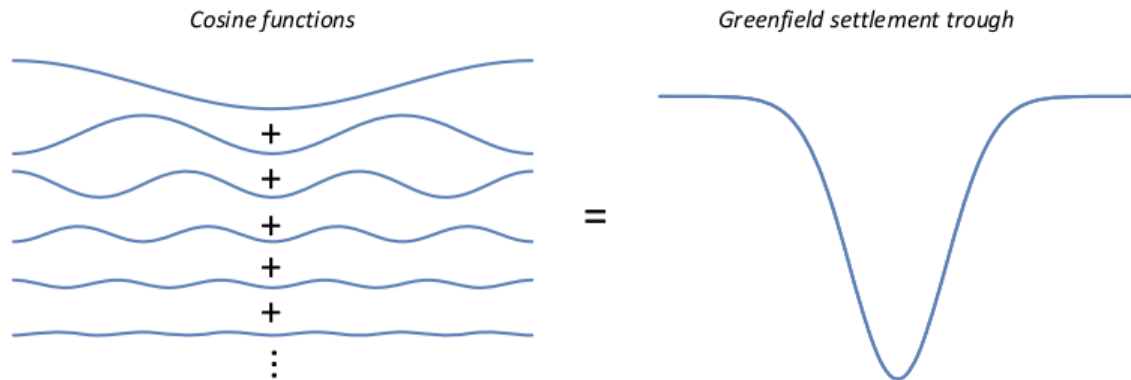


Figure 6: The Gaussian greenfield function is the superposition of cosine functions. From Klar (2018).

Soil-pipeline interaction forces can be represented using discretized section barrel loads. The barrel load is applied uniformly along the cross-sectional perimeter of the pipe. Klar *et al.* (2005) used barrel loads to define the soil-pipeline interaction at discrete points, where every point has a different magnitude. Klar (2018) defined both periodic barrel loads for the Greenfield settlement trough and arbitrary barrel loads – both of which are continuous.

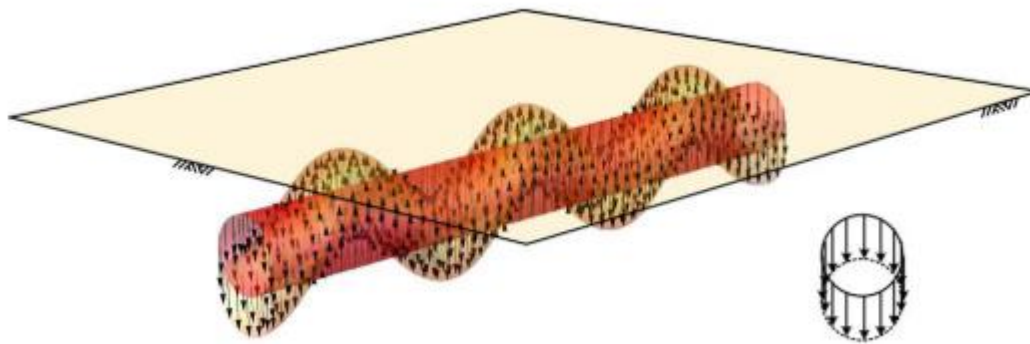


Figure 7: A sinusoidal, periodic barrel load. From Klar (2018).

Klar (2018) presents a sinusoidal periodic barrel load which varies in the horizontal direction (figure 7). A spatial frequency-dependent stiffness is determined by the periodic barrel load and the soil displacements:

$$k_{\omega}(\omega) = \frac{F(\omega)\cos(\omega x)}{U(\omega)\cos(\omega x)} = \frac{F(\omega)}{U(\omega)}, \quad (21)$$

where $F(\omega)$ is the amplitude of the periodic barrel load and $U(\omega)$ is the amplitude of the periodic soil displacements caused by the barrel load. Note that $k_{\omega}(\omega)$ is a constant in a Winkler model, which does not perfectly represent the soil response (Klar, 2018).

The soil displacements can be obtained by convolution of the soil's Greenfield response function to a point load. However, it is necessary to provide a reference point for the soil deformation to evaluate $U(\omega)$ due to the lack of cross-sectional compatibility. Klar (2018) defines the reference point in the centre of the pipe cross-section.

$$u(\omega, x) = \int_0^{2\pi} \int_{-\infty}^{\infty} \cos(\omega\xi) G_f(\theta, x, \xi) r_0 d\xi d\theta \quad (22)$$

Where $G_f(\theta; x, \xi)$ is the Green's function, which can be obtained using Mindlin's point load solution (Mindlin, 1936). The resulting equation, as follows, can be solved numerically:

$$u(\omega, x) = F(\omega) \cos(\omega x) \int_0^{2\pi} \lambda(\omega, \theta) d\theta \quad (23)$$

A closed form solution to $\lambda(\omega, \theta)$ exists and can be solved numerically Klar (2018). At infinite depth, the following analytical closed-form solution is obtained:

$$u(\omega, x) = F(\omega) \cos(\omega x) \frac{(6 - 8\nu)K_0(\omega r_0) + \omega r_0 K_1(\omega r_0)}{16G\pi(1 - \nu_s)} \quad (24)$$

where $K_0(x)$ and $K_1(x)$ are modified Bessel functions of the second, ν_s is Poisson's ratio of the soil and G is the shear modulus of the soil.

Hence, the spatial frequency-dependent stiffness at infinite depth is equal to:

$$k_{\omega, \infty}(\omega) = \frac{F(\omega)}{U(\omega)} = \frac{16G\pi(1 - \nu)}{(6 - 8\nu)K_0(\omega r_0) + \omega r_0 K_1(\omega r_0)} \quad (25)$$

Figure 8a and 8b show the soil stiffness at infinite depth and the normalized soil stiffness at finite depth, respectively. These two figures will be central to the results section of this thesis. It can be seen that the spatial frequency-dependent stiffness approaches zero when the spatial frequency is very low. Likewise, stiffness increases with increasing frequency and more rapidly as it reaches higher values. Figure 8b shows that burial depth has a big effect on spatial frequency-dependent stiffness for shallow pipelines. The difference between deep pipelines ($z_p/r_0 = 8$ and $z_p/r_0 = 16$) is rapidly converging, and the spatial frequency-dependent stiffness approaches the solution for at infinite depth.

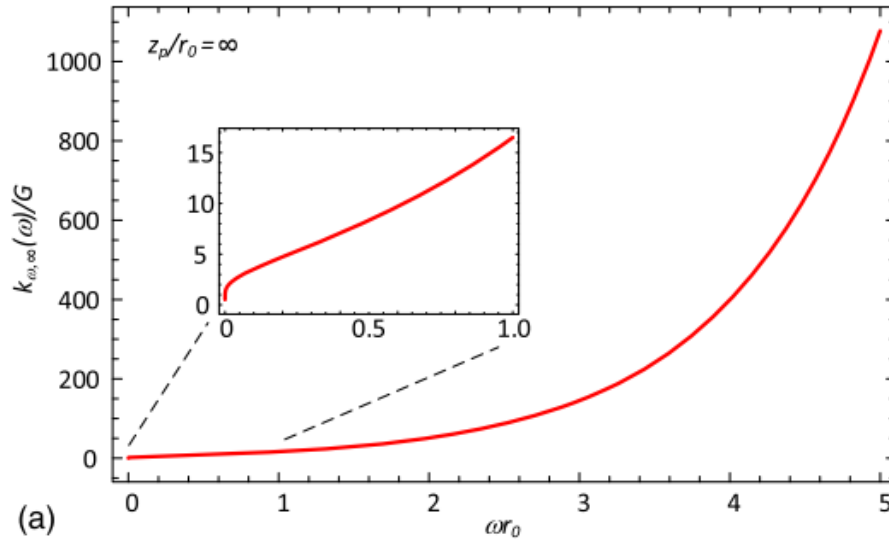


Figure 8a: Spatial frequency-dependent stiffness for a pipeline at infinite depth. From Klar (2018).

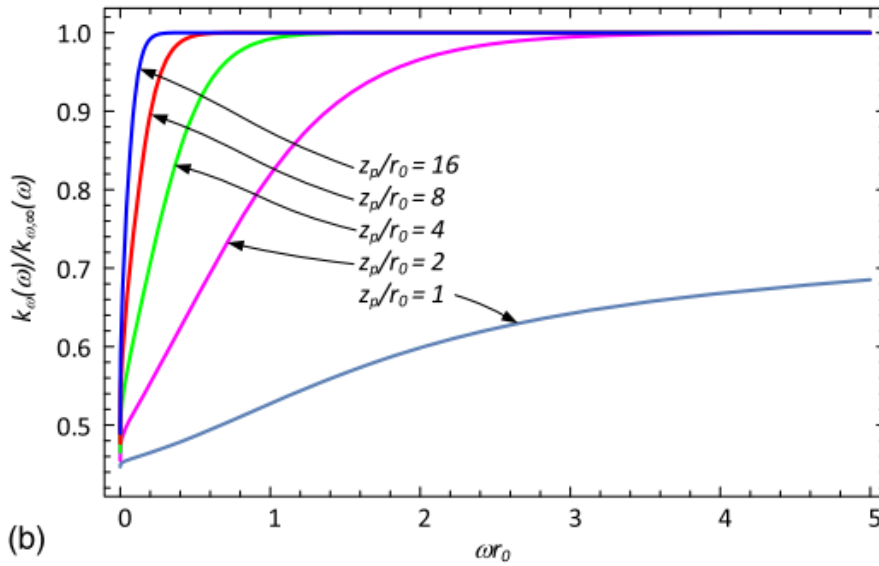


Figure 8b: Spatial frequency-dependent stiffness for different burial depths to pipeline radius ratios normalized by the solution at infinite depth. From Klar (2018).

The pipeline deformation as a response to the periodic Greenfield displacements of the soil is also periodic. Hence, the periodic pipeline displacements can be described by the following function:

$$u_p(x, \omega) = U_p(\omega) \cos(\omega x) \quad (26)$$

Assigning the properties of an Euler-Bernoulli beam to the pipeline, the soil-pipe interaction can be described by the (periodic) fourth order derivative:

$$-EI \frac{\partial^4 u_p(x, \omega)}{\partial x^4} = -EI \omega^4 U_p(\omega) \cos(\omega x) \quad (27)$$

Klar (2018) utilized the compatibility requirement to express the displacement of the pipeline as the superposition of the Greenfield displacements and the soil displacements caused by the pipeline. The resulting expression is as follows:

$$U_p(\omega) \cos(\omega x) = U_{gf}(\omega) \cos(\omega x) - \frac{EI\omega^4 U_p(\omega) \cos(\omega x)}{k_\omega(\omega)} \quad (28)$$

Which can easily be rearranged to obtain the following periodic pipeline displacement:

$$U_p(\omega) = \frac{k_\omega(\omega)}{EI\omega^4 + k_\omega(\omega)} U_{gf}(\omega) \quad (29)$$

The equation above shows that for an infinitely flexible pipeline ($EI = 0$), the pipeline displacement becomes equal to the Greenfield displacements. For a very rigid pipeline, the pipeline displacements approach zero.

It is also possible to express the pipeline deformation in the x-domain by inverse Fourier transform

$$u_p(x) = \sqrt{2/\pi} \int_0^\infty U_p(\omega) \cos(\omega x) d\omega \quad (30)$$

Which, after substituting the identities for $U_p(\omega)$ and $U_{gf}(\omega)$, gives:

$$u_p(x) = \sqrt{\frac{2}{\pi}} \int_0^\infty \frac{k_\omega(\omega)}{EI\omega^4 + k_\omega(\omega)} s_{max} i \exp\left(-\frac{1}{2} i^2 \omega^2\right) \cos(\omega x) d\omega \quad (31)$$

Klar (2018) also provides a solution that incorporates cross-sectional capability with the addition of a Fourier series expansion in the cross-section. Due to the complexity of the solution, only the solution presented above is considered in this thesis. Klar 2018 concluded that the barrel load solution is sufficient when $i/r_0 > 6$. Furthermore, simplified solutions such as the matrix-based continuum solution by Klar (2018) was evaluated, and it was concluded that the deviation of the simplified formulas is small.

2.5 Uplift mechanisms of pipelines buried in sand

Numerous studies have investigated the uplift resistance of a buried pipeline (Trautmann, C. H., O'Rourke, T. D., and Kulhawy, 1985; Schaminee, Zorn and Schotman, 1990; D. J. White, Barefoot and Bolton, 2001; Cheuk, White and Bolton, 2008). Several prediction models for uplift resistance and mobilization distance are available. Current industry practices for dimensioning of pipelines and uplift resistance usually follow the recommendation of DNV-RP-F110 by DNV GL. This thesis focuses on document DNV-RP-F110 by DNV GL but other prediction formulas are included for comparison.

Figure 10 presents a typical load-displacement response from full-scale pipeline pullout experiments such as Schaminee, Zorn and Schotman, (1990). The curves show a non-linear response of the soil-pipe interactions for loose sand and dense sands. They are often modelled as a linear elastic and perfectly plastic model with adequate accuracy. The initial behaviour is nearly linear elastic and soil softening only starts when most of the soil resistance is mobilized. The peak uplift load is typically fully mobilized when the soil displacement is $\partial_p = 0.005$ to $0.010H$ (DNV GL, 2007). Some studies report higher mobilization distances up to $0.015H$ (Trautmann, C. H., O'Rourke, T. D., and Kulhawy, 1985). Bransby *et al.* (2001) observed from finite element models of pipeline pullout tests that pipeline diameter had no effect on the mobilization distance.

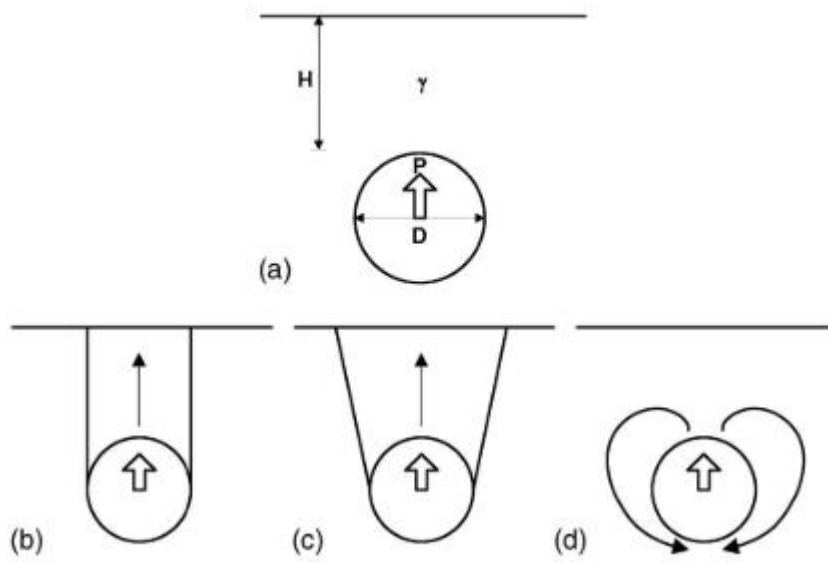


Figure 9: Different proposed pullout mechanisms. After Cheuk, White and Bolton, (2008).

Figure 9 shows the geometry of a buried pipeline with an applied external load. H is the coverage height measured from the top of the pipe. As the pipe starts to move, the soil restrains and resists the upwards movement. Different mechanisms have been suggested based on analytical and experimental models. The most basic prediction model assumes vertical slip surfaces and that the resistance to upwards movement is a combination of shear and the weight of soil. This gives the following formula for peak uplift resistance:

$$P = \left(1 + K \tan \phi \frac{H}{D}\right) \gamma' H D \quad (32)$$

DNV GL suggests using a vertical uplift resistance factor of $f = K * \tan \phi$:

$$P = \left(1 + f * \frac{H}{D}\right) \gamma' H D \quad (33)$$

Where K is the coefficient of earth pressure. Data across several studies show that a good fit is achieved by using at rest earth pressure for loose sand and passive earth pressure for medium or dense sand (DNV GL, 2007). Hence, the expected uplift resistance factor for a pipe buried in medium to dense sand is

$$f = K_p \tan \varphi = \frac{\tan \varphi}{(\sqrt{1 + \tan^2 \varphi} - \tan \varphi \sqrt{1 + r})^2} \quad (34)$$

Where the reference values for the roughness r is -1.00 and -0.97 for medium and dense sand, respectively.

Schaminee, Zorn and Schotman (1990) suggest $f_{LB} = 1.4 * (\tan \varphi - 0.5)$ as a lower bound for f , which DNV GL supports. The values are best used for friction angles below 40° . DNV GL recommends using $f_{UB} = f_{LB} + 0.38$ as the upper bound.

White, Barefoot and Bolton (2001) plotted a collection of uplift experiments and found that the uplift resistance is heavily dependent on relative density. They also carried out pipeline uplift experiments in a geotechnical centrifuge with displacement measurements using particle image velocimetry. The images showed that the incline of the slip surfaces were equal to the dilation angle (dilatancy measured in degrees).

DNV GL uses a trilinear curve to represent the uplift resistance and load-displacement curve, as shown in figure 10. This compares favourably to any elastoplastic model when compared to experimental studies. Data by (Trautmann, C. H., O'Rourke, T. D., and Kulhawy, 1985) supports a β -value around 0.2, and DNV GL suggests using peak uplift displacement ranging from 0.005 to 0.010H. Hence, a linear elastic behaviour is expected for 0.5% to 0.1% of H.

The pulling force at this threshold has been determined experimentally. The fraction of uplift capacity at the breakpoint $\frac{\partial}{\partial f} = \beta$ is denoted α and ranges from:

$\alpha \in [0.75, 0.85]$ for loose sand, and

$\alpha \in [0.65, 0.75]$ for medium or dense sand.

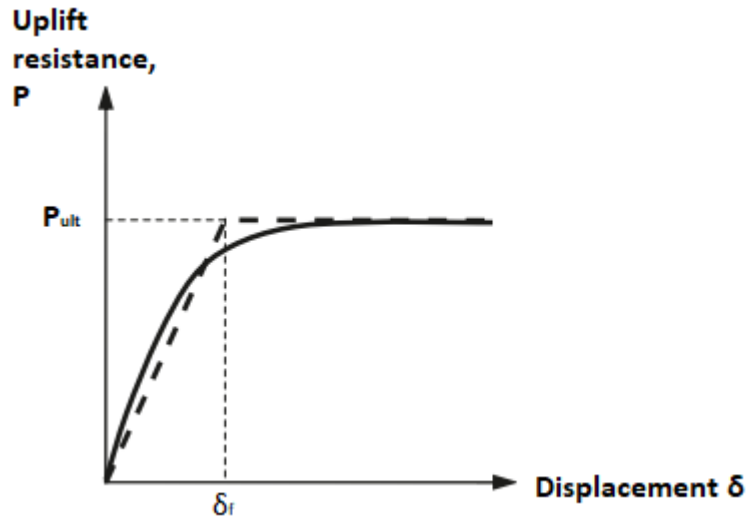


Figure 10a: Typical uplift response of a buried pipeline. After Wang, Shi and Ng, (2011).

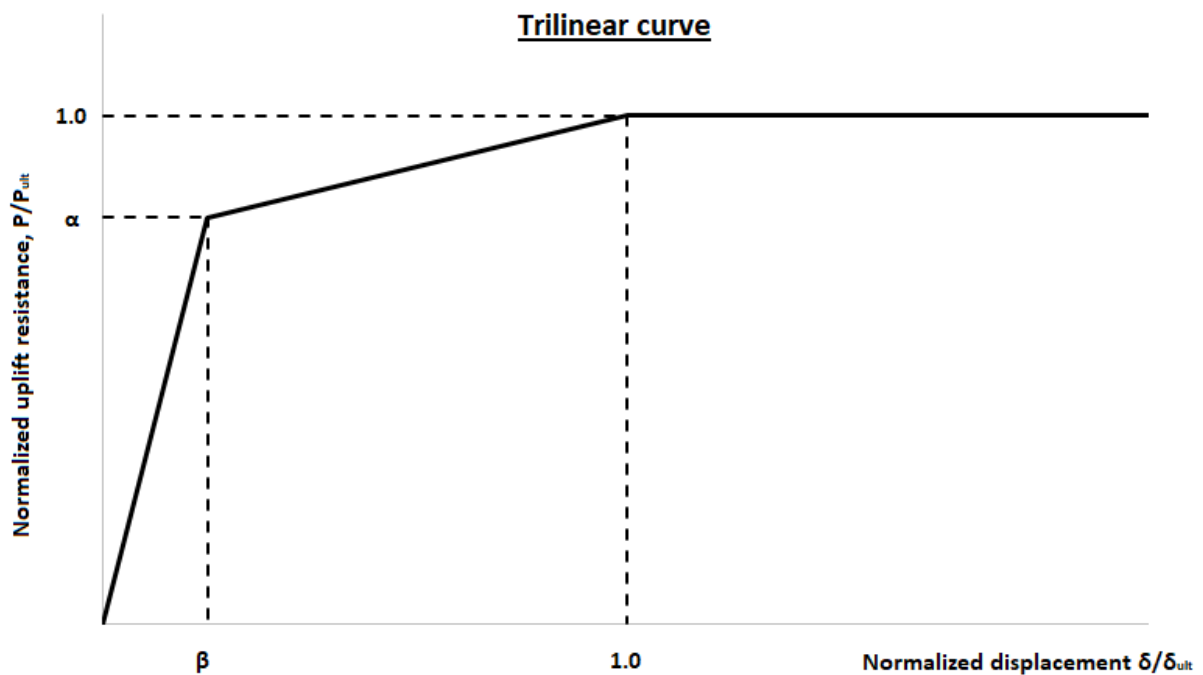


Figure 10b: A simplified trilinear curve after DNV-RP-F110 design recommendations. After (DNV GL, 2007).

Table 1 shows a summary of different prediction formulas of uplift resistance. The formulas are used in section 3.2.4 and show a large spread in the estimated maximum pullout resistance. DNV GL suggests using the pullout capacity by Schaminee, Zorn and Schotman (1990) (table 1), which is conservative for uplift resistance. DNV GL recommends using the

vertical slip line based prediction formula by Schaminee, Zorn and Schotman (1990). However this is in the context of a design criteria and this is conservative for estimating the maximum pullout resistance. The last three prediction formulas are all based on a sliding block mechanism with inclined slip lines, and therefore a more accurate prediction. D. J. White, Barefoot and Bolton (2001) is based on slip lines measured obtained with PIV (particle image velocimetry) in a centrifuge, and is the most rigorous formula. The PIV measurements showed that the incline of the slip lines is identical to the dilation angle ψ .

Table 1: Pullout response prediction formulas and reference.

Pullout resistance	Reference
$P = \gamma'HD + \gamma'H^2K\tan\phi$ (Reference value: $K * \tan(\phi') = 0.4$)	Schaminee, Zorn and Schotman (1990)
$P = \gamma'HD + \gamma'H^2\tan\phi_{max}$	Springman, Ng and Ellis (1994)
$P = \gamma'HD + \gamma'H^2\tan\phi\cos\phi_{crit}$	Vermeer (1985)
$P = \gamma'HD + \gamma'H^2\tan\psi$ $+ \gamma'H^2(\tan\phi_{max} - \tan\psi)$ $* [(1 + K_0) - (1 - K_0) \cos 2\psi/2]$	D J White, Barefoot and Bolton (2001)

2.6 Soil stiffness modelling

The continuum solution presented in this chapter incorporates an idealized isotropic linear elastic soil model. There are many advantages to performing the soil-structure analysis in the elastic domain. First, the elastic constitutive models are simple which makes them suitable for analytical solutions. Furthermore, the parameters are easy to determine and lastly, the required computational is relatively low.

Isotropic linear elasticity requires the following conditions to be satisfied:

- 1) E , ν , and G (or the bulk modulus K) are direction-independent.
- 2) The soil exhibits uncoupled behaviour between volumetric and shear responses.
- 3) Strains are recovered upon unloading.
- 4) E and ν are stress independent.

Generalized Hook's law is valid for isotropic soils and this leads to the following expression for the shear modulus:

$$G = \frac{E}{2(1 + \nu)} \quad (35)$$

Soils initially exhibit linear stress-strain response when loaded. This behaviour is restricted to small shear strains and the stress-strain curves become non-linear after yielding. Elastic or elastoplastic models cannot capture the behaviour of soil if large deformations take place. Figure 11 shows different types of idealized elastic and elastoplastic soil models.

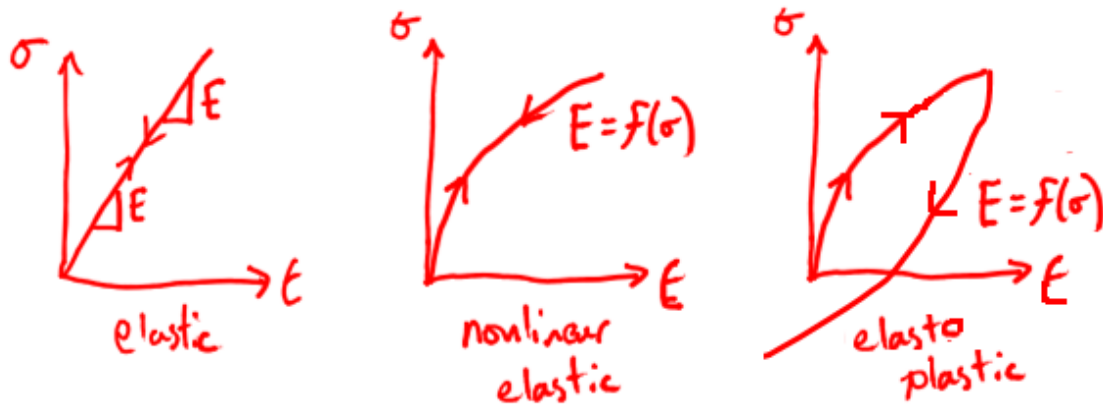


Figure 11: Three idealized soil models. The elastoplastic model shows the hysteresis that soil typically exhibit. Modified from class notes in SE248 at University of California, San Diego.

Figure 12 shows the stiffness degradation curves and stress levels of a typical sand, after. All soils have a maximum strain amplitude, the linear threshold strain γ_{tl} , which separates the very small strain regime from the small strain regime. The soil stiffness is nearly constant below this threshold value. A synthesis of published laboratory experiments by Vucetic (1994) indicate a linear elastic response for shear strain amplitudes up to 0.001 (i.e $\gamma_{tl} = 0.1\%$). Wichtman & Triantafyllidi (2010) obtained similar values for sandy soils. Stiffness decays rapidly in the small strains range. Between the linear threshold strain γ_{tl} and the volumetric threshold strain γ_{tv} , soil shows non-linear but elastic behaviour. No volume change or permanent changes occur and strains are still recoverable up to γ_{tv} , which is in the order of 0.01% for sands (Jia 2018). The reduction in shear strength when $\gamma = \gamma_{tv}$ varies greatly, from 0.6 and 0.85. For strains larger than γ_{tv} , soil deformations become irrecoverable. Another threshold value marks the beginning of the large strain range, where the stiffness is relatively small compared to the initial stiffness. Since the elastic continuum model assumes linear elastic behaviour, it is important to limit strains during experiments as much as possible.

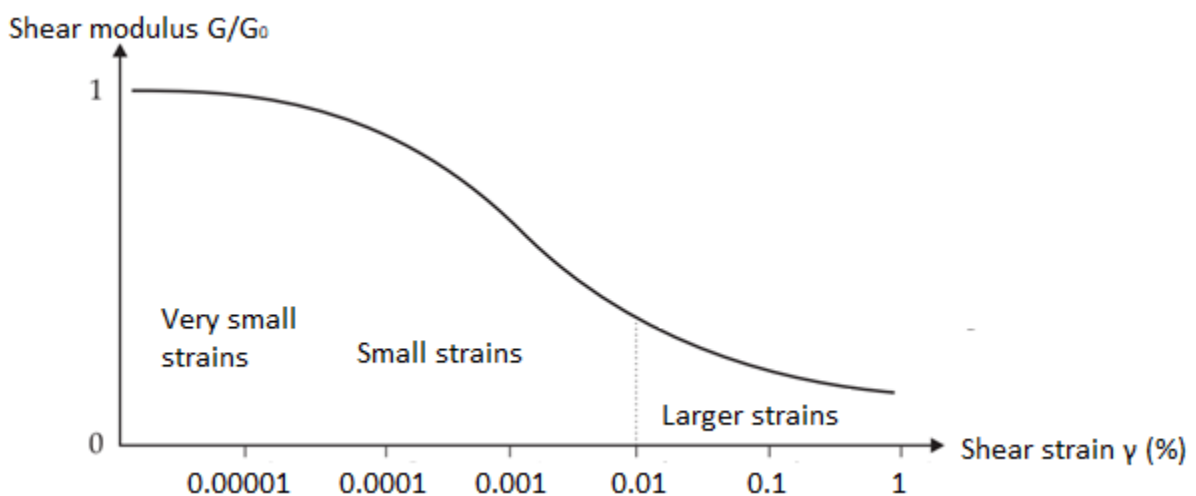


Figure 12: Typical stiffness degradation with increasing strains. After (Mair, 1993).

Table 2 shows the influence of different soil parameter on the stiffness of sands. Strain amplitude has already been covered in the previous paragraph; soil stiffness is conserved only at very small strains. The stiffness and rate of stiffness reduction with increasing strains are influenced by other soil parameters.

Table 2: Effect of different parameters on small-strain stiffness. After (Hardin and Drnevich, 1972) and Benz (2007).

Parameter	Impact on initial stiffness G_0	Impact on stiffness degradation
Strain amplitude	Important	Important
Confining stress	Important	Important
Void ratio	Important	Unimportant
Strain rate	Unimportant	Unimportant
Grain properties	Less important	Less important
Dilatancy	Unimportant	Unimportant

Soil stiffness is known to be dependent on confining stress – the larger the confining stress, the higher the stiffness. (Hardin and Richart Jr, 1963) proposed a power law between the initial shear modulus G_0 and the effective confining stress p' ,

$$G_0 \propto (p')^m \quad (36)$$

$m = 0.5$ is generally used for sands. The same paper also investigated the effect of void ratio in Ottawa sand. They proposed the following relationship between initial shear modulus G_0 and void ratio e :

$$G_0 \propto \frac{(2.17 - e)^2}{1 + e} \quad (37)$$

for round sand grains, and

$$G_0 \propto \frac{(2.97 - e)^2}{1 + e} \quad (38)$$

for angular sand grains.

Two simple formulas provide a good estimate of the stiffness, taking into account the density and confining stress. Biarez, Hicher and others, (1994) proposed that the initial Young's modulus E_0 (for granular soils and most fine-grained soils) depends on p' and e according to the following identity:

$$E_0 = \frac{140}{e} \sqrt{\frac{p'}{p_{ref}}} [MPa] \quad (39)$$

Hardin and Black (1969) proposed that G_0 for clayey soils and crushed sands is:

$$G_0 = 33 \frac{(2.97 - e)^2}{1 + e} \sqrt{\frac{p'}{p_{ref}}} [MPa] \quad (40)$$

Stiffness degradation defines the stiffness the decay of the true shear modulus G (i.e G/G_0) as a function of shear strain. Other than the strain amplitude, the most important parameter for small strain stiffness is confining stress. Wichtmann and Triantafyllidis (2009) carried out laboratory experiments on dry sands and found that the decay of the shear modulus is greatly influenced by strain rate in the small strain range. The soil behaviour is significantly more non-linear at low confining stress. On the other hand, void ratio does not affect the rate of stiffness decay with strain amplitude. Furthermore, strain rate only has a very minor effect on stiffness in the small-strange range based on many laboratory experiments and authors (Benz, 2007).

In summary, strain amplitude, confining stress and void ratio must be carefully considered for the laboratory 1G and centrifuge models. The most critical parameter is strain amplitude, which should ideally not exceed the small strain range to get good values for the continuum solution. While all analytical and finite element models will assume that stiffness is constant over the course of the simulation, this is not necessarily actually the case during laboratory experiments.

2.7 Centrifuge modelling

2.7.1 Scaling effects

Physical modelling in geotechnical engineering is a difficult task. The biggest challenge is that soil properties changes with stress and stress changes with depth. Testing of full-scale models is time-consuming, expensive and often impractical, therefore using a reduced scale model is common. A geotechnical centrifuge is a useful tool that allows scaling down a model while replicating the full-scale behaviour. By accelerating the package at the end of an arm, the soil essentially experiences a higher gravity than Earth's gravity. The model is accelerated so that gravity is increased from g to $n * g$ and the soil becomes n times heavier. In other words, stress can be scaled by a factor of n between the centrifuge model and the 1G prototype. Similarly, the strains also scale one-to-one. This ensures identical stress-strain curves between the model and the prototype which in turn gives similar behaviour.

With an n times increase in gravity and unaffected density (assuming negligible compaction of the soil), the stress at a depth z_m in the model is given by:

$$\sigma_{vm} = \rho n g z_m \quad (41)$$

The stress in the prototype is given by:

$$\sigma_{vp} = \rho g z_p \quad (42)$$

The model stress and the prototype stress is equal when $h_m = h_p/n$, hence the scale factor for lengths between the model and the prototype is $1/n$. Vertical stress is identical at depth z_m in the model and depth $z_p = n * z_m$ in the prototype. Measurements in the represent prototype parameters when multiplied by the scaling factor.

Other scaling laws in geotechnical engineering are summarized in table 3. It is particularly important to note that not only stresses but also strains are the same in the model and the prototype. The axial stiffness scales by a factor of n^2 , as

$$\frac{E_p A_p}{E_m A_m} = n^2 \quad (43)$$

Likewise, the bending stiffness scales as

$$\frac{E_p I_p}{E_m I_m} = n^4 \quad (44)$$

Table 3: Scaling laws in the centrifuge

Parameter	Notation	Unit	Scaling Law (model/prototype)
Gravity	G	m/s ²	n
Length	L	m	1/n
Area	A	m ²	1/n ²
Volume	V	m ³	1/n ³
Force	F, P	N = kg m/s ²	1/n ²
Density	ρ	kg/m ³	1
Unit Weight	γ	N/m ³	n
Stress	σ	N/m ²	1
Strain	ϵ or γ	- or %	1
Bending stiffness	EI	N/m ²	1/n ⁴
Axial stiffness	EA	N	1/n ²
Moment	M	Nm	1/n ³
Time	t	t	1/n

The scaling factor is decided by the centrifuge operator after the following relationship:

$$n = \frac{\omega^2 * R_e}{g} \quad (45)$$

Where ω is the angular velocity and R_e is the centrifuge radius at a reference location at model level.

Formula 45 reveals a weakness of centrifugal modelling. Since the acceleration depends on the distance to the axis of spin, the gravity experienced by the model soil at the surface and the bottom is not the same. This gives a non-linear stress distribution, which deviates from the prototype, and could lead to significantly different behaviour if the model is tall enough. Figure 13 compares the stress with depth in a centrifuge model and the corresponding prototype. Using 1/3 of the height as the reference level minimizes the error (Taylor, 1995). The model is under-stressed in the top two thirds and overstressed in the bottom third of its height. The maximum error in stress can be calculated as follows (Taylor, 1995):

$$\frac{h_m}{6R_e} * 100\% \quad (46)$$

if $R_e = R_t + h_m/3$, where R_t is the centrifuge radius at the top of the model.

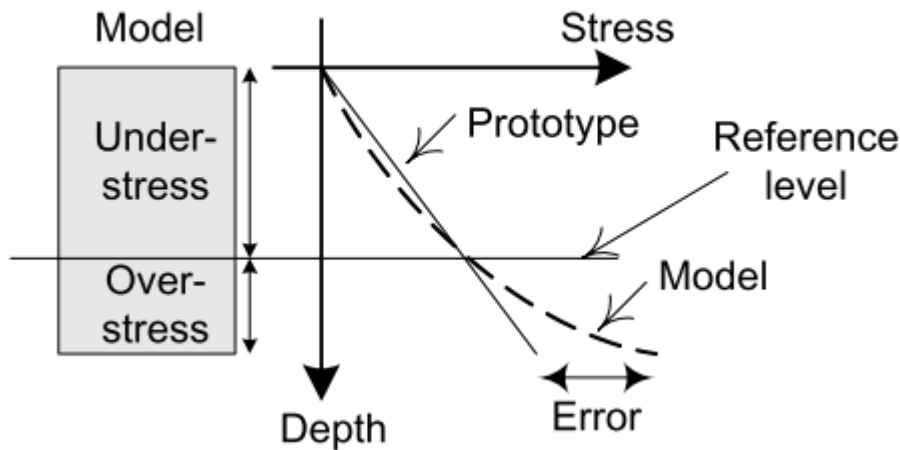


Figure 13: Comparison of stress in the centrifuge and the corresponding prototype. Notice the non-linear stress increase in the centrifuge model. From DTU internal document.

The errors are small for most geotechnical centrifuge experiments. For h_m/R_e less than 0.2, the maximum error is less than 3% for a typical model (Taylor, 1995). The maximum error occurs at the bottom of the sample and the error is relatively small above the reference level.

Similar to how the centrifuge radius is different at the top and the bottom, there is also a radial divergence which depends on the width of the model. The error is considered small if (Mair, 1979):

$$W / 0.5 * (R_t + R_b) < 0.2 \quad (47)$$

This is much more of a concern if a water table is present as it will be curved by the radial acceleration field.

2.7.2 Particle size limitations

The scaling laws also apply to soil grains and an important question is: should the soil particles be scaled down too? The answer is generally no, as this changes the stress-strain characteristics of the soil. For example, it would require using clay in the centrifuge to model a prototype with fine sand. This is obviously flawed and the grain size does not scale with a factor of N - for example, clay exhibits cohesion. By using the same type of soil that exists for the prototype, friction angle and soil density is conserved. Centrifuge experiments between 1 g and up to 120 g by (Byrne *et al.*, 2004) showed a change in relative density of 4%; For 50-60g, the change in relative density should be around 2%.

Soil generally behaves like a continuum and for modelling purposes, it makes more sense to not scale the particle size. Instead, the relative size of the model and the particles should be set according to guidelines. Phillips and Valsangkar (1987) suggest that the ratio of model structure to average particle size should be higher than 25 to 36. However, the value depends on the test and guidelines specific to different test types are available. Garnier *et al.* (2007) made a catalogue which includes the grain size effects on soil-structure interaction. No minimum pipeline diameter to grain size is established. Results in literature are consistent between centrifuge models and prototypes for uplift resistance. On the other hand, the mobilization distance does not scale but are in fact the same for the centrifuge model and the prototype *unscaled*. This indicates that mobilization distance is independent of the pipeline diameter, which is consistent with the finite element study by Bransby *et al.* (2001). Garnier *et al.* (2007) also report that the roughness of the model surface affects the scaling of shear strength mobilization. However, the roughness to grain size does not need to be scaled for a perfectly smooth interface. The interface is perfectly smooth for $R_{max}/d_{50} < 0.01$, which is the case for new aluminium and PVC pipes in sand.

2.8 Particle image velocimetry (PIV)

Particle Image Velocimetry (PIV) is a technique to measure displacement or velocity with digital photographs. The PIV method compares the particle position between two or more consecutive pictures. It was originally developed for velocity measurements in experimental fluid mechanic by capturing the movement of seeding particles. Particles are tracked individually if the number of seeding particles is low. If the seeding density is high, the image is divided into small interrogation areas, or meshes, with many particles. The movement is captured by interpolating and cross-correlation each mesh between two images.

Particle Image Velocimetry is also suitable for measurements in soil. In geotechnical engineering, most experiments have relatively low velocities and a high-speed camera is not required. Sand grains have a variety range of colours, therefore PIV can track the natural texture of the sand. Texture must be added to clays (White and Take, 2002).

The basic principle of PIV-analysis is presented by (White and Take, 2002) in figure 14. Frame 1 is split into small patches and the PIV software attempts to find the new position of each patch in frame 2. As can be seen from figure 14, the highest degree of correlation appears as a spike within the search patch. Finally, the PIV software returns the displacement vector by comparing the original coordinates of the patch and the new coordinates at this spike. The process can be repeated in by comparing a third consecutive picture with picture two, and so on.

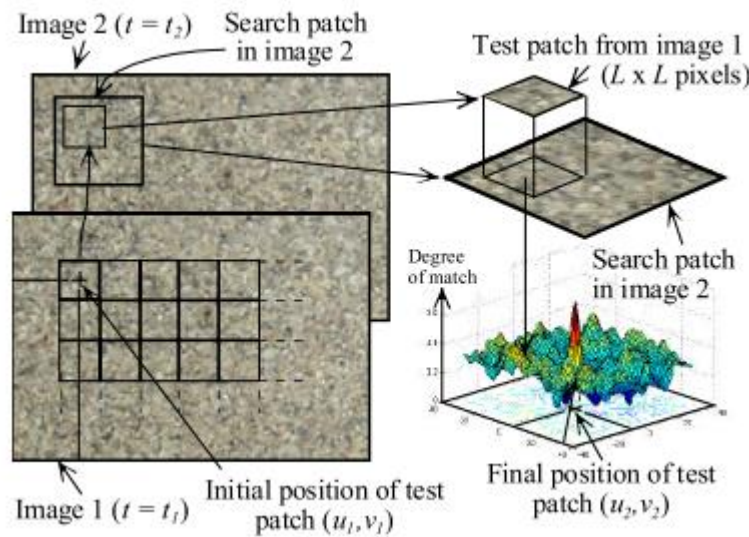


Figure 14: Correlation algorithm for the GeoPIV software. From White and Take, (2002).

A single camera captures 2D movement along a cross-section and the third displacement is invincible. Hence, the PIV technique is most suitable when particles do not change their position in this direction. Soil will generally move parallel to the window and many geotechnical engineering problems can be modelled in 2D. A symmetry cut is available for some 3D problems.

White and Take (2002) have developed a particle image velocimetry software specifically for soils, which will be used in this thesis. The MATLAB-based PIV software tracks spatial variation of brightness between images of soil. The accuracy is much higher than traditional PIV packages, which generally struggle with the obscurity present in soil texture. Validation tests by (White and Take, 2002) indicate that precision is a strong function of mesh size. (White and Take, 2002) provides a relationship between the precision and measurement array size, which is related to the interrogation patch size. The number of measurement points is equal to

$$n_{points} = \frac{WH}{L^2} \quad (48)$$

Where W and H is the width and height of the images, and L is the patch size.

More measurements points and a larger patch gives improves the precision.

White and Take (2002) also provide an empirical formula for the upper bound on error in pixels:

$$\rho_{pixel} = \frac{0.6}{L} + \frac{150000}{L^8} \quad (49)$$

The GeoPIV procedure is further explained in the methodology section.

3 Methodology

3.1 Theoretical framework

3.1.1 The Fourier series expansion of a function

Periodic functions may be expressed as a sum of sine and cosine terms, called a Fourier series. If $f(x)$ is a piecewise linear function in $-L < x < L$, then it can be expanded in a Fourier series as follows:

$$f(x) = \frac{a_0}{2} + \sum_{n=1}^{\infty} a_n \cos\left(\frac{n\pi x}{L}\right) + b_n \sin\left(\frac{n\pi x}{L}\right) \quad (50)$$

Where the Fourier coefficients a_0 , a_n and b_n are constants. By multiplying equation 50 with $\cos\left(\frac{n\pi x}{L}\right)$ or $\sin\left(\frac{n\pi x}{L}\right)$ and using orthogonality relations, one will find that the Fourier coefficients are given by

$$a_n = \frac{1}{L} \int_{-L}^L f(x) \cos\left(\frac{n\pi x}{L}\right) dx \quad (51)$$

$$b_n = \frac{1}{L} \int_{-L}^L f(x) \sin\left(\frac{n\pi x}{L}\right) dx \quad (52)$$

A useful and equivalent expression is:

$$f(x) = \sum_{n=-\infty}^{\infty} c_n e^{\frac{in\pi x}{L}} \quad (53)$$

$$\text{Where } c_n = \begin{cases} (a_n - ib_n)/2 & n < 0 \\ (a_n + ib_n)/2 & n > 0 \\ a_0/2 & n = 0 \end{cases}$$

Fourier series are useful for their ability to describe functions that are not continuous or differentiable as well as being easy to integrate and differentiate. Furthermore, each term is described in the Fourier expansion contains one characteristic frequency. This is particularly important for describing the response to a periodic input since the response usually is dependent on the frequency.

Take, for example, an even square wave function alternating in amplitude between h and $-h$ at an interval L (figure 15). By symmetry, we know that the cosine term $b_n = 0$ for all n . The a_n coefficients are found with formula 51:

$$a_n = \frac{1}{L} \int_{-L}^L f(x) \cos\left(\frac{n\pi x}{L}\right) dx \quad (54)$$

$$= \frac{2h}{n\pi} \left[\int_0^{L/2} \cos\left(\frac{n\pi x}{L}\right) dx - \int_{L/2}^L \cos\left(\frac{n\pi x}{L}\right) dx \right] \quad (55)$$

$$= \frac{2h}{n\pi} \left[\sin\left(\frac{n\pi x}{L}\right) \Big|_0^{L/2} - \sin\left(\frac{n\pi x}{L}\right) \Big|_{L/2}^L \right] \quad (56)$$

$$= \begin{cases} \frac{4h}{n\pi} (-1)^{n-1} \\ 2 \\ 0 \end{cases} \quad (57)$$

$$\Rightarrow f(x) = \frac{4h}{\pi} \left(\cos\left(\pi * \frac{x}{L}\right) - \frac{1}{3} \cos\left(\frac{3\pi x}{L}\right) + \frac{1}{5} \cos\left(\frac{5\pi x}{L}\right) \dots \right) \quad (58)$$

Plotting the first partial sums demonstrates the convergence of the Fourier series:

$$p1 = \frac{4h}{\pi} \left(\cos\left(\pi * \frac{x}{L}\right) \right)$$

$$p2 = \frac{4h}{\pi} \left(\cos\left(\pi * \frac{x}{L}\right) - \frac{1}{3} \cos\left(\frac{3\pi x}{L}\right) \right)$$

$$p3 = \frac{4h}{\pi} \left(\cos\left(\pi * \frac{x}{L}\right) - \frac{1}{3} \cos\left(\frac{3\pi x}{L}\right) + \frac{1}{5} \cos\left(\frac{5\pi x}{L}\right) \right)$$

$$p4 = \frac{4h}{\pi} \left(\cos\left(\pi * \frac{x}{L}\right) - \frac{1}{3} \cos\left(\frac{3\pi x}{L}\right) + \frac{1}{5} \cos\left(\frac{5\pi x}{L}\right) - \frac{1}{7} \cos\left(\frac{7\pi x}{L}\right) \right)$$

$$p5 = \frac{4h}{\pi} \left(\cos\left(\pi * \frac{x}{L}\right) - \frac{1}{3} \cos\left(\frac{3\pi x}{L}\right) + \frac{1}{5} \cos\left(\frac{5\pi x}{L}\right) - \frac{1}{7} \cos\left(\frac{7\pi x}{L}\right) + \frac{1}{9} \cos\left(\frac{9\pi x}{L}\right) \right)$$

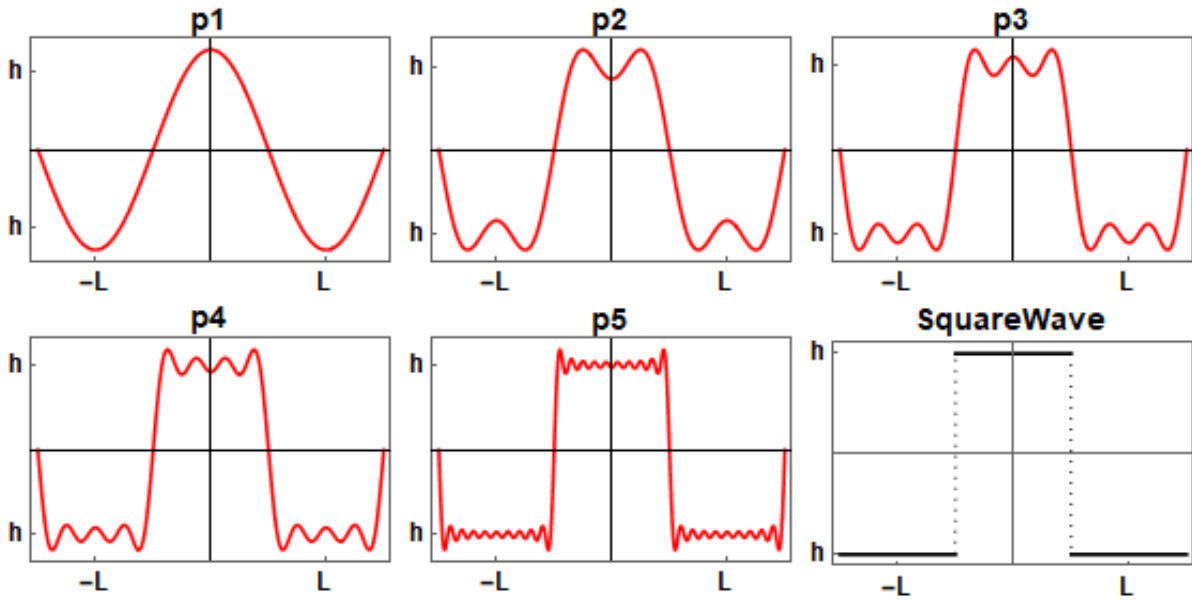


Figure 15: The square wave function as a Fourier series with an increasing number of harmonics.

It is clear from figure 15 that a finite number of terms n can be used to approximate the function. The amplitude spectrum decays by $1/n$, thereby allowing the representation of the function with only a few harmonics. By the 4th term, the shape of the represented square wave function is already obvious. Another fact demonstrated in figure 15 is the poor convergence around the discontinuities. The decay of the amplitude spectrum is faster for continuous function and, generally, the smoother the function, the faster the decay. Hence, fewer terms are needed to reach the required accuracy. For describing the response of a pipe at finite depth, (Klar, 2018) concluded that four terms are sufficient for normalized spatial frequency smaller than $\omega r_0 < 10$.

The Fourier transform represents a function defined over an infinite interval as a superposition of sinusoidal. It is required that $\int_{-\infty}^{\infty} |f(x)| dx$ is finite. To define the Fourier transform, it is natural to rewrite equation 53:

$$f(x) = \sum_{-\infty}^{\infty} c_n e^{\frac{in\pi x}{L}} = \sum_{-\infty}^{\infty} c_n e^{i\omega x}, \quad (59)$$

here the spatial frequency is

$$\omega = \frac{2\pi n}{L}$$

If the period L approaches infinity, and $\Delta\omega$ becomes infinitesimally small, the sum becomes the integral

$$f(\omega) = \frac{1}{2\pi} \int_{-\infty}^{\infty} f(x) e^{-i\omega x} dx \quad (60)$$

This result defines the Fourier transform. It is convenient to write the Fourier transform using the factor $1/\sqrt{2\pi}$:

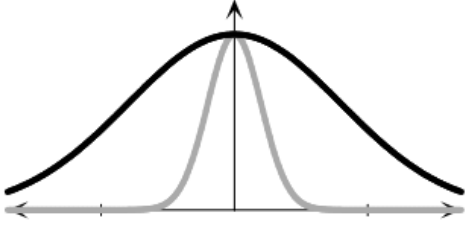
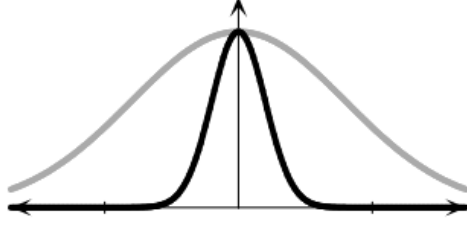
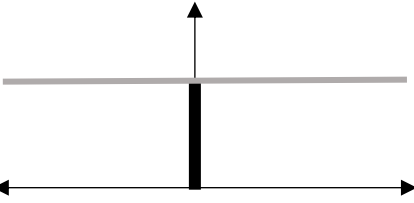
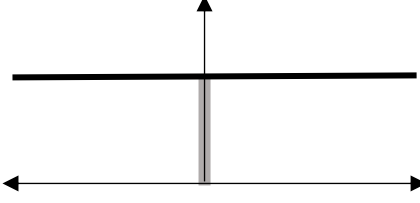
$$\tilde{f}(\omega) = \frac{1}{\sqrt{2\pi}} \int_{-\infty}^{\infty} f(x) e^{-i\omega x} dx, \quad (61)$$

which makes the inverse

$$f(x) = \frac{1}{\sqrt{2\pi}} \int_{-\infty}^{\infty} \tilde{f}(\omega) e^{-i\omega x} d\omega \quad (62)$$

An interesting feature is that the Fourier transform of a Gaussian is also a Gaussian. Furthermore, the Fourier transform conserves the width of the waveform; The width of the transformed waveform is the inverse of the original width. Table 4 summarizes some useful Fourier transforms.

Table 4: Relevant Fourier transforms in this thesis

<p>Gaussian</p> $f(x) = 1/\sqrt{2\pi x_0^2} e^{-t^2/2x_0^2}$ 	<p>Gaussian</p> $f(\omega) = e^{-\omega^2 x_0^2/2}$ 
<p>Delta dirac – "impulse function"</p> $f(t) = A\delta(t)$ 	<p>"Broadband function"</p> $f(\omega) = A$ 

3.1.2 Elastic continuum solution for a point load using Fourier expansion

This section summarizes a general elastic continuum solution taking into account the rotation of the element, as well as a degenerated solution for a concentrated load with no rotation of the element. The solution is derived from the continuum solution by Klar (2018). The degenerated solution is used later in this thesis.

The solution makes the following assumptions:

- a) The deformation of the beam and the soil are both elastic
- b) The beam behaves like an Euler-Bernoulli beam
- c) The function describing the pipeline deformation is periodic

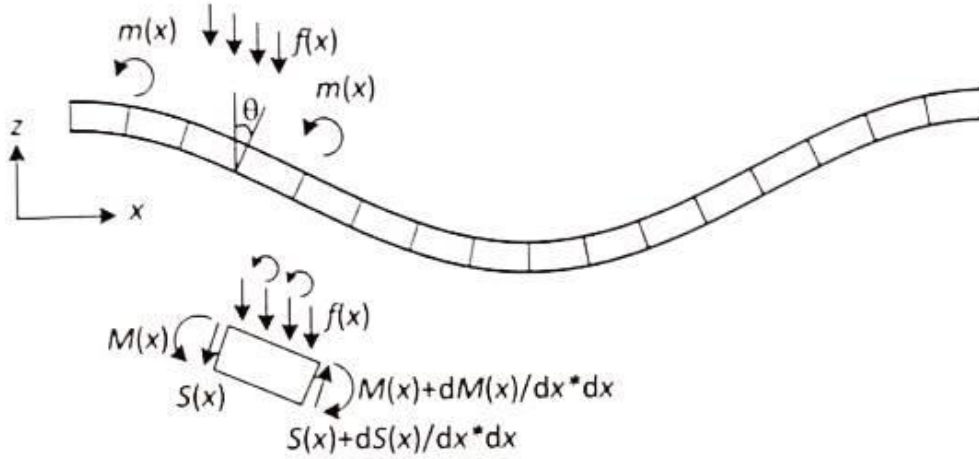


Figure 16: Forces in a beam element as a response to a load $f(x)$. Modified after an internal DTU document by professor Klar.

Figure 16 shows the internal forces as the result of an arbitrarily distributed load along the pipeline. Moment equilibrium of a differential element gives:

$$\frac{dM(x)}{dx} dx = m(x) * dx + S(x) * dx + f(x) * dx * \frac{dx}{2} \quad (63)$$

$$\frac{dM(x)}{dx} = m(x) + S(x) + f(x) * \frac{dx}{2} \quad (64)$$

The last term can be ignored since dx is infinitesimally small.

Based on Euler–Bernoulli beam theory and the beam equation $M(x) = -EI \frac{d^2 u(x)}{dx^2}$:

$$-EI \frac{d^4 u(x)}{dx^4} = \frac{dm(x)}{dx} + \frac{dS(x)}{dx} \quad (65)$$

Internal vertical equilibrium of the differential element requires that $\frac{dS(x)}{dx} = f(x)$, which results in:

$$-EI \frac{d^4 u(x)}{dx^4} + f(x) + \frac{dm(x)}{dx} = 0 \quad (66)$$

The corresponding equation in a Winkler system is

$$-EI \frac{d^4 u(x)}{dx^4} + k_{vv} u(x) + \frac{d(k_{\theta\theta} \theta(x))}{dx} = 0 \quad (67)$$

Finally, inserting $\theta(x) = -\frac{du(x)}{dx}$ gives:

$$-EI \frac{d^4 u(x)}{dx^4} + k_{vv} u(x) + k_{\theta\theta} \frac{d^2 u(x)}{dx^2} = 0 \quad (68)$$

For a harmonic function:

$$\omega^4 EI U_p + k_{vv} U_p - \omega^2 k_{\theta\theta} U_p = 0 \quad (69)$$

The deformation pattern of an Euler-Bernoulli beam in the frequency domain is defined as follows:

$$u_{zp}(x) = U_p \cos(\omega x) \quad (70)$$

$$u_{xp}(x, z) = U_p \omega \sin(\omega x) (z - Z_p) = \theta_p \sin(\omega x) (z - Z_p) \quad (71)$$

Similarly, the soil along the beam will have the following deformation pattern:

$$u_z(x) = U_z \cos(\omega x) \quad (72)$$

$$u_x(x, z) = \theta \sin(\omega x)(z - Z_p) \quad (73)$$

The soil resistance can now be defined as:

$$f(x) = F \cos(\omega x) = k_{\omega vv} \cos(\omega x) U_z + k_{\omega v\theta} \cos(\omega x) \theta \quad (74)$$

$$fm(x) = M \cos(\omega x) = k_{\omega \theta v} \cos(\omega x) U_z + k_{\omega \theta \theta} \cos(\omega x) \theta \quad (75)$$

On matrix form:

$$\begin{Bmatrix} F \\ M \end{Bmatrix} = \begin{bmatrix} k_{\omega vv} & k_{\omega v\theta} \\ k_{\omega \theta v} & k_{\omega \theta \theta} \end{bmatrix} \begin{Bmatrix} U_z \\ \theta \end{Bmatrix} \quad (76)$$

Where $k_{\omega vv}$, $k_{\omega v\theta}$, $k_{\omega \theta v}$ and $k_{\omega \theta \theta}$ are spatial frequency-dependent stiffness accounting for rotation of the elements.

The invertible matrix theorem gives the following flexibility modal matrix:

$$\begin{Bmatrix} U_z \\ \theta \end{Bmatrix} = \begin{bmatrix} \lambda_{\omega vv} & \lambda_{\omega v\theta} \\ \lambda_{\omega \theta v} & \lambda_{\omega \theta \theta} \end{bmatrix} \begin{Bmatrix} F \\ M \end{Bmatrix} \quad (77)$$

Where

$$\begin{aligned} \lambda_{\omega vv} &= \frac{k_{\omega \theta \theta}}{k_{\omega vv} k_{\omega \theta \theta} - \lambda_{\omega v\theta}^2} \\ \lambda_{\omega v\theta} &= \lambda_{\omega \theta v} = \frac{k_{\omega v\theta}}{\lambda_{\omega v\theta}^2 - k_{\omega vv} k_{\omega \theta \theta}} \\ \lambda_{\omega \theta \theta} &= \frac{k_{\omega vv}}{k_{\omega vv} k_{\omega \theta \theta} - \lambda_{\omega v\theta}^2} \end{aligned}$$

Since the beam and soil deform elastically, the superposition principle can be used. Vertical and rotational compatibility gives the following equations:

$$U_p \cos(\omega x) = U_{gf} \cos(\omega x) + U_z \cos(\omega x) \quad (78)$$

$$U_p = U_{gf} + (\lambda_{\omega vv}F + \lambda_{v\omega\theta}M), \quad (79)$$

and

$$\theta_p \sin(\omega x) = \omega U_p \sin(\omega x) = \theta_{gf} \sin(\omega x) + \theta \sin(\omega x) \quad (80)$$

$$\omega U_p = \theta_{gf} + (\lambda_{\omega v\theta}F + \lambda_{v\theta\theta}M) \quad (81)$$

The three unknowns are U_p , F and M . Three equations represent the pipeline behaviour:

$$-EI \frac{d^4 u(x)}{dx^4} + f(x) + \frac{dm(x)}{dx} = 0 \quad (82)$$

$$-EI \frac{d^4 (U_p \cos(\omega x))}{dx^4} + F \cos(\omega x) + \frac{d(M \sin(\omega x))}{dx} = 0 \quad (83)$$

$$\omega^4 EI U_p + F - \omega M = 0 \quad (84)$$

A solution of the three equations exists:

$$U_p = \frac{k_{vv} + \omega \left(k_{v\theta} + k_{\theta\theta} * \frac{\theta_{gf}}{U_{gf}} \right) + k_{v\theta} \frac{\theta_{gf}}{U_{gf}}}{EI\omega^4 + k_{vv} + 2k_{v\theta}\omega + k_{\theta\theta}\omega^2} U_{gf} \quad (85)$$

A degenerated solution exists for a point load (Appendix A.4):

$$\omega^4 EI U_p + F + \omega M = A_\omega \quad (86)$$

$$U_p = \frac{A_\omega}{EI\omega^4 + k_{vv} + 2k_{v\theta}\omega + k_{\theta\theta}\omega^2} \quad (87)$$

For a smooth pipeline, $k_{\theta\theta} = 0$ and $k_{v\theta} = 0$, the equation becomes

$$U_p = \frac{A_\omega}{EI\omega^4 + k_{vv}} \quad (88)$$

3.2 DTU geotechnical centrifuge

The DTU BYG geotechnical beam centrifuge has a capacity of 100 g-ton and can provide a gravitational acceleration of up to 95 g. The front page of this thesis shows the centrifuge with the attached strongbox and counterweight. The centrifuge radius from the axis of rotation to the hinge is 1.7 meters. The U-shaped yoke in the picture adds another 0.63 m, making the distance to the platform radius is 2.63 m. The DTU centrifuge can accelerate up to 350 kg of soil and test components. Sand samples can be prepared in the centrifuge facilities using sand rain or spot pouring methods.

A flight computer is located on the centrifuge and is remotely controlled from the control room. The centrifuge computer system has connections for up to two USB ports, 12 analogue inputs and 2 analogue outputs. The data acquisition system in this study consists of a load cell and a digital camera, connected to one of the analogue inputs and the USB port, respectively. The actuator is connected to both an input and an output. Applied force and displacement of the actuator can be obtained but is not considered reliable for the set up seen here. The force on the wire, and therefore the force applied on the pipe, is not equal to the measured force on the actuator. It can give an indication of the magnitude, however.

This study uses a rectangular container with one side made of Plexiglas. The rectangular container is 71 cm long, 50 cm wide and approximately 70 cm tall. The box is placed directly on the U-shaped yolk, leaving approximately 2.6-meter radius to the bottom of the sample ($R_b = 2.6 \text{ m}$).

3.3 Design of the centrifuge model

A custom fit experimental set up was made for the experiments in this study. The complete design of the model is available in the DTU archives or upon request to the author. A brief summary with illustrations is given here.

The design of the model satisfies the following test conditions:

- a) Modelling of a pipeline buried in sand subjected to a point load
- b) Sufficient length so that the response can be assumed to apply for a continuous and infinitely long pipeline
- c) Sufficient width to keep the boundary effects relatively small

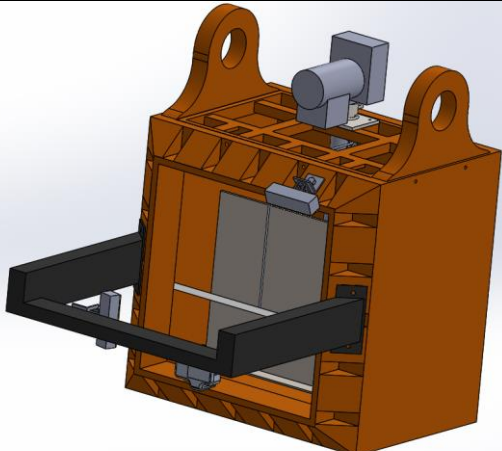
- d) Applied load or prescribed displacements are small enough so that the response of the soil is nearly elastic
- e) Accurate measurements of the applied load
- f) Obtain high-quality digital photographs in flight.
- g) Ideally, a total set up weight of 1 ton (9810 N) is not exceeded. This will reduce the maximum achievable g-force.

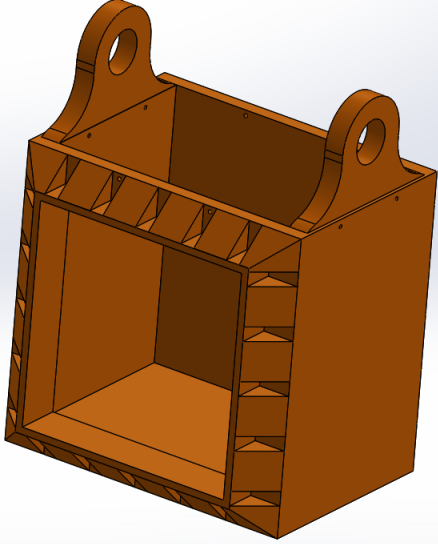
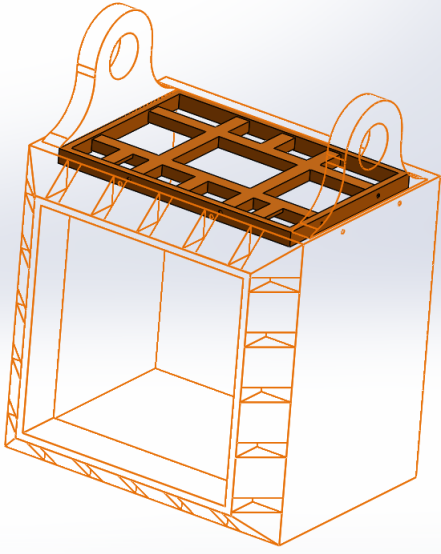
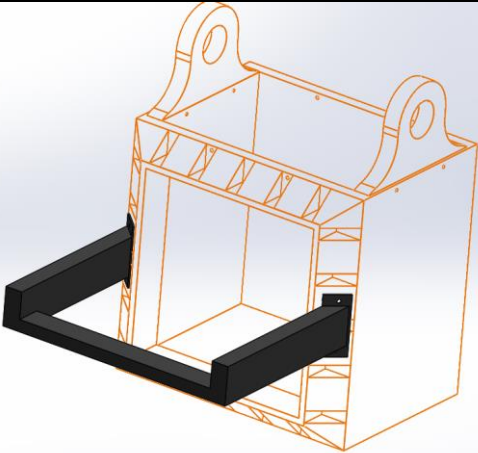
3.2.1 The model assembly

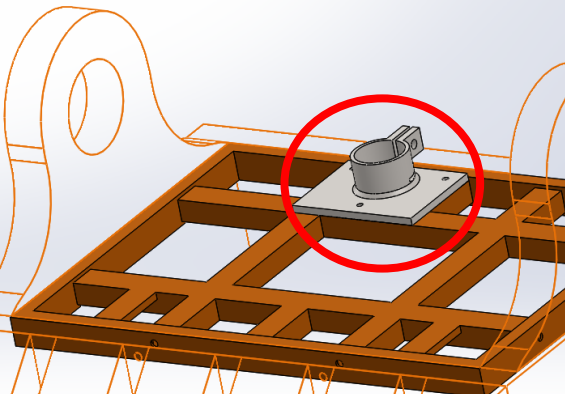
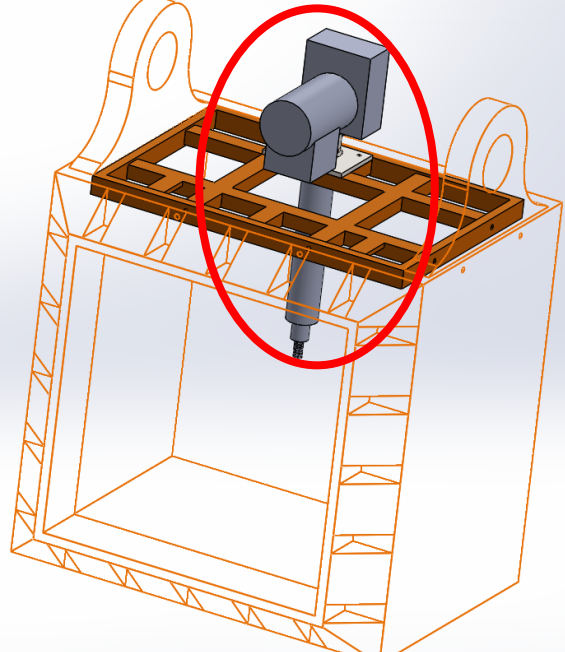
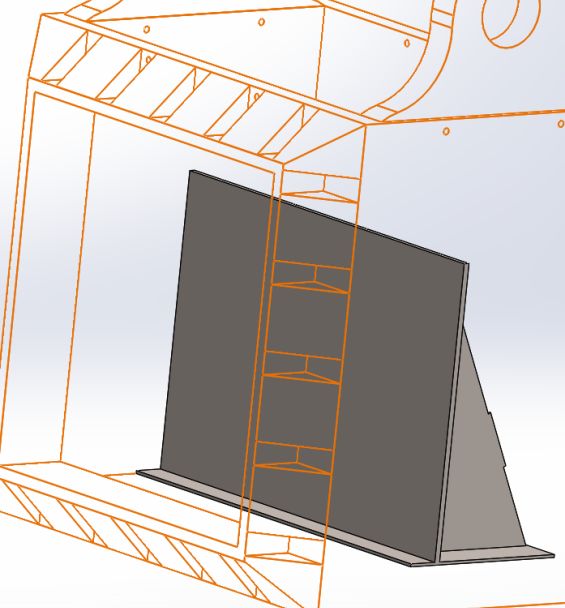
The model and the prototype both use a halfpipe, based on the assumption that a symmetry face exists here. This idea is the same as Vorster *et al.* (2005) but the load is applied differently. Now there are a few problems with this approach: First, there will be some friction between the half-pipe and the surface. To mitigate this, the window was greased where the pipe is. Secondly, the point load cannot physically be applied exactly at the top of the pipe, leading to eccentricity. Thirdly, installing the pipe is difficult as there is no lateral force pushing the pipe against the window until after the sand has covered it.

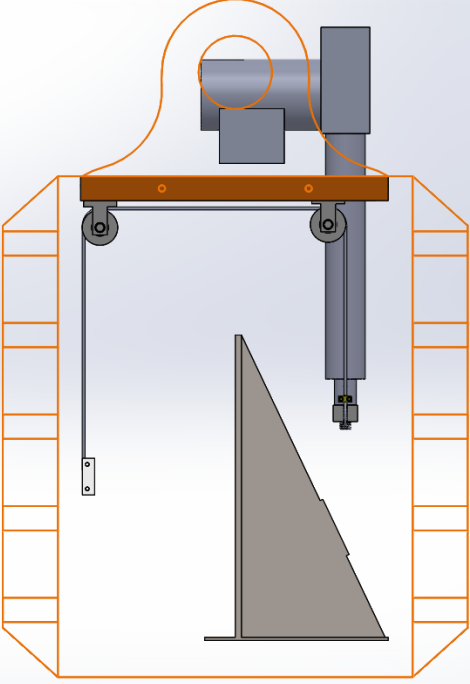
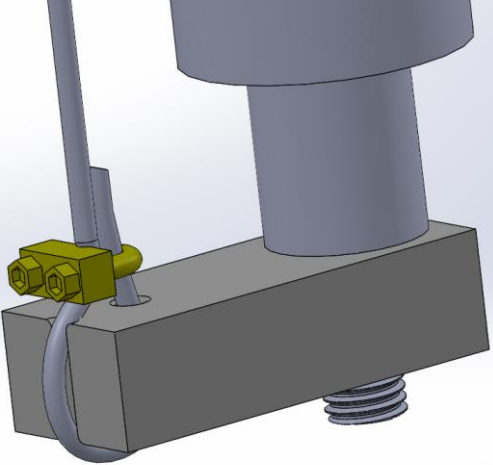
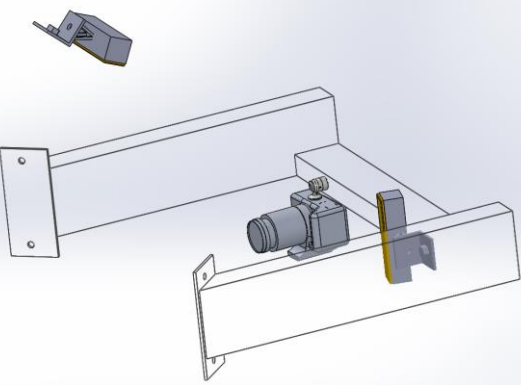
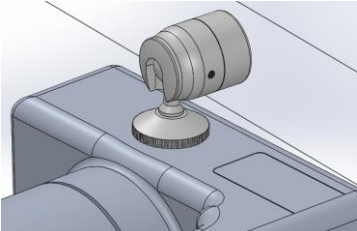
The different components are summarized here. Table 5 shows some of the CAD drawings that were made with SOLIDWORKS for this project. All parts are drawn to scale. The SOLIDWORKS files are available in the DTU archives for future use.

Table 5: A summary of the centrifuge model components, including the SOLIDWORKS drawings.

Component	SOLIDWORKS model	Comments
All components		

Strongbox		
Top rack		<p>Grease should be applied regularly on the contact surface between the rack and the centrifuge box. Use a solid blank to force it into place. Avoid installing it upside down.</p>
Camera mount		<p>The camera mount only has a few centimeters clearance from the floor during spin up and flight. No components should be placed on the outside of the mount.</p>

<p>Actuator mount</p>		<p>The inner radius of the tube is 0.5 mm higher than the radius of the actuator stem.</p>
<p>Actuator</p>		
		<p>The space in front of the plate is filled with soil. The (vertical) front plate and the wings take the horizontal force while the toe as well as downwards friction and normal forces prevent overturning.</p>

<p>Wire-pulley system</p>		<p>The load cell is attached to the horizontal part of the drawing (not shown here).</p>
<p>Wire-actuator connecting piece</p>		
<p>Camera and light system</p>		<p>The camera is attached to the camera mount with a mini ball head camera mount:</p> 

3.2.2 The strongbox

The basis and starting point of the experimental set up was the existing square strong box. The square strongbox has a window on one side, which allows visual monitoring of the specimen during the test. Physical space is limited due to the size of the strong box. The strongbox was therefore split in half to be able to place the actuator partly inside the box. The actuator is 0.55 m tall when the piston is completely retracted, too long to fit on top of the box. With this solution, half of the actuator is inside the square container. A separation wall was implemented to split the box in half, preserving the length and cutting the width in half. Only the half with the Plexiglass wall is filled with soil, while the other contains the actuator. A big advantage of splitting the width is that only half of the soil is required to achieve a set burial depth of the pipe. Figure 17 shows the very basic starting point for the model design.

The height of the separation wall is 0.5 m and soil samples are limited to this size, but all soil models in this study are less than 0.4 m tall. The separation wall is dimensioned for 0.5 m tall samples, but smaller samples cut down the preparation time and sand usage. Table 6 summarizes the model soil dimensions and the prototype dimension for based on a gravity scale of $n = 50$. After installing the separation wall, the soil will extend 71 cm in length, 25 cm in width and up to 50 cm in height.

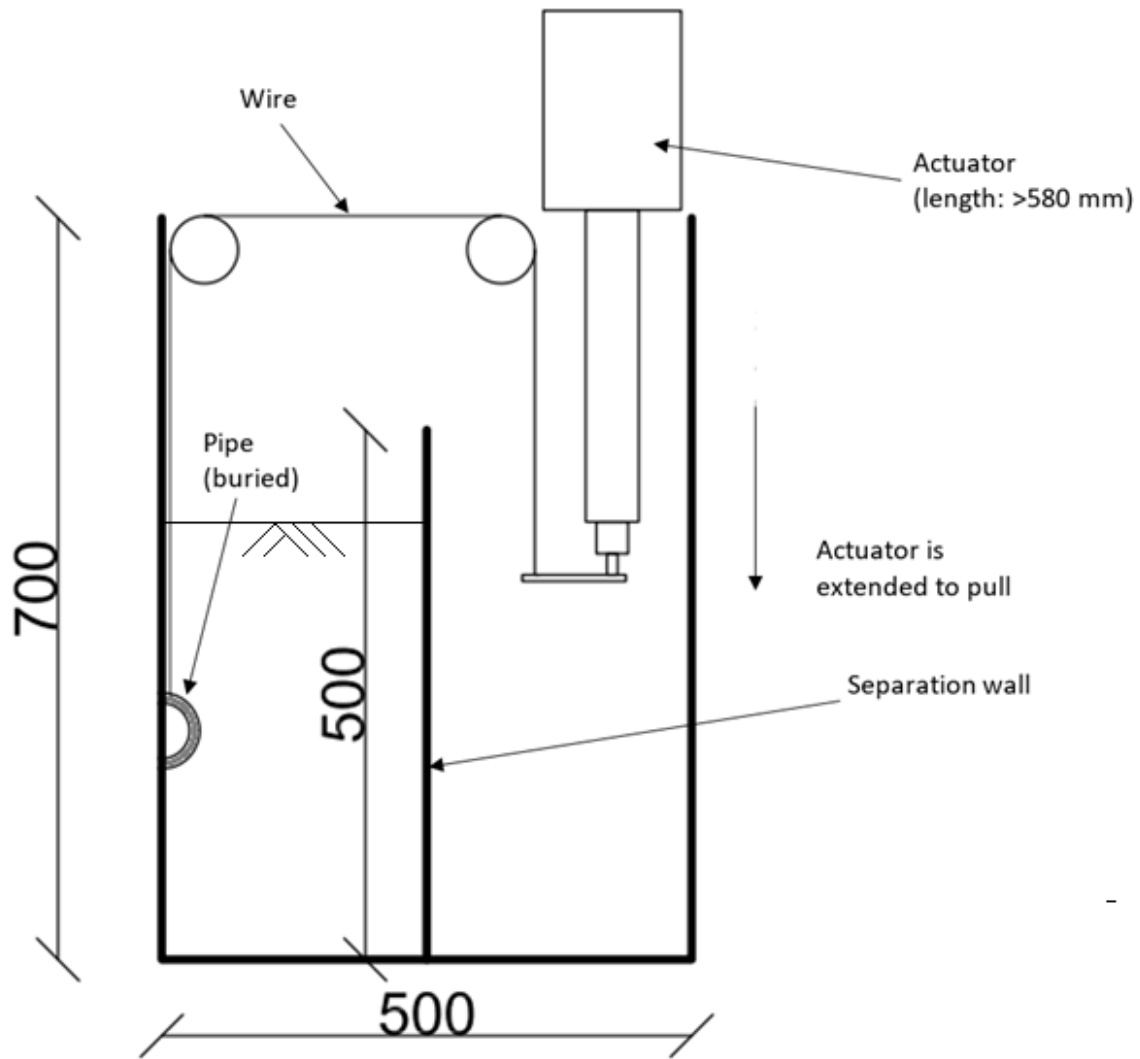


Figure 17: A simplified drawing of the experimental set up seen from the side. Dimensions are in millimetres.

3.2.3 The pipe

Several half-pipes were produced, of which all except one has a model diameter of 20 mm. The last pipe has a diameter of 40 mm. The 40 mm pipe was never actually used due to time constraints, but the dimensions are still justified here for any future projects. The main criterion of selection of pipe properties is the expected deformation shape. It is important that the stiffness and relative rigidity of each pipe results in a clear deformed shape. Ideally, there should be no displacement at and near both ends of the pipe so that the angle of deflection is zero (i.e. $\varphi(L/2) = \varphi(L/2) = 0$). This is the easiest way to ensure that the deformation shape is periodic. On the other hand, a very flexible pipe and low relative rigidity will quickly result in excessively large deformation close to where the point load is applied. In addition, the amount of measurement point per physical length with the PIV is limited, making this a poor choice of technology for big deformation gradients.

Table 6 presents four pipes that were made for the 1G and centrifuge tests. The pipe bending stiffness span three orders of magnitude. This setup can therefore be used for any centrifugal force between 1G and the maximum allowable G-force in the centrifuge. Note that inner radius is zero for pipe 2 to 4, meaning they are solid pipes.

Table 6: Properties of the four pipes made for this project

Pipe	Material	E_p (MPa)	r_o (mm)	r_i (mm)	I_p (mm ⁴)	L (mm)	EI (mm ⁴ /10 ⁶)
1	PVC	3400	10	8	4637.0	700	15.8
2	Aluminum	70000	10	0	7854.0	700	549.8
3	Brass	120000	10	0	7854.0	680	942.5
4*	Aluminum	70000	20	0	125663.7	700	8796.5

*Not used in this thesis

One of the major challenges of the experimental set up is how to connect the wire and the pipe. The wire and wire-pipe attachment can disturb the soil and contribute to the pullout resistance. Furthermore, the pipe must deform equally on the upper and lower side as the Euler-Bernoulli beam assumption in the elastic continuum solution requires a constant cross-section.

The DTU workshop provided PVC pipe with a radius of 10 mm and 2 mm wall thickness, which gives a suitable stiffness for 1G. Figure 18 shows the ready to use pipeline. The PVC pipe was cut to 700mm and cut in half with a band saw. A simple threaded hook screwed into the upper side, thereafter Epoxy glue was applied to reinforce the thread connection and create a bridge between the upper and lower side of the pipe. The width of the Epoxy glue bridge is approximately 1 cm. This ensures that the deflection of the top of the pipe is the same as the deflection of the bottom while having a minimal effect on the overall pipeline stiffness. The wire was then simply tied in a loop and hooked on. This pipe is only intended for 1G experiments. The solution is somewhat intrusive to the soil around the midpoint of the pipe, but the dimension of the hook and the wire are small relative to the area of the pipe. A big advantage of PVC is that the stress-strain curve of PVC is almost perfectly linear up until the fracture point. Most strains in the pipe are recoverable until at least 300% strain. Therefore the pipe can be pulled at repeatedly without being damaged. Also seen in figure 18 is the fibre optics that were installed. This is covered in section 3.11.

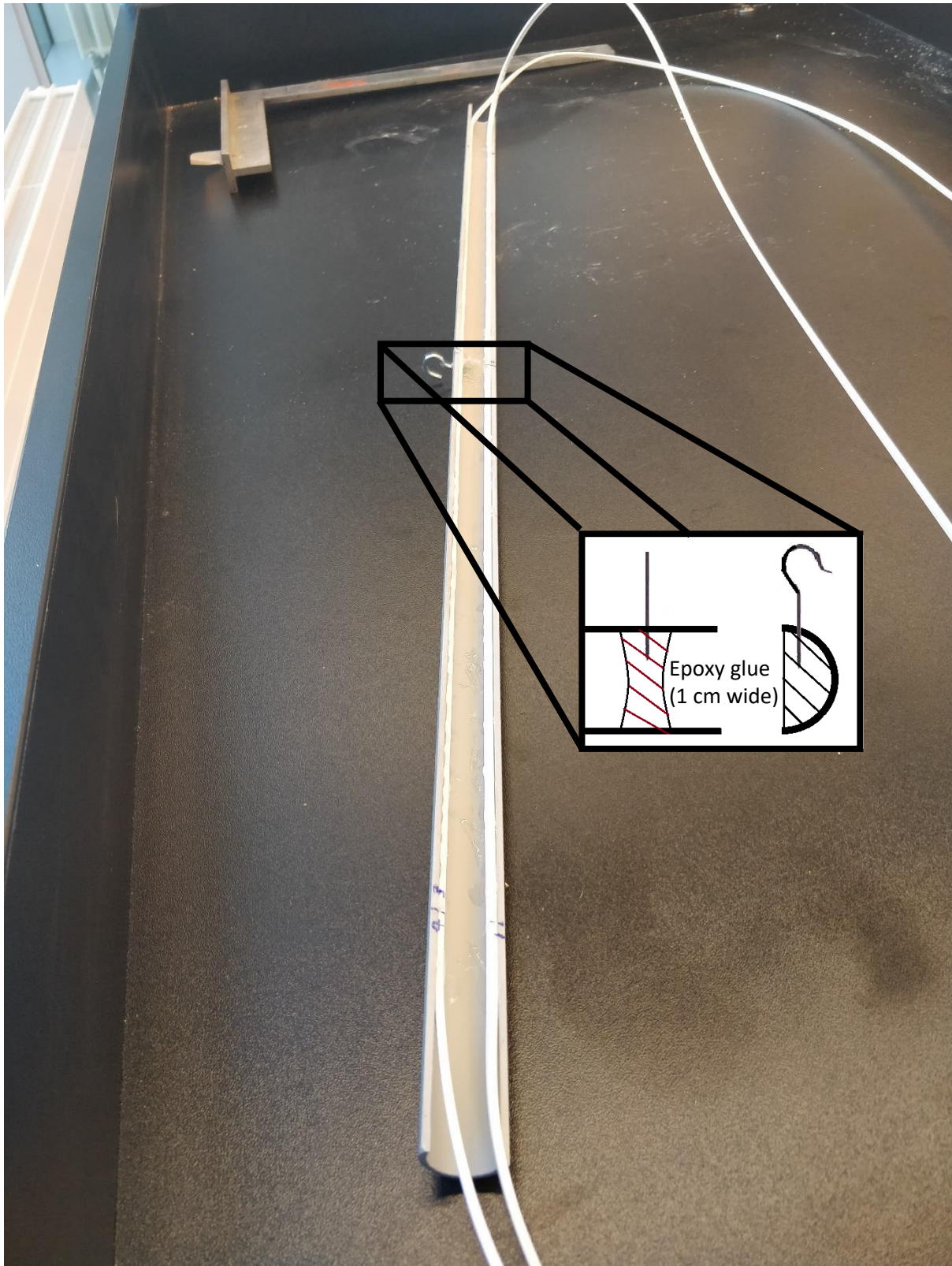


Figure 18: The PVC half-pipe

The pipe-wire attachment must withstand forces up to several kilonewtons in the centrifuge. The simple and obvious design was therefore a solid pipe in favour of a hollow pipe. This eliminates the concern with the cross section losing its original shape due to the point load or high soil pressure. The aluminium pipes were cut in half with a milling cutter

and the brass pipe was factory made. For all three metal pipes (pipe 2 to 4), a hole was drilled through the pipe, parallel with the cut. A wire sleeve was crimped on the other side, as shown in figure 19, which the manufacturer states can hold the rated breaking strength of the cable. This solution has the additional benefit of only disturbing a small area of the underlying soil, which interacts less with the pipe compared to the overlying soil.

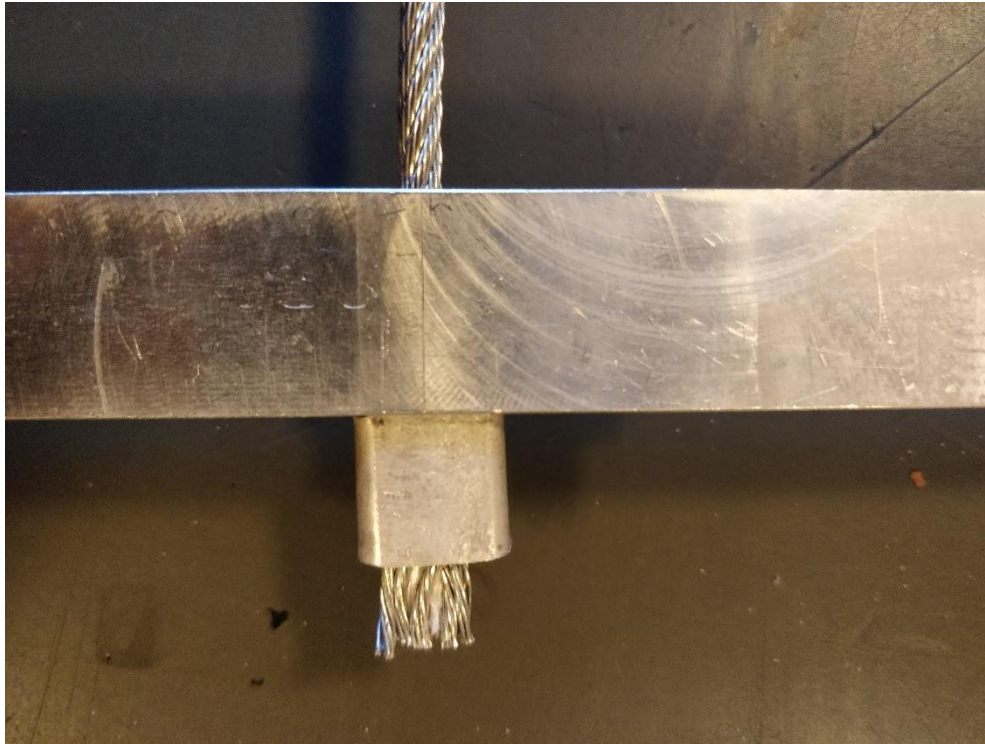


Figure 19: The wire-pipe attachment. In hindsight not a good solution; More on this in chapter 6.

An early goal of this model was to investigate different burial depth to diameter ratios, C/r_0 , and different relative rigidities, $R = E_p I_p / (E_s * d^4)$. As a rule of thumb and to minimize boundary effects of the walls, the distance from the bottom of the box to the pipe should be at least three pipe diameters and the distance from the pipe to the wall should be at least five pipe diameters. This supports a z_p/r_0 ratio of up to 20 for the 10 mm pipe and 7 for the 20 mm pipe for a 40 cm tall sample. Taller sample heights could be used if necessary but require even stronger wires. On the other hand, the model pipe dimensions should not be so small that the contact between individual sand grains is not continuous. Since studies on minimum pipe diameter to grain size ratios are inconclusive, the pipes should satisfy the basic rule of making the model dimensions at 25 to 36 bigger than the average grain size. A median grain size of 0.5 mm indicates that a diameter of 20 mm or higher is satisfactory, as $0.5\text{mm} * 36 = 18\text{ mm}$.

The model length of 70-71 cm is suitable for modelling pipes in the centrifuge. For a 71 cm solid pipe to satisfy the minimum length by Attewell, Yeates and Selby (1986), $L_{min} > 1/\lambda$, or $\lambda > 1/700\text{ mm}$, the maximum pipe radius is calculated as follows:

$$L > 1/\lambda = \sqrt[4]{\frac{K_{eff}}{4E_p I_p}} \quad (89)$$

Using the subgrade modulus of Vesic (Equation 8), results in the inequality

$$L > \frac{1}{\lambda} = 1.48 * r_0 \left(\frac{E_p * \pi r_0 / 4}{E_s r_0^4} \right)^{0.27} (1 - \nu_s^2)^{0.25} \quad (90)$$

A conservative estimate for minimum pipe length is obtained with a soil stiffness on the lower end, at shallow depth in 1G, in this case $E_s=10$ MPa. It should be noted that Vesic's subgrade modulus is based on a pipe at infinite depth, which is also conservative. For a solid aluminum pipe, the maximum radius is

$$700 > 1.48 * r_0 * \left(\frac{70000 * \pi * r_0^4 / 4}{30 * r_0^4} \right)^{0.27} * (1 - 0.25^2)^{0.25} \quad (91)$$

$$\Rightarrow r_0 < 47 \text{ mm}$$

The *recommended* minimum pipe length is $L_{rec} = 2.5/\lambda$, which requires a radius smaller than approximately 19 mm for a solid aluminium pipe, significantly less for stiffer metals. Table 7 below shows that all four pipes satisfy the minimum length. Pipe 1 to 3 also satisfy the recommended length, while Pipe 4 is within the minimum length. However, pipe 4 will be buried deeper than the 10 mm pipes (for the same z_p/r_0 ratio) and the increased confining pressure and soil stiffness should reduce the recommended length to less than the length of pipe 4. This also shows why steel pipes are not recommended for this set up as the high bending stiffness would require very large burial depths and therefore more sand.

Table 7: Recommended and minimum pipeline lengths for the continuous and periodic deflection profile assumption.

Pipe	Material	EI (mm ⁴ /10 ⁶)	r ₀ (mm)	E _s (MPa)	L (mm)	L _{min} (mm)	L _{rec} (mm)
1	PVC	13.9	10	1*	700	106.3	265.8
2	Aluminum	549.8	10	1*	700	277.4	693.5
2	Aluminum	549.8	10	10	700	149.0	372.5
3	Brass	942.5	10	10	680	172.3	430.7
4	Aluminum	8796.5	20	10	700	297.9	744.8
4	Aluminum	8796.5	20	20	700	247.1	617.8

* Soil stiffness near the surface in 1G experiments

3.2.4 The wire

The wire diameter should be as small as possible to minimize disturbance of the surrounding soil. The minimum wire diameter was calculated based on the expected pullout capacity. Table 8 shows the expected force required to pull out the $\varnothing 20$ pipes in 1G and 50G, respectively. Note that these are only reference values obtained from literature during the planning stage, as the specific sand to be used has yet to be determined. The predicted pullout capacity are to be recalculated once the relative density for the experiments are known, which the sand properties depend on.

Table 8: Predicted pullout capacity for a depths of 100 mm and 200 mm and a pipe radius of 10 mm.

Property	Value	Comments/sources
D (mm)	20	(Bolton, 1986) (Bolton, 1986; Latini and Zania, 2016; Puech and Garnier, 2017) (Latini and Zania, 2016) $1 - \sin(35)$; (Jaky 1948)
γ' (kPa)	16.2	
ϕ_{\max} (°)	40*	
ϕ_{crit} (°)	32	
ψ (°)	15	
K	0.43	

*Based on a confining pressure of 162 kPa.

	P (N) per 0.7 meter half-pipe, n = 1			
C (mm)	Scaminée et al. (1990)	Ng and Springman (1994)	Vermeer and Sutjiadi (1985)	White et al. (2001)
200	112*	210	178	142
100	34*	58	49	38

	P (kN) per 0.7 meter half-pipe, n = 50			
C (mm)	Scaminée et al. (1990)	Ng and Springman (1994)	Vermeer and Sutjiadi (1985)	White et al. (2001)
200	5.7*	10.6	9.0	7.2
100	1.7*	2.9	2.5	1.4

*Assuming $K * \tan(\varphi') = 0.4$ as recommended by Scaminée et al. (1990)

As evident by the table, the predicted pullout capacity varies between the four studies. Scaminée et al. (1990) is conservative. The 1G experiments therefore use a $\varnothing 1$ wire, which can handle loads in the order of 500-600N. A slightly smaller diameter could be used, but the 1 mm wire was calculated to have skin friction less than 1% of the pullout capacity. The centrifuge test are expected to reach pullout forces up to 10 kN, which suggest a diameter of at least 4 mm is the minimum diameter to achieve pullout and 5 mm for a guaranteed pullout. Working with a $\varnothing 5$ wire, pulleys and tight spaces is difficult, therefore the setup uses a $\varnothing 4$ wire with a minimum breaking load of 9.3 kN. This gives a factor of safety of at least three for the z_p/r_0 ratio of 10. The wire has a chance of breaking for z_p/r_0 ratios 20 or higher, but this is acceptable for two reasons: first, the potential consequences of the wire

breaking are small, second, achieving pullout is not the main goal of the test. It is still considered a successful experiment if the pipe only moves a fraction of the mobilization distance. Additionally, 9.3 kN is after the manufacturer has applied the, admittedly unknown, factor of safety. For experiments with pipe 4 (ø40), either a lower g-force or extremely high-grade wire rope is recommended.

The frictional forces between on the wire are calculated here. Interfacial friction between soil and solid surfaces is of the same form as the shear strength of soil-soil sliding, hence the following equation applicable for sliding between dry, cohesionless soil and any surface (including cables):

$$\tau = \sigma_n * \tan\phi' \quad (92)$$

Pullout tests on piles in sand by Ireland (1975) suggest the following skin friction, with reference value K=1.75:

$$P_0 = K\sigma'_v A_s \tan(\phi) \quad (93)$$

Using typical values for dry sand, the friction on 200 mm buried, ø4 wire at 50g is:

$$P_0 = 1.75 * \gamma * L_{wire}^2 * \pi d * \tan(\phi') * 0.5 \quad (94)$$

$$F_{wire} = 2.749 * \left(17 \left(\frac{kN}{m^3}\right) * 50\right) * 0.2^2 m^2 * d m * \tan(35^\circ) = 260 N \quad (95)$$

Table 9 shows the estimated wire friction for different potential tests. It can be concluded that friction on the wire is significant during the initial movement of the soil, especially for larger burial depth. Based on these numbers, the wire friction is a significant percent of total load on the wire during early loading, but this percentage decreases quickly. It would also affect the unloading of the pipe to some degree. K is likely too high and therefore this is a very conservative calculation.

Table 9: Predicted wire friction for representative 1g and 50g experiments.

Coverage, C (mm)	Wire diameter (mm)	Centrifuge acceleration, n (-)	F_{wire} (N) Ireland (1975)
100	1	1	0.3
200	1	1	1.3
100	4	50	65.45
200	4	50	261.8

3.2.5 The separation wall

The separation wall is 710 mm long steel plate with supports, dimensioned to take the earth pressure of 0.5 meters of sand at 60g. This is equivalent to a 50m meter wall and supporting 35 meters of sand at prototype scale which, needless to say, there is no established retaining wall design for. Fortunately, the model enjoys the benefit that it can be built with S355 grade steel unlike tall retention walls in the field. Several solutions were considered, but the ultimate design of the separation wall is similar to a traditional counterfort wall. Counterfort walls are typically the preferred solution for very tall walls with high earth pressure since the amount of concrete involved is less than that of other types. For walls above 8 to 10 meters, this is almost always used. While the amount of steel required for the separation wall is not a high cost either way, reducing the weight of this component in the centrifuge set up is.

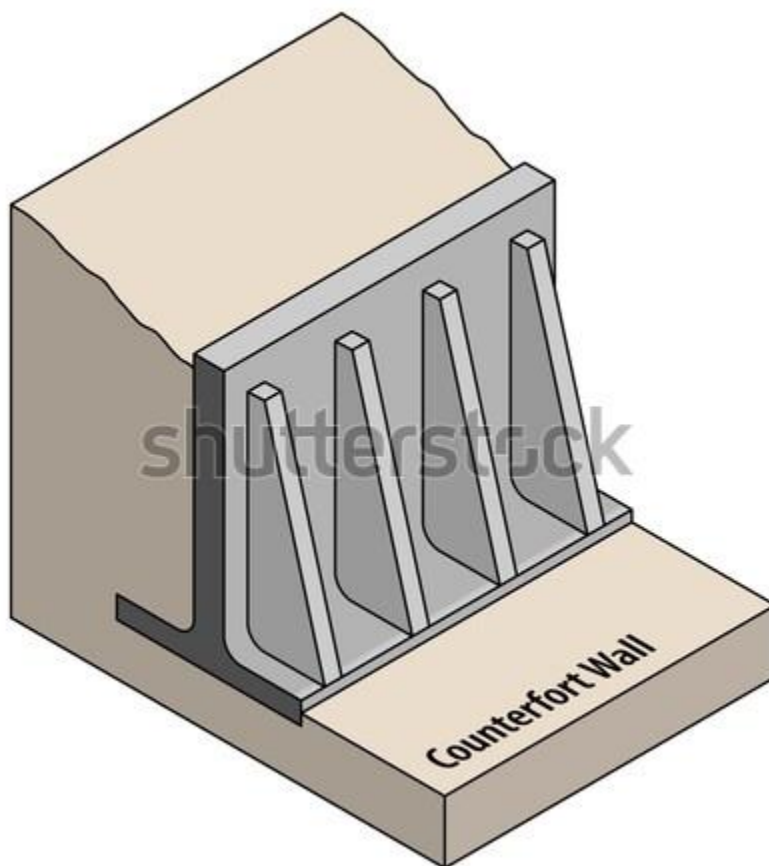


Figure 20: Typical design for a counterfort wall. Courtesy of shutterstock.com.

Spacing of counterforts is typically the same as the height of the construction according to Reinforced Concrete Design to Eurocodes: Design Theory and Examples, Fourth Edition, Edition 4.

After choosing the wall type, earth pressure is calculated to decide a suitable wall thickness and spacing of counterforts. The spacing counterforts in the field is typically the same as the

height of the wall, but this rule of thumb is not necessarily the most economical and efficient for a steel wall. Carefully note that the calculations are based on a centrifuge acceleration $n = 60$ for dry sand. The actual centrifuge tests are limited to 50g due to other concerns, but the wall itself can support higher accelerations up to 60-70g in future experiments. The wall pressure in the centrifuge is n times higher than 1g, therefore the wall pressure will be:

$$\sigma_v = n * \gamma * z \quad (96)$$

$$\sigma_h = n * K_0 * \gamma * z \quad (97)$$

The "at-rest" coefficient of lateral earth pressure, K_0 , is assumed as the design target is a rigid wall. This is the case for very small lateral strains of the soil, which can easily be controlled against the calculated horizontal displacement of the wall. The Canadian Foundation Engineering Manual, for instance, states that the transition from at-rest to active earth pressure occurs when the horizontal displacement at the top of the wall exceeds 1/1,000 of the wall height for dense sand (slightly higher for loose sand). Hence, the target for maximum displacement at the top of the wall is 0.5 mm or less.

Inserting conservative reference values for dry loose sand, $\gamma_d = 17.0 \frac{kN}{m^3}$ and $K_0 = 0.64$ (Murthy, 2002), the horizontal earth pressure is:

$$\sigma_h = 60 * 0.64 * 17 * z \left[\frac{kN}{m^2} \right] \quad (98)$$

$$\sigma_h = 652.8 * z \left[\frac{kN}{m^2} \right] \quad (99)$$

The pressure on the toe is:

$$\sigma_{v,bottom} = \sigma_v(z = 0.5) = 60 * 17 * 0.5 \left[\frac{kN}{m^2} \right] \quad (100)$$

$$\sigma_{v,bottom} = 510 \left[\frac{kN}{m^2} \right] \quad (101)$$

A SOLIDWORKS CAD model was built to try different designs. The best trade-off between the weight and the deflection of the wall was achieved with four counterforts. The outermost counterforts are closer to the edges of the wall because the edges are unsupported. Due to this design, the edges of the front plate act as cantilevers and while

the wall between the counterforts acts as simply supported beams. The optimal placement of the counterforts is easily found with standard equations for maximum deflections of the two cases.

The counterforts, vertical plate and bottom plate are welded together. There are eight, longitudinal welds connecting the counterforts to the bottom plate (one on each side) and three welds, transverse welds connecting the vertical wall to the bottom plate. The calculations are done for two cases:

- a) the longitudinal welds take all the force, and
- b) the transverse welds take all the force. The welds between the vertical wall and the counterforts take almost no force, hence no calculations are done here.

The required weld size was calculated according to Eurocode 3: Design of Steel Structures. The force resultant and location is:

$$P_0 = \frac{1}{2} * K_0 * n * \gamma * H^2 \quad (102)$$

$$P_0 = \frac{1}{2} * 0.64 * 60 * 17 \frac{kN}{m^3} * 0.5^2 m^2 * 0.71 m \quad (103)$$

$$P_0 = 57.9 kN \quad (104)$$

At height $H/3 = 166.7$ mm.

While dividing this resultant by eight and three would give a close estimate, a better estimate was calculated in fap2D showed below (figure 21a).

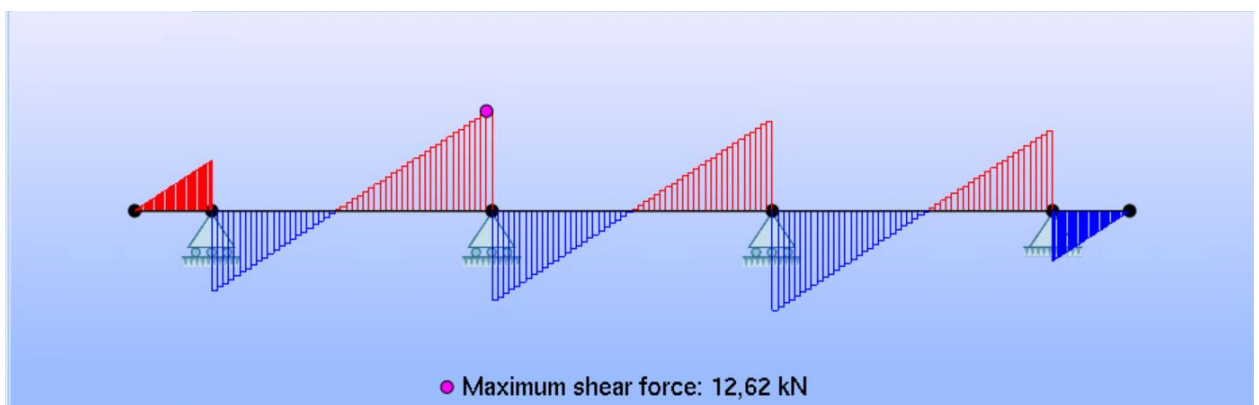


Figure 21a: Horizontal force on each of the four wings supporting the wall for case a. Each wing has two longitudinal welds connecting the wings to the bottom plate.

Hence, the force experienced by the eight welds is

$$N_{w,Ed} = \frac{1}{2} * 25.2 \text{ kN} = 12.6 \text{ kN} \quad (105)$$

Which means the minimum length of the longitudinal weld, assuming a weld thickness of 5mm, is:

$$N_{w,Rd} = \frac{f_u}{\sqrt{3} * \gamma_{M2} * \beta_w} * A_w \quad (106)$$

$$112.6 * 10^3 \text{ N} = \frac{510 \text{ N/mm}^2}{\sqrt{3} * 1.25 * 0.9} * 5 \text{ mm} * L_w \quad (107)$$

$$L_w = \frac{12.6 * 10^3 * \sqrt{3} * 1.25 * 0.9}{510 * 5} \text{ mm} \quad (108)$$

$$L_w \geq 9.6 \text{ mm} \quad (109)$$

Transverse weld

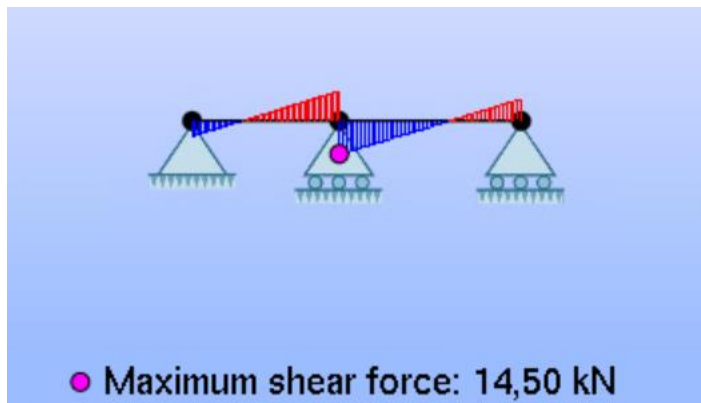


Figure 21b: Horizontal force on each of the welds connecting the all to the bottom plate for case b.

$$N_{w,Ed} = 14.5 \text{ kN} \quad (110)$$

$$N_{w,Rd} = \frac{f_u}{\sqrt{2} * \gamma_{M2} * \beta_w} \quad (111)$$

$$14.5 * 10^3 N = \frac{510 N/mm^2}{\sqrt{2} * 1.25 * 0.9} * 5mm * L_w \quad (112)$$

$$L_w = \frac{14.5 * 10^3 * \sqrt{2} * 1.25 * 0.9}{510 * 5} mm \quad (113)$$

$$L_w \geq 9.0 mm \quad (114)$$

The conclusion is that all longitudinal and transverse should be 10 mm or more assuming a 5 mm throat thickness. The actual length of the welds are around 20 mm.

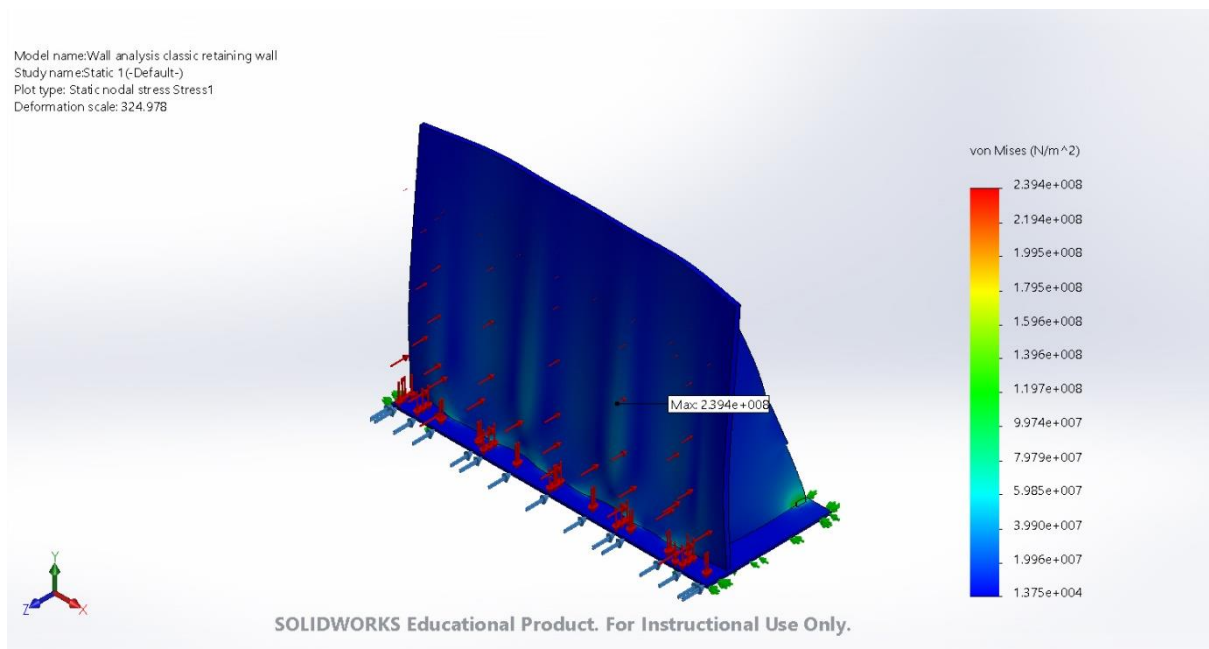


Figure 22: Von Mises stress in the separation wall with 0.5 m of sand at 60g. The model includes welded connections.

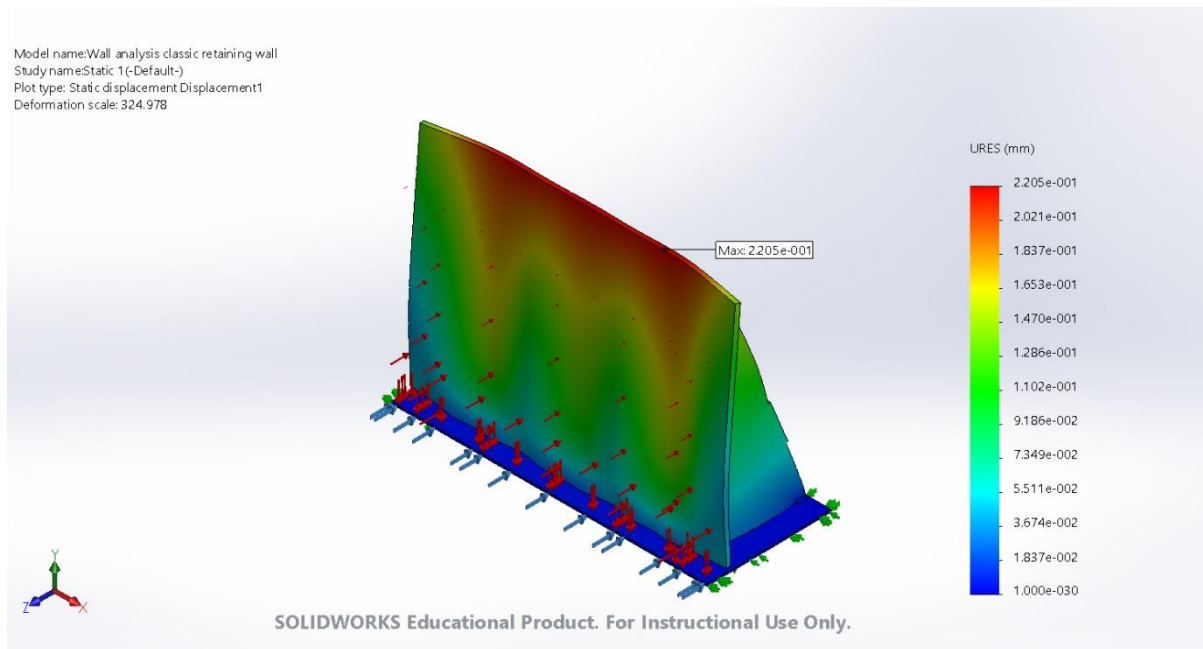


Figure 23: Displacement of the separation wall with 0.5 m of sand at 60g. The model includes welded connections.

The finite element calculations in SOLIDWORKS, which include the actual welds of the prototype, shows show the stress and displacement of the wall. The maximum von Mises stress is around 240 MPa and the maximum deflection, at the top of the wall, is 0.22 mm. Hence, the factor of safety is 1.48 with 0.5 meters of sand at 60g. This is assuming The complete analysis in SOLIDWORKS can be found in appendix B.1.

3.2.6 The camera mount

The camera must be placed a reasonable distance from the window: The closer to the sand, the higher accuracy, but the entire deformation shape must be captured. Due to the line of symmetry at the midpoint of the pipe, it is sufficient to only capture half of the pipe length. The length of the window is also smaller than the pipe and therefore 50 mm of the pipe is covered on each side; the target is to capture at least 600 cm. It was calculated that a 64° wide angle lense is able to capture half of the window from around 65 cm away. The camera mount is designed to extend as far as possible, 63 cm, with only a 5 cm safety clearance between the mount and the floor during flight.

Design and calculations for the camera mount do not involve any geotechnical considerations and will there only be included in appendix B.2. Class 8.8 M12 bolts can handle g-forces up to 100g after Eurocode 3 (but no higher). The threads are possibly made in cast iron and should be reinforced. More on this in chapter 6.

3.2.7 The camera

The camera is a 15.1 megapixel Canon EOS 50D. Pictures are captured with ISO 100 film setting, aperture at $f/22$, which are the recommended settings for sand (Bucher, 2007). The shutter speed is kept low for the centrifuge experiment to mitigate blur due to the vibrations.

3.4 Rotational speed

The rotational speed of the centrifuge arm is manually controlled from the operator room. Due to the size and weight of the square strong box and other components, the centrifuge can only achieve a gravitational acceleration of 60-70 g. The model is dimensioned to withstand this force, but the gravitational acceleration in this study is 50 g.

The unit of rotational speed in the DTU geotechnical centrifuge is revolutions per minute, or RPM. 1 RPM is $2\pi/60$ radians per second. Hence, the number of revolutions per minute to achieve a scaling factor $n=50$ is:

$$\omega = \frac{30}{\pi} \sqrt{\frac{ng}{R_e}} \text{ [RPM]} \quad (115)$$

The reference level is set to 2/3 of the height of the soil to reduce the maximum error. This also gives higher accuracy in the soil overlying the pipeline, which has the biggest influence on pullout capacity. The required RPM therefore depends on the height of the soil sample. The rotational speed is calculated here for a pipe of radius $r_0 = 10 \text{ mm}$, a z_p/r_0 ratio of 10 and a distance of three radii to the bottom of the soil sample. This gives a soil sample height of 27 cm, hence the distance from the axis of spin to 2/3 of the height of the soil sample for a is $R = 2.593$. The required rotational speed to get 50g at 2/3 of the height of the soil is

$$\omega = \frac{30}{\pi} \sqrt{\frac{50 * 9.81}{2.593}} \text{ [RPM]} \quad (116)$$

$$\omega = 131.34 \text{ RPM} \quad (117)$$

3.5 Calibration of load cells

The experiment used two load cells, one for weighting the setup and one for measuring the tension on the wire. A Bofors KRG-20 type U2A with a capacity of 20 kN was calibrated for the strongbox, which was expected to weigh around 1 tonne with all the components installed. A known reference weight of 2226.9 N showed good accuracy within ± 10 N, which is sufficient for balancing the counterweight. The calibration of the Bofors load cell is not included here as it does not affect the accuracy of the results. The load cell used to measure tension in the wire is a Philips PR 6246/13 C3, with a capacity of 10 kN. The accuracy class of the load cell is 0.008% of 1t, or about 0.8 N, according to the manufacturer. Signal fluctuations within the range of 0.3 mV were observed during the calibration and the average calibration factor was 9.5818. This means that the precision is around 2.9 N. Appendix C.1 contains the results from the calibration of the Philips PR 6246/13 C3 load cell.

The load cell is attached directly to the wire and exerts a significant force with its 20 N self-weight. This force is almost 1 kN at 50 g. The load cell is therefore initially suspended on wires to keep slack on the wire and avoid tension on the wiring system. When load is applied, the load cell will slowly rise until the cable is completely horizontal. This approach also ensures that the load increases slowly from zero as there is no sudden “release” of the load cell.

3.6 Centrifuge counterweight

The centrifuge must be balanced with counterweights, hence it is important to know the approximate weight and centre of mass of the centrifuge model. The counterweight calculations are available in appendix D.1. Weight and centre of mass for the new components are obtained either from the SOLIDWORKS model or with a scale (for simple geometries). Light components < 10 N are only considered towards the total weight, not centre of mass. The total weight with every component and sand included is 10325 N, or 1052.5 kg, which is slightly higher than the original target for the model, but not considered a problem. Total moment was well within safe limits (Refer to “sum of moments 3” in appendix D.1, which should not exceed 30 kg m). Based on the calculations, nine big steel plates (371.7 N or 37.89 kg) and zero small steel plates (123.9 N or 12.63 kg) gives the moment with the smallest difference between the counterweights and the centrifuge model.

On a side note, the total weight based on the SOLIDWORKS model is 10185.7 N, or 1038.3 kg. This indicates that the model is fairly accurate and the model-based centre of mass can be used safely. Obtaining the centre of mass is otherwise a complicated task.

3.7 Model preparation

3.7.1 Fontainebleau sand

All pullout tests were carried out in dry Fontainebleau sand. Fontainebleau sand is a fine sand from southeast of Paris in France, with a mean particle diameter around 0.2 mm. Fontainebleau sand has been used in many laboratory tests at DTU, including sand classification and triaxial tests, hence the properties are well-documented. Thrane (2011) summarizes the findings in a technical report, and the values here are taken directly from this report. Table 10 shows the classification data after Thrane (2011), page 12, based on classification tests were by Klinkvort & Hansen 2007. The classification tests include four sieve tests, eight pycnometer tests and four void ratio tests for minimum and maximum void ratio.

Table 10a: Properties of the Fontainebleau sand

Property	Symbol	Value
Average grain size	d_{50}	0.18
Specific gravity of particles	G_s	2.646
Minimum void ratio	e_{min}	0.548
Maximum void ratio	e_{max}	0.859

A useful finding from triaxial tests is the following relationship (Thrane, 2011):

$$\Delta \tan(\varphi) = -1.75\Delta e \quad (118)$$

Where the reference void ratio is $e = 0.599$.

(Latini and Zania, 2016) found that the friction angle ranges from 35° to 40° for medium dense sand ($I_d = 0.65$) and 40° to 42° for dense sands ($I_d = 0.80$). The secant Youngs modulus at 80% relative density and a confining pressure of 50 kPa is $E_{50} = 32.9 \text{ MPa}$. Increasing confining pressure or relative density resulted in generally higher Youngs modulus, but no such effect on the poisons ratio was observed. The poisons ratio varied from 0.20 to 0.48. The unloading and reloading slope was several times higher than the secant modulus, depending on confining pressure and relative density.

3.7.2 Sand pouring method

Sand samples at DTU are prepared with a spot poured by spot pouring hopper (SPH), originally made by Meier & Møller (2004) but has since then been modified slightly. The SPH setup consists of a 200 litres container, a flexible tube and a 16 mm nozzle with a sieve. The sieve promotes smooth and evenly distributed flow of the sand.

Two factors determine the density of the prepared sand sample: Fall height and flow rate. Density increases with increasing fall height and decreases with flow rate. Flow rate is controlled with the nozzle diameter, in this case 16 mm. The DTU hopper is hoisted down from the floor above and supports a drop height of approximately 0.7-0.8 meters, depending on the height of the sample. In theory, this setup can target loose samples around minimum void ratio to dense sand samples up to 90 to 95% relative density. A dense sample was targeted for this project, and the fall height was kept constant at around 0.75 meters by gradually hoisting the hopper.

Eight density cups were installed in the middle of the sand, four cups at around 5 cm from the bottom and four cups around pipe level. Table 10b and 10c show the results of the sand pouring. The average relative density appears to be around 81%. This is lower than expected RD, but the results are fairly consistent for all the locations and across all prepared sample.

The edge the container influence the sand sample. Zhao et al. (2006) recommend using a U-turn or circular travel pattern to mitigate this (Figure 24). Due to the rectangular shape of the container, a U-turn traveling loop was used (Figure 24), though in hindsight the circular travelling loop is the better choice to minimize variation directly over the pipe.

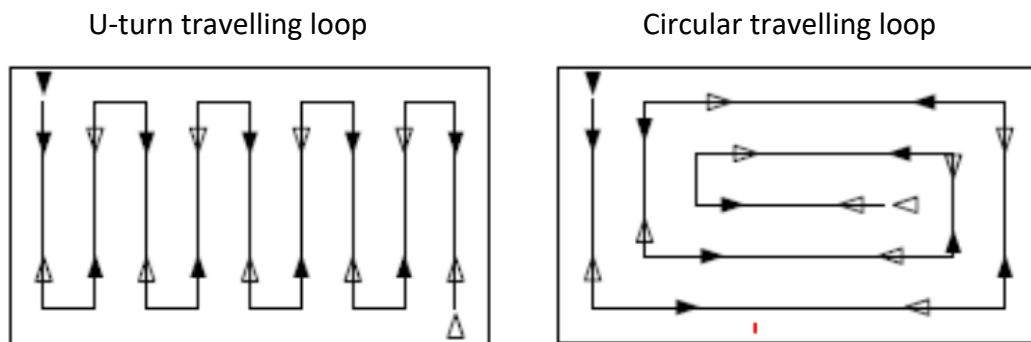


Figure 24: Potential travelling loops with the sand pouring hopper. From Zhao et al. (2006).

A major challenge was keeping the pipe presses against the window until it is completely covered. Marshall (2009) solved this by flipping the box horizontally – window down – before pouring sand. This solution is not feasible with the DTU strongbox without drastic modifications. Vorster *et al.*, (2006) installed thin plates that can be pulled out after the sand has been poured. The latter technique will certainly disturb the soil, so instead it was attempted to keep pressure manually and carefully avoid touching the sand. Some sand ended up on the inside of the pipes, which could increase friction and also affect the PIV results. This is likely due to the imperfect cut of the pipes and not as a result of technique. The PVC pipes and aluminium pipes had visibly uneven surfaces and sand got inside (particularly the latter). One the other hand, the brass pipe was factory-made and no sand got in between the pipe and the window. It is highly recommended to use high precision cutting methods in future tests.

Table 10b: Sand properties based on installed density cups from test 1

Test 1

Plastic cup #	Weight Full Cup (g)	Weight Empty Cup (g)	Weight with Water (g)	γ_{dry} (kN/m ³)	V_s (m ³)	V_v (m ³)	e	RD (%)
1	105.1	7.7	64.4	16.85	36.75	19.95	0.54	102.1
2	109.7	7.9	69.6	16.19	38.42	23.28	0.61	81.2
3	97.7	7.2	61	16.50	34.15	19.65	0.58	91.3
4	108.6	7.5	69.6	15.97	38.15	23.95	0.63	74.1
5	107.3	7.9	67	16.50	37.51	21.59	0.58	91.2
6	103.1	7.5	65.9	16.06	36.08	22.32	0.62	77.0
7	91	6.7	59.2	15.75	31.81	20.69	0.65	66.7
8	102.7	7.5	65.2	16.19	35.92	21.78	0.61	81.2
Average value:				16.16				80.40

Table 10c: Sand properties based on installed density cups from test 2

Test 2

Plastic cup #	Weight Full Cup (g)	Weight Empty Cup (g)	Weight with Water (g)	γ_{dry} (kN/m ³)	V_s (m ³)	V_v (m ³)	e	RD (%)
1	-	-	-					
2	108.2	8.2	69.1	16.11	37.74	23.16	0.61	78.7
3	98.6	7.2	61.2	16.60	34.49	19.51	0.57	94.5
4	109.2	7.9	68.7	16.34	38.23	22.57	0.59	86.3
5	108	7.9	67.6	16.45	37.77	21.93	0.58	89.6
6	102.1	7	65.5	15.95	35.89	22.61	0.63	73.3
7	91.6	7	59.8	15.72	31.92	20.88	0.65	65.5
8	102.1	7.6	65.1	16.12	35.66	21.84	0.61	79.1
Average value:				16.18				81.02

3.8 Test procedure

A total of four tests were carried out, three in Earth's gravity and one at 50g. Table 11 summarizes the four tests and respective properties. The experiments were performed chronologically in the order in this list.

Table 11: Test number and conditions for each test

Test	n []	r_0 [mm]	t [mm]	z_p/r_0 []	E_p [MPa]
1	1	10	2	21	3400
2	1	10	2	12	3400
3	1	10	-	12	70000
4	50	10	-	11	120000

All experiments incrementally load the pipe and pictures are taken at regular intervals from start to end. The camera is autofocused before the start of the test, after which the zoom and focus are locked. The focus point is set to the area around the pipe as it matters the most. The test procedure for test 1-2, test 3 and test 4 are described individually in this section due to several variations in method.

Test 1 and test 2

The baseline for the fibre optics is first defined at no load, using the calibrated settings from the fiber optics calibration test. Several zero displacement baseline pictures are also taken. The load is applied by carefully hooking physical loads at the end of the wire. This method allows careful monitoring of the displacements and full control of the loads, as opposed to the actuator, which is displacement controlled. The camera is set to take one photo per minute, which gives ample time to place or remove weights. Several loadings and unloadings of the pipe was carried out, partly to control the setup and partly to investigate the soil response. The loading regime goes as follows:

- 1) The wire is loaded in 2.45 N increments to 7.36 N and 9.81 N, for test 1 and test 2 respectively.
- 2) The load is removed
- 3) The load is applied back on in 2.45 N increments.
- 4) The pipe is loaded incrementally to 26.98 N and 34.34 N, for test 1 and test 2 respectively.
- 5) The load is removed
- 6) For test 1 only, one more loading up to 63.8 N and subsequent unloading was carried out.
- 7) Finally, the wire is loaded in 9.81-19.62 N increments until pullout.

Neither the exact pullout load nor the maximum mobilization distance can be found with this method. One can only conclude that the pullout capacity lies somewhere in between the last load before pullout and the final weight that caused pullout.

Test 3

The load cell is suspended with support wires to keep slack on the wire attached to the pipe. The pullout is performed by applying displacement-controlled loading using the actuator. The displacement of the actuator increases continuously until failure. Due to the extension and relaxation of the wiring system, the displacement of the pipeline is neither increasing at a fixed rate nor is the displacement identical with the actuator. A photo is taken every 5 seconds, which is the minimum time between photos for the camera. The load required for

pull-out is obtained with the load cell, but the exact maximum mobilization distance is unknown (unless the last picture coincides with the maximum capacity).

Test 4

The camera is focused before spinning the centrifuge as the focus motor can struggle during flight (which turned out to be the case). From a pilot test, it is known that the camera mount dips at high G-force and the camera is therefore pointed slightly above the pipe before spinning the centrifuge. The RPM is then slowly increased while the camera, light system and load cell are monitored. Some loads, slowly increasing from zero to around 200 N at 50g, was observed while spinning up the centrifuge. This is most likely due to the load cell suspension slightly giving in to the increasing weight.

The centrifuge box was spun to 131.34 RPM, equivalent to 50g at the reference level of the soil. Table 12 shows the error in the soil as a result of the non-linear variation of stress. Here n_m denotes the actual g-force in the sample, according to the formula $n_m = \omega^2 * R_e / g$. The maximum underestimation and overestimation of vertical stress is 3.5% and 6.5%, respectively. Putting the reference level to 2/3 of the soil height is particularly beneficial for this burial and coverage depth since the pipe is buried nearly at this level. Hence, the stress variation is nearly the same in the model and the prototype directly above the pipe. For instance, the error at the top of the pipe is only 0.3%. Furthermore, the bottom half of the sample has a negligible effect on the results in this experiment.

Table 12: Comparison of model and prototype stress for the centrifuge test (test 4)

n	50
RPM	131.34
ω (rad/s)	13.75
R_e (m)	2.593
γ (kN/m)	16.2

h_m (m)	h_p (m)	σ_p (kPa)	n_m	σ_m (kPa)
0	0	0	48.3	0.0
0.02	1	16.2	48.7	15.8
0.04	2	32.4	49.0	31.8
0.06	3	48.6	49.4	48.0
0.08	4	64.8	49.8	64.6
0.09	4.5	72.9	50.0	72.9
0.1	5	81	50.2	81.3
0.12	6	97.2	50.6	98.3
0.14	7	113.4	51.0	115.6
0.16	8	129.6	51.4	133.1
0.18	9	145.8	51.7	150.9
0.2	10	162	52.1	168.9
0.22	11	178.2	52.5	187.1

Comments

Vertical stress in model and prototype are identical
Top of the pipe
Bottom of the pipe

0.23	11.5	186.3	52.7	196.4
0.25	12.5	202.5	53.1	215.0
0.27	13.5	218.7	53.5	233.9

Maximum error at the bottom of the sample

3.9 GeoPIV

In this study, digital images are processed with GeoPIV-RG by Sam Stanier, an improved version of the old GeoPIV by (White and Take, 2002). The software is available for free at <http://www.geopivrg.com/> and runs directly in MATLAB.

First, an analysis mesh is created. Several patch sizes were experimented with, but the controlling factor turned out to be the number of wild vectors: For patch sizes 50x50 pixels or larger, almost no wild vectors appear. On the other hand, smaller patch sizes than this gave a large number of wild vectors that rendered the analysis almost useless. Figure 25 shows an example of a patch in GeoPIV. The pipe is masked and the images feature no control points.

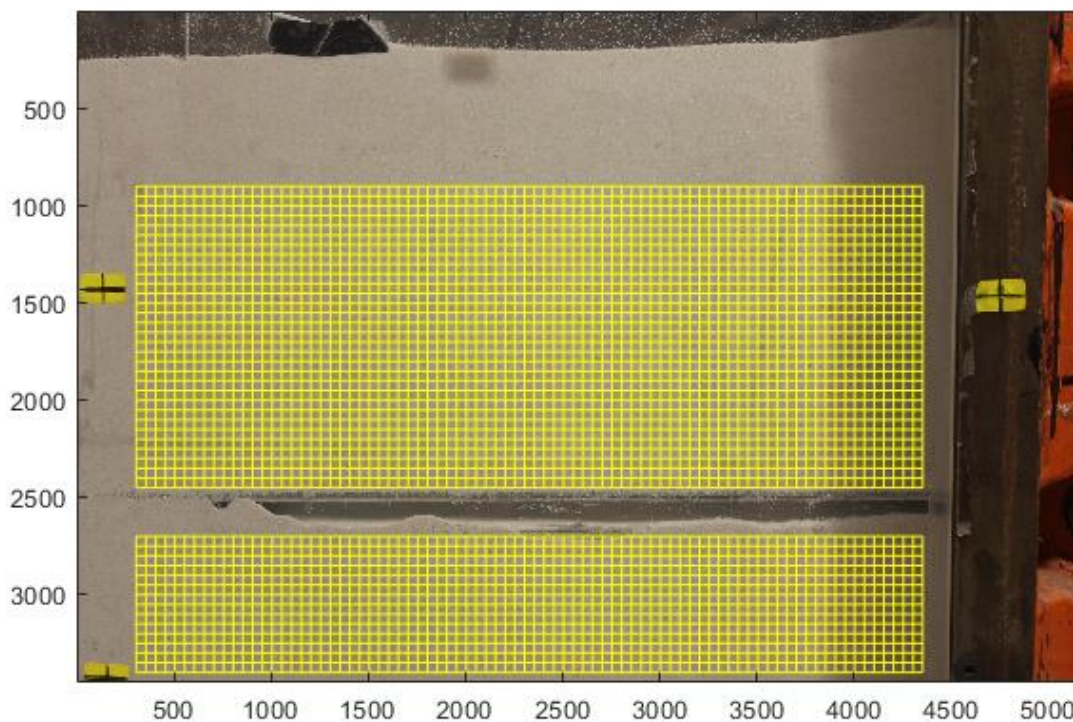


Figure 25: A typical mesh from the GeoPIV, in this case for test 1. Near-surface levels are avoided due to disturbance from the wire.

Second, a launch files is created. Other than the images and mesh file, the input features several choices for the deformation optimization exit tolerance, the maximum number of iterations, seed correlation coefficient tolerance and minimum coefficient correlation tolerance. The recommended default values were used for every analysis. The average

correlation coefficient was 0.85 for test 1 and 0.87 for test 2. No quivers are filtered out post-analysis except the occasional wild vector. The number of wild vectors were generally zero and never four in any test 1 and test 2 analyses. On the other hand, test 3 had several zones where sand was “falling” between the pipe and the window. This not only gives vectors that tend in the wrong direction, but at worst the patches are severely deformed.

```

5  % Files containing mesh or region of interest information
6  MESH_test1_general.txt 0
7  MESH_test1_general.jpg 0
8
9  % Analysis input parameters
10 analysis_mode 2
11 cutoff_diffnorm 1e-05
12 cutoff_iteration 10
13 seed_zncc_tol 0.9
14 min_zncc_tol 0.75
15
16 % Plots of analysis process
17 shows_plot_norm_corrcoef 1
18 show_surf_corrcoef 0
19 show_dx_disp_hist 1
20 show_dx_subpx_disp_hist 0
21 show_dy_disp_hist 0
22 show_dy_subpx_disp_hist 0
23 show_quiver 1
24 show_surf_dx 0
25 show_surf_dy 0
26 show_surf_dr 0
27
28 % Data path for analysis
29 C:\Users\danfja\Documents\MATLAB\GeoPIV_RG
30
31 % List of images to be analysed
32 IMG_6938.JPG
33 IMG_6991.JPG

```

Figure 26: Example of input file for GeoPIV-RG

A general issue with the analysis was that the frame moved to slightly move between pictures. The effect was more noticeable in the centrifuge; for the centrifuge experiment, the frame moved in the order of mm between two images. This is likely caused by physical movement of the camera mount or tripod as a small amount of sway is magnified by the distance to the window. Due to this issue, a MATLAB script was written to align the frames using the area below the pipe as a control zone (displacements here is expected to be exactly zero). The pixels are then reassigned to match the first image and the apparent displacement is subtracted from the displacement vectors based on the results from the GeoPIV.

Analyzing the area below the pipe gives an idea about the accuracy of the results. As an example, the mesh below is analysed between two frames taken right after each other with no load. The GeoPIV gave the following results:

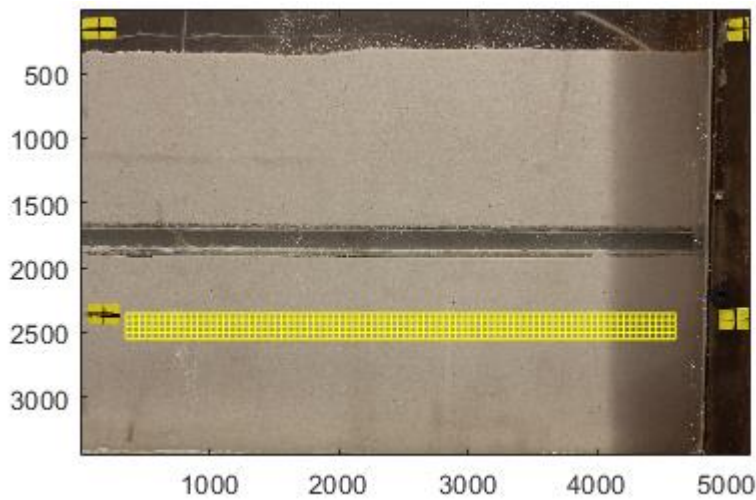


Figure 27a: The mesh is located under the pipe in an area where negligible displacements are expected.

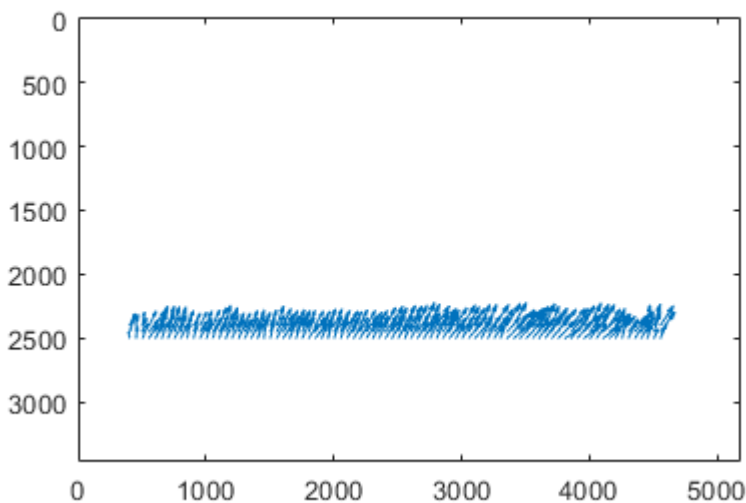


Figure 27b: The displacements vectors are skewed by a significant amount.

As can be seen from figure 27b, the arrows appear to be skewed in the upwards direction. However, the spread is extremely tight, with the following minimum, maximum and standard deviation for the vectors (table 13):

Table 13: Typical results from the error analysis

	Pixels	mm
Minimum value	0.047	0.0041
Maximum value	0.109	0.0095
Difference between highest and lowest value	0.062	0.0054
Standard deviation	0.024	0.0021

This is consistent with the accuracy achieved in other studies, including Marshall (2009).

In this case, the error is still very minor as the biggest apparent displacement is less than 0.01 mm, although this should be corrected for. Other frames showed much bigger displacement vectors up to 0.1 mm in 1G and between 0.5 to 1 mm in 50G. Without correcting for this, a systematic error is introduced and the centrifuge experiments are plainly useless due to the small movements wanted for this project. Due to the error in the correction, or the calibration arrows, the final error is the sum of the error from two analyses, but the final maximum error is still less than 0.01 mm.

3.10 Accuracy and precision of the GeoPIV

The accuracy in pixels depends on the mesh size (formula 49). A patch size of 50x50 gives the following accuracy in pixels:

$$\rho_{pixel} = \frac{0.6}{50} + \frac{150000}{50^8} = 0.012$$

The width of the frame is 5184 pixels and the captured length is approximately 350 mm (half of the pipe). This is equivalent to 0.0675 mm/pixel. Hence, the upper bound accuracy is in the range of a micrometer. Note that the captured length varies slightly. A mesh size of 50x50 pixels gives one measurement point approximately every 3.4 mm.

Precision is a function of measurement point array size, n_{points} , which is calculated as the total number of pixels divided by the mesh size

$$n_{points} = \frac{5184 * 3456}{50^2} = 7166$$

For this number of measurement points, the precision is (figure 3 in White and Take, 2002):

$$\frac{1}{1500000} * 5184 \text{ pixels}$$

$$\rightarrow 0.003456 \text{ pixels} = 0.00023 \text{ mm}$$

Or about 2-3 micrometers.

The measurement and precision of the GeoPIV software represents only one side of the accuracy and precision of the results. The accuracy of the displacement vectors depends to a large degree on the conversion from image space (pixels) to object-space values (for example in millimetres). The lengths were measured manually with the thumbstick, hence the final accuracy in object space is possibly 0.1 mm. Precision is affected by the images themselves. This includes human errors in handling the camera and changes in lighting. Achieving stable lighting with no flickering and changes is a challenging task in the

centrifuge. Another problem is lens distortion, often called the “fish eye” effect. The distortion is minimal in the middle but increases towards the edges of the image.

3.11 Fibre optics

Fiber optics were installed inside the PVC pipes to measure the strains in the pipe. The fibre optical cables were glued to the wall with Epoxy glue, ensuring continuous contact between the soil and the pipe wall. Figure 18 shows the pipe with the fibre optics. What can be seen is one continuous fibre that is glued to the upper half of the pipe, looped around and then glued to the lower half of the pipe. The distance from the centre of the cross section is 7 mm.

Calibration of the fibre optics was carried out by heating up 6 different points to obtain the relative locations. Based on the fibre optics calibration results, the following coordinates were established (table 14). Note that the fibre optics do not cover the entire length of the pipe, a necessary precaution due to space limitations in the centrifuge box.

Table 14: Calibration results which determine the location of six points, three points on the upper half and three points on the lower half of the pipe. Locations are relative to the midpoint.

	Lower fibre location (m)	Upper fibre location (m)
Start	0.264	0.262
Midpoint	0	0
End	-0.281	-0.283
Total length covered	0.545	0.545

The fibre optics gives the axial strains in microstrains. Moment can be calculated as follows,

$$M = \frac{(\varepsilon_L - \varepsilon_U)}{2 * y} * EI_{pipe} \quad (119)$$

Where $y = 7$ mm for this particular set up and carefully noting that the cross section is a semicircle.

The fibre optics are assumed infinitely flexible and therefore do not contribute to the stiffness of the pipe. Figure 28 shows a typical strain profile during. Some asymmetry can be observed, both between the right side and the left side as well as the upper fibre and the lower fibre. A preliminary analysis showed that off-setting the two strain curves to match the locations of the peaks gave almost identical moment diagrams.

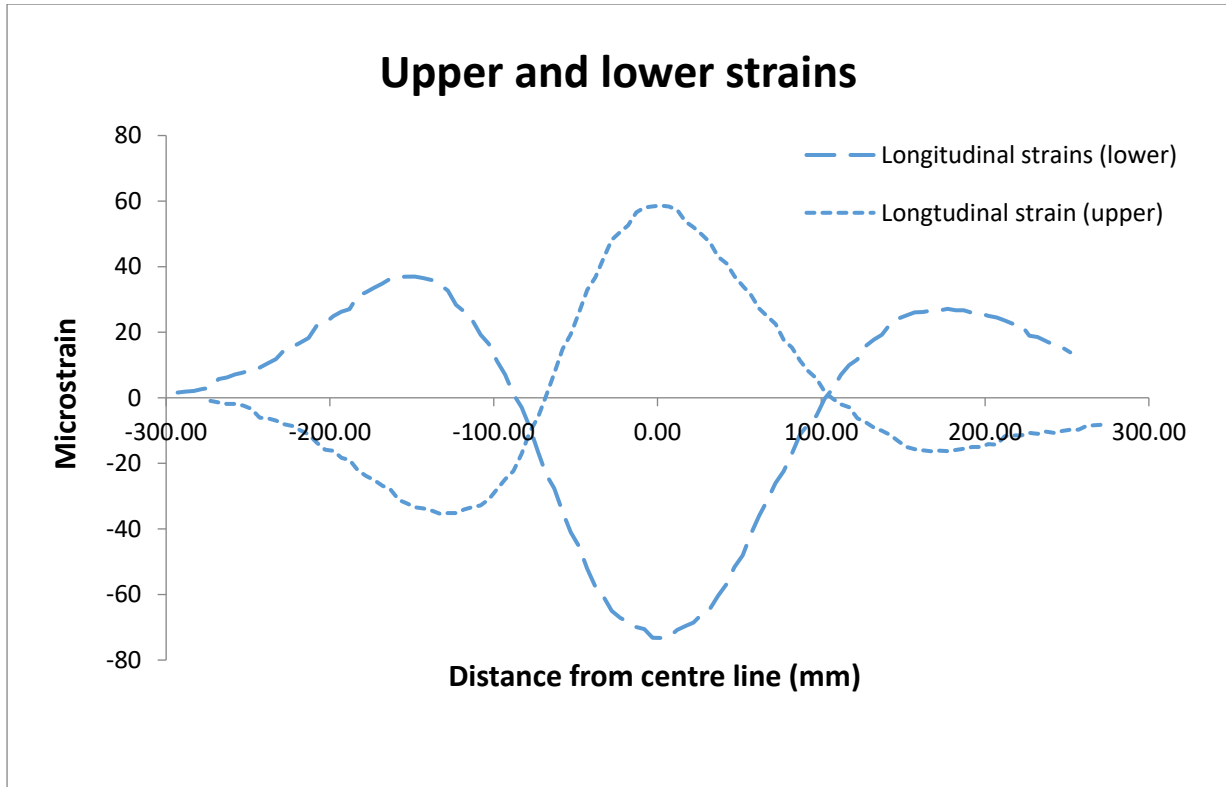


Figure 28: Typical microstrains recorded for a loaded pipe in test 1 and test 2.

3.12 Verification of the elastic continuum solution

Two Wolfram Mathematica script based on the continuum solution by Klar (2018) and section 3.1 has been developed as a part of this thesis. The script is summarized here, and the entire script is available in appendix A.1-A.4.

Results from numerical and experimental studies are then analysed in the frequency domain to verify the stability of the analytical solution.

3.12.1 Computed displacements with the elastic continuum solution

The first Mathematica script implements the elastic continuum solution for a pipe at infinite depth. This code solves the response of the pipeline in a "smooth" box, meaning the soil is allowed to flow around the pipe. The analytical solution describes the periodic response of a pipeline subjected to a Gaussian load, as illustrated by figure 29. The solution assumes symmetric displacement curves, i.e. $\delta(-x) = \delta(x)$. No rotation of the pipe occurs at the symmetry lines as $\delta(x)$ is continuous. Displacements at the symmetry lines are allowed by the model. Hence, the pipeline is fixed against rotation but not vertical displacement.

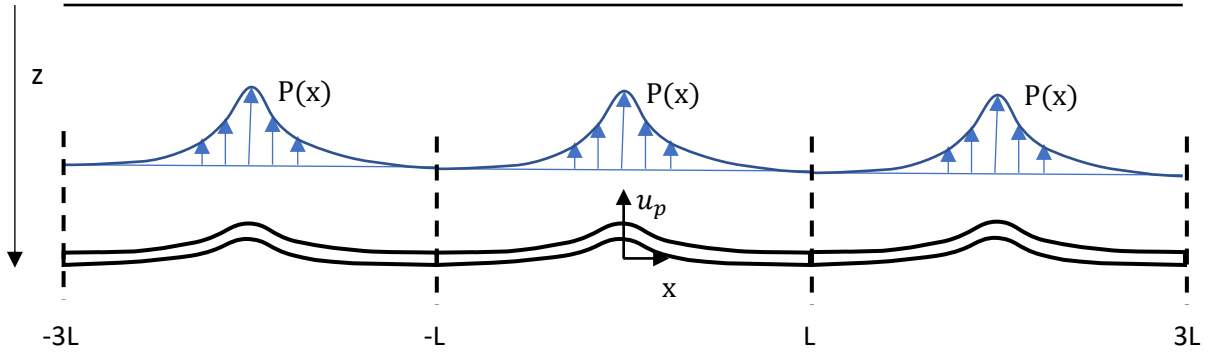


Figure 29: Pipeline periodic displacements. The continuum solution requires that u_p is continuous, therefore the deflection angle must be zero at each period.

The analytical method plots a theoretical displacement of a pipeline. The Gaussian load is defined as:

$$\delta[x_{-}] := P_0 * \frac{1}{a\pi^{1/2}} \exp\left[-\left(\frac{x}{a}\right)^2\right] \quad (120)$$

The integral of the Gaussian curve is $P_0 * 1$ and a is the standard distribution of the load. The same load is defined in the frequency domain as:

$$A0 = \frac{1}{L} \int_{-L}^L \delta[x] dx \quad (121)$$

$$An = \text{Table}\left[\text{Re}\left[\frac{1}{L} \int_{-L}^L \delta[x] \text{Cos}\left[\frac{i\pi x}{L}\right] dx\right], \{i, 1, n\}\right] \quad (122)$$

for which $\omega n = n\pi/L$. This creates a table of real-valued Fourier coefficients.

Now the Fourier coefficients and the spatial frequency-dependent stiffness for an infinitely deep pipeline is inserted into the equation for U_p (equation 88). Recall that that a closed form solution for the spatial frequency-dependent stiffness is known (equation 25), which will be defined in the Mathematica script as:

$$k\omega[\omega r0] := \frac{16 * G * \pi(1 - \nu)}{(6 - 8\nu)\text{BesselK}[0, \omega r0] + \omega r0\text{BesselK}[1, \omega r0]} \quad (123)$$

The amplitude of the periodic soil displacements in the Wolfram Mathematica script is:

$$\text{UpCoe} = \text{Table} \left[\frac{\text{An}[[i]]}{\text{EI} * \left(\frac{i\pi}{L}\right)^4 + k\omega \left[\frac{i\pi}{L} r_0\right]}, \{i, 1, n\} \right] \quad (124)$$

Lastly, recall that the pipeline displacement is written as $u_p(x, \omega) = U_p(\omega)\cos(\omega x)$. In Wolfram Mathematica this is defined as follows:

$$\text{up}[x_] := 0 + \sum_{i=1}^{\text{Dimensions}[\text{An}][[1]]} \text{UpCoe}[[i]] \text{Cos} \left[\frac{i\pi x}{L} \right] \quad (125)$$

The analytical solution will later be compared with numerical and experimental simulations. Measured model displacements are interpolated, integrated and transformed, then analysed in the frequency domain.

A proof of method can be found in Appendix A.1. The proof of method is easily demonstrated using the solution above to represent values from measurements, $up(L/10000), up(2L/10000), up(3L/10000) \dots up(L)$. Figure 29 shows the proof of method by replotting k_ω values derived from the continuum solution. As expected, each point matches the analytical solution for k_ω .

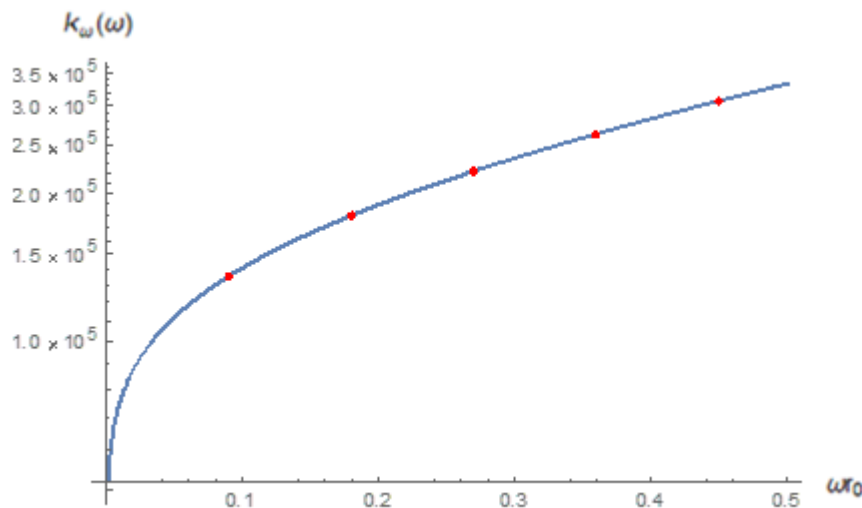


Figure 30: Values for k_ω replotted after the continuum solution. The input here is also based on the continuum solution and therefore a perfect match.

A key advantage of integrating values from measurements is that relatively few measurement points are sufficient. This is particularly important for the experimental study since larger patches gives more accurate measurements with the GeoPIV. This also means that some wild vectors can be simply be ignored without affecting the results.

3.12.2 Verification of elastic continuum solution with measured values

The second Mathematica script uses the displacements from experimental or numerical simulations to define the pipes deformation pattern. The Fourier coefficients are calculated as shown in the previous section, but only half of the box is analysed. A displacement function is created by interpolating the measured values, which in Mathematica simply calculated as follows:

$$\text{sampleval} = \text{Interpolation}[\text{Data}], \quad (126)$$

Where Data is a table of values x and $up(x)$.

The pipeline periodic displacement Fourier terms in this case are:

$$U0 = \frac{1}{L} \text{NIntegrate}[\text{sampleval}[x], \{x, -L, L\}] \quad (127)$$

$$Un = \text{Table}\left[\frac{1}{L} \text{NIntegrate}[\text{sampleval}[x] \text{Cos}\left[\frac{i\pi x}{L}\right], \{x, -L, L\}], \{i, 1, n\}\right] \quad (128)$$

Finally, the spatial frequency-dependent stiffness k_ω is obtained with the ratio between the amplitude of the barrel load and the periodic pipeline displacements. This is calculated with equation 88, which rearranged to solve for the spatial frequency stiffness becomes the following equation in Wolfram Mathematica:

$$K\omega\text{Res} = \text{Table}\left[\left\{\frac{i\pi}{L} * r0, \frac{\text{An}[[i]]}{Un[[i]]} - \frac{EI}{r0^4} * \left(\frac{i\pi}{L} * r0\right)^4\right\}, \{i, 1, n\}\right] \quad (129)$$

This creates a table of spatial frequency-dependent stiffness values for n harmonics ωr_0 . The experimentally or numerically based values for k_ω are then compared to analytically computed values. It is often useful to normalize the values for k_ω with the bulk modulus G .

4 Evaluation of the elastic continuum solution with numerical models

4.1 Modelling approach

This section conducts a study using numerical simulations of vertical pipeline displacement due to an applied load using COMSOL Multiphysics. The goal of this numerical study is to use the displacement as an input to the continuum solution, and analyse the pipeline response with the script in section 3.12. This procedure is similar to that of the experimental and analytical comparison, hence this section can be considered a proof of method ahead of the 1G and centrifuge experiments. A Wolfram Mathematica script based on the continuum solution by Klar (2018), presented in chapter 3, has been developed for this numerical study. The script is available in appendix A.2.

Three-dimensional finite element models of several buried pipelines have been made with COMSOL Multiphysics. The model was made using the Structural Mechanics Module for both the pipeline and the soil. This section only investigates linear elastic strains as this is one of the assumptions of the elastic continuum solution. The continuum mechanical approach in this analysis also assumes continuous contact between the soil and the pipe; that is, no flow-like behaviour is allowed. To summarize, all finite element models in this study makes the following basic assumptions:

1. Both materials (the buried pipeline and the surrounding soil) is continuous and elastic.
2. A linear relationship stress and strain.
3. Deformations are small

Several pipeline depths and radii were investigated. Different Young's moduli were also investigated but will not be included here as all the results are normalized by the bulk modulus. All findings from the numerical results and the continuum solution were consistent regardless of the Young's modulus.

The pipeline is subjected to a static, concentrated load at the centre point. This will cause the pipe to bulge in the middle, similar to what has been described earlier for the experimental model. Due to a natural limitation of finite element models, a point load cannot be applied as a surface (3D) load. Solving for a point load analytically is fully possible and easy to do, but this is not the case for numerical models. To work around this issue, a Gaussian load is distributed over a very small area to approximate a point load. This gives a narrow and concentrated load at the centre point, which rapidly approaches zero along the direction of the pipe. The result is very similar to the response to of point load while avoiding singularities or similar effects.

The third script (Appendix A.3) is similar to the second script (Appendix A.2) but uses measured values from experiments as input. The load function is also made much narrower for the experimental study.

4.1.1 The finite element model

The finite element model simulates the centrifuge experiment at 50g, down to the dimensions being 1/50 the size of a pipeline in the field. Non-linear effects of the centrifuge is not considered, however. Figure 31 shows the model dimensions of a typical model and its two components: The soil and the pipe. The box is 700 mm long, 500 mm wide and the underlying sand is 100 mm thick. Pipeline burial depth, pipe diameter and Young's modulus varied. In addition, the stiffness of the soil was calculated according to the prediction formula of Biarez, Hicher and others, (1994) (formula 39). Soil stiffness is constant with depth for each individual model. A Poisson's ratio of 0.25 was used for every simulation. Table 15 presents the different numerical models that are analysed.

The boundary conditions of the model are set as follows:

- Rollers at the bottom of the box
- Roller at both sides parallel with the pipe
- Symmetry at both sides normal to the pipe direction
- The top of the box is free

COMSOL Multiphysics features a boundary condition called symmetry. As the name indicates, the symmetry boundary condition at both ends of the pipe creates a periodic response.

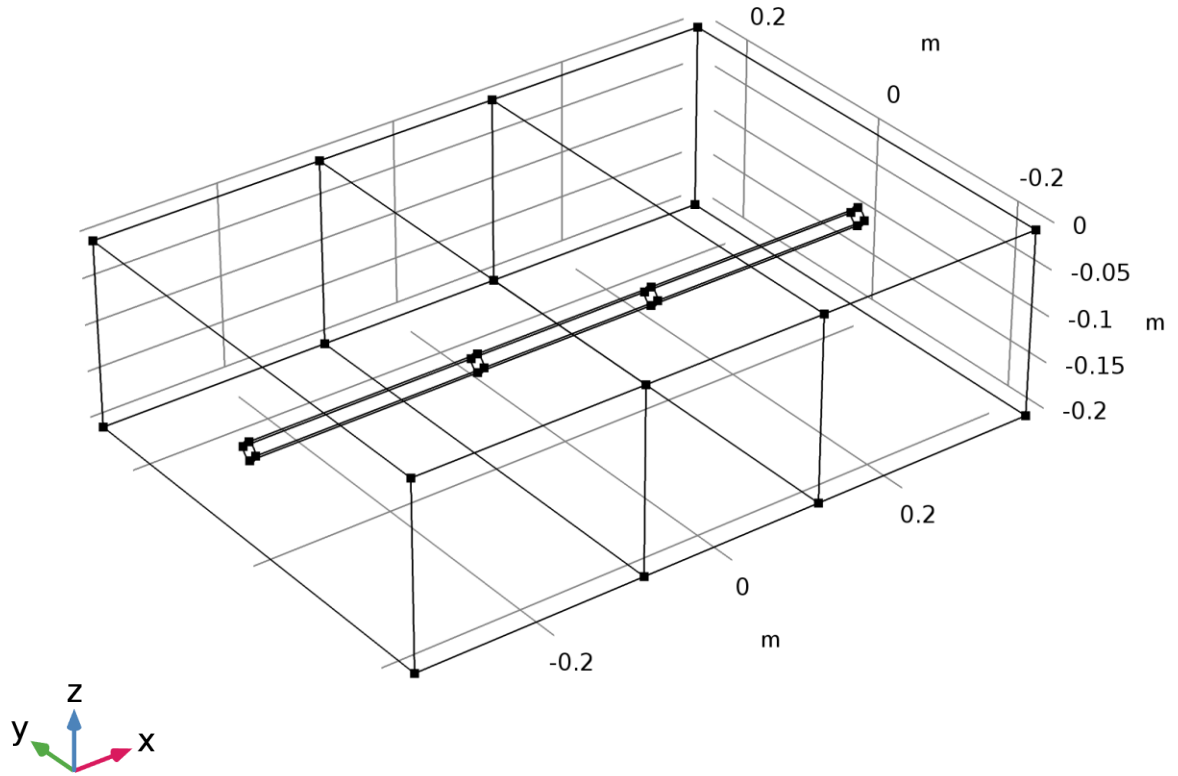


Figure 31: The buried pipeline model consists of two solid elements: a pipeline with and the surrounding material

The model acts as a single block of solid and continuous material, with different Young's modulus and poisons ratio. Every simulation presented here was carried out with an aluminium pipe with a Young's modulus of 70 000 MPa and a poisons ratio of 0.33. The pipe presented here is solid (as opposed to hollow), but the results should be valid for any cross section were. The load is applied as a surface load on the pipeline. The Gaussian surface is described by the formula.

$$\frac{P_0}{2 * 3.14 * r_0} * \frac{1}{a[m] * sqrt(3.14)} * exp\left(-\frac{(x)^2}{(a[m])^2}\right) \quad (130)$$

Where a is the standard deviation of the distribution and controls the spread of the load. The integral of the load function over the entire surface area of the pipe is exactly P_0 .

The load is centred at the midpoint of the pipeline. Figure 32 shows the surface load with $a = 0.015$ m, which was used for most experiments. Note that the load is concentrated in the middle and negligible elsewhere. Each pipeline was displaced approximately 0.1 mm for comparison purposes, except for the when the a-values were changed. Any load-displacement magnitude can be used as all experiments are linear elastic.

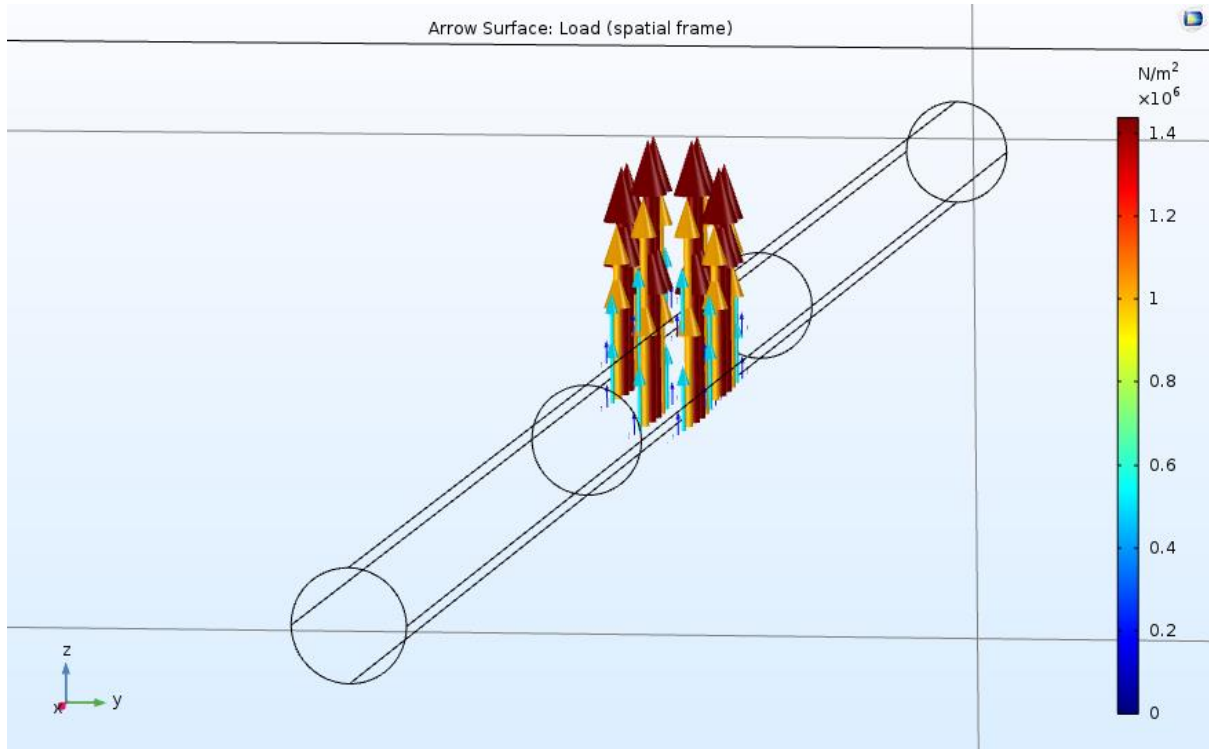


Figure 32: A narrow Gaussian surface load was applied as a point load cannot exist in a 3D space.

Table 15: Parameters of every simulation carried out

Simulation	r_0 (mm)	z_p (mm)	z_p/r_0	a (mm)	E_s (MPa)	P_0 (N)
1	5	25	5	0.015	79	550
2	5	50	10	0.015	112	860
3	5	75	15	0.015	137	1160
4	10	50	5	0.015	112	1610
5	10	100	10	0.015	158	2450
6	10	150	15	0.015	193	3050
7	20	100	5	0.015	158	5150
8	20	200	10	0.015	223	7550
9	20	300	15	0.015	281	9300
10	10	100	10	0.030	158	2450
11	10	100	10	0.045	158	2450
12	10	100	10	0.090	158	2450

Figure 33 shows a typical mesh from of the finite element models. This model is from simulation #5. The mesh is very fine for the pipe itself. The mesh of the surrounding soil is manually controlled. By dividing into three zones, where the middle zone uses utilize a very fine mesh, computation times were significantly reduced with no drawbacks. Displacements of the soil are low in the coarse mesh zone, therefore this mesh is sufficient.

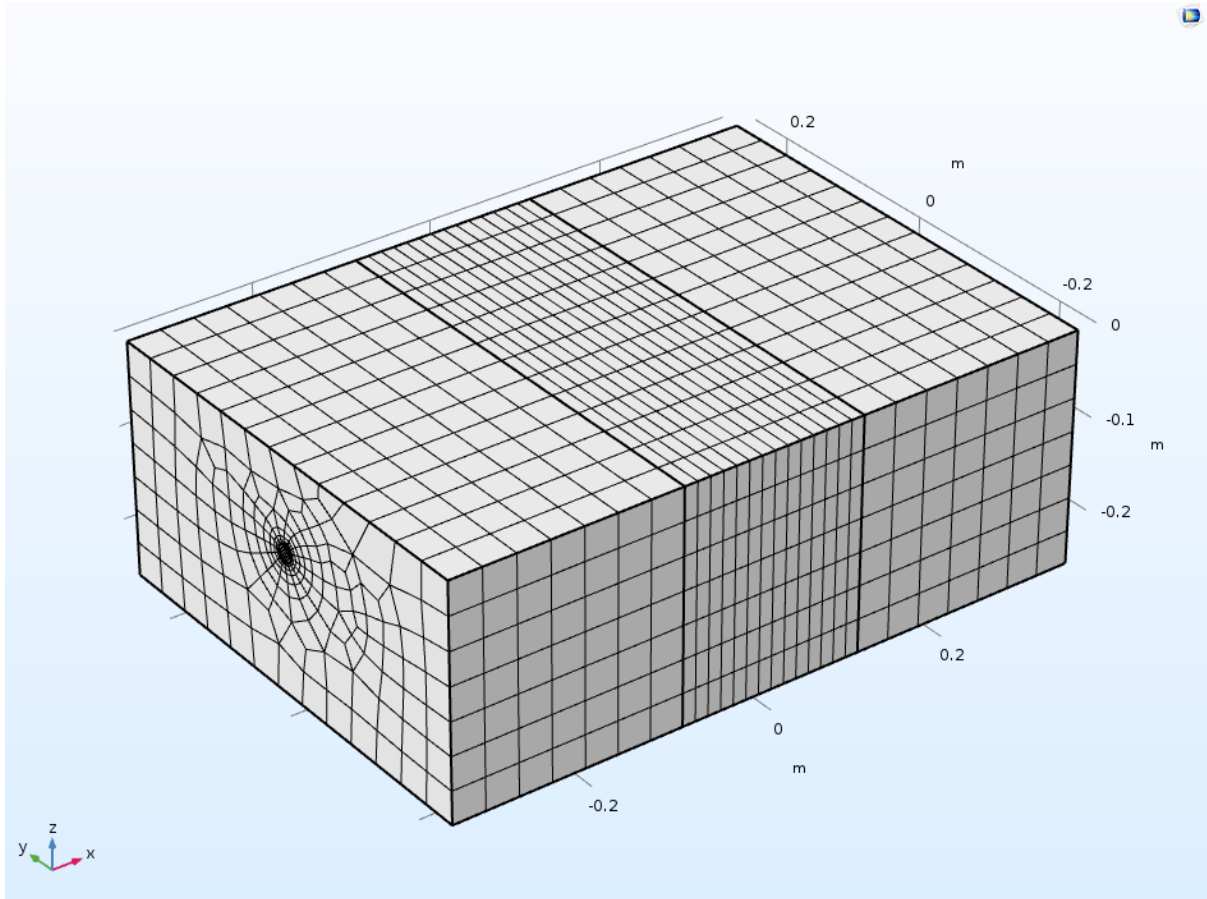


Figure 33: Typical finite element mesh

4.2 FEM results

This section briefly presents the deflection profile of the pipe. Pipe displacements are extracted from the finite element analysis at the top of the pipe, or $z = r_0$ and $y=0$. Note that displacements are identical at the top of the pipe and the bottom of the pipe. Displacement plots are normalized by v_{max} for illustration purposes; The value of v_{max} is $0.1 \text{ mm} \pm 0.05 \text{ mm}$. For the purpose of verifying comparing the values of spatial frequency-dependent stiffness, any load resulting in small displacements can be used as the FEM-model and the continuum is linear elastic. Other than analysing the displacements in the frequency domain to verify the continuum solution, the results can also indicate the suitability of the different relative rigidities (pipeline stiffness compared to soil stiffness). A suitable relative rigidity in this context gives a deflection profile that is neither too narrow nor too wide. The two scenarios will happen if the pipeline is too flexible and too stiff, respectively. A narrow deflection profile is not compatible with the PIV due to limitations in measurement points per mm, and a wide deflection profile voids the infinite pipeline assumption. This is, of course, only relevant for the success of experimental studies.

Displacement profile for different radii at the same depth

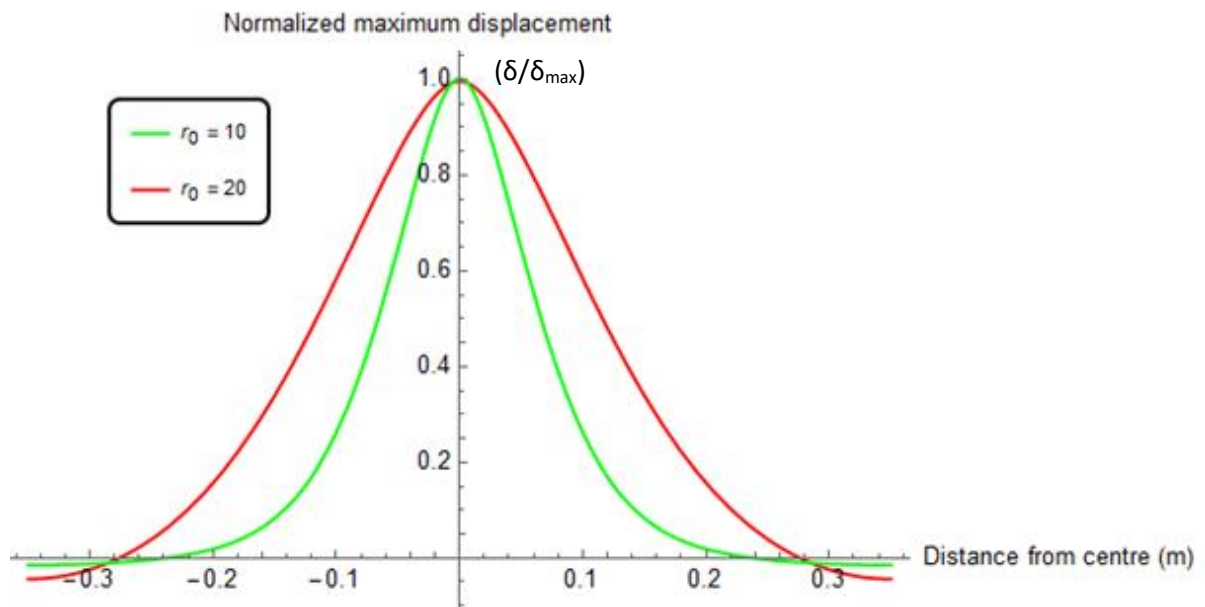


Figure 34: Pipeline displacement profile for two different pipeline radii.

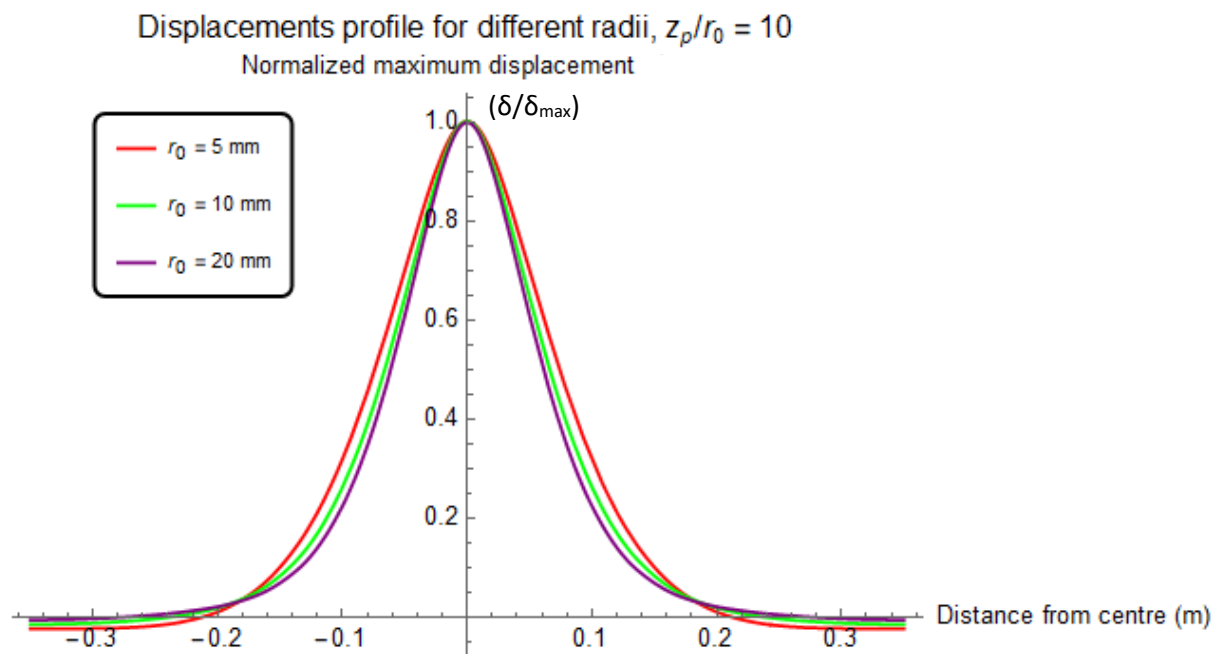


Figure 35: Pipeline displacement profile for three different pipe radii and the same z_p/r_0 ratio.

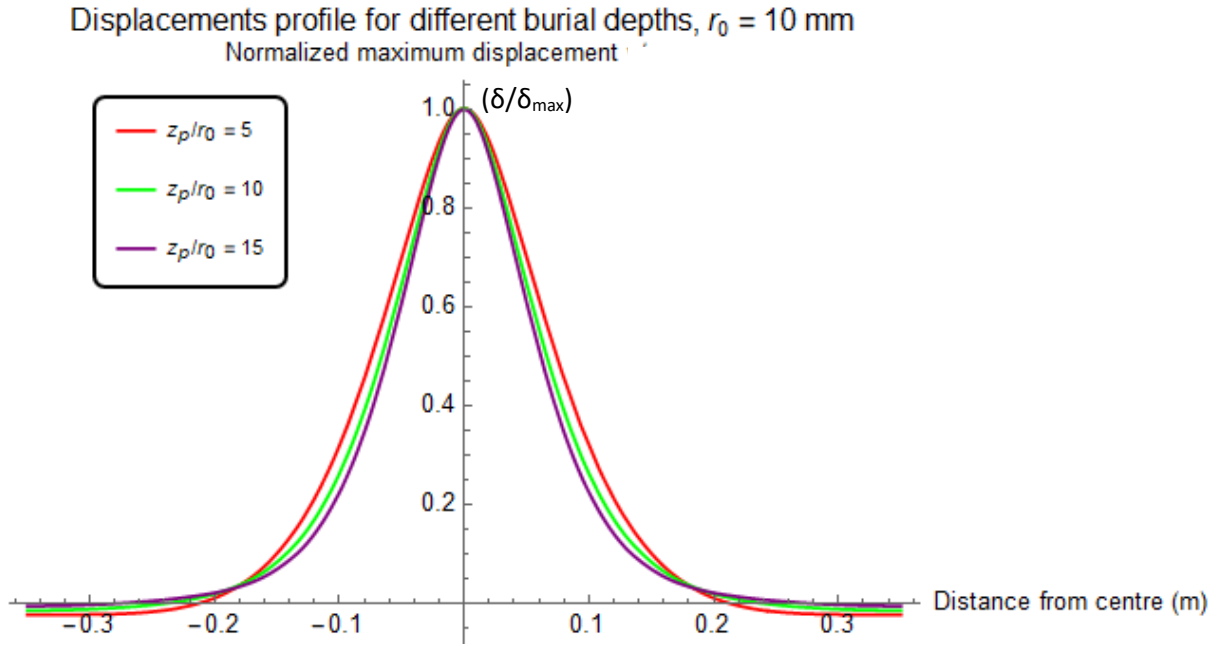


Figure 36: Pipeline displacement for three different z_p/r_0 ratios and the same pipe radius.

Figure 34 shows that a higher pipe radius buried at the same depth gives a wider deflection profile. This relationship will not be investigated further in this thesis, but the results are helpful in determining the suitability of the burial depth. It is clear from figure 34 that a pipeline with a 10 mm radius buried at 100 mm gives a suitable displacement profile, assuming the soil stiffness is predicted well. On the other hand, the pipe with a radius of 20 mm gives a deflection profile that is too wide. The latter scenario might be invalid for infinite pipe assumption in the elastic continuum solution in an experimental study due to rotation at the end of the pipe. As for the finite element model, symmetry and no rotation at the end of the pipe is ensured by the boundary condition. Figure 35 compares three different radii with the z_p/r_0 ratio remaining constant. Deflection profiles are fairly similar, although likely more by chance than as a general identity. However, it can be concluded that the varying the radii of a 700 mm long aluminium pipe at a z_p/r_0 ratio of 10 will give suitable deflection profiles in the centrifuge at 50g. Likewise, figure 36 shows that varying the z_p/r_0 ratio of a 10 mm radius and 700 mm aluminium pipe is a good choice. In summary, the properties of simulation 2, 5 and 8 is suitable for investigating different radii in the centrifuge at 50g. However, do note that a radius of 5 mm gives should only be used in fine sand to ensure that the soil acts as a continuum. Properties from simulation 4, 5 and 6 is suitable for investigating different z_p/r_0 ratios.

4.3 Comparison of analytical and numerical solutions

Displacements from simulation 1 to 9 are analysed in the frequency domain here. The analyses script is provided in Appendix A.3 and also explained closer in the methodology section. The load function is the same as in section 3.12.2 and the input values are given in table 15.

The following figures plots for spatial frequency-dependent soil stiffness for three different burial depths. All obtained k_ω values are normalized by the bulk modulus G and compared to the analytical solution for spatial frequency-dependent stiffness at infinite depth $k_{\omega,\infty}$. It should be noted that the value of the bulk modulus does not affect the normalized curve $k_{\omega,\infty}/G$. Figure 37 a, b and c shows the spatial frequency-dependent soil stiffness for pipelines of radius 5 mm, 10 mm and 15 mm, in that order.

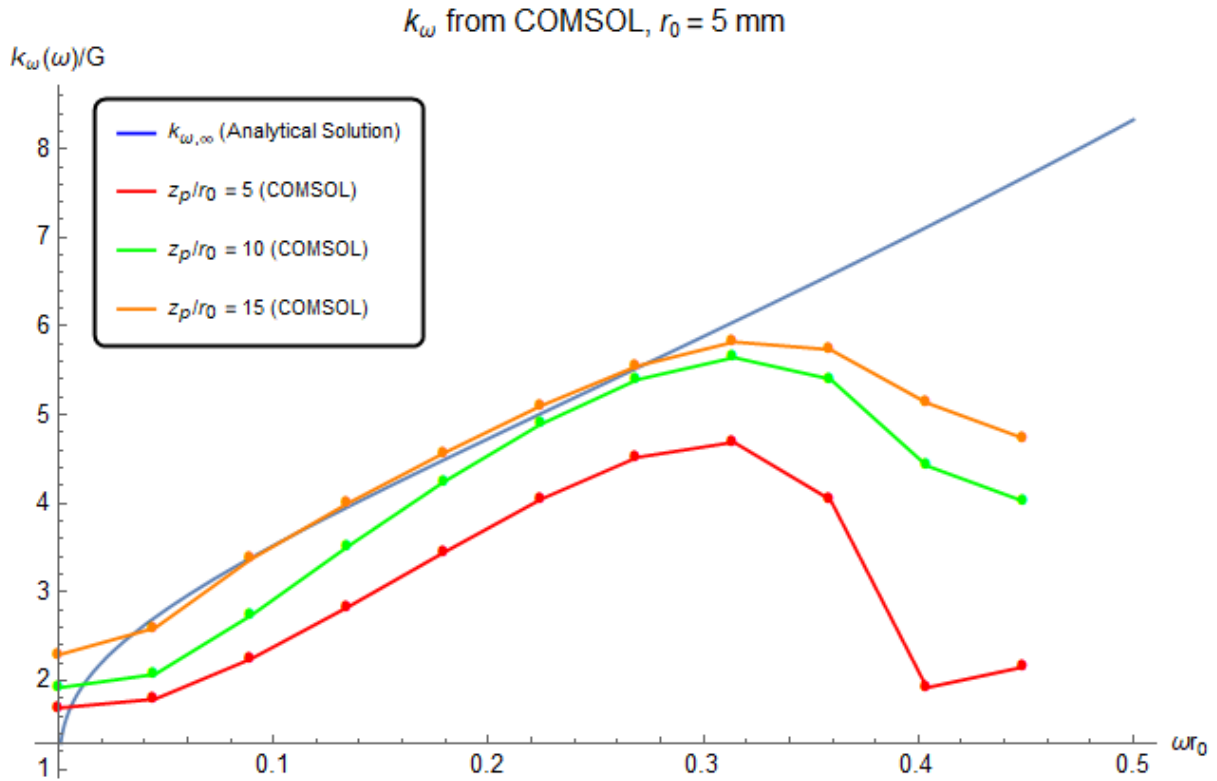


Figure 37a: Spatial frequency-dependent stiffness for $r_0 = 5$ mm at different depths and compared to the solution for an infinite pipe.

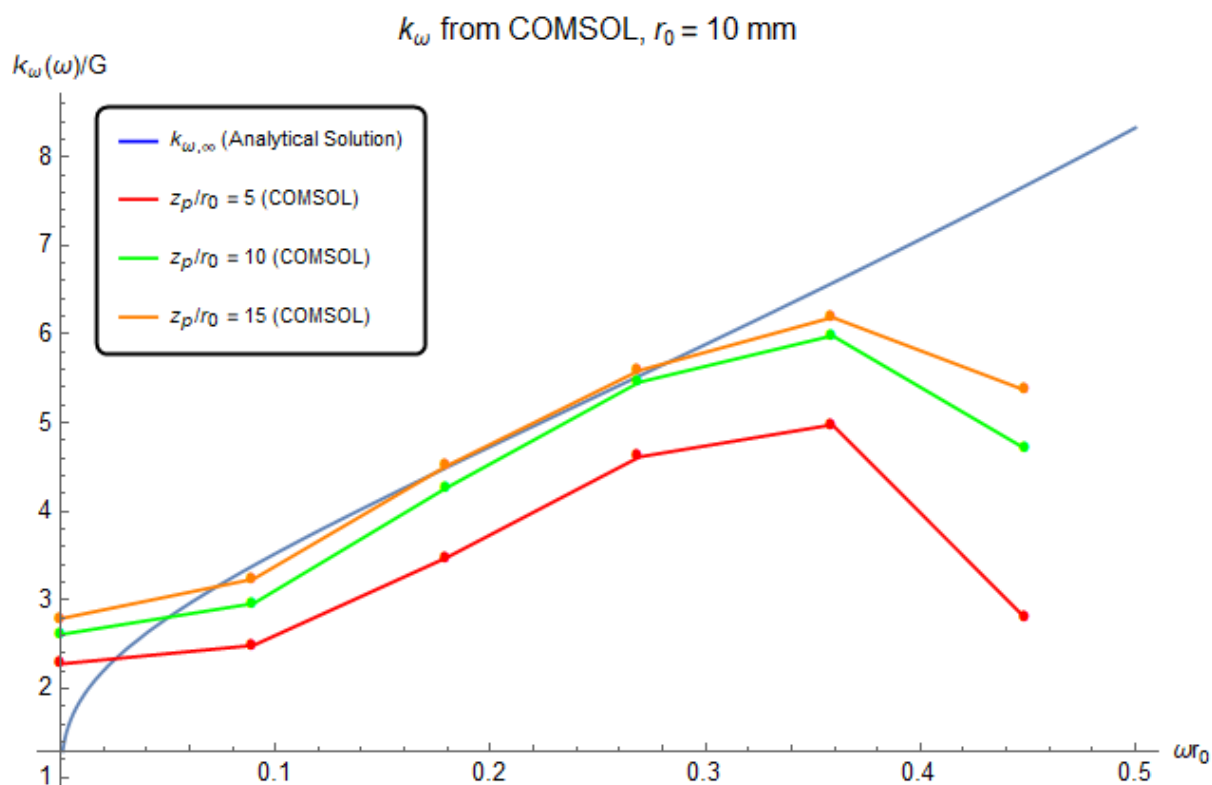


Figure 37b: Spatial frequency-dependent stiffness for $r_0 = 10$ mm at different depths and compared to the solution for an infinite pipe.

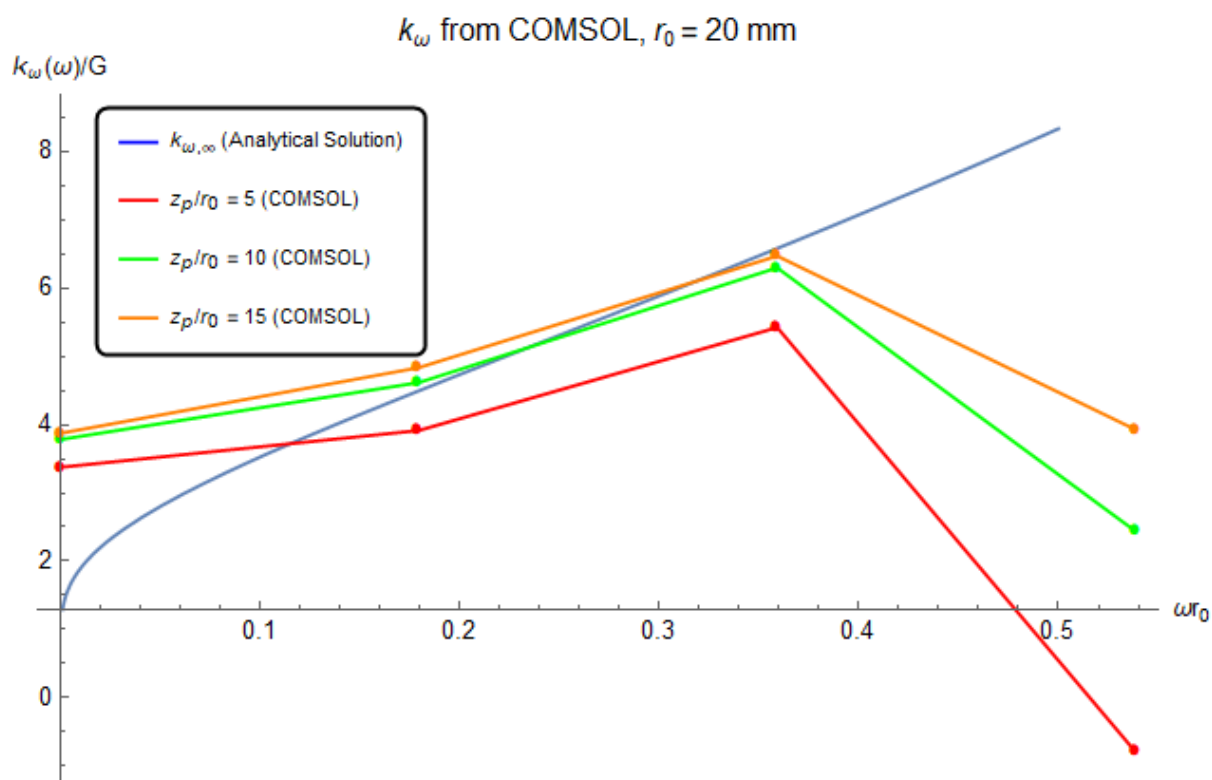


Figure 37c: Spatial frequency-dependent stiffness for $r_0 = 20$ mm at different depths and compared to the solution for an infinite pipe.

Figure 37 a, b and c demonstrate that several harmonics can be obtained from measured values. It is apparent from this table that the solution becomes unstable around $\omega r_0 = 0.3$ to 0.4 . This is observed in all three cases. The number of harmonics that can be obtained is therefore dependent on the radius. Remember that four to five harmonics is enough to accurately describe the global response of the pipeline values, though fewer harmonics could still provide some utility. The results also reveal that a Winkler model is not sufficient to model the pipeline response; If this was the case, the spatial frequency-dependent stiffness would be constant for all spatial frequencies.

It can be seen that the solution at large depths quickly approaches the solution for an infinitely deep pipeline. The spatial frequency-dependent stiffness for a z_p/r_0 ratio of 15 almost perfectly matches the solution for values for an infinitely deep pipeline, except for low spatial frequencies near zero. This is consistent with the findings in (Klar, 2018). The k_ω values decrease with decreasing depth. The ratio $k_\omega/k_{\omega_\infty}$ is significantly less than unity for the first three harmonics, minus the first harmonic, but the two curves are almost perfectly aligned by the fourth harmonic. This result can also be seen in (Klar, 2018) for a comparable z_p/r_0 ratio. Lastly, a z_p/r_0 ratio of 5 gives smaller k_ω values, compared to the infinitely deep pipeline, for all non-zero spatial frequencies in the range of valid values. For all simulations, the spatial frequency-dependent stiffness does not approach zero when the spatial frequency becomes zero. The spatial frequency-dependent stiffness for finite burial depths are not expected to approach zero in the near zero spatial frequency range, as this is a property of infinite depth.

4.4 Sensitivity test a-values

This section changes the a-values while keeping all other input values the same. The purpose is to investigate the sensitivity of the solution to the load function. The equation used to calculate the spatial frequency-dependent stiffness uses the degenerate solution for a point-load. Therefore, the sensitivity test will indicate the validity of this assumption, or more specifically: how wide can the load be distributed before the response is not accurately described by the point load solution. This is important because a real point load cannot physically exist, but can still be assumed for a very concentrated load. For example, the point load in the centrifuge set up is a wire clamp with a significant width. The experimental setup in this will distribute the load over less than 5 mm ($a = 0.005$ m) for the 1G test and approximately 15 mm ($a=0.015$ m) for centrifuge tests based on these results.

The spatial frequency-dependent stiffness for three different a-values is presented in figure 1. As shown in the figure, the width the load is distributed over clearly affects the validity of the analytical solution for a point load. Large a-values should therefore be avoided with the point load degenerate solution.

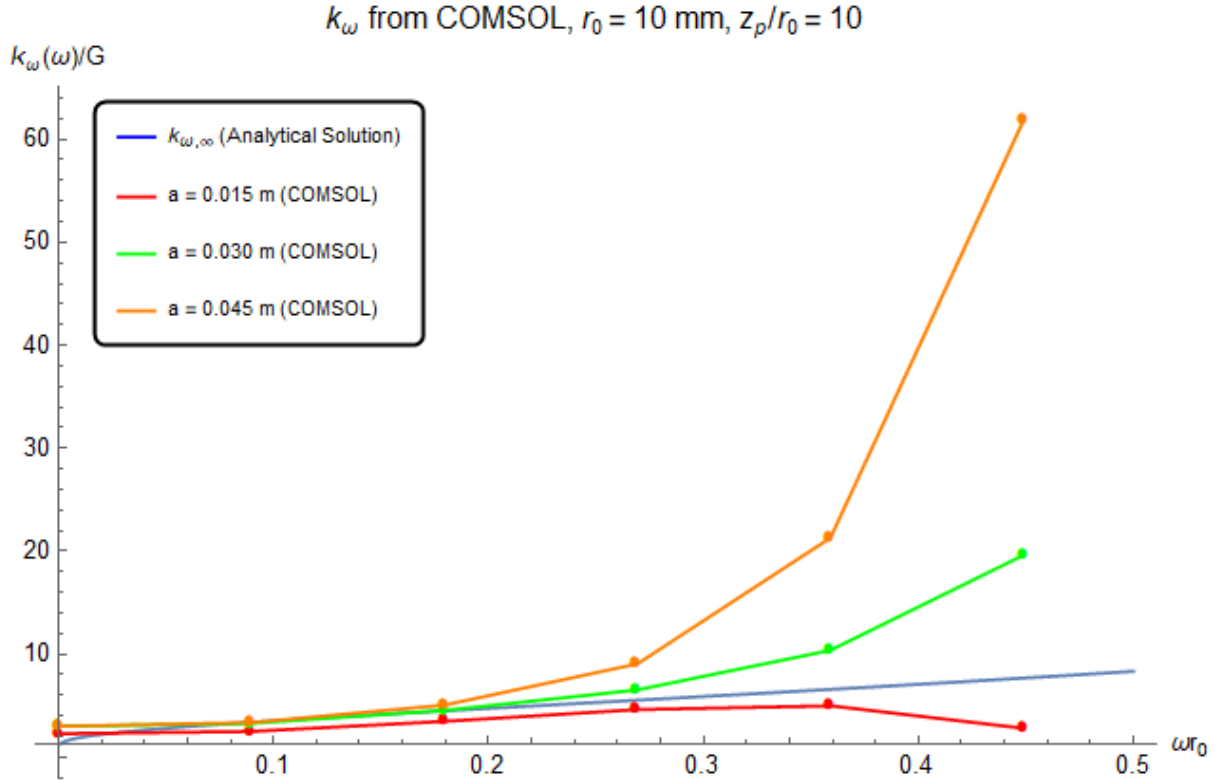


Figure 38: Spatial frequency-dependent stiffness for different a -values, where a controls the width of the Gaussian function.

4.5 Summary

This section showed response of a buried pipeline to a vertical surface load based on a finite element analysis in COMSOL Multiphysics. The model features the same dimensions and properties as the centrifuge model in this thesis. The Young's modulus of the soil represents the predicted values for the same depth at an increased gravity of 50g. A linear elastic soil stiffness is incorporated since this is one of the key assumptions of the elastic continuum solution by (Klar, 2018). The load is distributed as a narrow Gaussian to emulate the response of a pipeline due to a point load.

Transverse deflection profiles for different pipe radii r_0 and burial depths z_p were investigated. Several dependencies on pipeline radius, depth and z_p/r_0 ratio are established. The finite element analysis also indicates that a 10 mm aluminum pipeline is suitable for the centrifuge test as it clearly maintains a deflection angle of zero at the ends.

The displacements are analysed in the frequency domain to obtain the spatial frequency-dependent stiffness k_ω . Values for k_ω are calculated for all the simulations and compared to the analytical solution and findings in Klar 2018.

5 Experimental test results

Test results from four pullout tests are presented and analysed here. Section 3.8 explains the test procedure for each test. As a reminder, the following tests were carried out (table 16):

Table 16: Test number and conditions for each test

Test	n []	r_0 [mm]	t [mm]	z_p/r_0 []	E_p [MPa]
1	1	10	2	21	3400
2	1	10	2	12	3400
3	1	10	-	12	70000
4	50	10	-	11	120000

This chapter aims is to identify the deformation pattern of the pipe as well as soil displacements and potential soil-structure interaction mechanisms. The emphasis will be on test 1 and test 2 as they have the most reliable data. The PIV measurements from test 3 have limited use and the centrifuge test, test 4, even more so. All displacements measurements were carried out with GeoPIV-RG. The program is described in section 2.8 and the specific procedure for this study is presented in chapter 3.9.

5.1 PVC pipe in 1G (test 1 and test 2)

Two pullout tests were carried out to assess the effect of a point load on a thin-walled PVC pipe. The two tests involve different burial depths but are otherwise identical. Pictures were taken manually and at regular intervals each time the load was increased. Most load steps had multiple pictures were taken, from which several conclusions can be made: First, the pictures almost universally gave the same results for two different pictures at the same load step. One exception to this was wild vectors, which was often found to be worse in specific frames and seemed to disappear for a different image at the same load.. Second, it can be concluded that no significant creep, relaxation of the wire system or other time-dependent effects have affected the results. This chapter generally shows the results from the first image taken at each load step, but additional pictures where used to control the results or reduce the number of wild vectors.

This section presents the load-displacement curve of the pipe, followed by the displacement field of the surrounding soil and the corresponding strains in the overlying soil, followed by the pipeline deflection. Finally, the results are analysed in the frequency domain to verify the stability of the elastic continuum solution.

5.1.1 Pipeline uplift response

Maximum displacement according to the GeoPIV and fiber optics is both shown here. The purpose is both to give an overview of the load steps and corresponding pipe movement at

the point load as well as compare the pullout response of a flexible pipe with existing prediction formulas on rigid pipes. To the author's knowledge, this is the first attempt to study the pullout capacity of a flexible pipe. All prediction formulas in presented here assume a rigid pipe, meaning displacement is uniform along the pipe. Soil resistance (soil stiffness) is drastically reduced with large displacement, and the soil resistance may develop differently for a flexible pipe where displacement is concentrated in the middle.

The theoretical pipelines displacement is calculated according to DNV-RP-F110. Three prediction models for uplift resistance and load-displacement curve are included: A lower and an upper bound as well as the prediction model for dense sand and a roughness of 0.97. All curves are based on (Schaminee, Zorn and Schotman, 1990), which is known to underpredict the pullout resistance. Other prediction formulas are presented and compared at the bottom of this subsection. The pullout resistance is based on the following parameters:

$$\begin{aligned} r_0 &= 0.02 \text{ m} \\ L &= 0.7 \text{ m} \\ \gamma' &= 16.2 \text{ kPa} \\ \phi &= 40^\circ* \end{aligned}$$

*Based on tests by Latini and Zania, (2016)

Which gives the following measured and theoretical uplift load-displacement response:

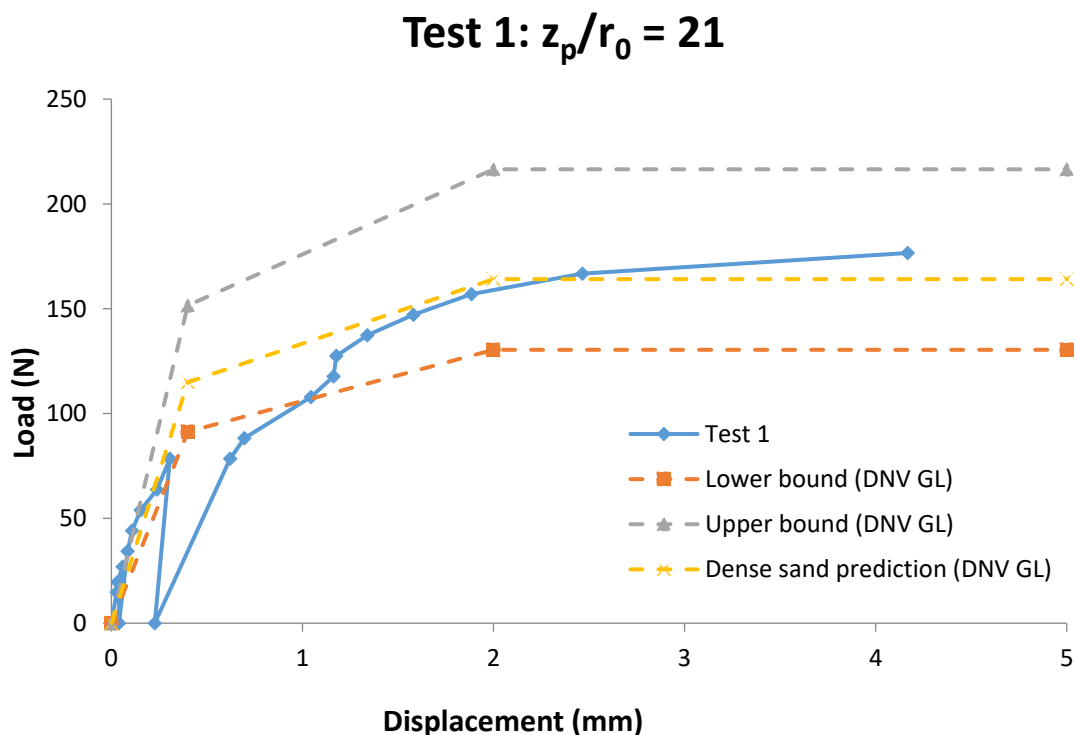


Figure 39a: Load-displacements curves for test 1, based on the maximum measured displacement in the sand at pipe level.

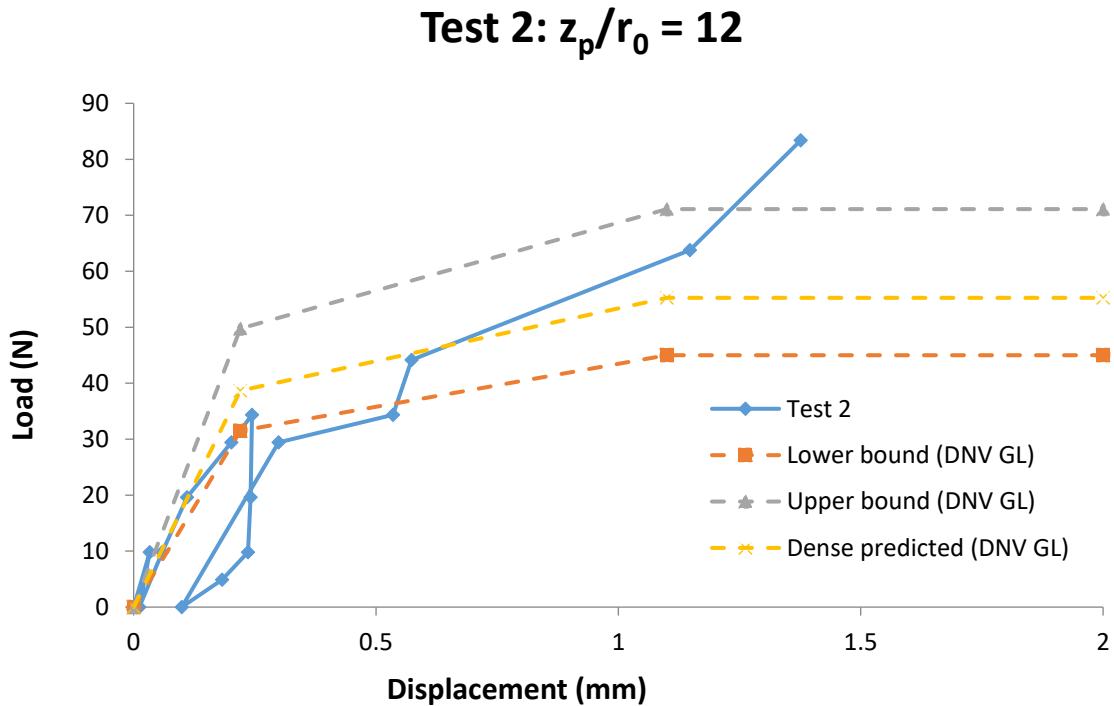


Figure 39b: Load-displacement curves for test 2, based on the maximum measured displacement in the sand at pipe level. Pullout occurred at the final load step shown here, at 83.4 N

Some general observations can be made from the two plots for test 1 and test 2 (figure 39a and 39b). The first thing to note is that the pipeline does not follow the original displacement path upon unloading and reloading. The measured displacement clearly shows a hysteric reaction to cyclic loading. Soil-pipe stiffness is several times higher on reloading, which is in agreement with literature, and the deformation of the pipeline does not return to zero when the pipe is completely unloaded. Interestingly, the incline of the load-displacement curve is approximately the same during the reload phases. In general, this is expected behaviour and consistent with the hysteric response of soil in many cyclic loading studies.

Both plots show that that the pipeline uplift response is predicted fairly well by the trilinear curve. Initial stiffness is higher than the upper bound, but this is very much expected as the trilinear curve assumes a linear-elastic response using a secant modulus. Due to the loading and reloading, the measured displacement falls outside of the upper and lower bound prediction formulas. However, the measured displacement would generally remain inside the upper and lower bound curves if the hysteric response is accounted for. The data also supports using $\beta=0.2$ as the location of first break in the tri-linear model. On the other hand, the maximum mobilization distance is underpredicted significantly. This does not invalidate the prediction formulas but simply means that the maximum displacement before pullout is higher for a flexible pipe.

Lastly, the ultimate load capacity was well within the upper and lower bound curves for test 1, but the upper bound was exceeded in test 2. However, the measured ultimate load

capacity is higher than the load experienced by the pipe for several reasons. This will be discussed further in chapter 6. It is also a possibility that the eccentricity of the point load caused the pipe to rotate. Rotation of the pipe was observed in test 1; here the pullout was arrested due to rotation of the pipe, therefore the pipe never was pulled out completely. Figure 40 explains this closer. The ultimate load capacity was defined at 176.6 N in this case as the soil clearly failed at the next load step, 186.4 N. It is plausible that the pullout capacity was reached between 63.8 N and 83.4 in test 2. This would explain the unexpected jump in displacement between these two loads. Pullout in test 2 occurred at 83.4 N when it was attempted to apply more load.

Table 17 presents the ultimate load capacity according to the prediction formulas included in chapter 2.5 (table 1). As previously stated, predicted ultimate load capacity varies significantly. None of these prediction formulas are close to the measured load in test 1 and test 2. Pullout capacity is generally overpredicted for test 1 with the latter three formulas containing ϕ'_{\max} . Since this depends on the identity by Bolton (1964), which function grows rapidly and validity is questionable at low confining pressure, a good prediction value is difficult to obtain. Based on the results of the test, using the prediction formula by Schaminee, Zorn and Schotman, (1990) for passive earth pressure has the best performance, at least for small scale pipes.

Table 17: Predicted and measured pullout capacity for the halfpipe in test 1 and test 2.

N (-)	1	
D (m)	0.02	
γ' (kPa)	16	
ϕ_{\max} (°)	53/54	(Bolton, 1986)
ϕ_{crit} (°)	32	Latini and Zania, (2016)
ψ (°)	15	Latini and Zania, (2016)
K	0.43	

*Based on RD=82% and σ_3 at depths of 200 mm and 100 mm, respectively.

Test	H (mm)	Measured values (N)	Ultimate load capacity F_{ult} (N)			
			Scaminée et al. (1990)	Ng, Springman (1994)	Vermeer, Sutjiadi (1985)	White et al. (2001)
1	200	176.6	112.0	315.3	267.4	200.2
2	110	83.4	33.6	89.1	75.6	36

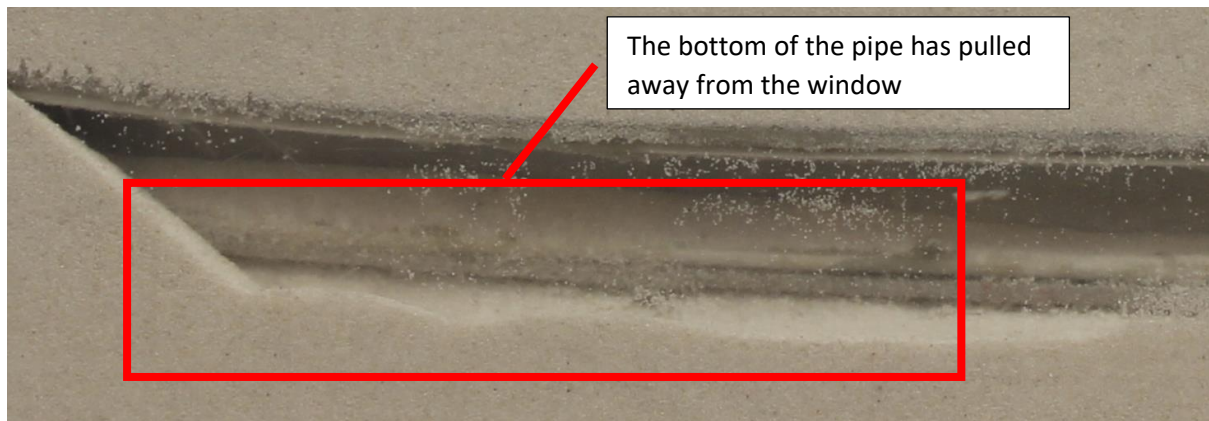


Figure 40: Rotation of the pipe arrested the pullout of the pipe during test 1. The load here is 196.2 N, which is two load steps after obvious failure was observed.

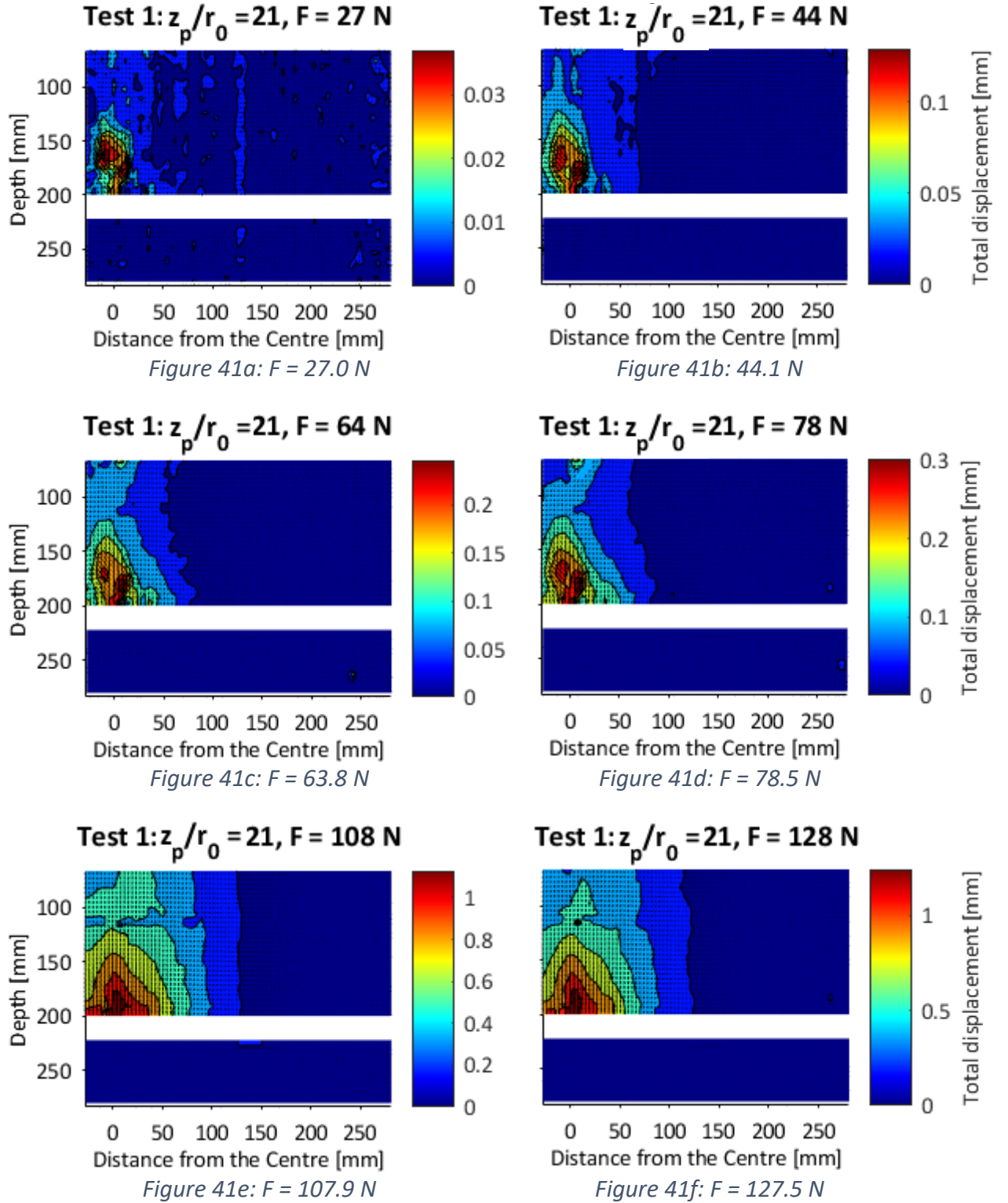
5.1.2 Displacement field of the surrounding soil

Total displacement field of the soil with increasing load is shown here. Contour plots have been used to show the magnitude and direction of the total displacement. Appendix E include the full size version of these images as well as vector plots alone. Each of the figures 41a-g and 42a-f shows the total displacement relative to before the pipe was loaded. The load in the figures refers to the first time it was loaded to this point (and the highest the soil has experienced thus far). This is clearly marked in the figure text where relevant. All vectors are normalized with the maximum displacement, which approximate values can either be extracted from the load-displacement curves or the colourbar, meaning that the scale changes between figures. Likewise, the contour plot scaling is not constant. The chosen loads represent different load stages all the way to near the point failure, and figures are organized so that the maximum total displacement is fairly comparable between figure 41a and figure 41a, figure 41b and figure 41b, etc. Note that part of the pipe is hidden behind the wall, but the total displacement plots all indicate that the displacement is zero here. Pipe and soil properties were also intentionally chosen to achieve zero displacement at the ends.

Soil displacements – $z_p/r_0 = 21$

Figure 41a-f presents the total displacement field at 27.0 N, 44.1N, 63.8N, 78.5N, 107.9 N, 127.5N. Bigger images of the same contour plots are available in appendix E.1. One additional load step, $F = 157.0\text{N}$, is also available in appendix E.1.

Figure 41a-f: Contour plot of total displacement at different loads. The pipeline is masked out and appears as a white bar in the figures. Note that the scale of the colorbar varies from figure to figure. The y-axis is the same for every picture and y=0 is at surface level.



The following observations can be made from the above figures:

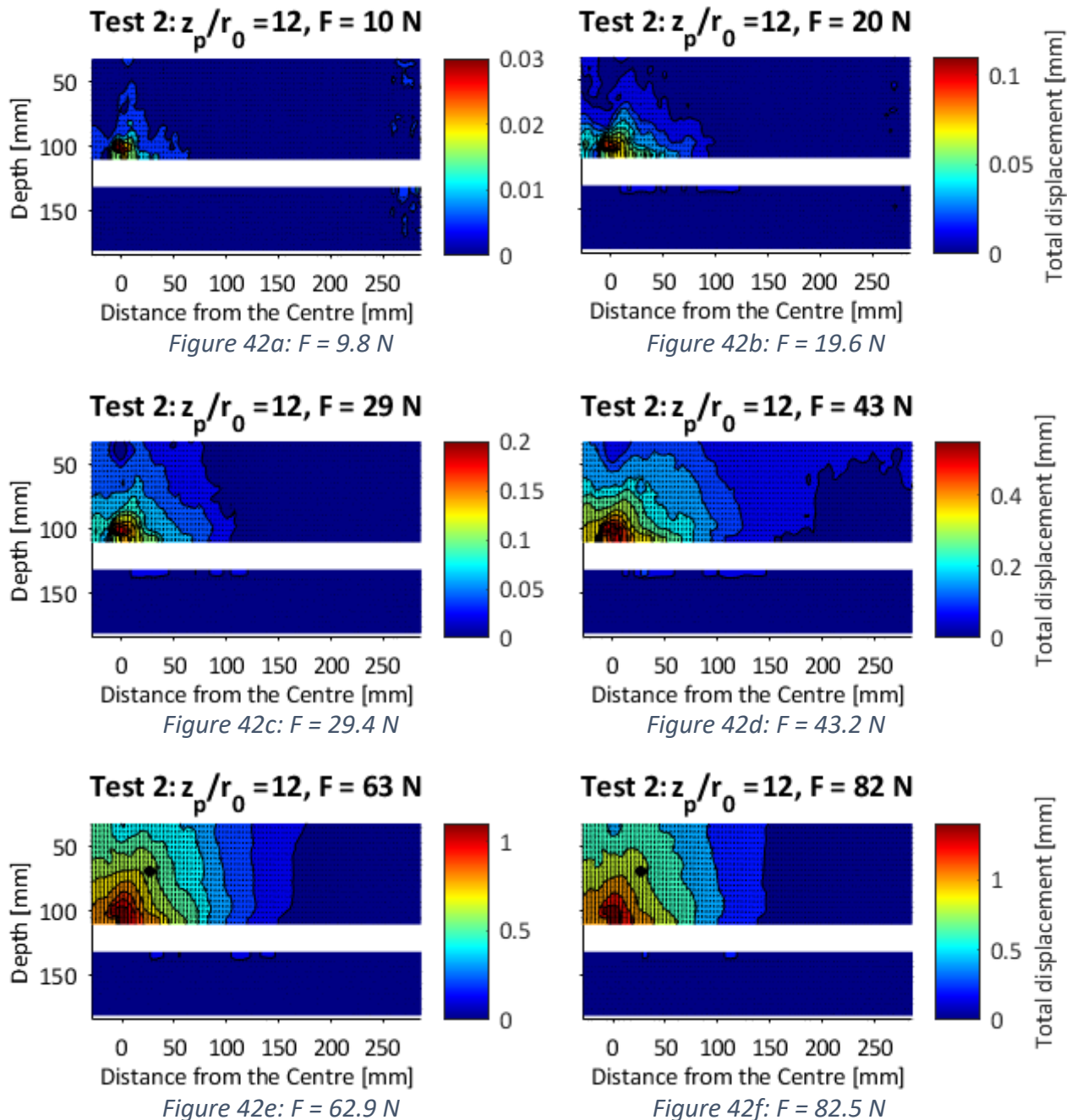
- a) At a load of 25 N, total displacements are generally concentrated to the immediate area around the point load. The most striking observation is that maximum soil displacement occurs not directly over the pipe but almost two pipe diameters above. This can at partly be explained by the larger horizontal displacement in this area. It is a possibility that the wire or the wire attachment have contributed to the maximum displacement. Another likely explanation is the stress and displacements are distribute non-uniformly due variety in relative density. The displacements are small beyond a pipe diameter from the centre line and near zero beyond the 60 mm mark. Note that the patchy appearance of the contour plot is due to the lower end of the scale being around the accuracy of the PIV.
- b) At $F = 44$ N, the total displacements are distributed similarly to the ones measured at 25 N; the magnitude has increased drastically but otherwise the contour plot remains largely the same. The horizontal component of the displacement vectors in the middle remain significant. Displacements are slowly moving out to the sides but remain negligible at the 60 mm mark. The chart shows that little to no soil movement occurs beneath the pipe.
- c) At $F = 64$ N, once again the magnitude has increased drastically. Note that an unload-reload cycle has occurred between this and the previous figure. The soil is clearly starting to form a chimney-like displacement mechanism. The pipe is more or less restrained except the central 60 mm on each side of the point load.
- d) At $F = 78$ N, the chimney-like displacement mechanism develops further. Some strain is creeping in from the top. Maximum displacement is now observed directly above the pipe.
- e) At $F = 108$ N, the displacements are distributed in more or less continuous zones. The chimney has developed fully and the displacements zone is finally getting wider. Even now, the majority of the pipe is almost completely restrained. The displacement has increased drastically around the centre line, indicating that the combined soil and pipe resistance is low under the chimney. The vertical displacements dominate the horizontal displacements.
- f) At $F = 128$ N, the displacements are distributed almost identically to $F = 108$ N but higher in magnitude. The soil is close to failure around the middle of the pipe. It is clear that the pipe is approaching pull-out around the centre line first.
- g) At $F = 157$ N, part of the pipeline is now in pullout and the soil is near failure in a large zone around the centre. Not that this is one load step before pullout. The figure shows that pullout occurs in the middle first. Once width of the failure zone is

wide enough (or length of the pipe exceeding the maximum mobilization distance), the total soil resistance is rapidly overcome and pullout occurs. It can be concluded that pullout of a flexible pipe is governed by the soil resistance in the chimney-like zone in the middle.

Soil displacements – $z_p/r_0 = 12$

Figure 42 presents the total displacement field at 9.8 N, 19.6 N, 29.4 N, 43.2 N, 62.9 N and 82.5 N. Bigger images of the same contour plots are available in Appendix E.1

Figure 42a-f: Contour plot of total displacement at different loads during test 2. The pipeline is masked out and appears as a white bar in the figures. Note that the scale of the colorbar varies. The y-axis is the same for every picture and $y=0$ is at surface level.



The following observations can be made from the above figures:

- a) At a load of 10 N, any displacement is generally centred to the immediate area around the point load. Just like test 1, maximum soil displacement is observed some distance above the pipe. The location of the maximum displacement is not the same as the one observed in test 1 and it is unlikely that the pipe-wire attachment pulled on the soil at this location. In contrast to test 1, the horizontal displacements are practically non-existent here. In fact, the largest obtained horizontal displacements with the PIV was 0.0096 mm which is smaller than the accuracy of around 0.01 mm.
- b) At $F = 21$ N, the displacement increase in width and height. Maximum displacement is still localized some distance above the pipe. Most of the displacement occurs at or around pipe level, however. Test 1 showed a much taller displacement zone at similar total displacement magnitudes. Some clutter can be observed below the pipe, but this is likely due to the edge of the pipe being slightly inside the interrogation area.
- c) At $F = 29$ N, the width of the displacement zone is still increasing. Displacements are observed until around 100 mm – five pipe diameters – from the pipe. This is in contrast to test 1, where displacements were not observed beyond 60 mm – three pipe diameters – from the centre line until much higher displacements were reached. A chimney-like displacement mechanism is starting to develop
- d) At $F = 44$ N, the width of the displacement zone is still increasing. Some further development in the chimney can be observed, but there is some lag in the middle and near the surface. Maximum displacement is still observed some distance from the pipe but the displacement is increasing more at pipe level. Displacements are observed as far away as 150 mm.
- e) At $F = 64$ N, a more obvious chimney-like pattern can be observed. The width of the displacement zone remains stable. Magnitudes have increased drastically with total displacements more than doubling in most areas. Maximum displacement now occurs at pipe level, possibly with a small failure zone at the very centre.
- f) At $F = 128$ N, the displacements are distributed almost identically to $F = 108$ N but higher in magnitude. The soil is close to failure around the middle of the pipe. It is clear that the pipe is approaching pull-out around the centre line first. Maximum mobilization distance has been exceeded for approximately 100 mm of the pipe, which is now in pullout.

5.1.3 Engineering shear strain in overlying soil

Total shear strain in the overlying soil is shown here. The meshes used for the GeoPIV analysis is those shown in section 5.1.2, however the strains below the pipe have been excluded as the strain here is zero for all practical purposes. All strains shown here represents the engineering shear strain, which is calculated by the formula

$$\gamma = \sqrt{(\epsilon_{xx} - \epsilon_{zz})^2 + (2\epsilon_{xz})^2} \quad (131)$$

Where plain-strain conditions are assumed. Engineering strain and strains are used interchangeably from now on.

Strains are obtained with the GeoPIV using the built-in strain subroutine. The algorithm uses triangular elements and the displacements as input to determine the rotation and compression of the elements. The strain contour plots show all strains exceeding 1% as the same colour for illustration purposes. Very large but concentrated strains were observed at high loads. The strain data is sensitive to general scatter and errors in the displacement vectors. For instance, some erroneous displacements vectors on the far right side of the pipe give large strains. Only large and continuous strains are considered for this analysis, and the clutter on the right side is ignored. Symmetric observations are also emphasized.

Table 18 summarizes the maximum strain not limited to 1% at each load step. It can be seen from the table that strains are generally much higher in tests 1 than test 2. This is despite the much higher displacement in test 2 at the same load. This shows that the soil flows more unconstrained with lower coverage depth since the elements deform less. On the other, the soil is compressed more in test 2 due to the higher overburden pressure. Comparing figure 43 and figure 44 also reveals that the maximum shear strain is higher in test 1 but the area with shear strains exceeding 1% is much bigger in test 2. It can be concluded that the strains are more concentrated with higher coverage depth and more evenly distributed with lower coverage depth.

Table 18: Maximum shear strain observed in test 1 and test 2.

Test 1		Test 2	
Load (N)	Maximum shear strain (%)	Load (N)	Maximum shear strain (%)
25	0.91	10	0.21
44	2.27	20	0.33
64	2.99	29	0.73
78	3.34	44	1.39
108	3.38	64	1.98
128	4.45	78	2.97

Engineering strains – $z_p/r_0 = 21$

Figure 43a-f presents the engineering strain field above the pipe at 27.0 N, 44.1N, 63.8N, 107.9 N, 127.5N. Bigger images of the same contour plots are available appendix E.2 Two additional load steps, $F = 78.5\text{N}$ and $F = 157.0\text{N}$, are available in Appendix E.2.

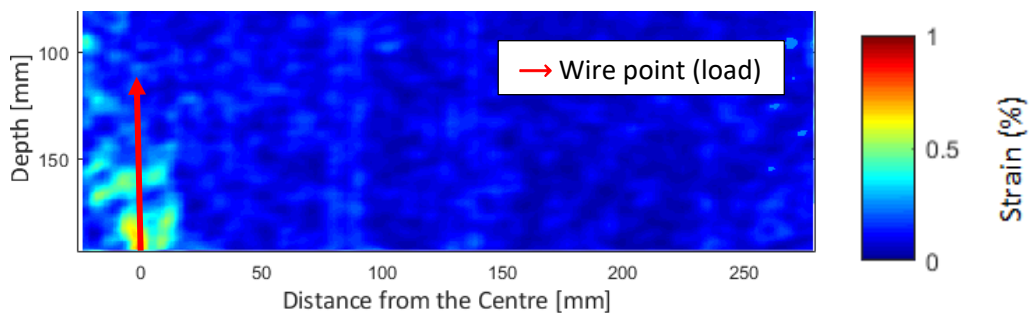


Figure 43a: Contour plot of engineering shear strain at 27.0 N

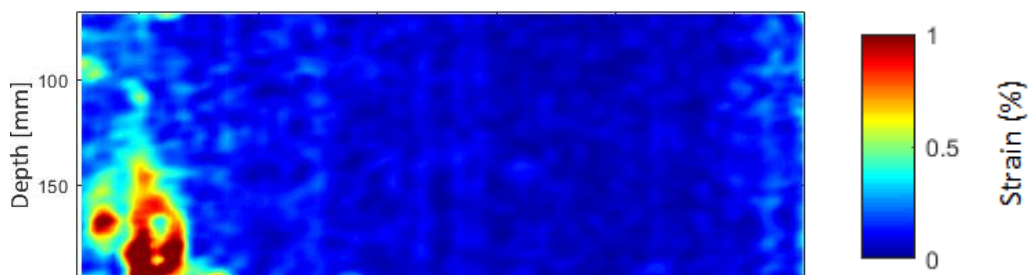


Figure 43b: Contour plot of engineering shear strain at 44.1 N

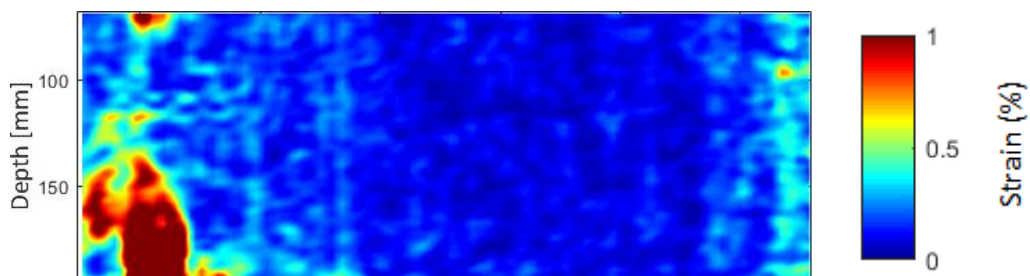


Figure 43c: Contour plot of engineering shear strain at 63.8 N

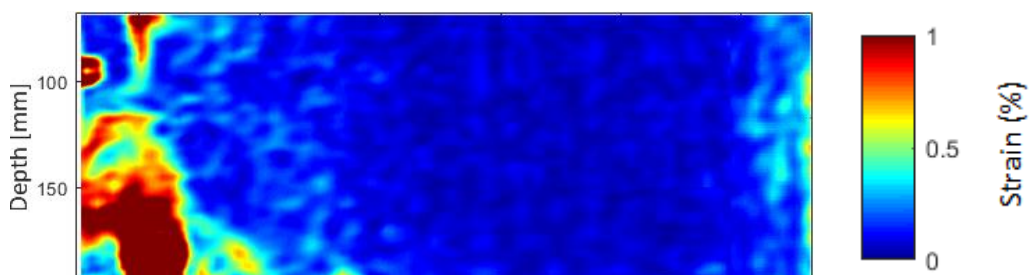


Figure 43e: Contour plot of engineering shear strain at 107.9 N

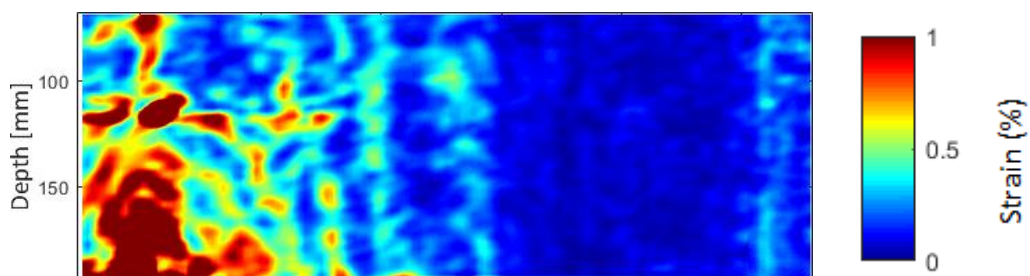


Figure 43f: Contour plot of engineering shear strain at 127.5 N

Based on figure 43a-f, the following observations on shear strains during test 1 can be made:

- a) At a load of 25 N, shear strains are low except for a very concentrated area immediately over the point load. Soil stiffness degradation is limited and an elastic response is likely a fair assumption. Maximum shear strain is observed at pipe level, which is expected due to the large compressive forces here.
- b) At a load of 44 N, two large shear bands can be observed above the centre of the pipe. It is already clear that soil stiffness degradation is significant. An additional, small shear band appears on the left side. The beginning of the leftmost shear zone can be observed as a small pocket at lower loads and is likely due to discontinuous relative density after the sand preparation.
- c) + d) A broad, vertical shear band above the centre of the pipe at $F = 64$ to 78 N. The shear band does not extend much further between the two loads. A small vertical shear band can be seen creeping in from the surface of the soil
- e) + f) Starting from loads of 108 N and larger, the shear strain plots are cluttered and it is difficult to reliably determine the shear mechanism. There are indications that a wide, chimney-like shear zone is forming. The soil near the surface is generally experiencing low strains except for a narrow shear band at the centre line.
- g) A clear chimney-like mechanism can be observed at $F = 157$ N. Large strains appear along the pipe and almost half of the soil covering the pipe is starting to give in. Reliable displacement data could not be obtained closer to failure than this, but it is clear that a large zone is giving in and excessive soil strains are proliferating to the side along the pipe.

Engineering strains – $z_p/r_0 = 12$

Figure 44a-f presents the engineering strain field above the pipe 9.8 N, 19.6 N, 29.4 N, 43.2 N, 62.9 N and 82.5 N. Bigger images of the same contour plots are available appendix E.2

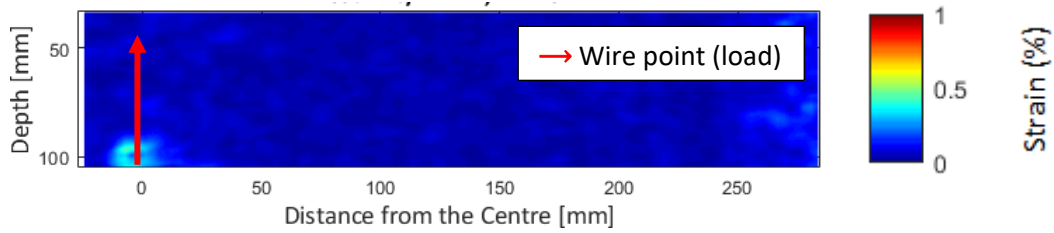


Figure 44a: Contour plot of engineering shear strain at 9.8 N
(First time loaded to 9.8 N)

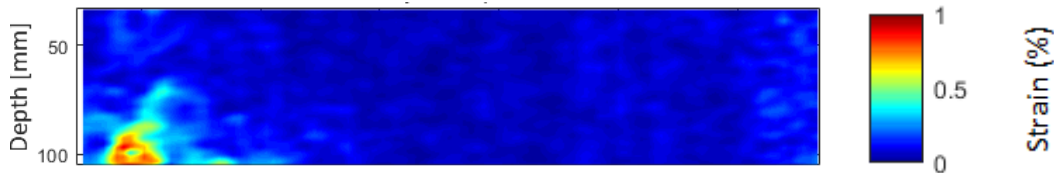


Figure 44b: Contour plot of engineering shear strain at 19.6 N
(First time loaded to 19.6 N)

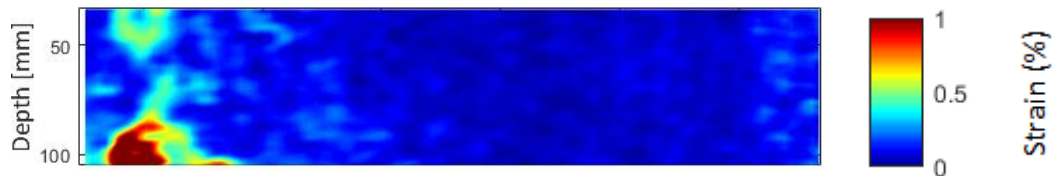


Figure 44c: Contour plot of engineering shear strain at 29.4 N
(First time loaded to 29.4 N)

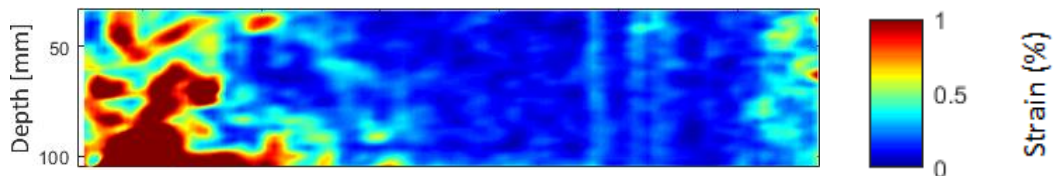


Figure 44d: Contour plot of engineering shear strain at 43.2 N

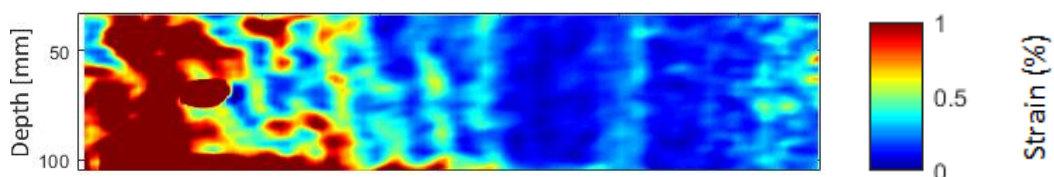


Figure 44e: Contour plot of engineering shear strain at 62.9 N

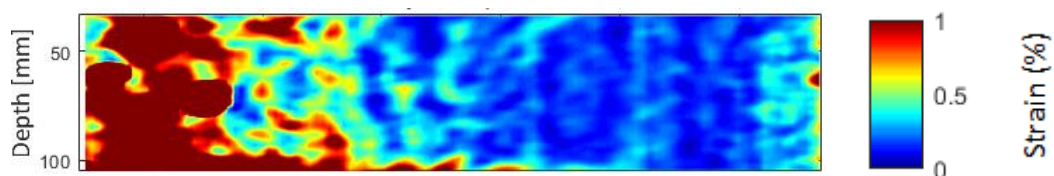


Figure 44f: Contour plot of engineering shear strain at 82.5 N

Based on figure 44a-f, the following observations on shear strains during test 1 can be made:

- a) At a load of 10 N, small strains are observed throughout the soil for the soil surrounding the point load. The maximum strain is just exceeding the 0.1% threshold in this shear zone, but the area is very small.
- b) At $F = 21$ N, the shear zone develops further. The biggest strains start to approach 1%. Significant strains can be observed in a triangular area around the centre. Soil stiffness degradation has occurred.
- c) At $F = 29$ N, a clear shear band has started to from pipe level all the way to the surface. Extensive shear strains are observed around the point load.
- d) At a load of 44 N, the shear band is extending and the chimney-like mechanism can be observed. A broad shear zone along the pipe has appeared. A nearly elastic response is not an accurate assumption at this point.
- e) + f) A broad, chimney-like zone has developed at $F = 64$. The shearing zone is very similar when the load is increased to $F = 78$ N. Displacement increased significantly between the two figures, indicating that the soil is giving in in the red zone. The soil is fairly disturbed along the pipe, and almost half the length of the pipe is covered in heavily degraded soil. This failure mechanism is similar to the one observed in the final stages of test 1.

5.1.4 Volumetric strain

Volumetric strains for a select few cases are shown here. Negative values indicate dilation and positive values indicate contraction. Similarly to the engineering strains analysis, results here are very sensitive to scatter and error in the displacement vectors. This section will therefore only consider large, continuous zones for analysing volumetric strains. Volumetric strain data was extremely cluttered at higher loads, hence only a couple of images at lower loads are shown here. The contour plot is limited to $\pm 1\%$ for illustration purposes, and volumetric strains smaller than -1% or larger than 1% are respectively shown as 1% and -1% in the plots.

The volumetric strain plots show two different behaviour for high and low coverage depths ($z_p/r_0 = 12$ and $z_p/r_0 = 21$, respectively). Compressive behaviour immediately around the point load is seen in both cases. However, the compression zone is limited to a small area at pipe level for the latter case. With low coverage depth, dilative soil dominates most of the overlying soil. Magnitudes of the compression and dilation zones were roughly equal in the GeoPIV analysis. Volumetric strains are predominantly positive during early loading with high coverage depth, forming a compression shear band. Two vertically oriented, dilative

shear bands can be observed next to the original compression shear band at $F = 78 \text{ N}$ in test 1. A more dilative behaviour is expected for lower overburden pressure.

Test 1: $z_p/r_0 = 21$, $F = 34.3 \text{ N}$

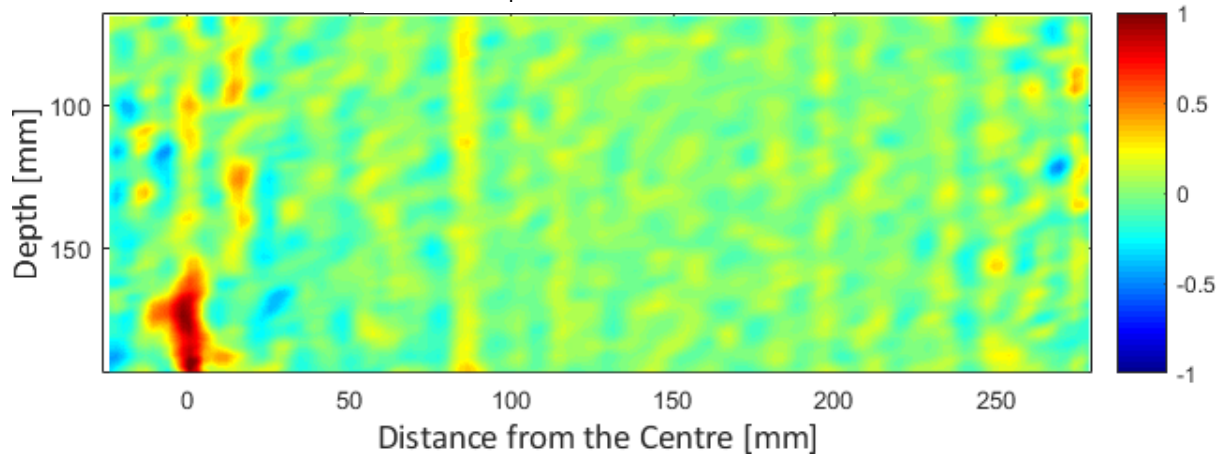


Figure 45a: Contour plot of volumetric strains in % at 34.3 N for test 1

Test 1: $z_p/r_0 = 21$, $F = 78.5 \text{ N}$

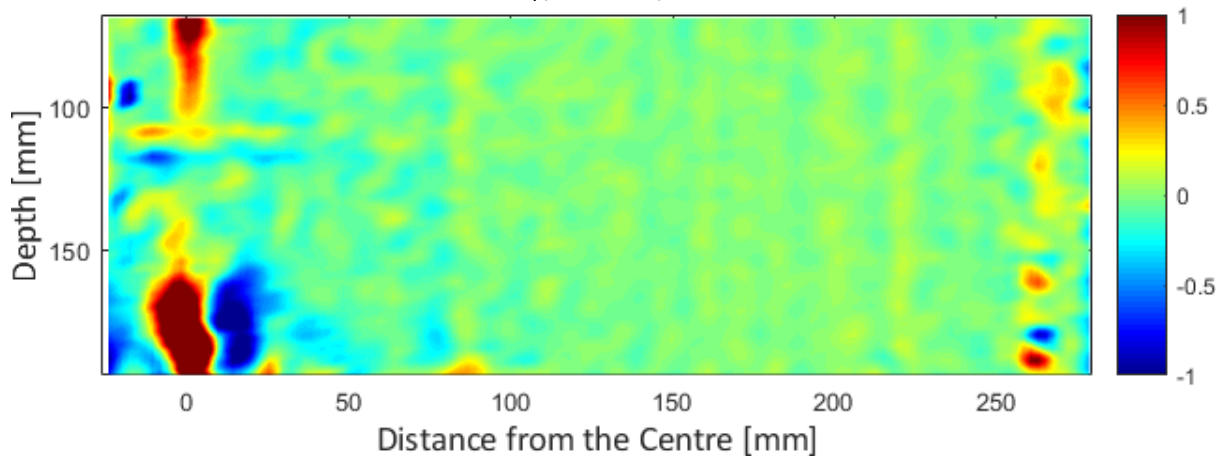


Figure 45b: Contour plot of volumetric strains in % at 78.5 N for test 1

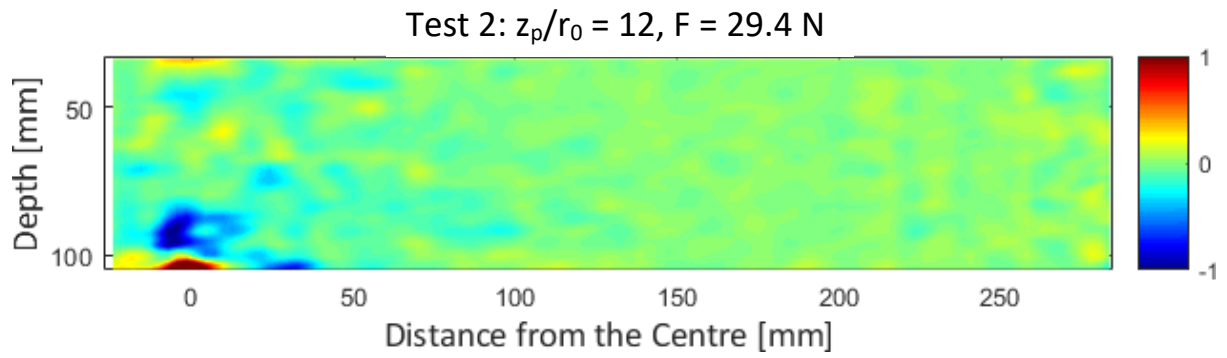


Figure 45c: Contour plot of volumetric strains in % at 29.4 N for test 2

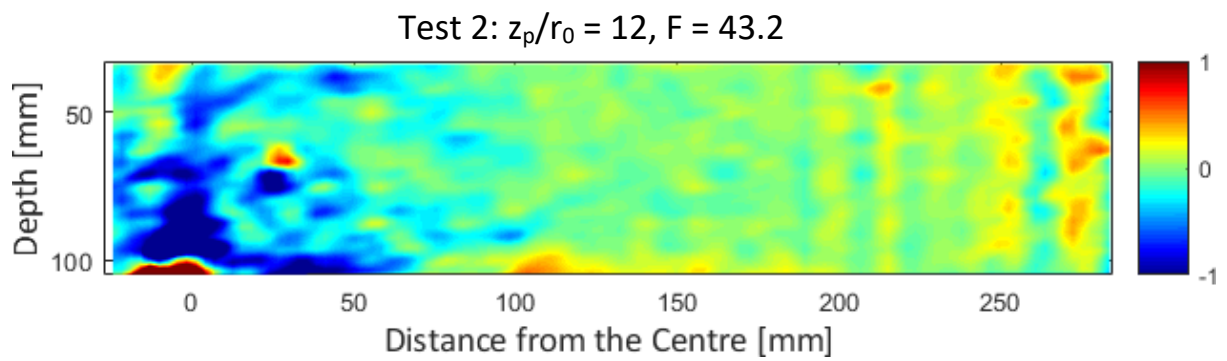


Figure 45d: Contour plot of volumetric strains in % at 43.2 N for test 2

5.1.5 Deflection shape of the pipeline

Vertical displacements at pipe level are presented here. The displacements are obtained with the meshes shown in figure 46 and figure 48. It is assumed that the vertical displacement of soil in contact with the pipe is identical to the deflection of the pipe. Section 5.1.9 explores this further by comparing the estimated moment from the PIV analyses and the fiber optics.

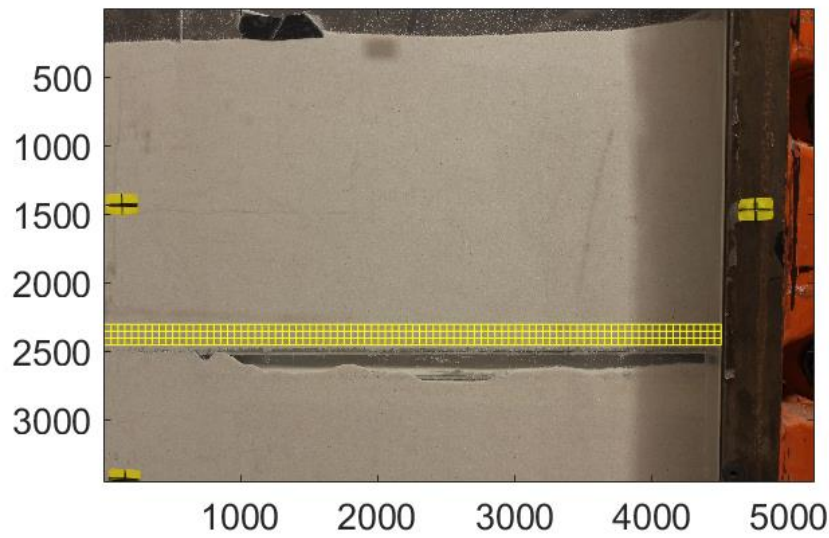


Figure 46: Mesh used to obtain the displacements at pipe level in test 1

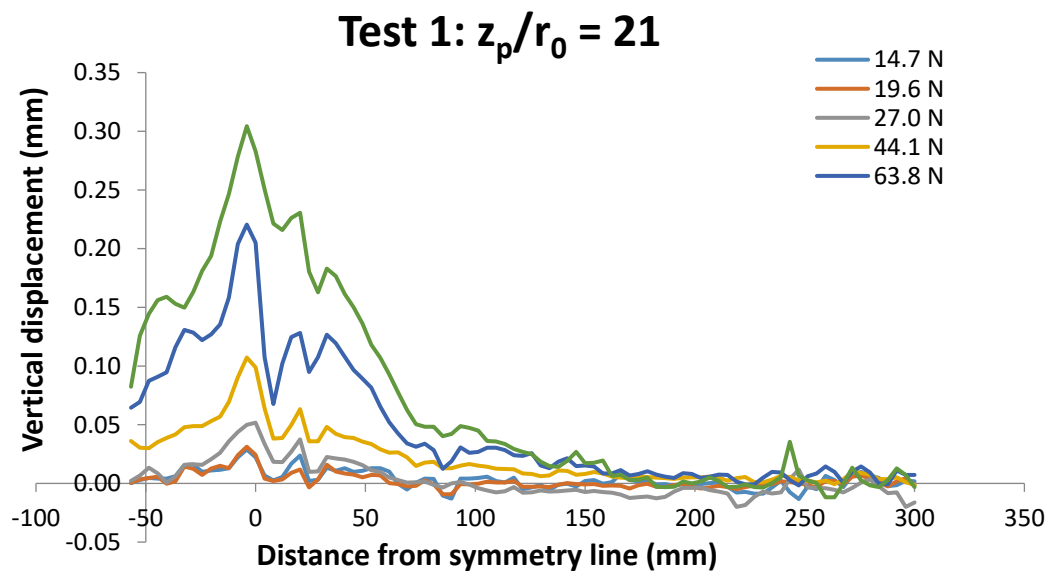


Figure 47: Displacement profile at pipe level, assumed to be one-to-one with the deflection profile of the pipe, in test 1

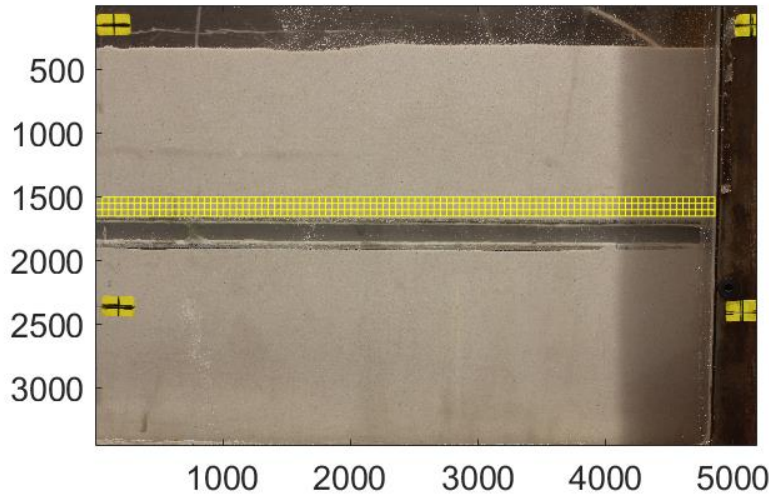


Figure 48: Mesh used to obtain the displacements at pipe level in test 1

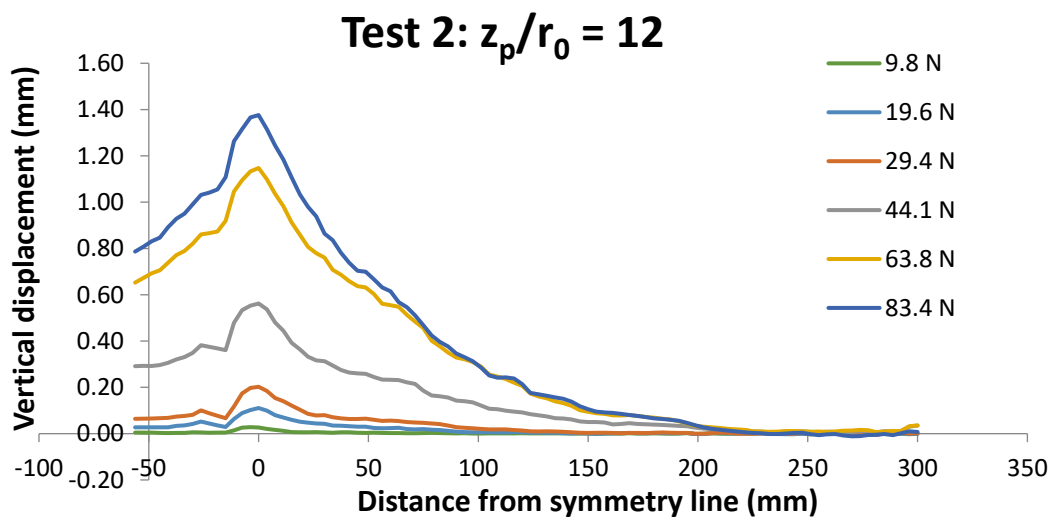


Figure 49: Displacement profile at pipe level, assumed to be one-to-one with the deflection profile of the pipe, in test 2

Both figure 47 and figure 49 clearly shows a consistent displacement profile over the course of each experiment. Hence, the irregular shape of the two profiles partly stems from some non-uniformity in the sand. Displacement data show significant scatter for test 1 and negligible scatter for test 2. Initial pipe deflection is observed primarily in the middle, near the point. Furthermore, the first load steps give a nearly identical deflection shape, only with larger magnitudes, indicating the pipeline response is elastic. A breakpoint can be seen where the displacements move further out on the x-axis and the shape of the curve changes. The breakpoint appears to occurs 44.1 N in test 1 and 29.4 N in test 2, which is fairly consistent with the trilinear curve after DNV GL. However, the exact breakpoint is

difficult to determine and the actual transition point could also lie between two load steps. Near failure, it can be observed that about 300 to 400 mm of the pipeline is in pullout.

MATLAB's built-in fit function was used with a Gaussian error function to obtain the best fit at different load steps. All function were centered to $x = 0$ for the inflection point value. Table 19 and table 20 presents the Gaussian best fit as well as goodness of fit (R^2) for the measured displacements at pipe level. The function that defines the pipeline deflection profile is the Gaussian error function:

$$f(x) = v_{max} * \exp\left(-\left(\frac{x}{2i}\right)^2\right) \quad (132)$$

Where v_{max} is the maximum displacement and i is the inflection point.

Data from both test 1 and test 2 shows that a Gaussian approximation can be used to describe the deflection profile of the pipeline itself for large loads and deformations. Several deflection profiles were fitted to the Gaussian error function with R^2 -values higher than 95% and up to 99%. Two examples are shown in Figure 50 and 51. It can be seen that the Gaussian fit is very good overall but misses the mark around the maximum vertical displacement; More specifically, the maximum displacement predicted by the Gaussian error function is always lower than the measured maximum displacements. The functions also indicate that the inflection point travels further out with higher load, although the effect is neither linear nor predictable in any other way. This is in line with observations from the displacement fields in section 5.1.2, particularly for test 1: The pullout zone is stable and nearly constant in width for several load steps, then the large displacements start to propagate towards the sides. A poor Gaussian fit was overserved for very small displacements, though this might be more due to the PIV accuracy and data scatter rather. The data here is inconclusive. This could indicate that data small-strain displacement data (and therefore elastic soil conditions) for is too inaccurate for the analyses.

Table 19: Gaussian Best Fit to the Pipeline Displacement in test 1

Load (N)	Maximum vertical disp., v_{max} (mm)	Offset from centre (mm)	Inflection point, i (mm)	R^2
14.7	0.013	1.31	25.51	0.60
27.0	0.025	-1.46	20.28	0.69
44.2	0.045	-2.41	32.12	0.82
63.8	0.117	-3.00	31.95	0.93
78.5	0.170	-2.22	31.81	0.96
107.9	0.905	-2.76	43.00	0.99

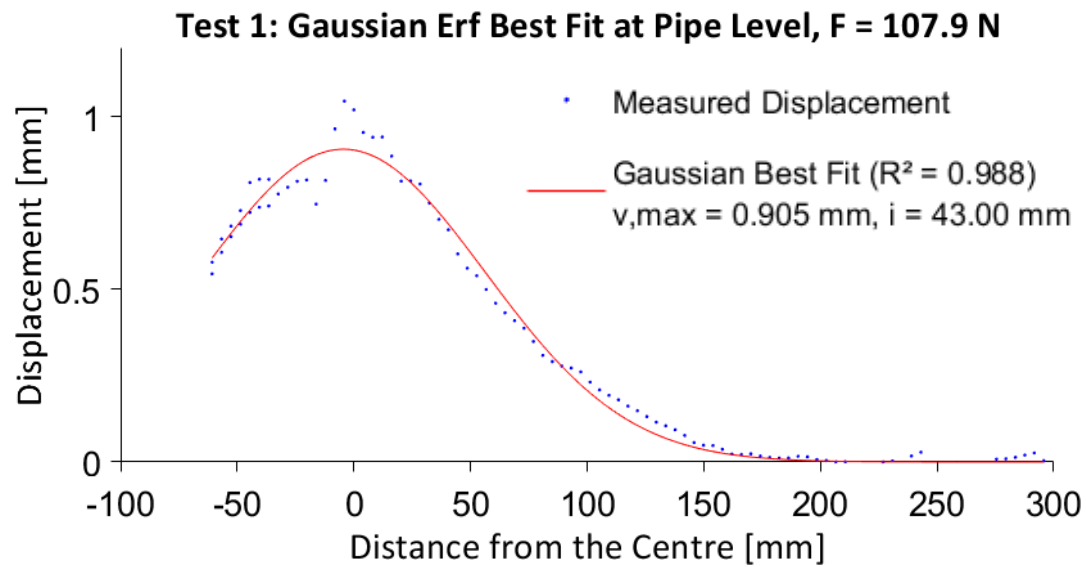


Figure 50: Typical Gaussian fitted to measured data in test 1

Table 20: Gaussian Best Fit to the Pipeline Displacement in test 2

Load (N)	Maximum vertical disp., v_{\max} (mm)	Offset from centre (mm)	Inflection point, i (mm)	R^2
9.8	0.026	-0.92	7.93	0.79
19.6	0.064	2.20	25.51	0.86
29.4	0.114	2.04	32.08	0.86
43.2	0.360	-2.85	48.17	0.94
62.9	0.816	-2.69	49.41	0.98
82.5	0.832	-2.83	51.91	0.97

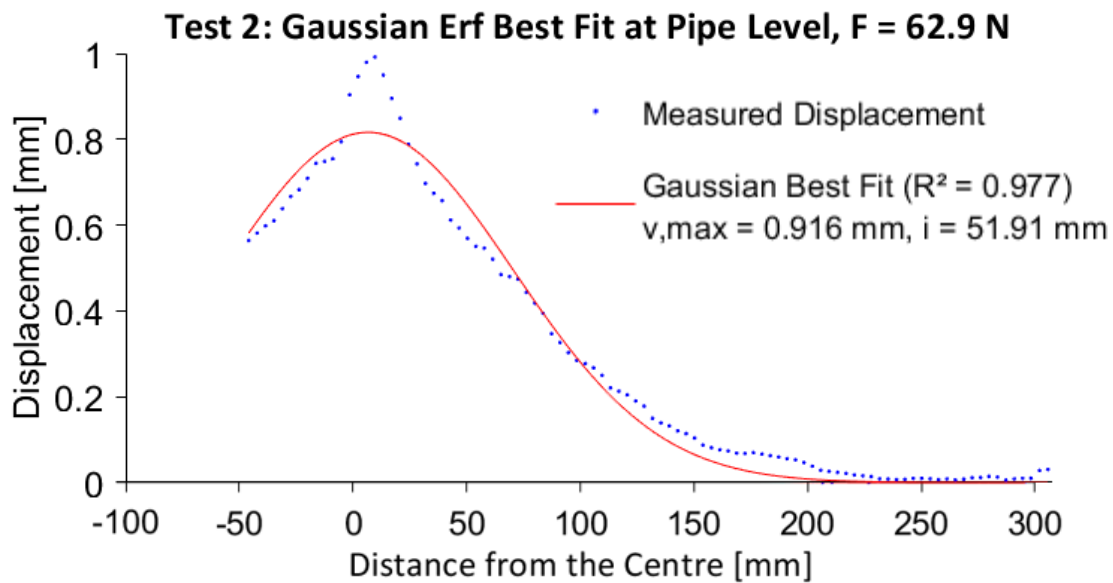


Figure 51: Typical Gaussian fitted to measured data in test 2

5.1.6 Ground displacement profile

This section fits investigates the fit of a Gaussian curve to the subsurface ground displacements induced by the pipeline. A Gaussian function is commonly used to describe the surface and subsurface settlement trough caused by tunnelling. Several have also fitted a Gaussian curve to the ground surface displacements over a pipe burst with R^2 values above 95 %. The soil displacements in the present study is therefore expected to be described by a Gaussian as well. In this case, the ground displacements are induced by the upwards movement of the pipe itself. Like earlier analyses in this thesis, the displacement profile of the soil directly above the pipeline is assumed to be nearly identical to the pipeline displacement.

The ground heave profile was obtained with GeoPIV, at pipe level and above, for several load steps. A typical subsurface soil heave profile for test 2 is presented in figure 52b. A similar analysis was conducted for test 1, but the displacement profiles throughout the soil were found to be far less predictable, though some of the same trends could be observed. Only test 2 is analysed here as this was the only test with a satisfactory goodness of fit at different depths (R^2 -values > 0.90). Vertical displacements were found to be greatly disturbed by the wire close to the surface. Due to this, the displacements at or close to surface level is not analysed here.

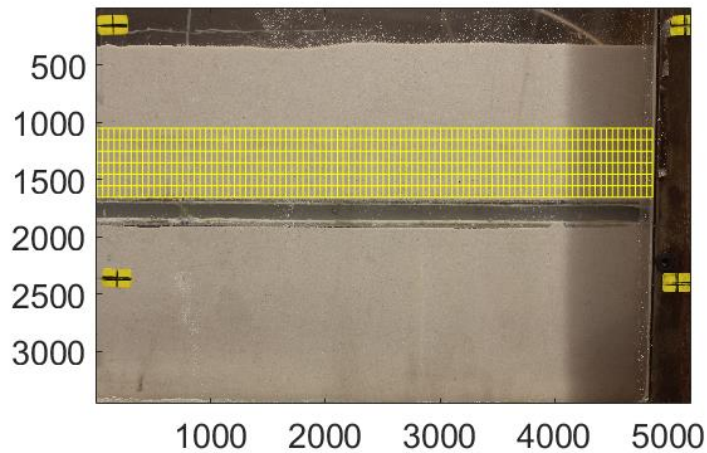


Figure 52a: Mesh used to get soil heave profile. Near-surface levels are excluded due to low accuracy.

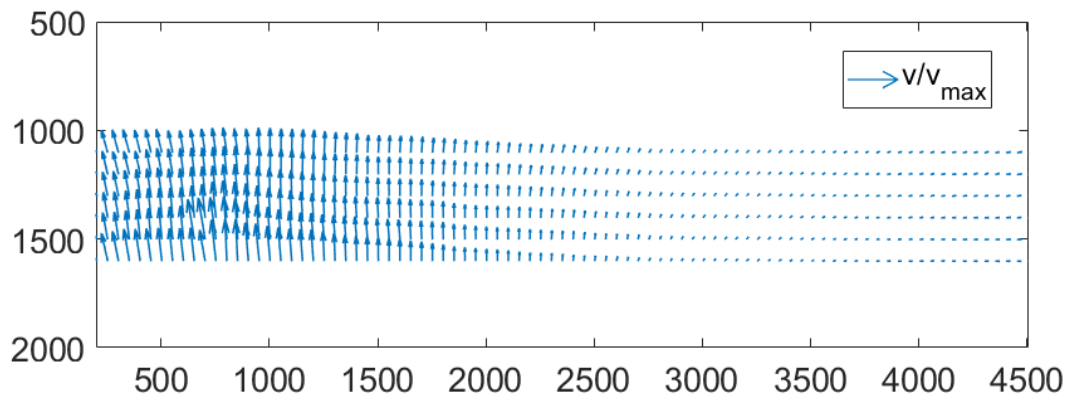


Figure 52b: Soil heave profile

Figure 52b shows the ground heave propagating through the soil with decreasing magnitudes. The data is fairly symmetric around the centre line. It is clear that the inflection point is shifting outwards with decreasing depth. This can be seen as the vertical displacements are significantly more concentrated around the centre for each level closer to the pipe. Figure 53 shows the inflection point at different levels. The plot reveals that the inflection point decreases almost linearly with depth. Furthermore, the average decline is the more or less identical for four different loads. The linearity increases with larger displacements. Note that this section does not show displacement profile for shallow depths. It is unclear from the PIV data whether the inflection point continues to increase linearly all the way to the surface.

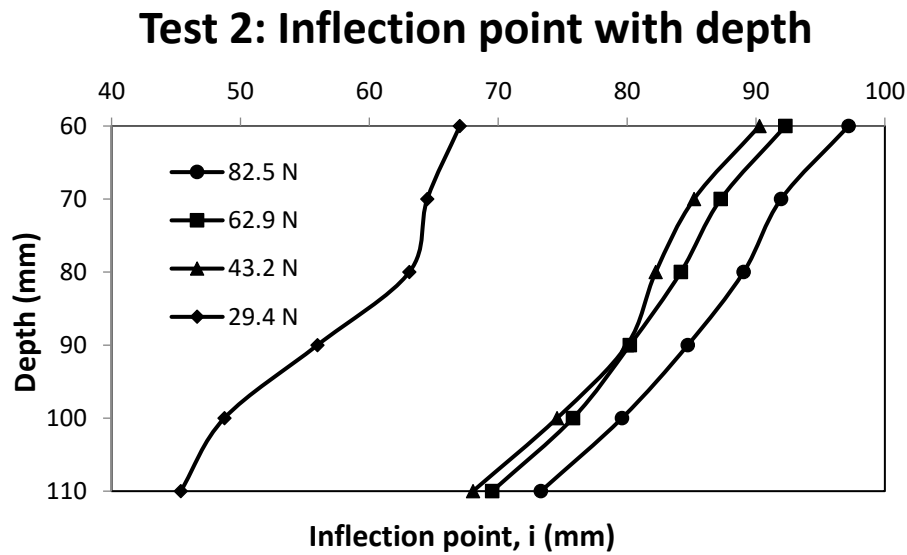


Figure 53: Inflection point of the Gaussian best fit with depth

Previous studies have reported that the subsurface displacements over a new tunnel also takes the shape of a Gaussian, with a nearly linear relationship between inflection point and depth. It is interesting to note that a linear relationship can also be observed for ground displacements transverse with a vertically bulging pipeline.

5.1.7 Fiber optics data

Moment and load based on the fibre optical monitoring is presented here. Moment has been derived with the longitudinal strain in the top and bottom fibre after the directions explained in chapter 3.11. Positive moment indicates the tension side of the pipe. The spatial resolution is 0.100231 mm and the distance between each sensor point 0.500003 cm. The data points and calibration are the same for test 1 and test 2. Loads are estimated by using the double derivative of the moment multiplied with the stiffness EI_{pipe} for the halfpipe. The double derivative was obtained using the second symmetric derivative and numerical derivation with a 10-point arm. A 10-point arm was found to eliminate observable scatter.

Figure 54a and figure 54b shows the moment for test 1 and test 2, respectively. The load steps represent the first time the pipe was loaded to this level; in other words the hysteresis is not shown in these figures. Maximum moment is observed around the point load, which is expected, though somewhat off centre in test 1. The curves are fairly symmetric, but the right hand moment ($x > 0$) is significantly lower than the left hand side. Since both moment charts show this tendency, it is likely that the imprecise installation of the fibre optics gives a systematic error.

The charts show that moments increase with each load step, both on the compression and the tension side. The increase in maximum moment is almost perfectly linear during early and med-stage loading. A linear response can be observed until the loads of 44.1 N and 34.3 N for test 1 and test 2, respectively. Moment increases faster per load after this point, likely due to strain-softening in the soil. The fibre optics data suggest that the pipeline response is linear after the break-point, although smaller load increments is necessary to confirm this. Interestingly, the inflection point of the moment curves moves outwards with increasing loads, which is shown in the resulting load charts. This indicates that more of the pipeline length is in pullout and the length of completely restrained pipe is going down.

-space left blank intentionally-

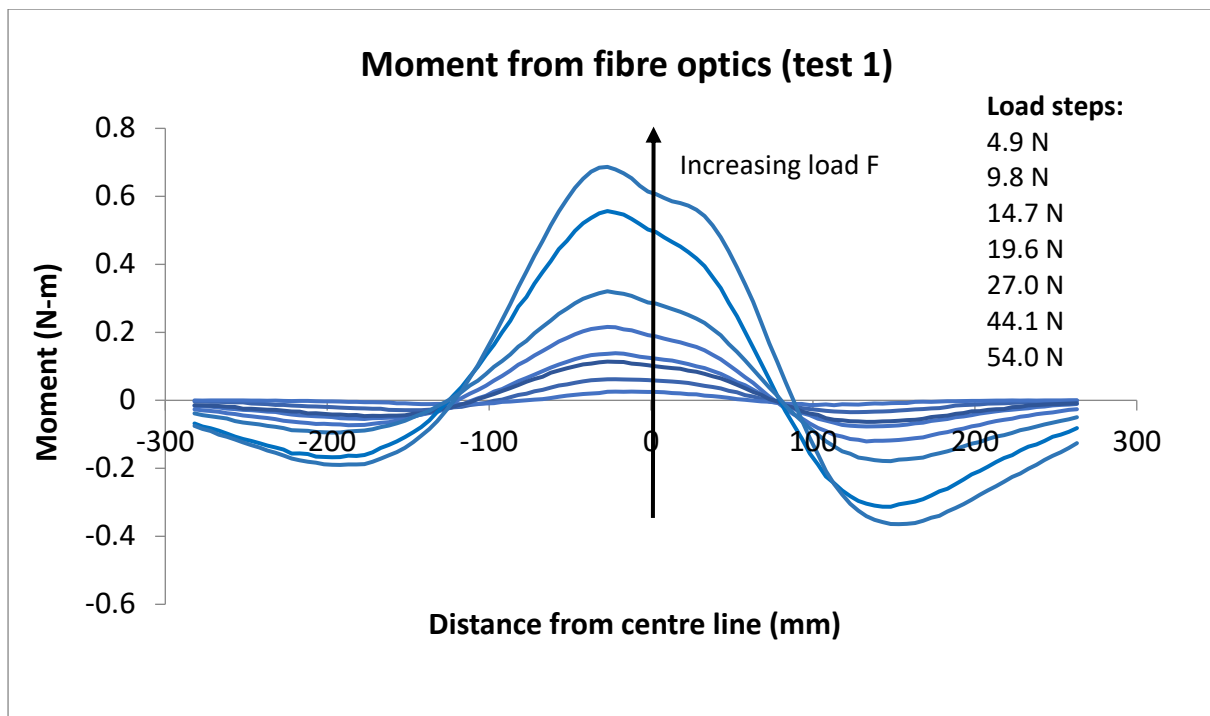


Figure 54a: Moment derived from fiber optics strains in test 1

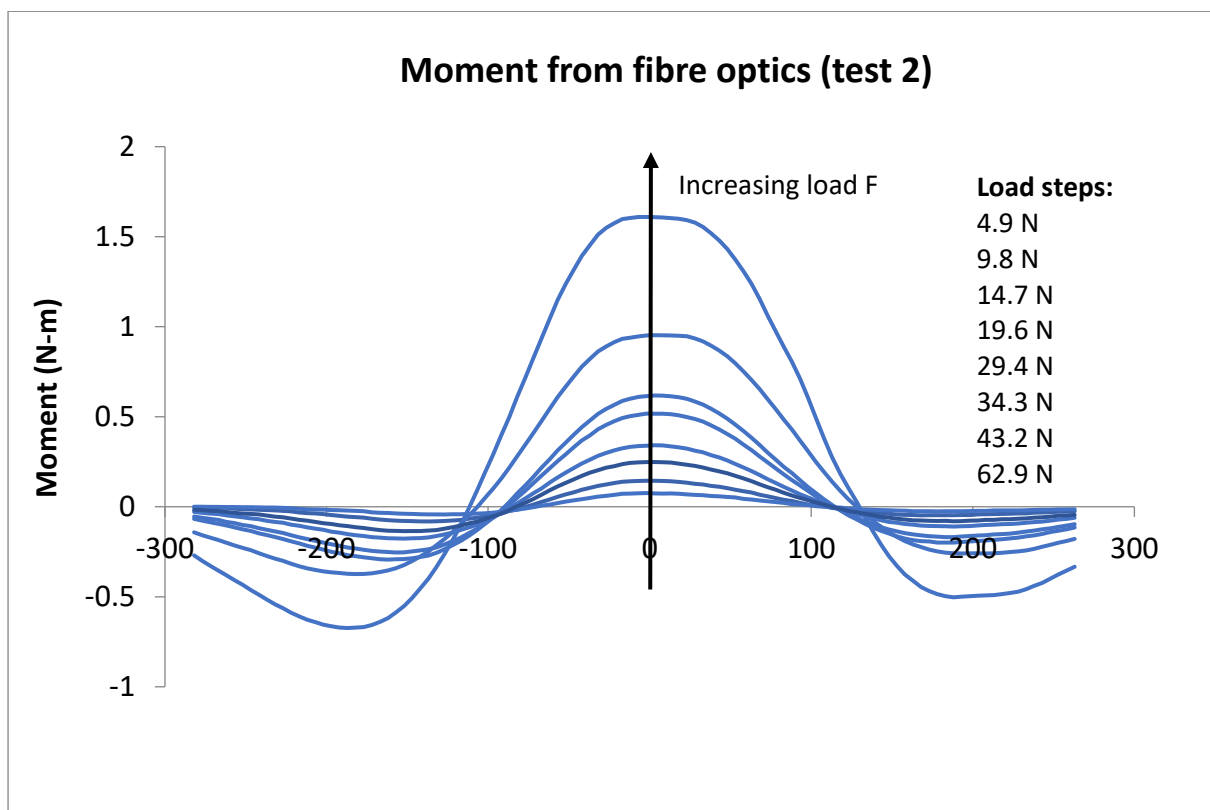


Figure 54b: Moment derived from fiber optics strains in test 2

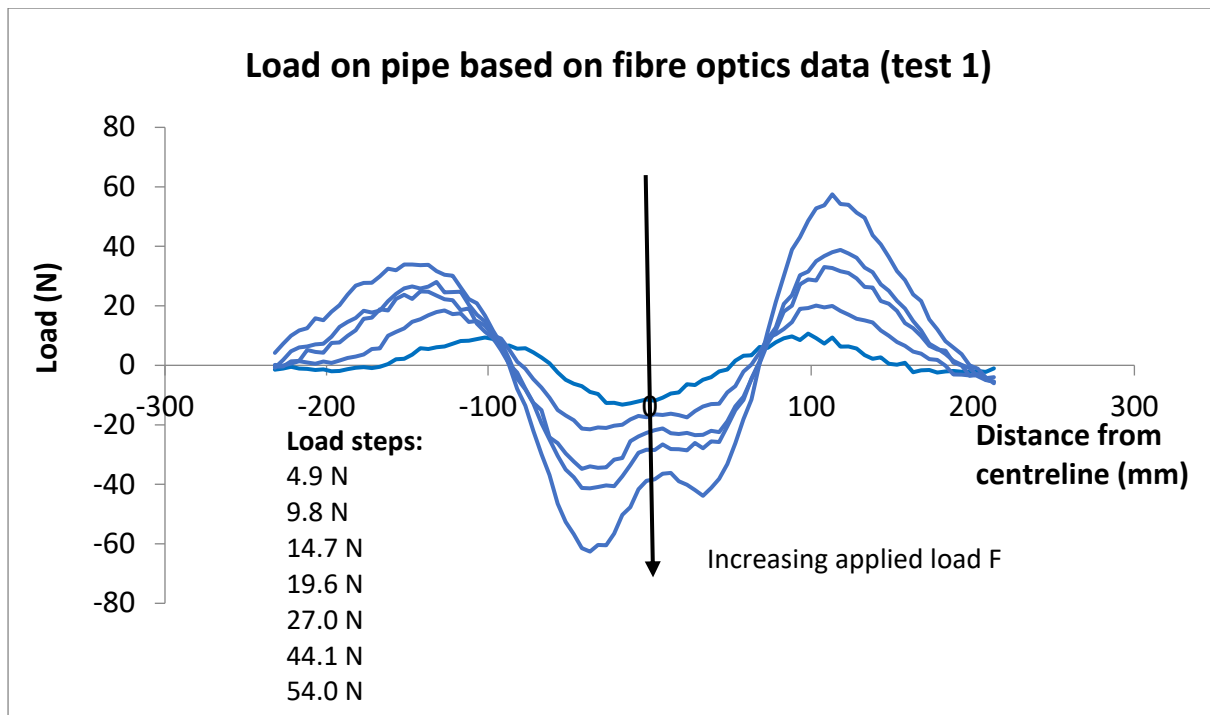


Figure 55a: Load on the pipe from the surrounding soil, derived from fiber optics strains in test 1

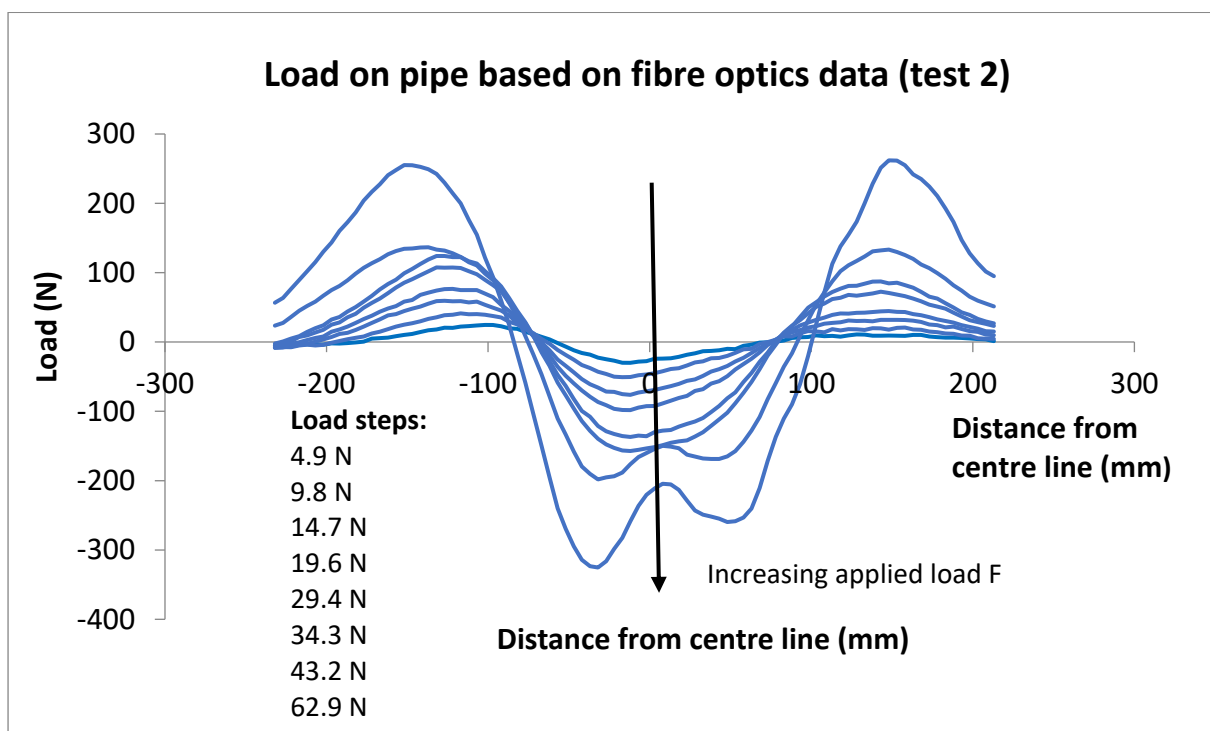


Figure 55b: Load on the pipe from the surrounding soil, derived from fiber optics strains in test 2

5.1.8 Load-displacement curves derived from the fibre optics moment and PIV displacements

This section estimates the load on the pipe *applied by the soil* based on the fibre optics data. Loads are derived from the double derivative of the moment. Due to the point load, the load from the soil cannot be calculated at the centre ($x = 0$). This effect was avoided by moving 2.5 pipe radii away from the centre. The load is obtained at four different points of the pipeline.

The soil load plotted against the displacement from PIV data gives valuable information about the pipeline-soil interaction. For example, the spring coefficient for a Winkler model can be obtained. The effective subgrade modulus in the Winkler model is equal to

$$K_{eff} = \frac{u_p(x, y)}{P(x, y)} \quad (134)$$

Figure 56a and figure 56b presents the load-displacement curves at 25 mm and 50 mm from the centre line on both the left side and the right side. Carefully note that the highest load in figure 56a is only halfway to failure, while the highest load in figure 56b is close to failure. Both charts also ignore the loading-unloading cycles. This is due to missing fibre optics data. Figure 56a exhibits some clutter in the first few load points, after which the curves are almost linear. There is a large spread between the four curves, however. More interesting is the results in figure 56b, which shows load-displacement curves all the way to near-failure. Soil-softening can clearly be observed in this case. The breakpoint in the load-displacement curve appears to be around 0.1 mm, a displacement equal to around 9-10% of the coverage height.

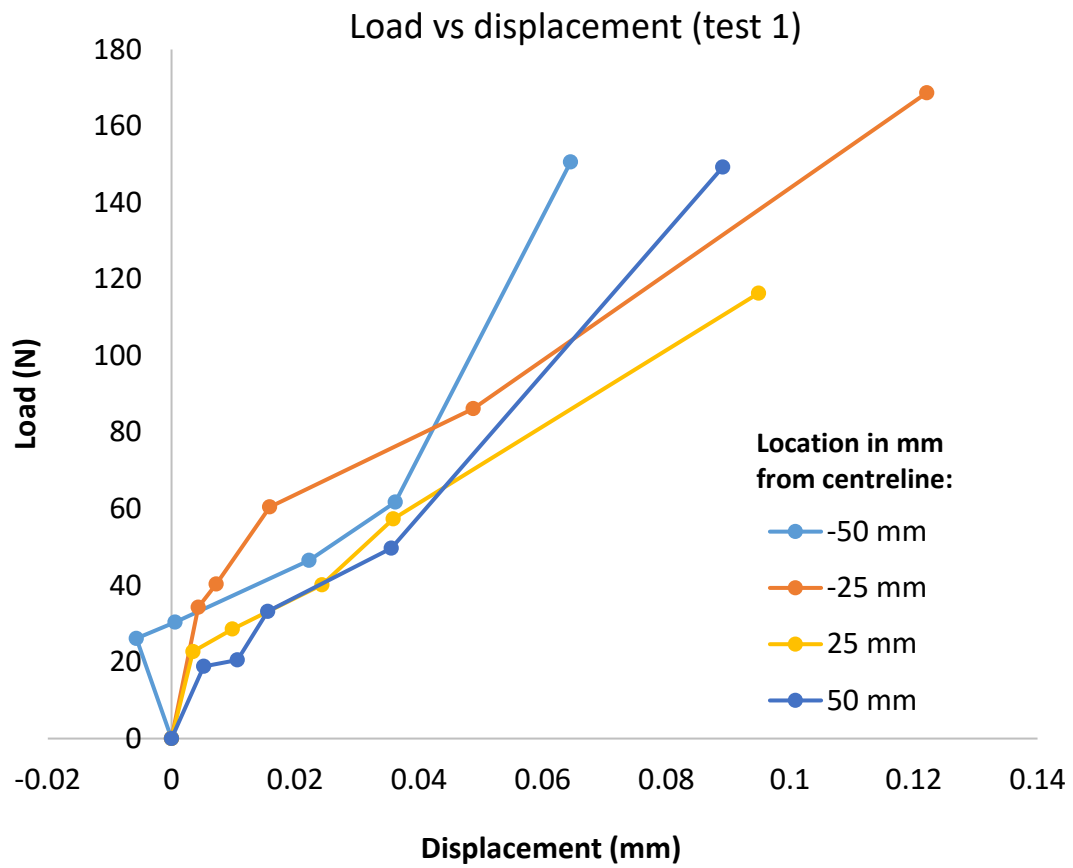


Figure 56: Soil load-displacement curves from test 1

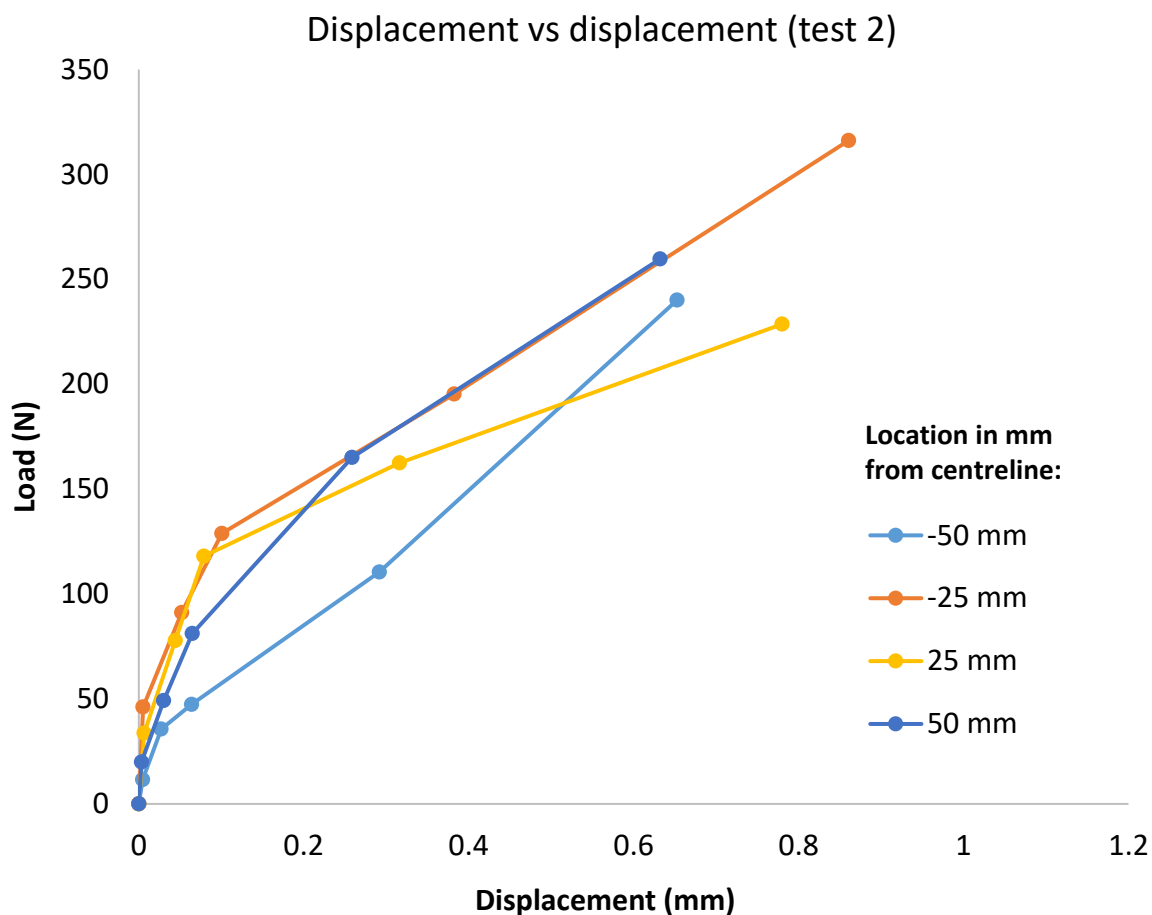


Figure 56b: Soil load-displacement curves from test 2

Table 21 and table 22 gives the estimated Winkler-model pipe-soil subgrade modulus at different loads and points for each test. The values in this table are secant moduli. The subgrade modulus can be compared to the spatial frequency-dependent stiffness in section 5.4. Once again, only the latter test includes data close to failure. This is clearly seen in the reduction of K_{eff} .

Table 21: Estimated effective subgrade modulus at different points of the pipe in test 1

Load (N)	Measurement point (mm); K_{eff} (kN/m)				Average K_{eff} (kN/m)
	-50 mm	-25 mm	25 mm	50 mm	
27.0	-	5579.3	2904.0	1928.1	3470.5
44.1	2092.8	3809.8	1650.7	2134.9	2422.1
63.8	1706.4	1766.5	1600.2	1399.1	1618.1
78.5	2334.0	1381.6	1225.8	1675.0	1654.1

Table 22: Estimated effective subgrade modulus at different points of the pipe in test 1

	Measurement point (mm); K _{eff} (kN/m)				
Load (N)	-50 mm	-25 mm	25 mm	50 mm	Average K _{eff} (kN/m)
27.0	2438.4	8922.4	5176.3	5912.5	5612.4
44.1	1316.2	1751.5	1758.4	1630.2	1614.1
63.8	740.2	1278.8	1496.4	1251.9	1191.8
78.5	378.8	510.9	514.0	638.5	510.5

5.1.9 Comparison of fibre optics and PIV data

This section compares the results from two physical measurement methods: Fiber-optical measurements of strain in the pipe and PIV of the soil surrounding the pipe. The validity of the assumption that soil displacement at pipe level are the same as the pipe itself is also examined. Moments are derived from the PIV-data using the same numerical derivation technique as section 5.1.7. It was noticed that the maximum moment was reduced drastically with increasing Δh in the numerical integration. In this case, a 12 point arm was used to reduce scatter as much as possible while maintaining enough measurement points. This indicates that the data at hand from the PIV does not give a precise estimate of the pipe moment.

Figures 57 and 58 show the moment in the pipe based on fibre optics and PIV data. First off, the maximum moment derived from the PIV data is in good agreement with the fibre optics during early loading. The gap between the PIV derived moment diagrams and the fibre optics data increases with higher loads. Second, the PIV data gives two inflection points in the moment curve and a much narrower first inflection point. Third, the PIV indicate zero strain towards each end of the pipe. Clearly, the pipe experience significant strains despite the soil not moving. The two data sets largely do not agree even for overall trends, except for the location of the peak moment and the order of magnitude. Among the plausible explanations for the deviation is slight but significant deformation of the cross-section.

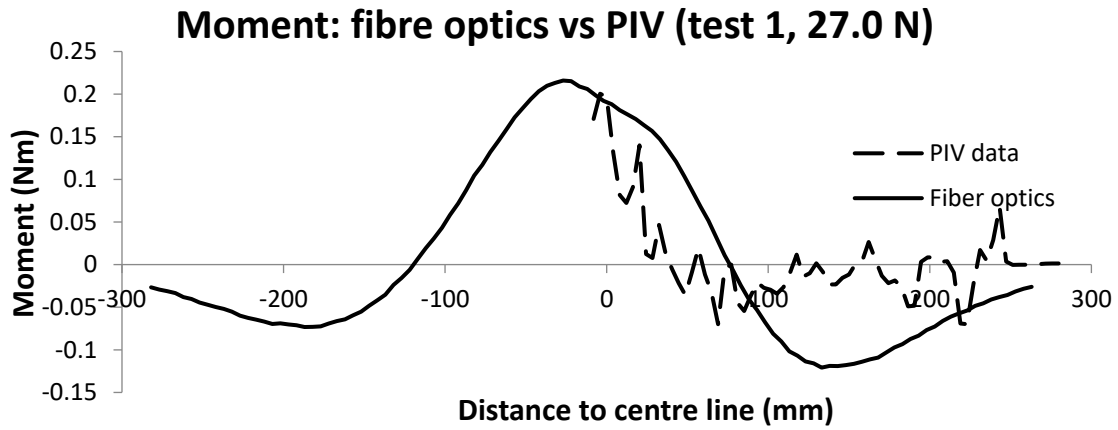


Figure 57a: Comparison on moments based on fibre optics and PIV measurements at 27.0 N, test 1

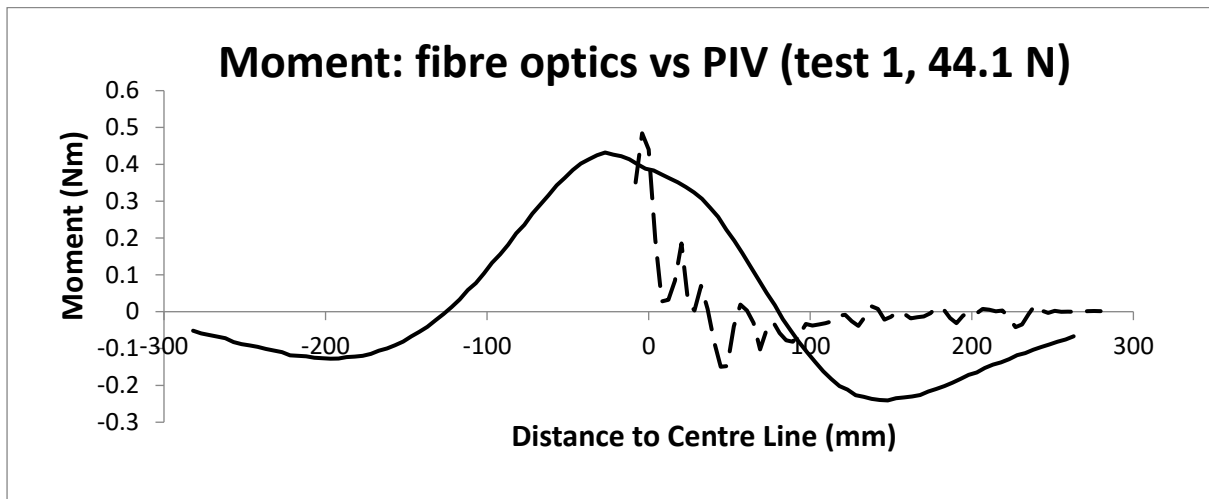


Figure 57b: Comparison on moments based on fibre optics and PIV measurements at 44.1 N, test 1

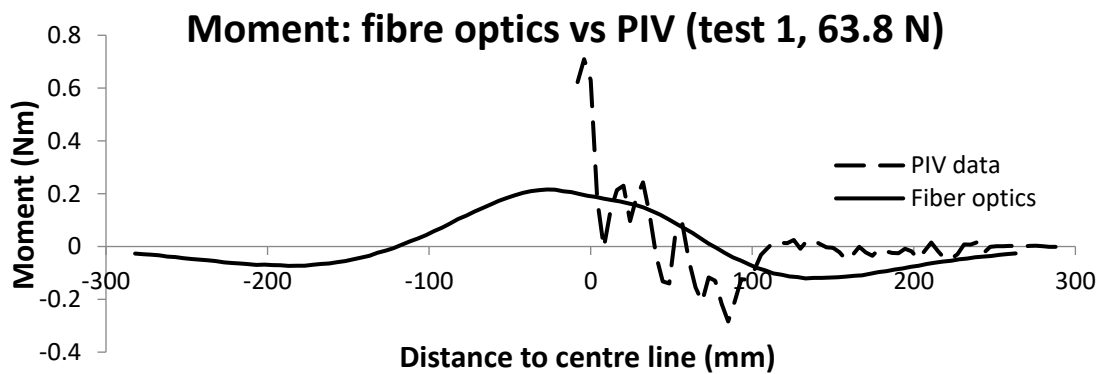


Figure 57c: Comparison on moments based on fibre optics and PIV measurements at 63.8 N, test 1

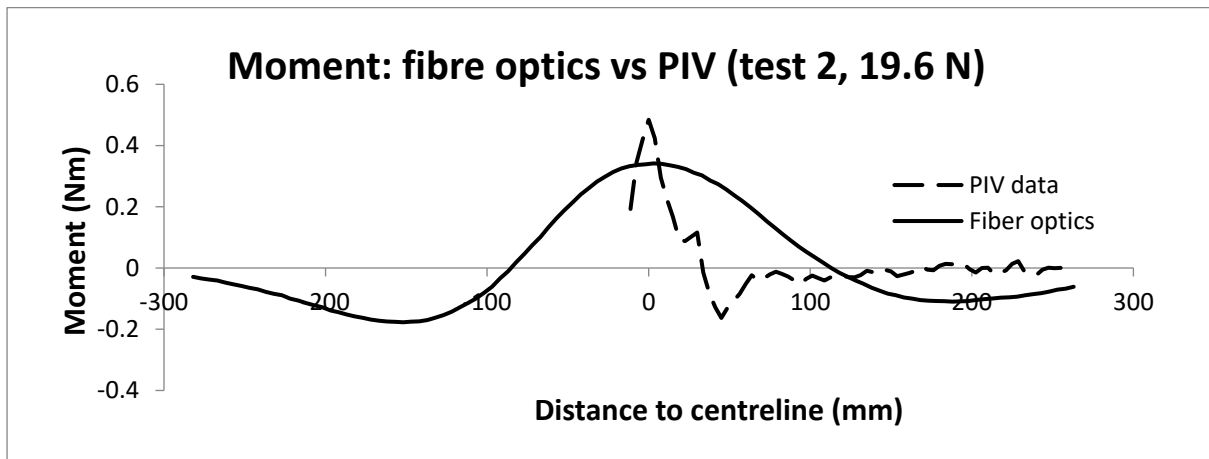


Figure 58a: Comparison on moments based on fibre optics and PIV measurements at 19.6 N, test 2

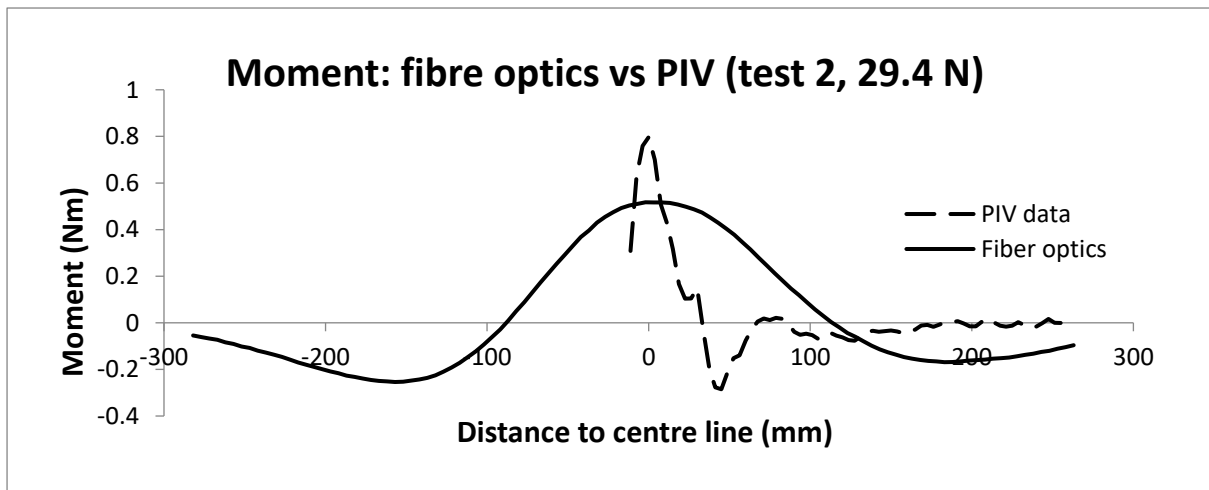


Figure 58b: Comparison on moments based on fibre optics and PIV measurements at 29.4N, test 2

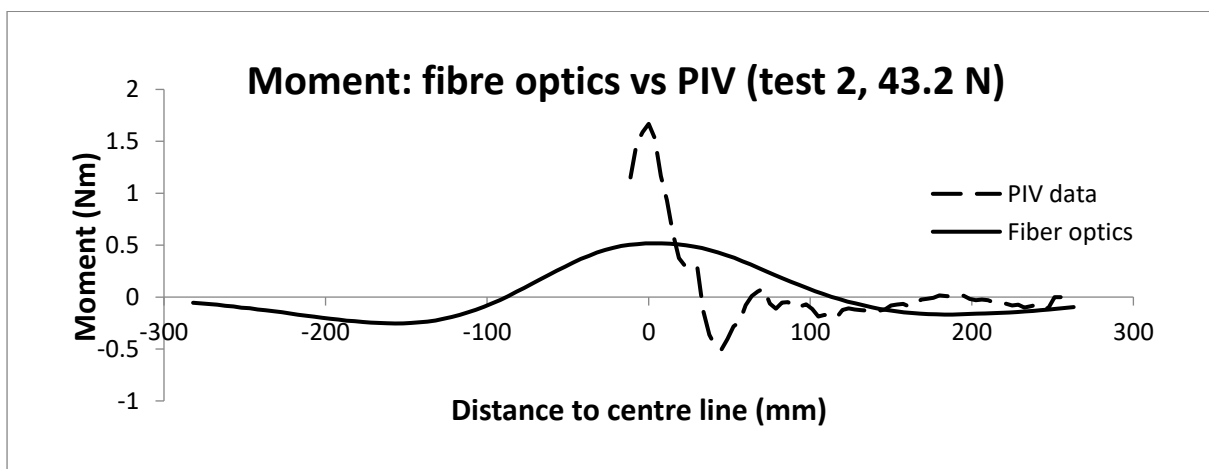


Figure 58c: Comparison on moments based on fibre optics and PIV measurements at 43.2 N, test 2

5.2 Aluminium pipe with fixed ends in 1G (test 3)

Deflection of the pipe during test 3 is presented here. Due to the faulty data, this section revolves around the pipe design. Due to sand falling into the gap between the pipe and the sand, the general displacement field above the pipe cannot be obtained. It can be seen from the images that sand is pouring into the gap between the pipe and the window, making the PIV results here invalid. However, this did not occur everywhere along the pipe and the displacement could be obtained for some regions. The displacement of the sand above the middle of the pipe was found to be reliable. The main goals are to determine:

- If the pipeline is constraint against rotation, and
- If the pipeline is constraint against vertical displacement
- Investigate the pullout response of the pipeline based on the boundary conditions of the pipeline.

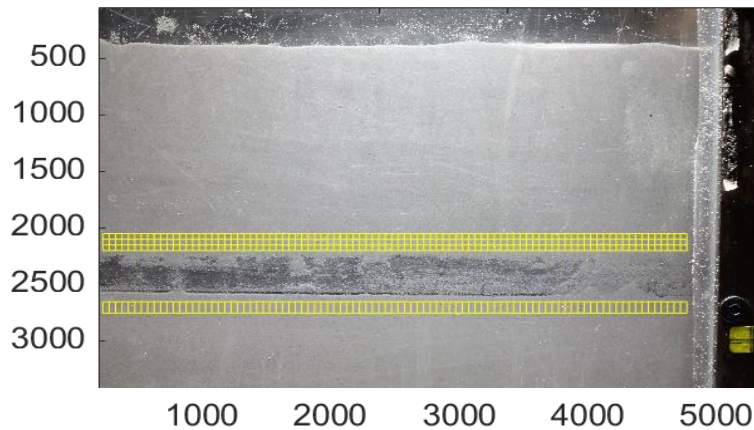


Figure 59: Mesh used to obtain displacements of the pipe in test 3

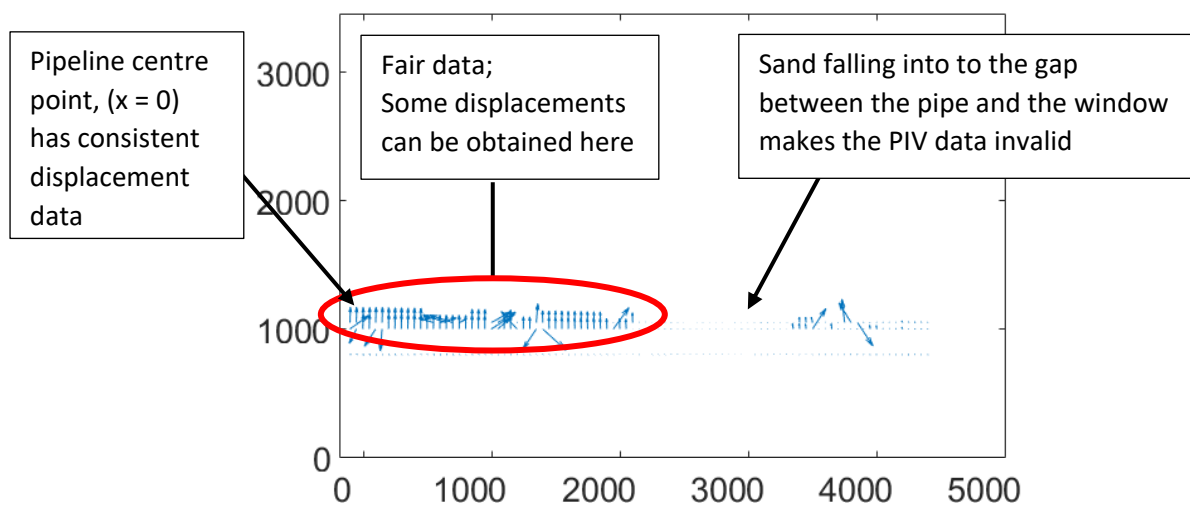


Figure 60: Typical results from the PIV analysis in test 3.

Figure 60 shows a typical result from the GeoPIV analysis. Displacement data is valid around the midpoint of the pipe, where sand did not fall into the gap between the pipe and the window. The maximum displacement was verified by comparison of surrounding displacements vectors.

Based on a quantitative and qualitative analysis of the images, it is clear that the ends of the pipe has no rotation, at least until a load of 335 N. It also appears that the displacement is zero at the ends of the pipe based on the PIV data in this range. Displacements vectors are negligible between approximately 290 to 300 mm (five measurement points from the PIV) from the pipe centreline for loads up to 335 N. Hence, it is safe to assume that the pipe is fixed against rotation and vertical displacement at both ends for loads up to at least 335 N in this test. This observation is further reinforced by the fact that the forces far exceeded the predicted pullout force in literature. Note that the ends are likely fixed against rotation and vertical displacement beyond 335 N, but this is impossible to verify as the last 50 mm of the pipe is hidden behind the wall. Figure 62 shows the pipe after pullout; It is likely that the fixed end broke down right near the pullout load. Large, plastic deformations of the pipe can be observed in figure 61.



Figure 61: Pipeline deflection at the last image taken before failure. It is difficult to say if rotation occurs at the end of the pipe, but it is entirely plausible that the ends are still fixed. Also note that sand is falling into the gap between the pipe and the window.

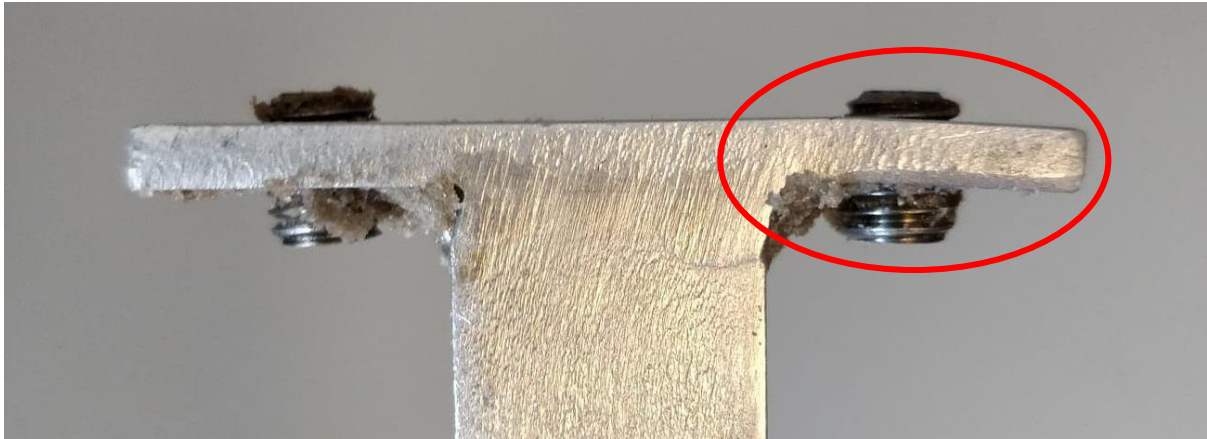


Figure 62: The end of the pipe, which is supposed to prevent rotation, was damaged after the test. This shows the construction worked as intended until failure.

Figure 63 shows the pipeline load-displacement curve at the centre of the pipe. The response appears to be more or less linear until 0.68 mm. Significant soil softening can be observed between the measurement at 0.68 mm and the measurement at 1.74 mm. Remember that pullout of a free pipeline would typically be observed around 1 mm displacement; After this point, the pipe itself governs the deflection. It appears that the pipeline deformation is plastic at a load of 551.3 N, with a maximum displacement of 6.65 mm. This means that the yield point was reached between 3.99 and 6.65 mm deformation. The exact properties of the pipeline is unknown, however it is more important to establish that the aluminium is deforming elastically at least until the pullout capacity of the soil was reached – which figure 63 shows is the case.

Test 3: $z_p/r_0 = 12$, pipeline load-displacement

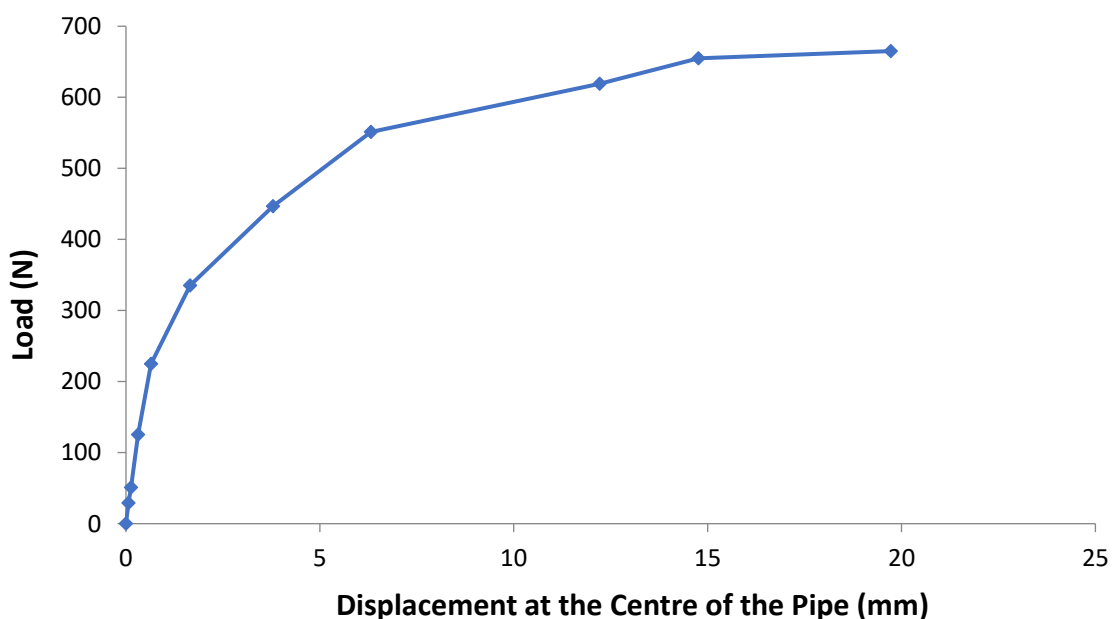


Figure 63: Load-displacement curve based on load cell measurements and measure displacements of the soil at pipe level.

The load applied by the soil on the pipe can be estimated by subtracting the predicted force required to displace an equivalent beam the same distance but without the soil coverage. The rest of the measured force is attributed to soil resistance. This was calculated based on classic beam theory and assuming that both ends are fixed. The results were originally quite unrealistic, so one final consideration has been made: During early loading, rotation and displacements are zero starting at approximately 290 mm. Hence, the pipe resistance is better idealized by a 580 mm long pipe as opposed to a length of 700 mm. This gives the following pullout response (figure 64):

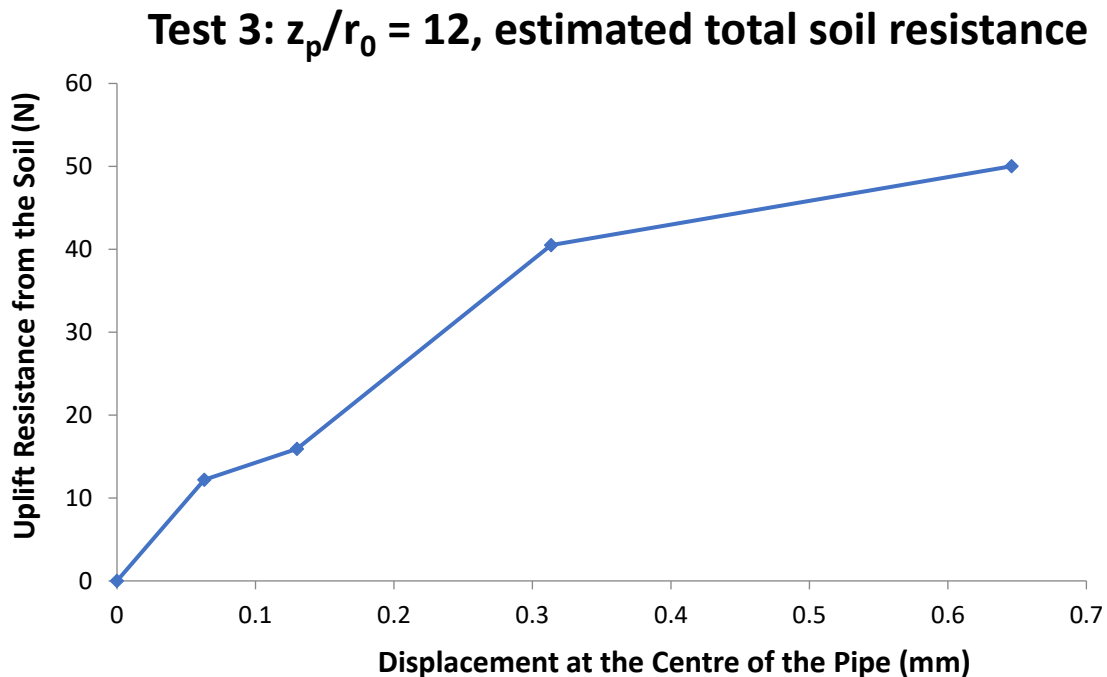


Figure 64: Estimated soil resistance vs maximum displacement of the pipe

The pullout capacity is within the lower and upper bound solution after DNV GL. Furthermore, the mobilization distance falls within the range reported in literature. Using a 700 mm long idealized beam gives a pullout capacity of more than 120 N, which far exceeds the upper bound. Soil resistance during early loading agrees relatively poorly with the prediction curves by DNV GL; a much stiffer behaviour is expected.

5.3 Centrifuge test results (test 4)

The load cell shows that the pipe experienced a load of 1370 N and the pullout capacity was not exceeded. However, the timing of the image acquisition means that there is only displacement data for loads up to 1331.1 N. Furthermore, the load cell shows that the pipe was already loaded to 1221.8 N at before reaching 50g.

The deflection profile of the pipe at 50g and different loads are presented in figure 65. Measured displacements in the underlying soil have been subtracted from the displacement in this figure. The profile exhibits a lot of jumps that do not represent the actual pipeline

displacement. Considering that all four deflection profiles show the unexpected jumps at the same location, the irregular shape is unlikely to come from the GeoPIV analysis. One plausible explanation is that the overlying sand has displaced irregularly during the spinning up of the centrifuge. The displacements are relative to an image taken before the centrifuge accelerated.

The estimated upper bound load at the peak displacement of 0.93 mm is 1357.3 N, meaning the measured displacements are within the upper bound.

Due to the poor displacement measurements, the results in this test will not be analysed further. It is clear that the experimental set up needs some refinements. This will be discussed further in chapter 6.

The increasing load during spin up can be explained by the combination of the self-weight of the load cell and compaction of the underlying soil. Based on the GeoPIV results, compaction in the underlying soil at pipe level is approximately 1.5%.

Test 4: Pipeline displacements at 50g

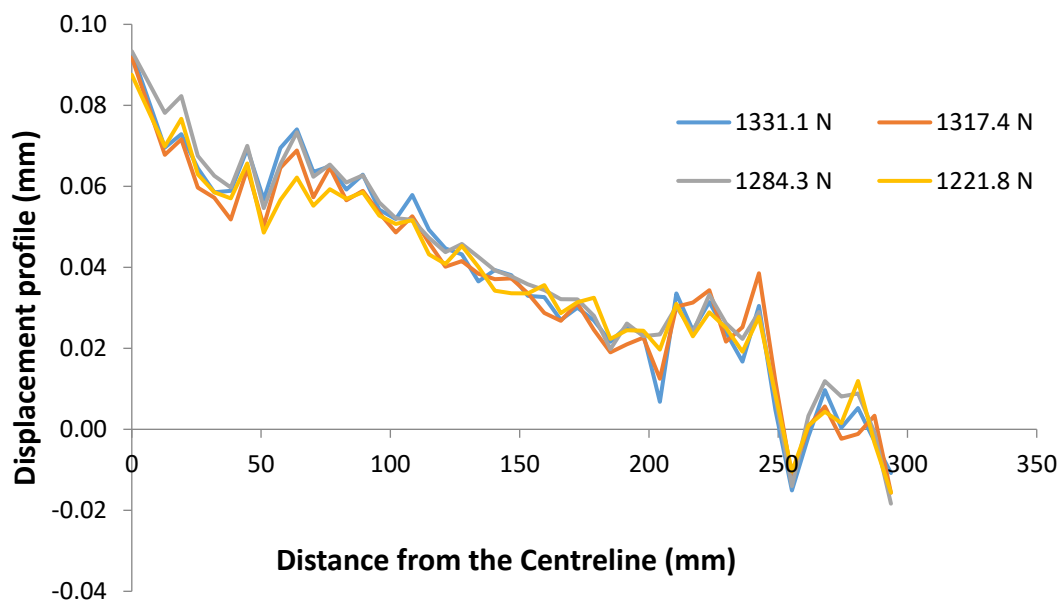


Figure 65: Displacement profile at pipe level during test 4. The data shows some unexpected jumps and scatter which is consistent for all four curves.

5.4 Evaluation of elastic continuum solution and experimental results

This section analyses the displacements from GeoPIV measurements in the frequency domain. The general approach is the same as the one in section 4.3 and explained more in

detail under the methodology chapter. Transverse displacements along the pipe and point load force constitute the input. Since the experimental model involves a half pipe, the point load is multiplied by two but the second moment of area is that of a circular cross-section for the elastic continuum solution. Assuming no friction between the window and the pipe, deflection for the half-pipe will be the same for half the load compared to the response of a buried complete, circular pipe. The script comparing the experimental results with the elastic continuum solution can be found in appendix A.3. The calculations assume that the pipeline response is symmetric at $x = 0$, where x is the horizontal, transverse coordinate. Displacements for $-x$ and x are averaged to get a more representative deflection profile, since the measured displacements had weak symmetry.

Figure 66a and figure 66b presents the frequency-dependent soil-stiffness for two different z_p/r_0 ratios. The first four harmonics are calculated for four different loads in each figure. Smaller loads are not included due to data scatter. Recall that the spatial frequency dependent stiffness should be the same at different loads if the soil is linear elastic.

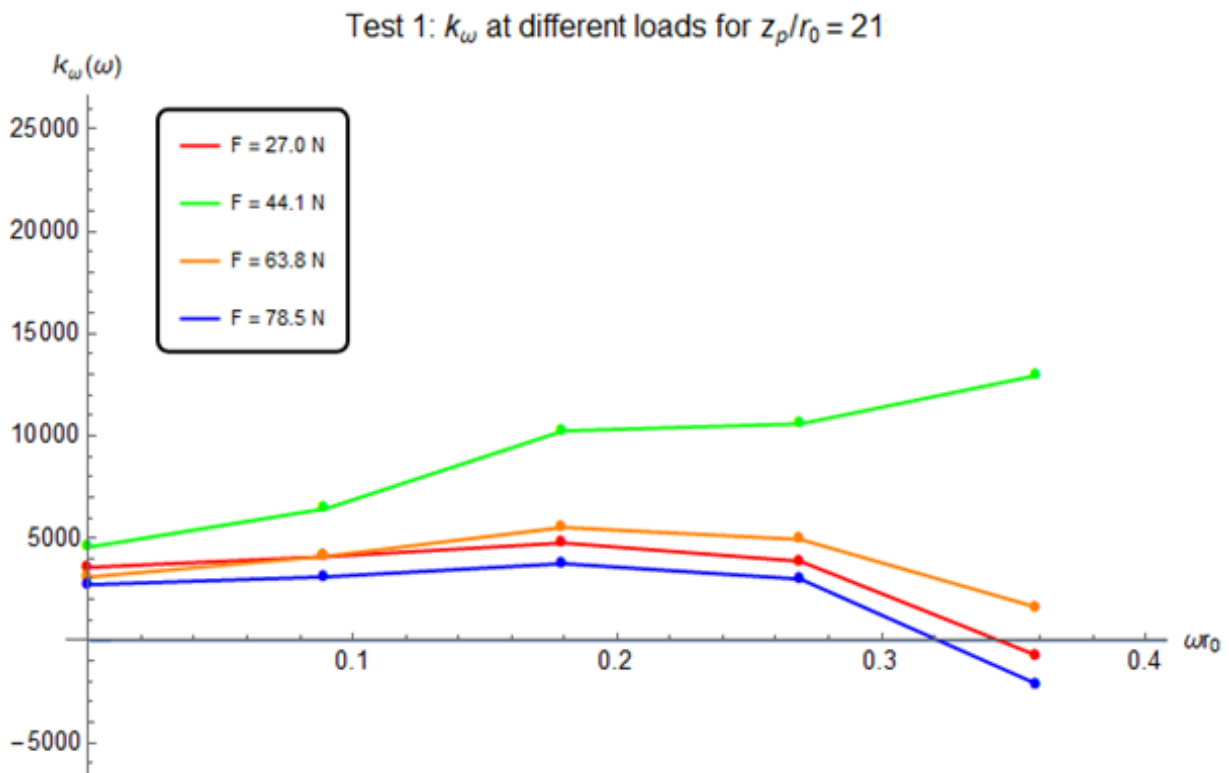


Figure 66a: Spatial frequency-dependent stiffness at different loads from test 1.

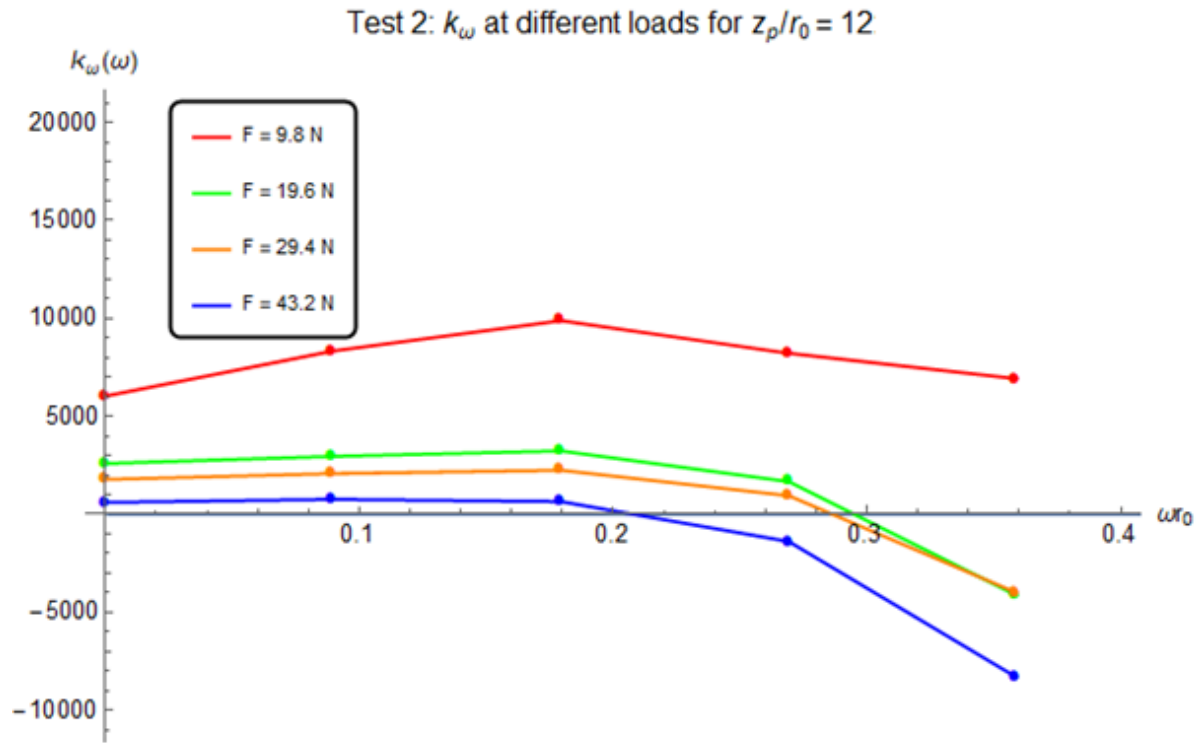


Figure 66b: Spatial frequency-dependent stiffness at different loads from test 2.

Both figures show three curves that closely follow the same increase and reduction in spatial frequency-dependent stiffness. Considering the overall pattern, it is possible that the run-away curves not matching the others come from errors in the data.

The figures are quite revealing in several ways. First, both figures exhibit small changes in spatial frequency-dependent stiffness for the first two to three harmonics – until the continuum solution becomes unstable and drops. Indeed, it is possible based on this data that $k_\omega(\omega)$ is a constant. This result suggests that the pipeline behavior is accurately described by the Winkler-model. If the $k_\omega(\omega)$ is indeed that constant, the value can be compared directly to the estimated effective subgrade modulus in table 21 and table 22. A quick and general comparison shows that the spring stiffness from the load-displacements curves underestimates the assumed constant $k_\omega(\omega)$; The values are off by a factor of around 2 in the first test and a factor of around 1.5 in the second test. Both approaches show that the spring stiffness is generally decreasing with increasing loads, likely attributed to larger displacements causing soil stiffness degradation. If one considers the poor match between the fibre optics and the PIV data, it is entirely feasible that the spring coefficients from the Winkler-modulus and the continuum solution are in fact the same. Additionally, the external (point) load experienced by the pipeline could be significantly lower than the measured loads due to friction. It is therefore likely that all k_ω -values are significantly overestimated. Marshall *et al.* (2012) found a significant lag in PIV data attributed to boundary friction, which could explain some or most of the deviation between the Winkler based and continuum solution based spring coefficients. The experiments in this thesis have the

additional disadvantage of two pulleys which could exhibit frictional forces. Additional tests and more accurate displacement data is necessary to confirm whether or not $k_{\omega}(\omega)$ is a constant.

Secondly, spatial frequency-dependent stiffness does not tend to zero as the spatial frequency becomes very small. This was also observed in the finite element model. These results strongly indicate that the spatial frequency-dependent stiffness is not zero for $\omega = 0$.

Thirdly, the spatial frequency increases with increasing burial depth. This is expected and the same tendency was shown in the numerical analysis as well as the original paper by Klar (2018). Klar found that the difference between z_p/r_0 ratios of 8 and 16 is fairly minor and approaching the solution for an infinitely deep pipeline. Comparing the spatial frequency-dependent stiffness at comparable displacements, more specifically $F=78.5$ and $F=29.4$, shows that the former is about 1.1 to 1.2 times higher than the latter for the first few harmonics. It is likely that k_{ω} is close to $k_{\omega,inf}$ for test 2 due to the very high z_p/r_0 ratio.

A small comment on the soil stiffness:

It is interesting to find the bulk modulus that fits the data to the $k_{\omega,inf}$. This can also be compared to the predicted initial soil stiffness. The values are shown in table 23. In this case, the soil stiffness according to Biarez et al. (1994) is used. These are reference values and only useful for indicating the stiffness degradation. The spatial frequency-dependent stiffness is normalized by the bulk modulus G to match the analytical solution for an infinitely deep pipe. Table 23 shows the estimated Young's modulus for the loads 27.0 N and 19.6 N in test 1 and test 2, respectively. It is likely that significant soil degradation up exceeding 80% has occurred for the measurements at this load.

Table 23: Estimated Young's modulus compared to predicted initial Young's modulus after Biarez et al. 1994

Test	Burial depth (mm)	n (-)	p' (kPa)	$E_{s,initial}$ (MPa) (Biarez et al. 1994)	E (MPa) fitting k_{ω}/G to $k_{\omega,inf}/G$	ν
1	210	1	2.1	32	6	0.25
2	120	1	1.1	23	4	0.25

5.5 Summary

Two pullout tests studied the response of a thin-walled PVC pipe. The same half-pipe is used for both experiments at different the burial depths, respectively $z_p/r_0 = 21$ and $z_p/r_0 = 12$. The particle image velocimetry program GeoPIV measured the displacements of the soil surrounding the pipeline. Fibre optics installed inside the pipe measured the transverse pipe strains.

The pipeline uplift response is investigated using the displacements from the GeoPIV. A load-displacement curve measured at the pipeline centre is plotted, including several

unloads and reloads of the pipeline. The measured maximum displacement is compared with prediction formulas for uplift resistance of a pipe. Furthermore, the soil strains and the development of a failure mechanism in the overlying soil are identified based on displacements in the overlying soil.

Pipeline deflection profiles are investigated at different loads for the two tests. A Gaussian best fit is introduced including goodness of fit. This is a well-documented shape of the settlement trough and pipeline deflection over a tunnel and could possibly be used to describe the soil and pipe displacement over a pipeline.

Moment and load experienced by the pipe with distance from the centre are estimated through the fibre optics data. Moment and load curves are plotted at different loads to investigate the pipe-soil interactions. Load-displacements curves show the stiffness of the soil with increasing loads and also indicates a value for the spring coefficient in the Winkler model.

Lastly, the measured displacements from the two tests were analyzed in the frequency domain. Spatial frequency-dependent stiffness were obtained at different loads for both tests. A general comparison to the Winkler model was considered. The magnitude of stiffness degradation was assessed by comparing normalized spatial frequency-dependent stiffness values from the experiments to the solution at infinite depth.

6 Conclusions and recommendations

6.1 Conclusions

Perhaps the most important conclusion from the finite element model is that a spatial frequency dependency for the soil stiffness exists. This means that the Winkler model does not perfectly represent the soil response and confirms the utility of the elastic continuum solution. The spatial frequency-dependent stiffness is also clearly depth-dependent.

Analysis of the computed results also showed good agreement with the findings by Klar (2018). The spatial frequency-dependent stiffness at a z_p/r_0 ratio of 15 appears to converge with the solution for an infinitely deep pipeline, except for very small frequencies ωr_0 . The same convergence is found in Klar (2018) for similar z_p/r_0 ratios. The k_ω for a z_p/r_0 ratio of 10 are still close to $k_{\omega,\infty}$, but the difference is quite large for lower burial depths and frequencies up to $\omega r_0 = 0.4$. In Klar (2018), the curves are observed to approach $k_{\omega,\infty}$ with increasing spatial frequency and eventually converge. Similar trends can be observed in the numerical model based on $k_\omega(\omega)$, at least up until the point where the solution becomes unstable. The solution becomes unstable at spatial frequencies exceeding $\omega r_0 = 0.3$ to 0.4 regardless of pipeline radius and depth. This makes it difficult to arrive at a definitive conclusion regarding the relationship between k_ω and $k_{\omega,\infty}$ at higher spatial frequencies. A sufficient number of k_ω values to describe the pipeline response were obtained with the smaller pipe radii (5 mm and 10 mm). In contrast to the analytical solutions in Klar (2018), the spatial frequency-dependent stiffness obtained from the numerical models do not approach zero as ωr_0 becomes small.

Four experimental pullout test have been carried out to investigate the transverse displacements of a pipeline. However, conclusions here are only based on the first two tests. Pipeline displacements of the flexible pipe in test 1 and test 2 were compared to prediction models for rigid pipes in literature. The results reveal that the general pipeline response is similar to that of a rigid pipe. Plotting the applied load against the maximum displacement of the pipeline showed good agreement with trilinear curves after recommended practice by DNG GL (DNV-RP-F110). However, maximum mobilization distance from both experiments exceeds 0.005-0.010 times the coverage height by, the rule of thumb in DNV-RP-F110. This is not surprising as the GeoPIV analyses showed that most of the pipe is completely restrained by the soil, which allows the middle of the pipe to be in pullout before the rest of the pipe. Measured pullout capacity did not unanimously agree with the most common prediction models in literature. However, it should be noted that the prediction models generally do not agree between them either. A model for based on passive earth pressure theory appears to give the best fit to test data, which is also the recommended model of choice for medium to dense sands in DNV-RP-F110.

The displacements and resulting strains in the overlying soil show the developing failure mechanism, from small strains all the way to failure. Strains are initially concentrated around the middle of the pipe, where the point load is applied. The strains increase in

magnitude but remain negligible more than five pipeline radii from the center line at small loads. Strains propagate in height and a clear chimney-mechanism can be observed in both tests. When applied load well exceeds half of the pullout capacity, the strains start moving out to the sides. It appears that pullout is reached when large strains are present in the soil and have propagated up to 10 pipeline diameters to each side. No displacements or strains were observed over the outermost parts of the pipe up until the point of failure. This has important implications for structural monitoring as failure can propagate from a small and local region to a zone twice the length or more without warning. It is also interesting to note that the underlying soil experience zero strains. Continuous contact between the soil and the pipe is not maintained, and a gap is generated under the pipe.

The deflection profiles of the pipe subjected to a point load, as well as the soil deformation in the overlying soil, are well described by the Gaussian error function with R^2 -values up to 0.99. The inflection point of the Gaussian appears to increase linearly with depth, which has also been observed above a tunnel. These findings could mean that similar models can be used to describe the response of a pipeline due to external loads from a point load and tunnel induced ground displacements. A Gaussian is commonly used to describe the settlement trough over a pipeline and the resulting deflection of the pipe.

Data from fibre optics installed on the inside of the pipe gives accurate measurements of the strains, which in turn can be used to estimate bending moment and load. This makes the fibre optics a potentially useful monitoring tool of buried pipelines. The maximum moment of the pipeline is linear for small displacements but increases at a faster rate at larger loads. The break point coincided with soil displacement measurements. A direct comparison of the moment derived from the soil displacements at pipe level did not show good agreement. The soil displacement based moment curves are much narrower than those established by the fibre optics results. Load applied by the soil was based on the moment diagrams with good accuracy, which is useful for estimating the spring coefficient in the Winkler model. The load-displacement curves show a linear response in the small strain range and subsequent stiffness degradation with increasing loads.

As with the numerical models, the pipeline deflection profile was analysed in the frequency domain, and the spatial frequency-dependent stiffness was established at different burial depths. Little spatial frequency dependency was observed and $k_\omega(\omega)$ could possibly be a constant. The potential constant $k_\omega(\omega)$ was in the same range as the spring coefficient in the Winkler model for both tests, further reinforcing this relationship. The soil is rather well described by the Winkler model based on these results. However, the strains far exceed the linear elastic range in some of the overlying soil and therefore does not invalidate the spatial frequency dependency in the continuum solution. At least two of the k_ω -curves undeniably show spatial frequency dependency, and the soil is mostly in the small strain range at 9.8 N in test 2 where this was observed.

6.2 Validity of the results

There are some limitations to be aware of for the numerical model. The model assumes no gravity which means that the overlying soil can displace more freely than what is the case for a pipe in the field. The finite element model also showed large strains in the underlying soil compared to the overlying soil. Overall, all the conditions of the elastic continuum solution are maintained and the results confirming the continuum solution should be valid. Inaccuracies could arise from the mesh. The mesh of the soil was kept to equal to half the width of the applied load to reduce computation time. Hence, the soil response may not be accurately model over the width of the applied load. This could also explain why the continuum solution becomes unstable for large spatial frequencies.

The experimental results are influenced by several factors. First, force applied experienced by the pipe is almost certainly lower than the measured load. Friction forces on the wire from the pulley system as well as the window-half-pipe interface means that the measured load is higher than the actual load applied to the pipe. Beyond calculating the predicted skin friction on the wire (section 3.2.4), it is unknown to which degree the pulling force is affected by friction. Secondly, the soil was loaded and unloaded several times which certainly affect the pipeline and soil displacement for subsequent load. A hysteresis is obvious for; the data as the load-displacement curve does not return to its original value when reloaded. This particularly affects the mobilization distance. The PIV measurements showed significant scatter, to the point where the deflection profile at small strains could not be used in the elastic continuum solution. Even at larger loads and displacements, the scatter is significant. It is highly recommended that future experiments use a higher resolution camera, place it closer to the window or forgoing of the measurement technique altogether. The fibre optics data also showed some problems with measurements as the moment curves are far from symmetric. This might be due to the pipeline itself displacing asymmetrically or flawed installation of the fiber optics inside the pipe. The fibre optics was able to measure the smallest loads with good accuracy based on the maximum moment. Any change in tension on the wire was captured (even pressing on the pipe with a finger). Due to the scatter of the PIV data as well as non-linear soil behaviour, any conclusions regarding the elastic continuum solution are unsettled.

6.3 Recommended improvements to the centrifuge model

Test 4 is useful as a trial run but the centrifuge model is clearly not ready. Here are the recommended improvements to the centrifuge model:

- 1) The threaded holes for the camera mount bolts in the centrifuge box for the camera mount bolts are weak and **must** be remade or reinforced. The centrifuge box is likely made out of cast iron (though the author was unable to confirm this) which is much weaker than construction steel. It was observed after the centrifuge test that one of the bolts was almost ripped out. A threaded insert would solve this.

2) The camera needs to be stabilized better. The large camera mount works well (other than the problem with the threaded holes), but the camera should be attached better to the mount. Remember to calculate the swing radius of the camera if a new solution is made as there is very little clearance. The existing set up works well for low accelerations up to maximum 10-20 g.

3) A different solution for attaching the wire to the pipe could be considered or the current one should be improved. The idea presented in this thesis should work but the clamp turned out to be weak. Proper crimping tools could solve this without changing the setup. Pulling tests should be carried out to establish the strength of the pipe-wire attachment.

4) Avoid displacement control during spin-up of the centrifuge and avoid tension in the wire before the start of the pullout tests. The self-weight of the load cell applies a very significant load which disturbs the results of the pullout tests. The current solution (using wires to hold the load cell) does not work as intended.

5) The current load cell is difficult to attach to the wiring system due to its physical length. Shorter load cells are available and should be considered.

6) Installing the pipeline without getting sand on the inside is difficult with the current set up. There are different solutions to press the pipe against the window while pouring sand at the cost of disturbing the sand. The pros could potentially outweigh the cons as sand on falling into the gap affects both frictions at the interface as well as the GeoPIV results.

7) One problem with the current set up and the elastic continuum solution (if this is the goal of additional experiments) is that measurements at very small displacements are the most valuable. This is also very difficult to obtain good data for as scatter becomes significant. Among the possible solutions is simply a more expensive camera. A second, independent measurement of displacements of the pipeline could be considered.

With these changes, the setup should give more accurate results similar to the 1G tests in this thesis. The setup can also be modified to do pullout tests on other buried structures such as piles.

Lastly, it should be noted that the 1g experiments worked really well and gave more accurate valuable information than expected. Running additional 1g experiments or small accelerations up to 10g would give good data without taking a lot of time. But DO reinforce the camera mount threaded bolt holes even for low g-forces.

6.4 Further Research

Firstly, the findings in this thesis are interesting and it is worthwhile to conduct additional experiments with this setup at DTU or a similar setup elsewhere. Additional studies can look into different burial depths and pipeline radii. Few studies are available on the pullout response of a deforming pipeline. All available prediction formulas for pullout capacity and

maximum mobilization distance only consider a perfectly rigid pipeline. While the results of the test show that at least the pullout capacity is fairly well-predicted, the prediction formulas should be expanded to account for transverse pipe displacements. A point load situation occurs frequently in the field. The numerical test results show that the elastic continuum solution successfully describes the response of a pipeline (additional experimental results with very small displacements in the elastic range are likely to find the same). Obtaining a range of spatial frequency-dependent stiffness values for different burial depths and pipeline radii is extremely useful as they better describe the pipeline response than the spring coefficients in the Winkler-model.

Monitoring the pipeline with fibre optics was successful and can be used both for additional experiments as well as other experiments with pipelines. The implications for field monitoring are huge; the fibre optics are cheap compared to other structural and ground monitoring solution and, perhaps more importantly, monitoring is continuous along the pipe. The installation and calibration of the pipeline was uncomplicated and the solution presented in this thesis could easily be implemented for large-scale pipelines.

The elastic continuum solution overall works well but shows some limitations due to the idealized, constant soil stiffness. The solution could be expanded to account for stress-variation in the soil with depth. The spatial frequency-dependent stiffnesses obtained from the tests indicate that the real k_w values do not approach zero as the spatial frequency becomes small. This is clearly a simplification and limitation of the continuum solution in its current state.

7 Bibliography

Figures have been reprinted with permission of the respective copyright owners and/or authors.

General design of the steel components of the centrifuge model were based on EN 1993-1-9:2006 Eurocode 3: Design of steel structures – Part 1-9: Fatigue, CEN, Brussels, 2006.

Atkinson, J. H. and Potts, D. M. (1977) 'Subsidence above shallow tunnels in soft ground', *Journal of Geotechnical and Geoenvironmental Engineering*, 103(Proc. Paper 11318 Proceeding).

Attewell, P. B., Yeates, J. and Selby, A. R. (1986) 'Soil movements induced by tunnelling and their effects on pipelines and structures'. Methuen, Inc., New York, NY.

Benz, T. (2007) *Small-Strain Stiffness of Soils and its Numerical Consequences*, Ph.D. Thesis. doi: 10.1097/mpg.0000000000000537.

Biarez, J., Hicher, P.-Y. and others (1994) *Elementary mechanics of soil behaviour: saturated remoulded soils*. AA Balkema.

Bolton, M. D. (1986) 'Strength and dilatancy of sands', *Geotechnique*, 36(1), pp. 65–78.

Bransby, M. F. *et al.* (2001) 'Numerical and centrifuge modeling of the upheaval resistance of buried pipelines', in *Proc. OMAE*.

Bucher, C. (2007) *LIGHTING PHOTO WORKSHOP*. Wiley Publishing, Inc.

Byrne, P. M. *et al.* (2004) 'Numerical modeling of liquefaction and comparison with centrifuge tests', *Canadian Geotechnical Journal*. NRC Research Press, 41(2), pp. 193–211.

Cheuk, C. Y., White, D. J. and Bolton, M. D. (2008) 'Uplift Mechanisms of Pipes Buried in Sand', *Journal of Geotechnical and Geoenvironmental Engineering*, 134(2), pp. 154–163. doi: 10.1061/(ASCE)1090-0241(2008)134:2(154).

DNV GL (2007) 'Dnv-Rp-F110', (October), pp. 1–64.

Garnier, J. *et al.* (2007) 'Catalogue of scaling laws and similitude questions in geotechnical centrifuge modelling', *International Journal of Physical Modelling in Geotechnics*, 7(3), pp. 01-23. doi: 10.1680/ijpmg.2007.070301.

Hardin, B. O. and Black, W. (1969) 'Closure on vibration modulus of normally consolidated clay', *Journal of Soil Mechanics & Foundations Div.*

Hardin, B. O. and Drnevich, V. P. (1972) 'Shear modulus and damping in soils: design equations and curves', *Journal of Soil Mechanics & Foundations Div*, 98(sm7).

Hardin, B. O. and Richart Jr, F. E. (1963) 'Elastic wave velocities in granular soils', *Journal of Soil Mechanics & Foundations Div*, 89(Proc. Paper 3407).

Ireland, H. O. (1975) 'Pulling tests on piles in sand', in *Proc 4th Int Conf Soil Mech Found Eng*,

Vol 2, pp. 43–46.

Klar, A. *et al.* (2005) 'Soil—pipe interaction due to tunnelling: comparison between Winkler and elastic continuum solutions', *Géotechnique*, 55(6), pp. 461–466. doi: 10.1680/geot.2005.55.6.461.

Klar, A. (2018) 'Elastic Continuum Solution for Tunneling Effects on Buried Pipelines Using Fourier Expansion', 144(9), pp. 1–10. doi: 10.1061/(ASCE)GT.1943-5606.0001945.

Klar, A., Elkayam, I. and Marshall, A. M. (2016) 'Design Oriented Linear-Equivalent Approach for Evaluating the Effect of Tunneling on Pipelines', *Journal of Geotechnical and Geoenvironmental Engineering*, 142(1), p. 04015062. doi: 10.1061/(ASCE)GT.1943-5606.0001376.

Klar, A. and Marshall, A. M. (2015) 'Linear elastic tunnel pipeline interaction: the existence and consequence of volume loss equality', *Géotechnique*, 1(9), pp. 1–5. doi: 10.1680/geot14.P.173.

Latini, C. and Zania, V. (2016) 'Triaxial tests in Fontainebleau sand'.

Mair, R. J. (1979) 'Centrifugal Modelling of Tunnel Construction in Soft Clay', p. 256.

Mair, R. J. (1993) 'Developments in geotechnical engineering research: application to tunnels and deep excavations', in *Proceedings of Institution of Civil Engineers: Civil Engineering*, pp. 27–41.

Mair, R. J. and Taylor, R. N. (1996) 'Theme lecture: Bored tunnelling in the urban environment'. Available at: https://www.issmge.org/uploads/publications/1/31/1997_04_0049.pdf.

Mair, R. J., Taylor, R. N. and Bracegirdle, A. (1993) 'Subsurface settlement profiles above tunnels in clays', *Géotechnique*, 43(2), pp. 315–320. doi: 10.1680/geot.1993.43.2.315.

Marshall, A. M. (2009) 'Tunnelling in sand and its effect on pipelines and piles', *Engineering Department*, PhD Thesis(March), p. 250.

Marshall, A. M. *et al.* (2012) 'Tunnels in sands: the effect of size, depth and volume loss on greenfield displacements', *Géotechnique*, 62(5), pp. 385–399. doi: 10.1680/geot.10.P.047.

Marshall, A. M., Klar, A. and Mair, R. J. (2010) 'Tunneling beneath Buried Pipes: View of Soil Strain and Its Effect on Pipeline Behavior', *Journal of Geotechnical and Geoenvironmental Engineering*, 136(12), pp. 1664–1672. doi: 10.1061/(ASCE)GT.1943-5606.0000390.

Mindlin, Raymond D. "Force at a point in the interior of a semi-infinite solid." *physics* 7.5 (1936): 195-202.

Murthy, V. N. S. (2002) *Geotechnical engineering: principles and practices of soil mechanics and foundation engineering*. CRC press.

O'reilly, M. P. and New, B. M. (1982) *Settlements above tunnels in the United Kingdom-their magnitude and prediction*.

Peck, R. B. (1969) 'Deep excavations and tunneling in soft ground', *Proc. 7th ICSMFE, 1969*, pp. 225–290.

- Phillips, R. and Valsangkar, A. J. (1987) *An experimental investigation of factors affecting penetration resistance in granular soils in centrifuge modelling*. University of Cambridge Department of Engineering.
- Puech, A. and Garnier, J. (2017) *Design of Piles Under Cyclic Loading: SOLCYP Recommendations*. John Wiley & Sons.
- Schaminee, P. E. L., Zorn, N. F. and Schotman, G. J. M. (1990) 'Soil Response for Pipeline Upheaval Buckling Analyses: Full-Scale Laboratory Tests and Modelling', *Offshore Technology Conference*, pp. 563–572. doi: 10.4043/6486-MS.
- Schmidt, B. (1969) 'Settlements and ground movements associated with tunnelling in soil', *PhD Thesis*. University of Illinois.
- Springman, S. M., Ng, C. W. W. and Ellis, E. A. (1994) *Centrifuge and analytical studies of full height bridge abutment on piled foundation subjected to lateral loading*. Department of Engineering, University of Cambridge.
- Taylor, R. N. (1995) *Geotechnical Centrifuge Technology*. Blackie Academic & Professional. doi: 10.15713/ins.mmj.3.
- Thrane, C. (2011) 'Centrifuge modelling of large diameter pile in sand subject to lateral loading'.
- Trautmann, C. H., O'Rourke, T. D., and Kulhawy, F. H. (1985) 'Uplift force-displacement response of buried pipe', *Journal of the geotechnical engineering division*, 111(9), pp. 1061–1076.
- Vermeer, P. A. (1985) 'The uplift resistance of shallow embedded anchors', in *Proc. 11th. Int. Conf. On SMFE*, pp. 1635–1938.
- Vorster, T. E. et al. (2005) 'Estimating the Effects of Tunneling on Existing Pipelines', *Journal of Geotechnical and Geoenvironmental Engineering*, 131(11), pp. 1399–1410. doi: 10.1061/(ASCE)1090-0241(2005)131:11(1399).
- Vorster, T. E. B. (2005) *Effects of tunnelling on buried pipes*. University of Cambridge.
- Vorster, T. E. B. et al. (2006a) 'Centrifuge modelling of the effect of tunnelling on buried pipelines : mechanisms observed', *Geotechnical Aspects of Underground Construction in Soft Ground*, pp. 327–333. doi: 10.1201/NOE0415391245.ch43.
- Vorster, T. E. B. et al. (2006b) 'Centrifuge modelling of the effect of tunnelling on buried pipelines : mechanisms observed', *Geotechnical Aspects of Underground Construction in Soft Ground*, (September), pp. 327–333. doi: 10.1201/NOE0415391245.ch43.
- Wang, Y., Shi, J. and Ng, C. W. W. (2011) 'Numerical modeling of tunneling effect on buried pipelines', *Canadian Geotechnical Journal*, 48(7), pp. 1125–1137. doi: 10.1139/t11-024.
- White, D. J., Barefoot, A. J. and Bolton, M. D. (2001) 'Centrifuge modelling of upheaval buckling in sand', *International Journal of Physical Modeling in Geotechnics*, 2, pp. 19–28.
- White, D. J., Barefoot, A. J. and Bolton, M. D. (2001) 'Centrifuge Modelling of Upheaval Buckling in Sand Centrifuge Modelling of Upheaval Buckling in Sand', 314(September 2000).

White, D. J. and Take, W. a. (2002) 'GeoPIV: Particle Image Velocimetry (PIV) software for use in geotechnical testing', *Cambridge University Engineering Department Technical Report*, 322(October), p. 15.

Wichtmann, T. and Triantafyllidis, T. (2009) 'On the correlation of "static" and "dynamic" stiffness moduli of non-cohesive soils', *Bautechnik*. Wiley Online Library, 86(S1), pp. 28–39.

APPENDIX A.1

(*APPENDIX A.1: Pipeline response and spacial frequency
dependent stiffness based on the elastic continuum solution*)

Quit[]

L = 0.350 (*size of the box*);

n = 10;

r0 = 0.01;

a = 0.015;

$\delta[x_] := 2.45 * \frac{1}{a \pi^{1/2}} \text{Exp}\left[-\left(\frac{x}{a}\right)^2\right]$ (*The load function*)

$A0 = \frac{1}{L} \int_{-L}^L \delta[x] dx$;

An = Table[Re[$\frac{1}{L} \int_{-L}^L \delta[x] \text{Cos}\left[\frac{i \pi x}{L}\right] dx$], {i, 1, n}];

(*Fourier coeffecients for the amplitude
of the harmonic barell load. For which $\omega i = \frac{i \pi}{L}$ *)

EI = 70000000 $\left(\frac{\pi r0^4}{4}\right)$; (*in MPa*)

v = 0.25;

$G = \frac{158 * 1000}{2 * (1 + v)}$;

$k\omega[\omega r0_] := \frac{16 * G * \pi (1 - v)}{(6 - 8 v) \text{BesselK}[0, \omega r0] + \omega r0 \text{BesselK}[1, \omega r0]}$;

UpCoe = Table[$\frac{An[[i]]}{EI * \left(\frac{i \pi}{L}\right)^4 + k\omega\left[\frac{i \pi}{L} r0\right]}$, {i, 1, n}];

(*Fourier coeffecients for the amplitude of the soil displacements*)

$up[x_] := 0 + \sum_{i=1}^{\text{Dimensions}[An][[1]]} \text{UpCoe}[[i]] \text{Cos}\left[\frac{i \pi x}{L}\right]$

(*Global response of the pipeline*)

In[*]:= An

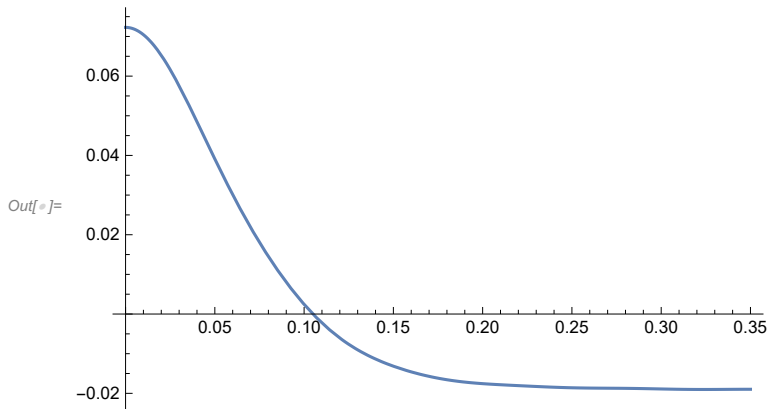
Out[*]= {39.9982, 39.9927, 39.9837, 39.971, 39.9547, 39.9348, 39.9113, 39.8841, 39.8534, 39.8191}

In[*]:= Integrate[$\delta[x]$, {x, -L, L}]

Out[*]= 2.45

2 | $k_{\text{omega}} r_0 = 10$, $z_p = 100.\text{nb}$

```
In[ ]:= Plot[up[x] * 1000, {x, 0, L}, PlotRange -> All]
```



(* Let see if we can resolve the soil reaction model from this*);

```
In[ ]:= (*First we will create a long data table, representing values from measurements*)
```

```
data = Table[{ $\frac{i}{10000} * L$ , up[ $\frac{i}{10000} * L$ ]}, {i, 0, 10000}];
```

```
In[ ]:= sampleval = Interpolation[data];
```

(*Symmetry is assumed for the solution*)

```
U0 =  $\frac{2}{L}$  NIntegrate[sampleval[x], {x, 0, L}];
```

```
Un = Table[ $\frac{2}{L}$  NIntegrate[sampleval[x] Cos[ $\frac{i \pi x}{L}$ ], {x, 0, L}], {i, 1, n}];
```

(*for which $\omega_i = \frac{i \pi}{L}$ *)

NIntegrate: NIntegrate failed to converge to prescribed accuracy after 9 recursive bisections in x near {x} = {6.27731 × 10⁻⁹}.
NIntegrate obtained 1.9269999550035333`*^-20 and 4.495101684265511`*^-17 for the integral and error estimates.

```
In[ ]:= KwRes = Table[{ $\frac{i \pi}{L} * r_0$ ,  $\frac{An[[i]]}{Un[[i]]} - EI * \left(\frac{i \pi}{L}\right)^4$ }, {i, 1, n}];
```

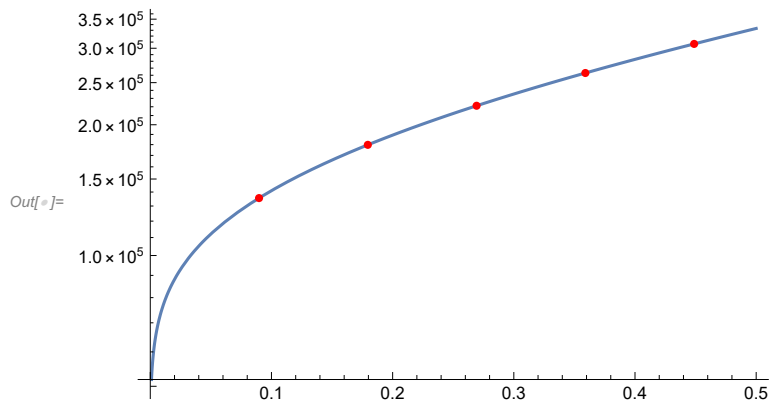
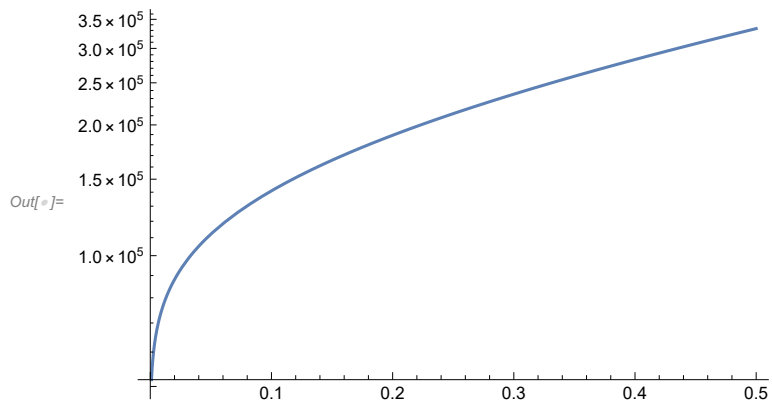
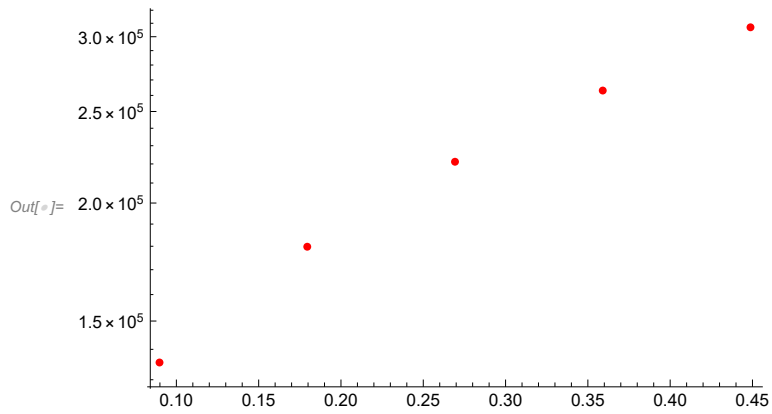
```
In[ ]:= KwRes
```

```
Out[ ]:= {{0.0897598, 135579.}, {0.17952, 179791.},  
          {0.269279, 221175.}, {0.359039, 263103.}, {0.448799, 306965.}}
```

```

In[ ]:= p1 = ListLogPlot[KwRes, PlotStyle -> Red]
p2 = LogPlot[kw[τ], {τ, 0.001, 0.5}, PlotRange -> All]
Show[p2, p1]

```



```
Quit[]
```

APPENDIX A.2

(*APPENDIX A.2: k_ω from COMSOL Multiphysics simulations.

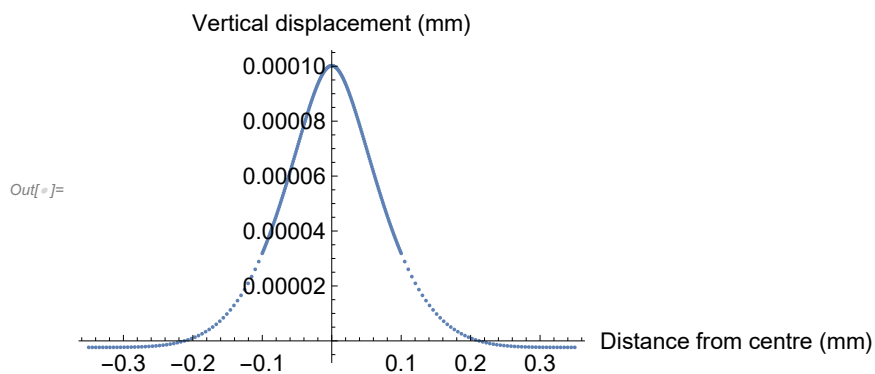
This is an example using the properties from simulation 4 ($r_\theta=10$ and $z_p=50$ *)

Quit[]

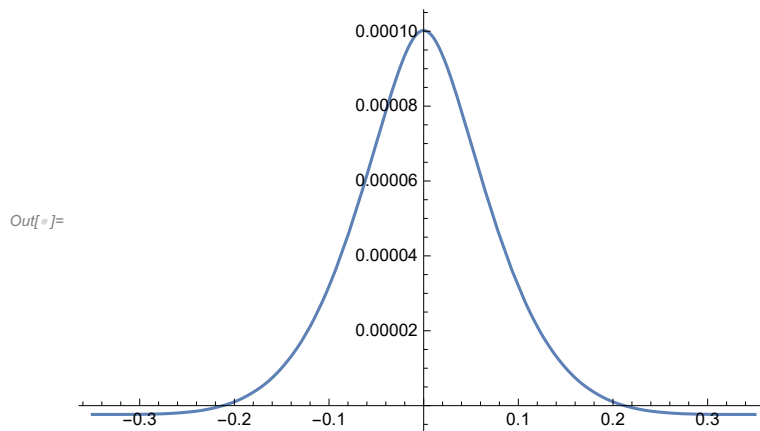
sampleval = Interpolation[Comsol]

(*Where Comsol is a table of the vertical displacements of the pipeline and the x-coordinate for each point ($-0.350 < x < 0.350$). Not shown in this APPENDIX for practical purposes.)

In[]:= ListPlot[Comsol, AxesLabel → {"Distance from centre (mm)", "Vertical displacement (mm)"}, LabelStyle → {12, GrayLevel[0]}]



In[]:= Plot[sampleval[x], {x, -0.35, 0.35}]



```

In[ ]:= v = 0.25;
G =  $\frac{112 * 1000}{2 * (1 + v)}$ ;
L = 0.35 (*size of the box*);
n = 5;
r0 = 0.01;
a = 0.015;

δ[x_] := 1.61  $\frac{1}{a (\pi)^{1/2}}$  Exp[- $\left(\frac{x}{a}\right)^2$ ]

A0 =  $\frac{1}{L} \int_{-L}^L \delta[x] dx$ ;
An = Table[Re[ $\frac{1}{L} \int_{-L}^L \delta[x] \cos\left[\frac{i \pi x}{L}\right] dx$ ], {i, 1, n}] (*for which ωi= $\frac{i \pi}{L}$ *)

EI = 70000000 *  $\frac{\pi (r0)^4}{4}$ 

Out[ ]:= {4.5792, 4.51736, 4.41615, 4.27825, 4.10726}

Out[ ]:= 0.549779

In[ ]:= U0 =  $\frac{1}{L}$  NIntegrate[sampleval[x], {x, -0.9999999 * L, 0.9999999 * L}]

Out[ ]:= 0.0000450682

In[ ]:= An

Out[ ]:= {4.5792, 4.51736, 4.41615, 4.27825, 4.10726}

In[ ]:=

Un = Table[ $\frac{1}{L}$  NIntegrate[sampleval[x] Cos[ $\frac{i \pi x}{L}$ ], {x, -L, L}], {i, 1, n}]

(*for which ωi= $\frac{i \pi}{L}$ *)

Out[ ]:= {0.0000398027, 0.0000212191, 8.90623 × 10-6, 3.76405 × 10-6, 1.74353 × 10-6}

KwRes = Table[{ $\frac{i \pi}{L} * r0$ ,  $\frac{\frac{An[[i]]}{Un[[i]]} - \frac{EI}{r0^4} * \left(\frac{i \pi}{L} * r0\right)^4}{G}$ }, {i, 1, n}]

Out[ ]:= {{0.0897598, 2.48837}, {0.17952, 3.47749},
{0.269279, 4.61566}, {0.359039, 4.97792}, {0.448799, 2.79592}}

In[ ]:= Insert[KwRes, {0,  $\frac{A0}{U0}$ }, 1]

Out[ ]:= {{0, 2.27829}, {0.0897598, 2.48837}, {0.17952, 3.47749},
{0.269279, 4.61566}, {0.359039, 4.97792}, {0.448799, 2.79592}}

```

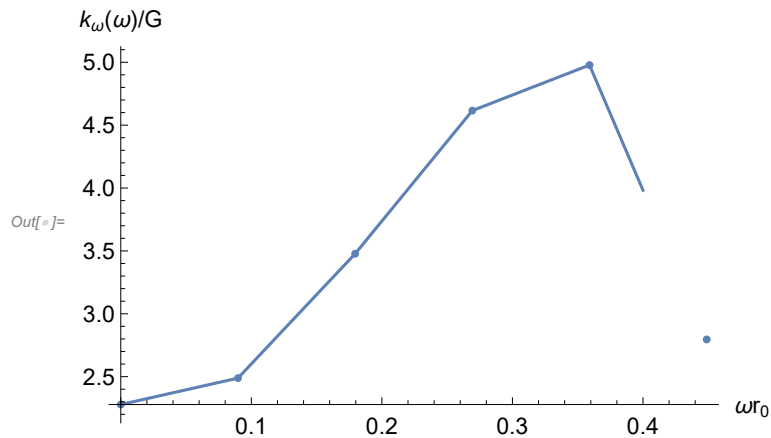
```
In[ ]:= Kvals = Interpolation[Insert[KwRes, {0,  $\frac{A0}{U0 \cdot G}$ }, 1], InterpolationOrder → 1]
```

```
Out[ ]:= InterpolatingFunction[  Domain: {{0., 0.449}}  
Output: scalar
```

```
In[ ]:= p1 = Plot[Kvals[x], {x, 0, 0.4}, PlotRange → All];
```

```
p2 = ListPlot[Insert[KwRes, {0,  $\frac{A0}{U0 \cdot G}$ }, 1]];
```

```
Show[p1, p2, PlotRange → All,  
AxesLabel → {" $\omega r_0$ ", " $k_\omega(\omega)/G$ "}, LabelStyle → {12, GrayLevel[0]}]
```



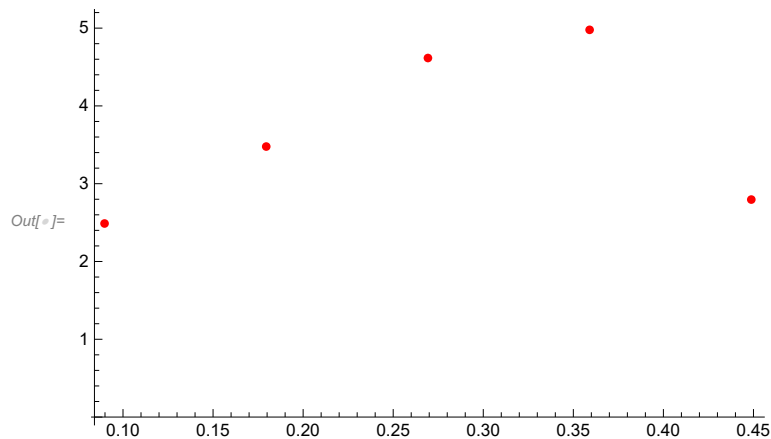
Kvals[0.3]

8.78545

An / Un

{59.6179, 179.452, 599.918, 1559.76, 3274.46, 5900.58, 9512.83, 14127.6, 19659.4, 26049.9}

```
In[ ]:= p1 = ListPlot[KwRes, PlotStyle → Red]
```



4 | *komega from comsol r0 = 10, zp = 50.nb*

Quit[]

APPENDIX A.3

(*APPENDIX A.3: k_ω from the experimental tests.

This is an example from test 2 at a load of 43.2 N*)

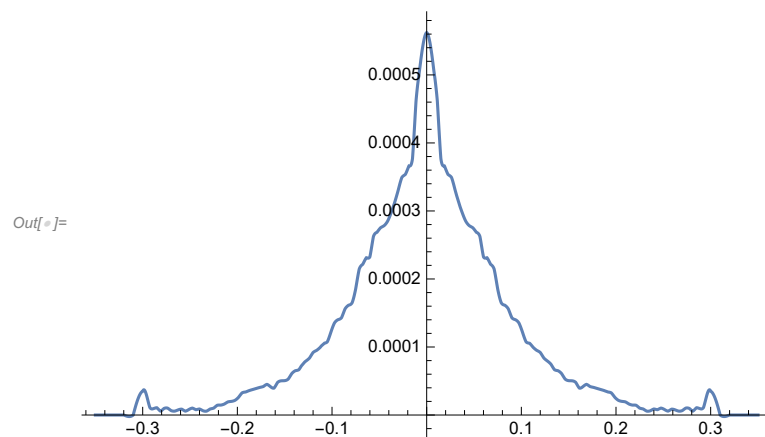
Quit[]

sampleval = Interpolation[PIV]

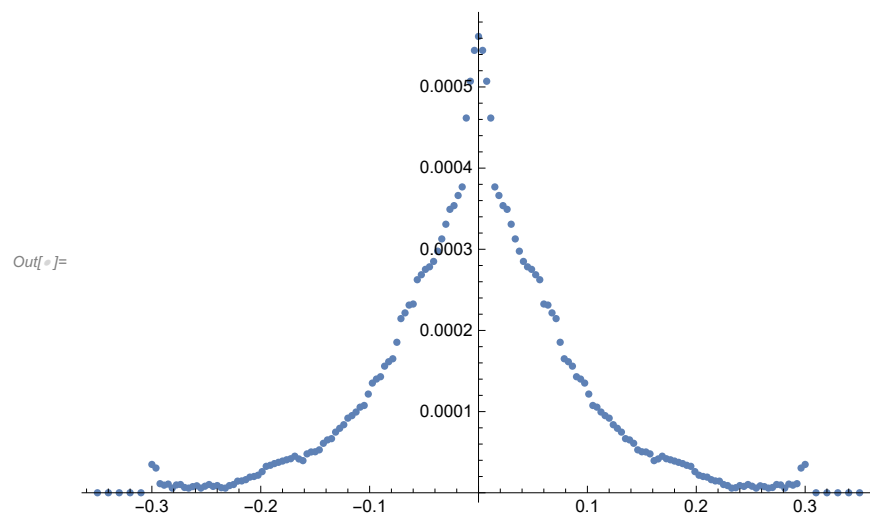
(*Where PIV is a table of measured vertical displacements of the pipeline and the x-coordinate for each point ($-0.350 < x < 0.350$). Displacements at both ends of the pipe are extrapolated. Not shown in this APPENDIX for practical purposes.)

Out[]:= InterpolatingFunction[  Domain: {{-0.35, 0.35}}
Output: scalar]

In[]:= Plot[sampleval[x], {x, -0.35, 0.35}]

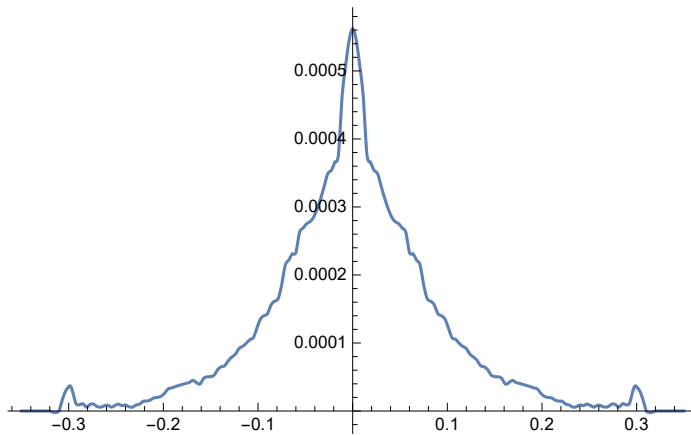


ListPlot[PIV]



In[]:= Plot[sampleval[x], {x, -0.350, 0.350}]

Out[]:=



$\nu = 0.25;$

$G = \frac{23 * 1000}{2 * (1 + \nu)};$

$L = 0.350 (* \text{size of the box} *);$

$n = 4;$

$r0 = 0.01;$

$a = 0.00001;$

$t = 0.002;$

$\delta[x_] := 2 * 0.0432 \frac{1}{a (\pi)^{1/2}} \text{Exp}\left[-\left(\frac{x}{a}\right)^2\right]$

(*The load is multiplied by a factor of 2 since the pipe is a half-pipe*)

$A0 = \frac{1}{L} \int_{-L}^L \delta[x] dx;$

$An = \text{Table}\left[\text{Re}\left[\frac{1}{L} \int_{-L}^L \delta[x] \cos\left[\frac{i \pi x}{L}\right] dx\right], \{i, 1, n\}\right] (* \text{for which } \omega_i = \frac{i \pi}{L} *)$

$EI = 3400000 \left(\frac{\pi r0^4}{4} - \frac{\pi (r0 - t)^4}{4} \right);$

(*Bending stiffness of an equivalent complete pipe*)

Out[]:= {0.251429, 0.251429, 0.251429, 0.251429}

In[]:= {0.25142857092214277`, 0.2514285694028568`, 0.25142856687071335`, 0.2514285633257127`}

Out[]:= {0.251429, 0.251429, 0.251429, 0.251429}

In[]:= $U0 = \frac{1}{L} \text{NIntegrate}[\text{sampleval}[x], \{x, -0.9999999 * L, 0.9999999 * L\}]$

Out[]:= 0.000205099

In[]:= An

Out[]:= {0.251429, 0.251429, 0.251429, 0.251429}

In[]:=

```
Un = Table[ $\frac{1}{L}$  NIntegrate[sampleval[x] Cos[ $\frac{i \pi x}{L}$ ], {x, -L, L}], {i, 1, n}]
```

(*for which $\omega_i = \frac{i \pi}{L}$ *)

Out[]:= {0.000153778, 0.0000855787, 0.0000455735, 0.0000262844}

```
KwRes = Table[{ $\frac{i \pi}{L} * r\theta$ ,  $\frac{\frac{An[[i]]}{Un[[i]]} - \frac{EI}{r\theta^4} * (\frac{i \pi}{L} * r\theta)^4}{G}$ }, {i, 1, n}]
```

Out[]:= {{0.0897598, 0.166595}, {0.17952, 0.141364}, {0.269279, -0.301358}, {0.359039, -1.80795}}

In[]:= Insert[KwRes, {0, $\frac{A\theta}{U\theta}$ }, 1]

Out[]:= {{0, 0.133249}, {0.0897598, 0.166595},
{0.17952, 0.141364}, {0.269279, -0.301358}, {0.359039, -1.80795}}

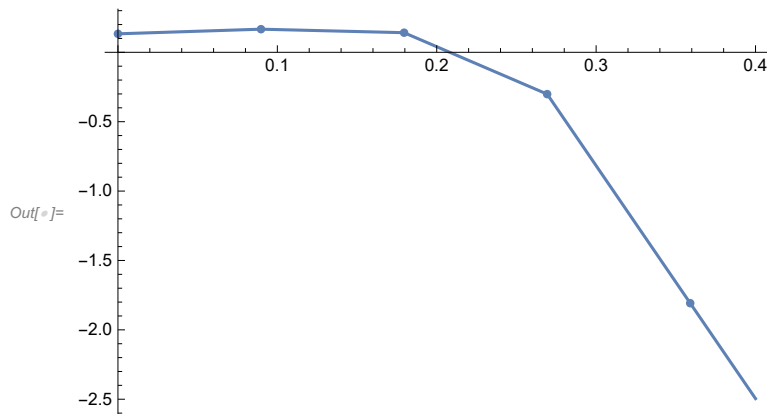
In[]:= Kvals = Interpolation[Insert[KwRes, {0, $\frac{A\theta}{U\theta}$ }, 1], InterpolationOrder -> 1]

Out[]:= InterpolatingFunction[  Domain: {{0., 0.359}}
Output: scalar

In[]:= p1 = Plot[Kvals[x], {x, 0, 0.4}, PlotRange -> All];

```
p2 = ListPlot[Insert[KwRes, {0,  $\frac{A\theta}{U\theta}$ }, 1]];
```

```
Show[p1, p2, PlotRange -> All]
```



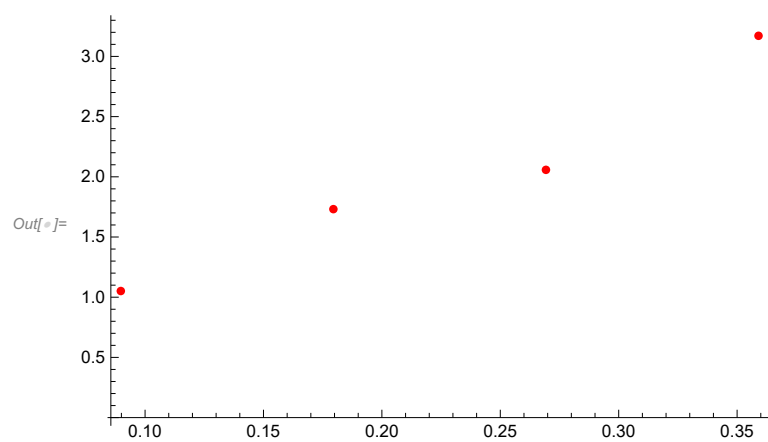
```
Kvals[0.3]
```

```
8.78545
```

```
An / Un
```

```
{59.6179, 179.452, 599.918, 1559.76, 3274.46, 5900.58, 9512.83, 14127.6, 19659.4, 26049.9}
```

```
In[ ]:= p1 = ListPlot[KwRes, PlotStyle -> Red]
```



```
Quit[]
```

APPENDIX A.4

(*APPENDIX A.4: Solution of a point load*)

Quit[]

$$\lambda_{vv} = \frac{k_{\theta\theta}}{-k_{v\theta}^2 + k_{vv} k_{\theta\theta}};$$

$$\lambda_{\theta\theta} = \frac{k_{vv}}{-k_{v\theta}^2 + k_{vv} k_{\theta\theta}};$$

$$\lambda_{v\theta} = \frac{k_{v\theta}}{k_{v\theta}^2 - k_{vv} k_{\theta\theta}};$$

$$\text{eq1} = (\omega * \text{Up} == 0 + (\lambda_{v\theta} * F + \lambda_{\theta\theta} * M));$$

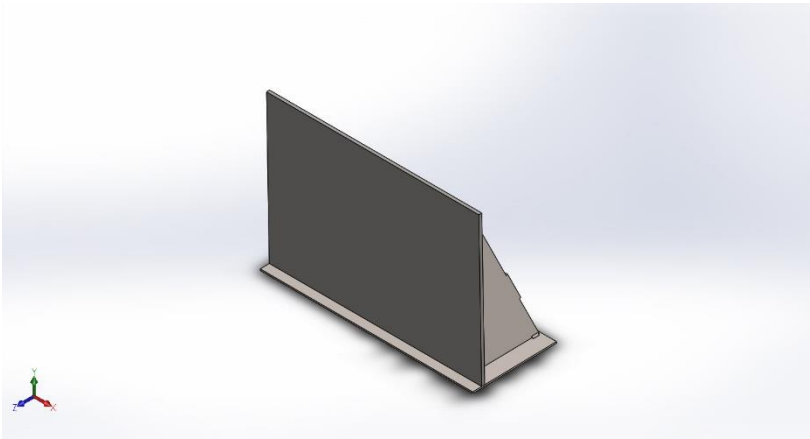
$$\text{eq2} = (\text{Up} == 0 + (\lambda_{vv} * F + \lambda_{v\theta} * M));$$

$$\text{eq3} = (\omega^4 EI * \text{Up} + F + \omega * M == A\omega);$$

FullSimplify[Solve[{eq1, eq2, eq3}, {Up, F, M}]]

$$\left\{ \left\{ \text{Up} \rightarrow \frac{A\omega}{k_{vv} + 2 k_{v\theta} \omega + k_{\theta\theta} \omega^2 + EI \omega^4}, \right. \right. \\ \left. \left. F \rightarrow \frac{A\omega (k_{vv} + k_{v\theta} \omega)}{k_{vv} + \omega (2 k_{v\theta} + k_{\theta\theta} \omega + EI \omega^3)}, M \rightarrow \frac{A\omega (k_{v\theta} + k_{\theta\theta} \omega)}{k_{vv} + \omega (2 k_{v\theta} + k_{\theta\theta} \omega + EI \omega^3)} \right\} \right\}$$

$$\left\{ \left\{ \text{Up} \rightarrow \frac{A\omega}{k_{vv} + 2 k_{v\theta} \omega + k_{\theta\theta} \omega^2 + EI \omega^4}, \right. \right. \\ \left. \left. F \rightarrow \frac{A\omega (k_{vv} + k_{v\theta} \omega)}{k_{vv} + \omega (2 k_{v\theta} + k_{\theta\theta} \omega + EI \omega^3)}, M \rightarrow \frac{A\omega (k_{v\theta} + k_{\theta\theta} \omega)}{k_{vv} + \omega (2 k_{v\theta} + k_{\theta\theta} \omega + EI \omega^3)} \right\} \right\}$$



Description
No Data

APPENDIX B.1: Simulation of Separation Wall

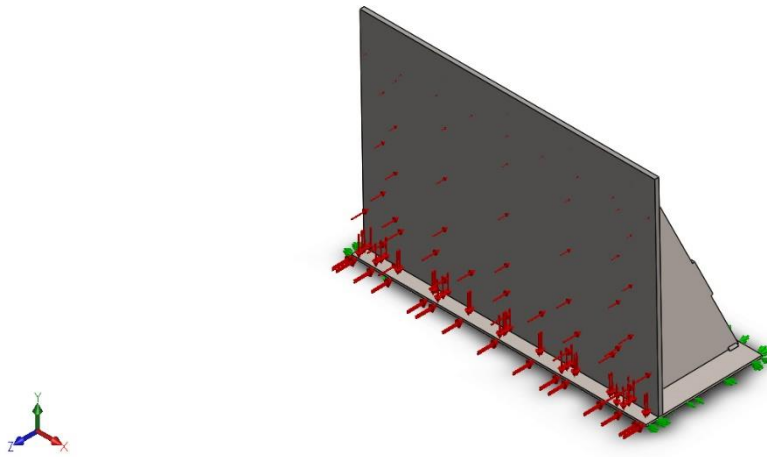
Date: Monday, October 22, 2018
Designer: Solidworks
Study name: Static 1
Analysis type: Static

Table of Contents

Description.....	1
Assumptions	2
Model Information	2
Study Properties	3
Units	3
Material Properties	4
Loads and Fixtures.....	5
Connector Definitions.....	6
Contact Information.....	6
Mesh information	7
Sensor Details	8
Resultant Forces	8
Beams	8
Study Results	9
Conclusion	11

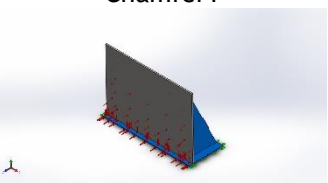
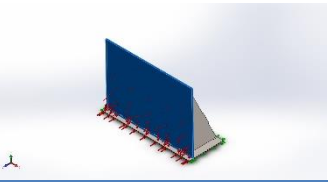
Assumptions

Model Information



Model name: Wall analysis classic retaining wall
Current Configuration: Default

Solid Bodies

Document Name and Reference	Treated As	Volumetric Properties	Document Path/Date Modified
Chamfer1 	Solid Body	Mass:18.9544 kg Volume:0.00246161 m ³ Density:7700 kg/m ³ Weight:185.753 N	C:\Users\danie\Documents\SOLIDWORKS files\Classic support.SLDPRT Oct 22 16:28:35 2018
Cut-Extrude1 	Solid Body	Mass:27.7022 kg Volume:0.00355156 m ³ Density:7800 kg/m ³ Weight:271.481 N	C:\Users\danie\Documents\SOLIDWORKS files\Wall.SLDPRT Oct 22 16:16:47 2018

Study Properties

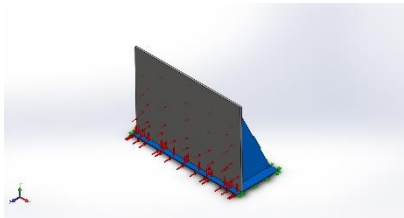
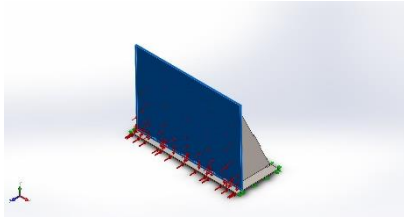
Study name	Static 1
Analysis type	Static
Mesh type	Solid Mesh
Thermal Effect:	On
Thermal option	Include temperature loads
Zero strain temperature	298 Kelvin
Include fluid pressure effects from SOLIDWORKS Flow Simulation	Off
Solver type	FFEPlus
Inplane Effect:	Off
Soft Spring:	Off
Inertial Relief:	Off
Incompatible bonding options	Automatic
Large displacement	On
Compute free body forces	On
Friction	Off
Use Adaptive Method:	Off
Result folder	SOLIDWORKS document (C:\Users\danie\Documents\SOLIDWORKS files)

Units

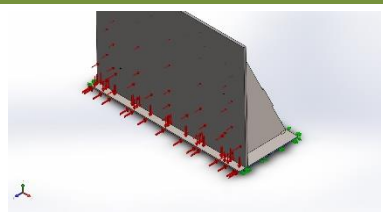
Unit system:	SI (MKS)
Length/Displacement	mm
Temperature	Kelvin
Angular velocity	Rad/sec
Pressure/Stress	N/m ²

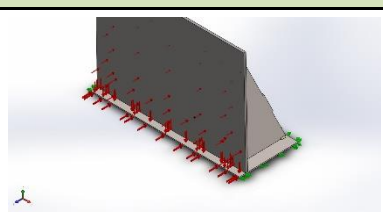


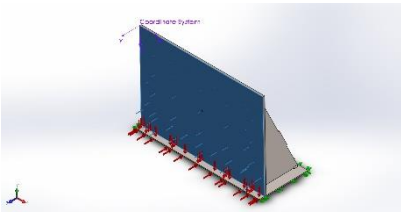
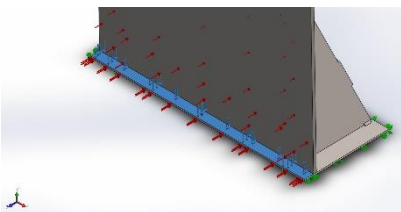
Material Properties

Model Reference	Properties	Components
	Name: S355 Steel Model type: Linear Elastic Isotropic Default failure criterion: Unknown Yield strength: 3.55e+008 N/m ² Tensile strength: 4.70e+008 N/m ² Elastic modulus: 2.1e+011 N/m ² Poisson's ratio: 0.28 Mass density: 7700 kg/m ³ Shear modulus: 7.9e+010 N/m ² Thermal expansion coefficient: 1.3e-005 /Kelvin	SolidBody 2 (Support-1)
Curve Data:N/A		
	Name: S355 Steel Model type: Linear Elastic Isotropic Default failure criterion: Unknown Yield strength: 3.55e+008 N/m ² Tensile strength: 4.70e+008 N/m ² Elastic modulus: 2.1e+011 N/m ² Poisson's ratio: 0.28 Mass density: 7800 kg/m ³ Shear modulus: 7.9e+010 N/m ² Thermal expansion coefficient: 1.3e-005 /Kelvin	SolidBody 1(Cut-Extrude1)(Wall-1)
Curve Data:N/A		

Loads and Fixtures

Fixture name	Fixture Image	Fixture Details		
Roller/Slider-12		Entities: 3 face(s) Type: Roller/Slider		
Resultant Forces				
Components	X	Y	Z	Resultant
Reaction force(N)	1.52588e-005	-2550.44	59534.6	59589.2
Reaction Moment(N.m)	0	0	0	0

Roller/Slider-14		Entities: 1 face(s) Type: Roller/Slider		
Resultant Forces				
Components	X	Y	Z	Resultant
Reaction force(N)	-1.03184	9633.66	9788.76	13734.2
Reaction Moment(N.m)	0	0	0	0

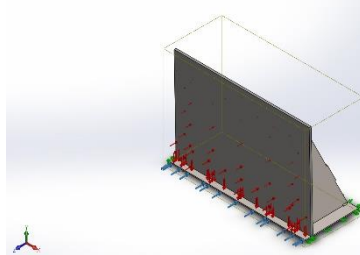
Load name	Load Image	Load Details
Pressure-1		Entities: 1 face(s) Type: Normal to selected face Value: 1 Units: N/m ² Equation: 652800*"z" (m) Ref Coord Sys: Coordinate System1 Coord Sys Type: Cartesian Phase Angle: 0 Units: deg
Pressure-2		Entities: 1 face(s) Type: Normal to selected face Value: 460800 Units: N/m ² Phase Angle: 0 Units: deg



Connector Definitions

No Data

Contact Information

Contact	Contact Image	Contact Properties
Global Contact		Type: Bonded Components: 1 component(s) Options: Compatible mesh

Mesh information

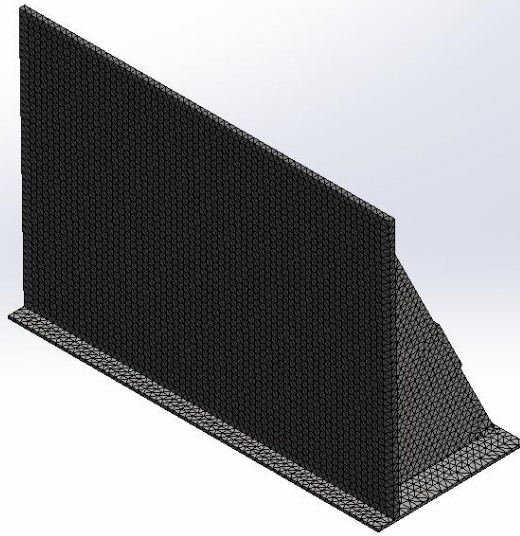
Mesh type	Solid Mesh
Mesher Used:	Standard mesh
Automatic Transition:	Off
Include Mesh Auto Loops:	Off
Jacobian points	4 Points
Element Size	11.3905 mm
Tolerance	0.569524 mm
Mesh Quality Plot	High
Remesh failed parts with incompatible mesh	Off

Mesh information - Details

Total Nodes	91309
Total Elements	47300
Maximum Aspect Ratio	8.7269
% of elements with Aspect Ratio < 3	95.3
% of elements with Aspect Ratio > 10	0
% of distorted elements(Jacobian)	0
Time to complete mesh(hh:mm:ss):	00:00:11
Computer name:	



Model name: Wall analysis classic retaining wall
 Study name: Static 1 (-Default-)
 Mesh type: Solid Mesh



SOLIDWORKS Educational Product. For Instructional Use Only.

Sensor Details

No Data

Resultant Forces

Reaction forces

Selection set	Units	Sum X	Sum Y	Sum Z	Resultant
Entire Model	N	1.52588e-005	8699.9	59744.9	60375

Reaction Moments

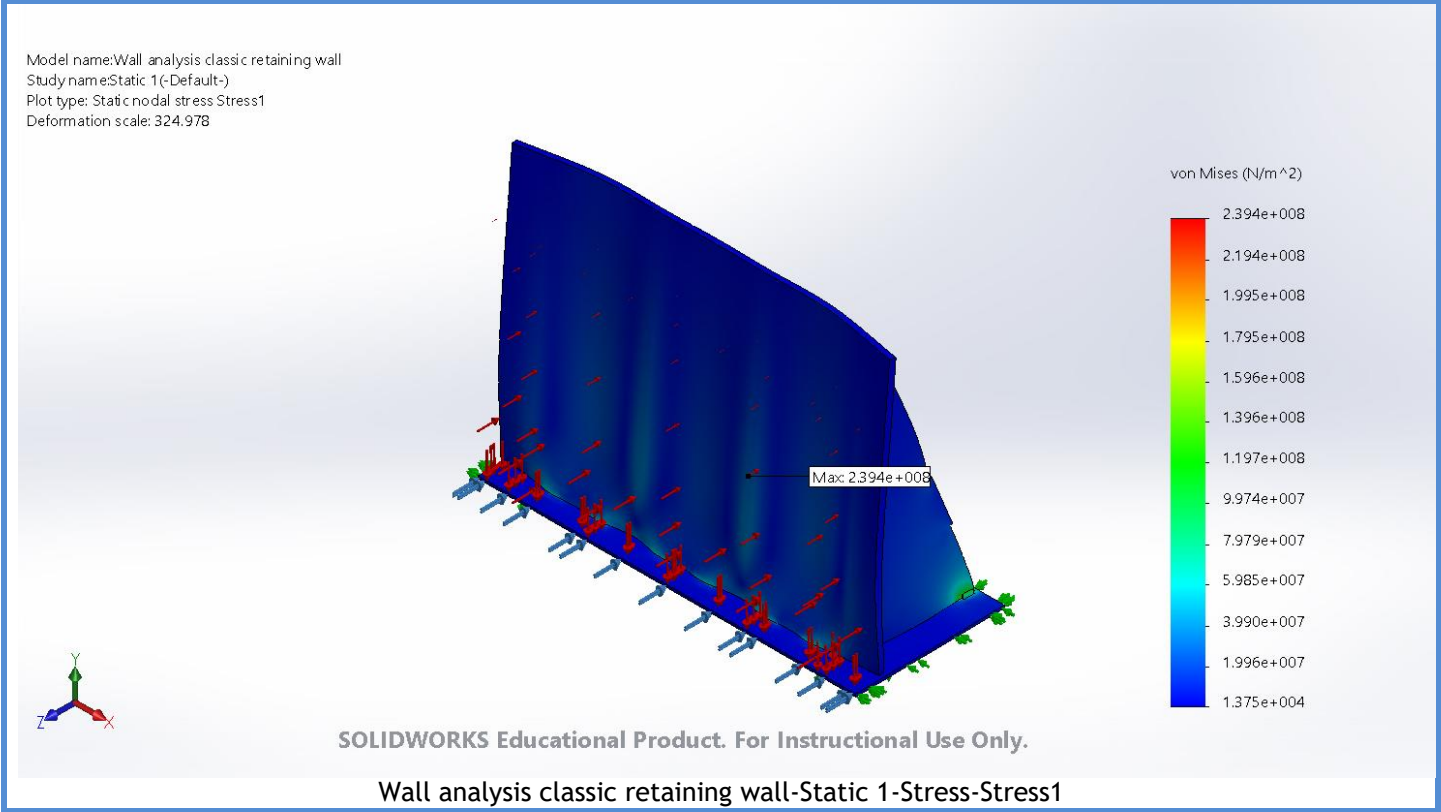
Selection set	Units	Sum X	Sum Y	Sum Z	Resultant
Entire Model	N.m	0	0	0	0

Beams

No Data

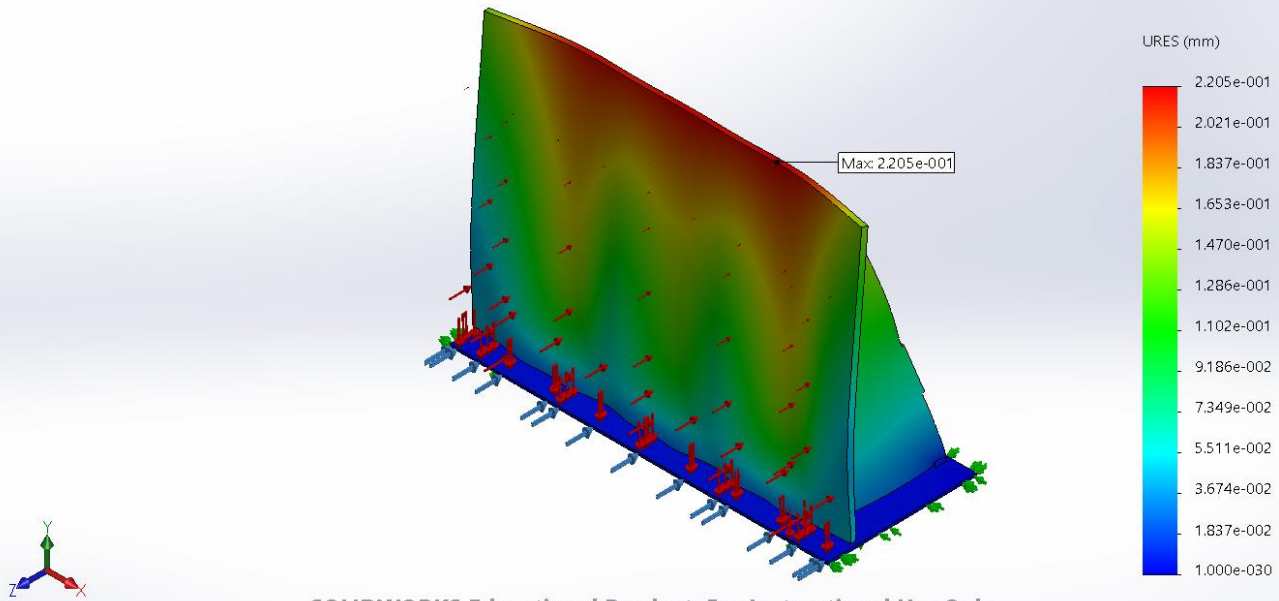
Study Results

Name	Type	Min	Max
Stress1	VON: von Mises Stress	1.375e+004N/m^2 Node: 52297	2.394e+008N/m^2 Node: 48089



Name	Type	Min	Max
Displacement1	URES: Resultant Displacement	0.000e+000mm Node: 6762	2.205e-001mm Node: 69607

Model name: Wall analysis classic retaining wall
 Study name: Static 1 (-Default-)
 Plot type: Static displacement Displacement1
 Deformation scale: 324.978

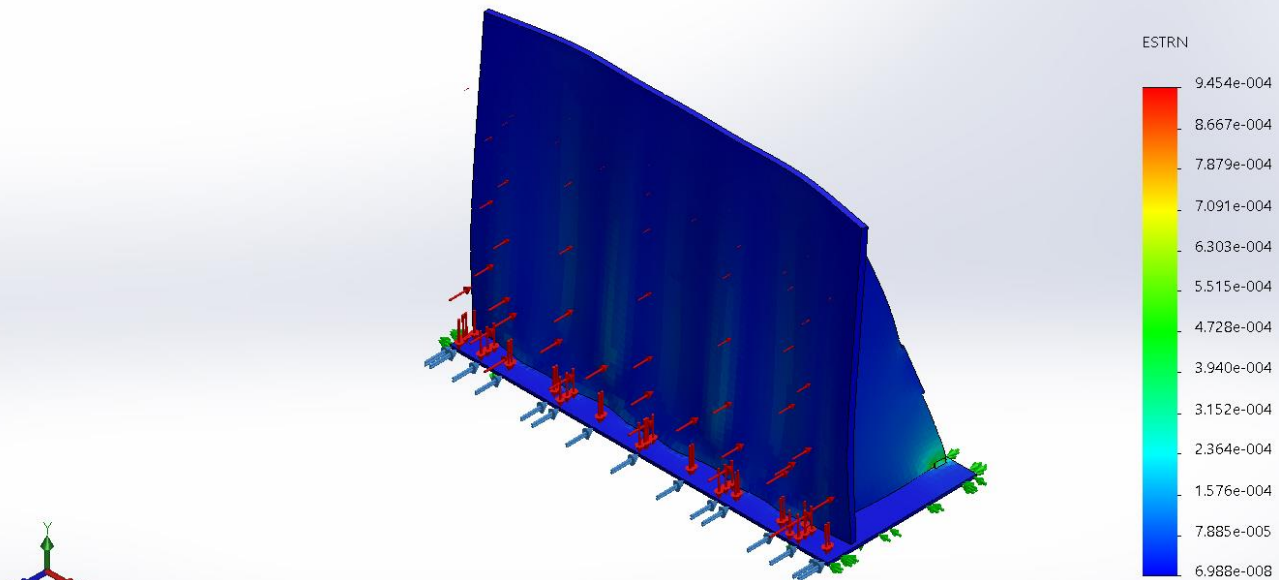


SOLIDWORKS Educational Product. For Instructional Use Only.

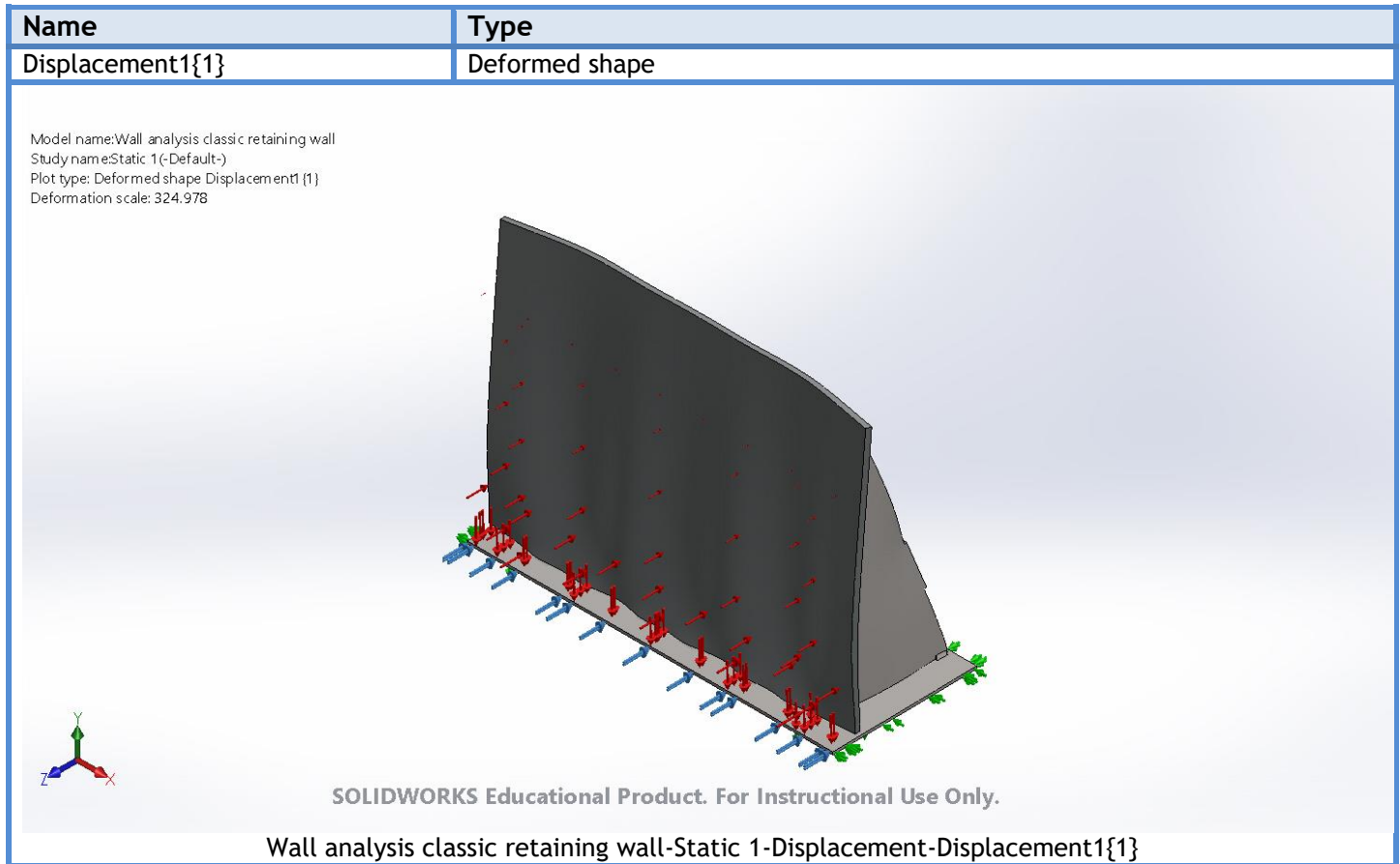
Wall analysis classic retaining wall-Static 1-Displacement-Displacement1

Name	Type	Min	Max
Strain1	ESTRN: Equivalent Strain	6.988e-008 Element: 37326	9.454e-004 Element: 18660

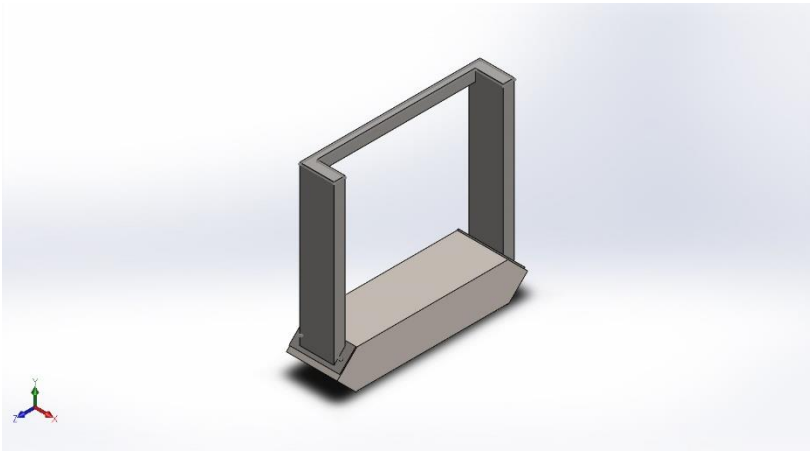
Model name: Wall analysis classic retaining wall
 Study name: Static 1 (-Default-)
 Plot type: Static strain Strain1
 Deformation scale: 324.978



SOLIDWORKS Educational Product. For Instructional Use Only.



Conclusion



Description
No Data

APPENDIX B.2: Simulation of Camera Mount Bolts

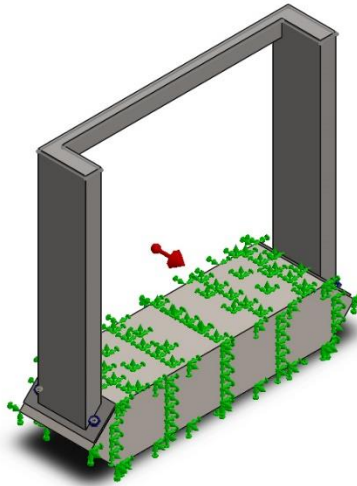
Date: Tuesday, October 2, 2018
Designer: Solidworks
Study name: Static 1
Analysis type: Static

Table of Contents

Description.....	1
Assumptions	2
Model Information	2
Study Properties	3
Units	3
Material Properties	4
Loads and Fixtures.....	5
Connector Definitions.....	6
Contact Information.....	7
Mesh information	8
Sensor Details	9
Resultant Forces	9
Beams.....	9
Study Results	10
Conclusion	13

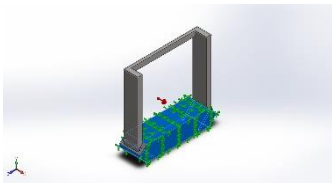

Assumptions

Model Information



Model name: Bolt analysis hole wizard
Current Configuration: Default

Solid Bodies

Document Name and Reference	Treated As	Volumetric Properties	Document Path/Date Modified
Boss-Extrude5 	Solid Body	Mass:155.466 kg Volume:0.0201904 m ³ Density:7700 kg/m ³ Weight:1523.57 N	C:\Users\danie\Documents\SOLIDWORKS files\base no holes.SLDPRT Oct 02 11:22:24 2018
Boss-Extrude4 	Solid Body	Mass:27.5133 kg Volume:0.00352734 m ³ Density:7800 kg/m ³ Weight:269.63 N	C:\Users\danie\Documents\SOLIDWORKS files\camera mount no holes.SLDPRT Oct 02 14:11:16 2018



Study Properties

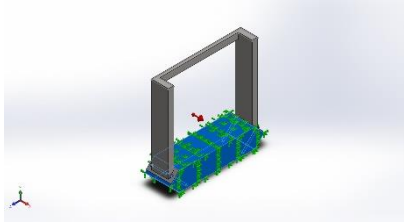
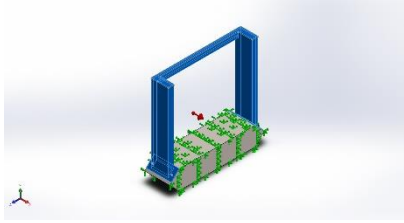
Study name	Static 1
Analysis type	Static
Mesh type	Solid Mesh
Thermal Effect:	On
Thermal option	Include temperature loads
Zero strain temperature	298 Kelvin
Include fluid pressure effects from SOLIDWORKS Flow Simulation	Off
Solver type	FFEPlus
Inplane Effect:	Off
Soft Spring:	Off
Inertial Relief:	Off
Incompatible bonding options	Automatic
Large displacement	Off
Compute free body forces	On
Friction	Off
Use Adaptive Method:	Off
Result folder	SOLIDWORKS document (C:\Users\danie\Documents\SOLIDWORKS files)

Units

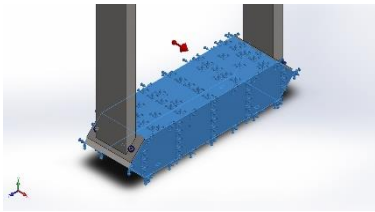
Unit system:	SI (MKS)
Length/Displacement	mm
Temperature	Kelvin
Angular velocity	Rad/sec
Pressure/Stress	N/m ²

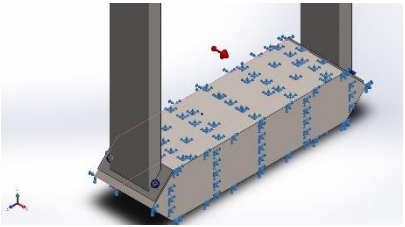


Material Properties

Model Reference	Properties	Components
	Name: S355 Steel Model type: Linear Elastic Isotropic Default failure criterion: Max von Mises Stress Yield strength: 3.55e+008 N/m ² Tensile strength: 4.70e+008 N/m ² Elastic modulus: 2.1e+011 N/m ² Poisson's ratio: 0.28 Mass density: 7700 kg/m ³ Shear modulus: 7.9e+010 N/m ² Thermal expansion coefficient: 1.3e-005 /Kelvin	SolidBody 1(Boss-Extrude5)(base no holes-1)
Curve Data:N/A		
	Name: SE355 steel Model type: Linear Elastic Isotropic Default failure criterion: Max von Mises Stress Yield strength: 3.55+008 N/m ² Tensile strength: 4.70e+008 N/m ² Elastic modulus: 2.1e+011 N/m ² Poisson's ratio: 0.28 Mass density: 7800 kg/m ³ Shear modulus: 7.9e+010 N/m ² Thermal expansion coefficient: 1.3e-005 /Kelvin	SolidBody 1(Boss-Extrude4)(camera mount no holes-1)
Curve Data:N/A		

Loads and Fixtures

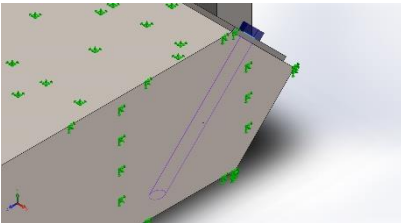
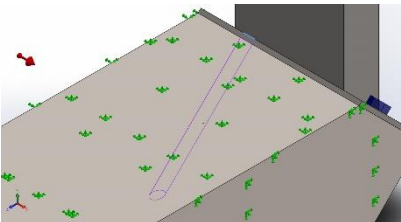
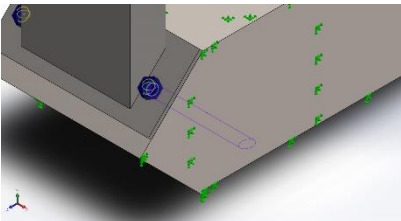
Fixture name	Fixture Image	Fixture Details			
Fixed-1		Entities: 4 face(s) Type: Fixed Geometry			
Resultant Forces					
Components	X	Y	Z	Resultant	
Reaction force(N)	-179505	1.20264	-8.81079	179505	
Reaction Moment(N.m)	0	0	0	0	

Load name	Load Image	Load Details
Gravity-1		Reference: Face< 1 > Values: 0 0 -981 Units: m/s^2



Connector Definitions

Pin/Bolt/Bearing Connector

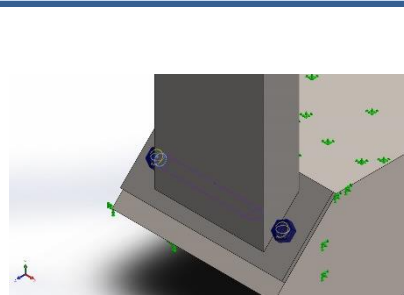
Model Reference	Connector Details	Strength Details		
 Counterbore Screw-1	Entities: 1 edge(s), 1 face(s) Type: Bolt(Head/Nut diameter)(Count erbore screw) Head diameter: 18 mm Nominal shank diameter: 12 Preload (Torque): 70 Young's modulus: 2.1e+011 Poisson's ratio: 0.28 Preload units: N.m	No Data		
Connector Forces				
Type	X-Component	Y-Component	Z-Component	Resultant
Axial Force (N)	0	16772	-16772	23720
Shear Force (N)	2349.6	-1982.5	-1982.5	3658
Bending moment (N.m)	112.37	67.269	67.269	147.23
 Counterbore Screw-2	Entities: 1 edge(s), 1 face(s) Type: Bolt(Head/Nut diameter)(Count erbore screw) Head diameter: 18 mm Nominal shank diameter: 12 Preload (Torque): 70 Young's modulus: 2.1e+011 Poisson's ratio: 0.28 Preload units: N.m	No Data		
Connector Forces				
Type	X-Component	Y-Component	Z-Component	Resultant
Axial Force (N)	0	25851	-25851	36560
Shear Force (N)	2829.8	9545.8	9545.8	13793
Bending moment (N.m)	-534.16	85.885	85.885	547.8
	Entities: 1 edge(s), 1 face(s) Type: Bolt(Head/Nut diameter)(Count erbore screw) Head diameter: 18 mm Nominal shank diameter: 12	No Data		



Counterbore Screw-3	Preload (Torque): 70 Young's modulus: 2.1e+011 Poisson's ratio: 0.28 Preload units: N.m	
---------------------	--	--

Connector Forces

Type	X-Component	Y-Component	Z-Component	Resultant
Axial Force (N)	0	16851	16851	23832
Shear Force (N)	2323	-1845.6	1845.6	3494
Bending moment (N.m)	-105.87	-67.071	67.071	142.15



Counterbore Screw-4

Entities: 1 edge(s), 1 face(s)
Type: Bolt(Head/Nut diameter)(Counterbore screw)
Head diameter: 18 mm
Nominal shank diameter: 12
Preload (Torque): 70
Young's modulus: 2.1e+011
Poisson's ratio: 0.28
Preload units: N.m

No Data

Connector Forces

Type	X-Component	Y-Component	Z-Component	Resultant
Axial Force (N)	0	25043	25043	35416
Shear Force (N)	2884.5	9530.9	-9530.9	13784
Bending moment (N.m)	541.29	-88.945	88.945	555.71

Contact Information

Contact	Contact Image	Contact Properties
Global Contact		Type: No penetration (Surface to surface) Components: 1 component(s) Friction Value: 0.5



Mesh information

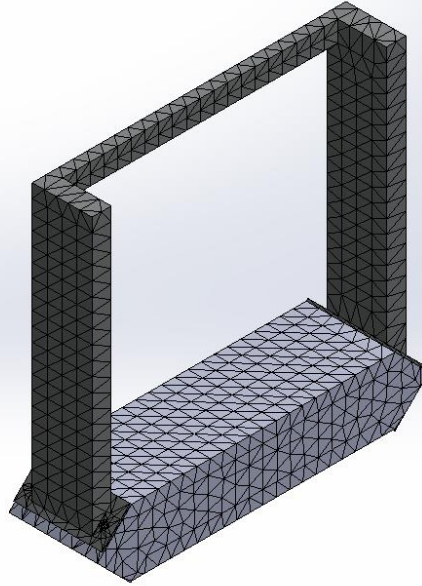
Mesh type	Solid Mesh
Mesher Used:	Standard mesh
Automatic Transition:	Off
Include Mesh Auto Loops:	Off
Jacobian points	4 Points
Element Size	31.2351 mm
Tolerance	1.56175 mm
Mesh Quality Plot	High
Remesh failed parts with incompatible mesh	Off

Mesh information - Details

Total Nodes	20201
Total Elements	11700
Maximum Aspect Ratio	25.203
% of elements with Aspect Ratio < 3	64.3
% of elements with Aspect Ratio > 10	0.299
% of distorted elements(Jacobian)	0
Time to complete mesh(hh:mm:ss):	00:00:02
Computer name:	



Model name: Bolt analysis hole wizard
 Study name: Static 1 (-Default-)
 Mesh type: Solid Mesh



SOLIDWORKS Educational Product. For Instructional Use Only.

Sensor Details

No Data

Resultant Forces

Reaction forces

Selection set	Units	Sum X	Sum Y	Sum Z	Resultant
Entire Model	N	-179505	1.20264	-8.81079	179505

Reaction Moments

Selection set	Units	Sum X	Sum Y	Sum Z	Resultant
Entire Model	N.m	0	0	0	0

Beams

No Data



SOLIDWORKS

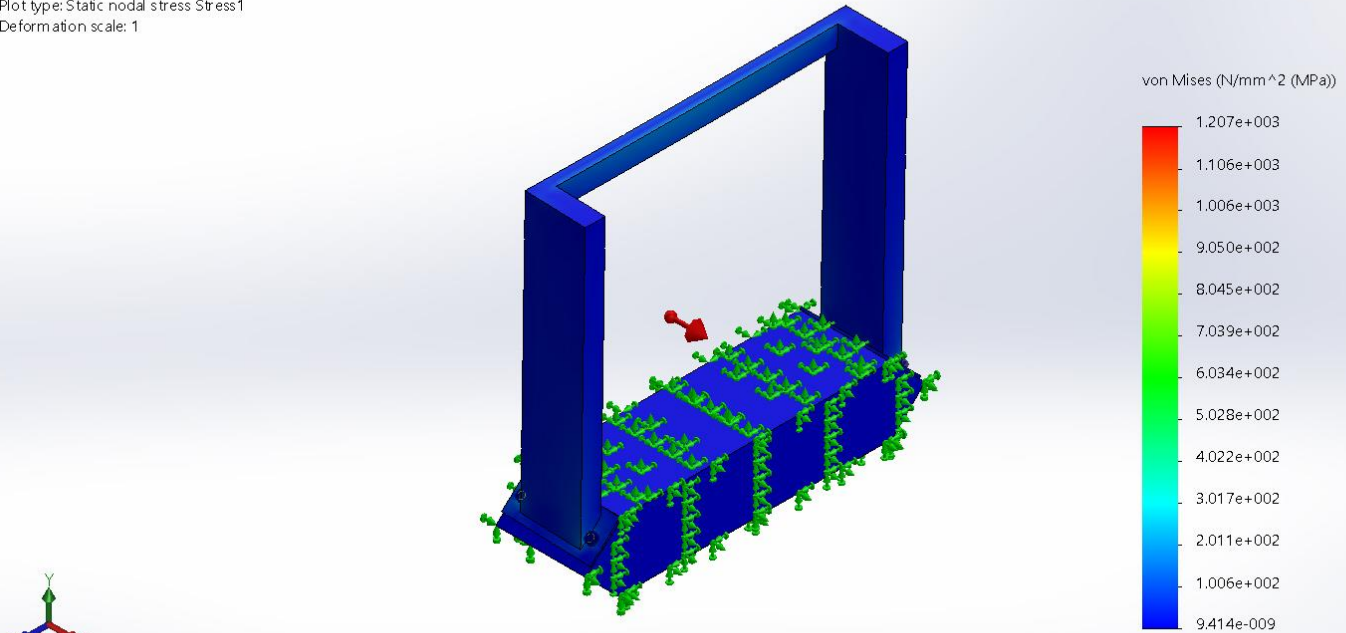
Analyzed with SOLIDWORKS Simulation

Simulation of Bolt analysis hole wizard

Study Results

Name	Type	Min	Max
Stress1	VON: von Mises Stress	9.414e-009N/mm ² (MPa) Node: 10425	1.207e+003N/mm ² (MPa) Node: 19933

Model name: Bolt analysis hole wizard
Study name: Static 1 (-Default-)
Plot type: Static nodal stress Stress1
Deformation scale: 1



SOLIDWORKS Educational Product. For Instructional Use Only.

Bolt analysis hole wizard-Static 1-Stress-Stress1

Name	Type	Min	Max
Displacement1	URES: Resultant Displacement	0.000e+000mm Node: 1	1.543e+001mm Node: 17686

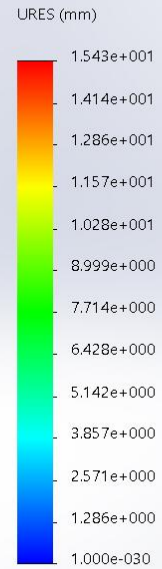
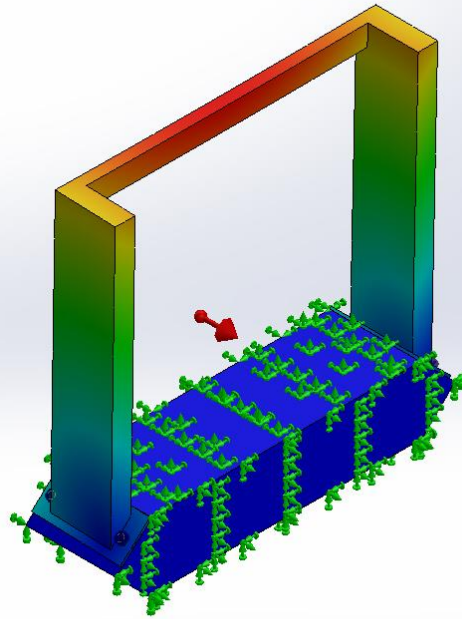


SOLIDWORKS

Analyzed with SOLIDWORKS Simulation

Simulation of Bolt analysis hole wizard

Model name: Bolt analysis hole wizard
 Study name: Static 1 (-Default-)
 Plot type: Static displacement Displacement1
 Deformation scale: 1



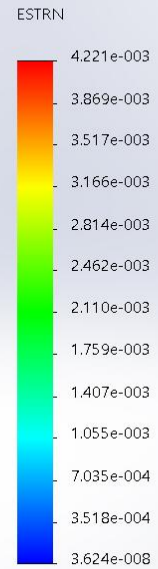
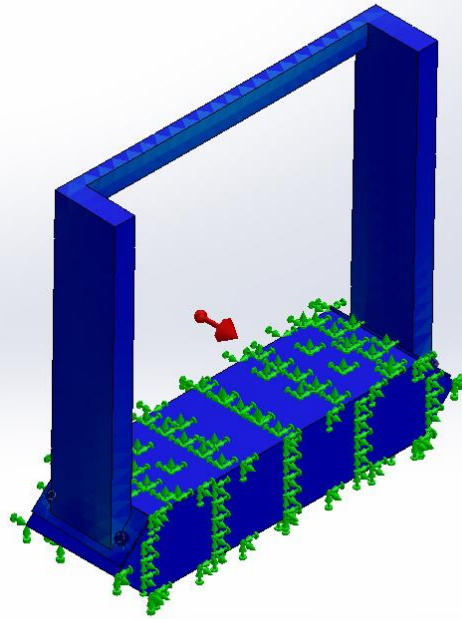
SOLIDWORKS Educational Product. For Instructional Use Only.

Bolt analysis hole wizard-Static 1-Displacement-Displacement1

Name	Type	Min	Max
Strain1	ESTRN: Equivalent Strain	3.624e-008 Element: 1745	4.221e-003 Element: 10137



Model name: Bolt analysis hole wizard
 Study name: Static 1 (-Default-)
 Plot type: Static strain Strain1
 Deformation scale: 1

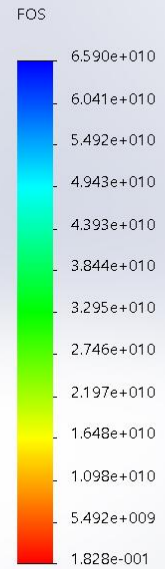
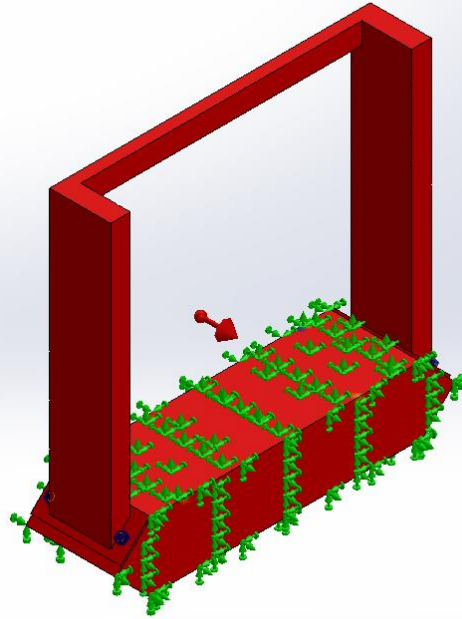


SOLIDWORKS Educational Product. For Instructional Use Only.

Bolt analysis hole wizard-Static 1-Strain-Strain1

Name	Type	Min	Max
Factor of Safety1	Automatic	1.828e-001 Node: 19933	6.590e+010 Node: 10425

Model name: Bolt analysis hole wizard
Study name: Static 1 (-Default-)
Plot type: Factor of Safety Factor of Safety1
Criterion: Automatic
Factor of safety distribution: Min FOS = 0.18



SOLIDWORKS Educational Product. For Instructional Use Only.

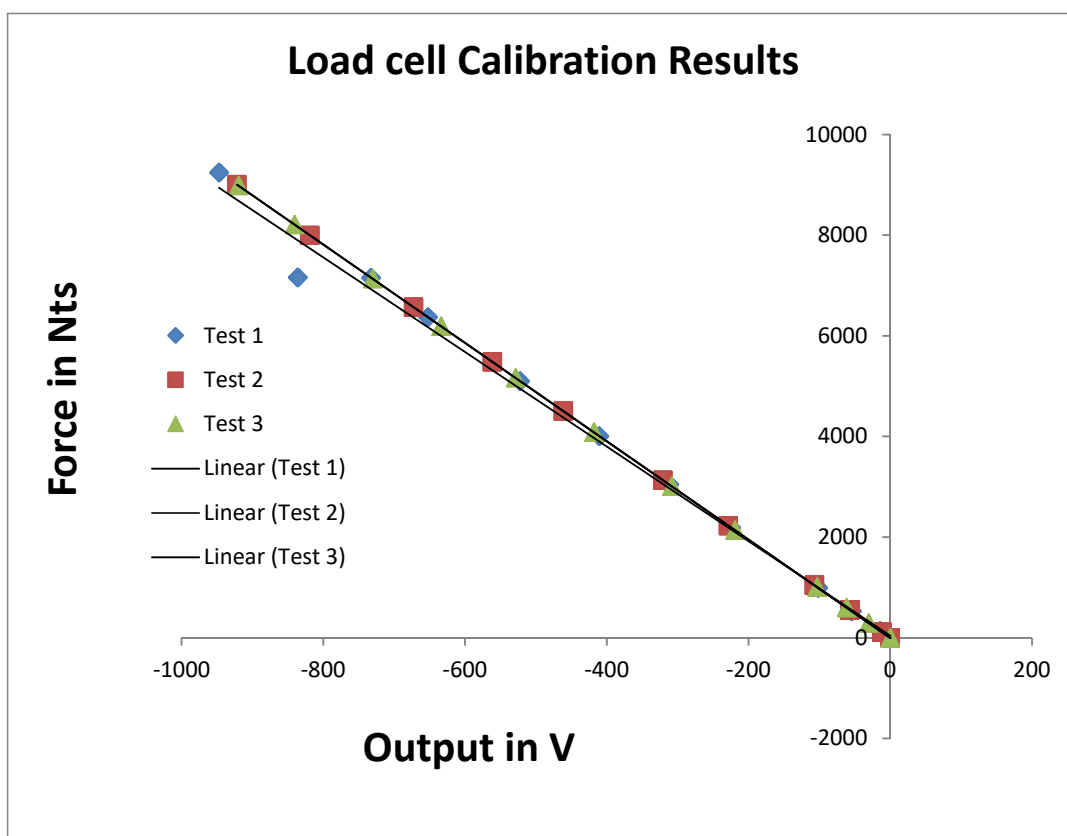
Bolt analysis hole wizard-Static 1-Factor of Safety-Factor of Safety1

Conclusion

Calibration of Philips PR 6246/13 C3

Date:	25-02-19
Person:	FJÆSTAD
Transducer:	Philips PR 6246/13 C3
Type:	
Serial number:	1300083
Output unit	Nt
Temperature	20°C
Range (Min/Max)	0/-10kN
Accuracy of resolution	+/-0.3mV
Reference instrument:	SN7853
Resolution of reference	1Nt
Voltage supply	5
Reference unit	V
Calibration interval	

Calibration result (Unit = a * Voltage + b)				
Test	1	2	3	All data
Calibration constant, a, [Nt/V]	-9.3977	-9.7659	-9.7694	-9.5818
Calibration constant, b, [Nt]	41.6152	0.7206	-0.6325	13.9011
Constant of regression	0.9942	1.0000	1.0000	0.9971



Data

Test 1		Test 2		Test 3	
# data	68		59		51
Unit	Voltage	Unit	Voltage	Unit	Voltage
Nt	V	Nt	V	Nt	V
0	-1.451E-01	0	-5.932E-02	0	-8.586E-02
0	-3.557E-02	0	-7.995E-02	0	-4.210E-02
0	-1.759E-02	0	9.227E-02	0	-8.351E-03
0	-1.032E-02	0	1.107E-01	0	-1.219E-02
0	-5.950E-02	0	1.098E-01	0	-6.220E-02
0	-5.387E-02	0	4.321E-03	296	-3.039E+01
0	-1.300E-01	0	-1.773E-03	296	-3.034E+01
0	-4.453E-02	0	6.102E-02	296	-3.038E+01
0	-5.515E-02	0	6.879E-02	603	-6.162E+01
0	7.374E-02	112	-1.132E+01	603	-6.185E+01
0	-8.038E-03	112	-1.151E+01	603	-6.184E+01
0	-6.036E-02	112	-1.147E+01	603	-6.180E+01
0	1.107E-01	112	-1.155E+01	603	-6.182E+01
0	-2.941E-02	112	-1.154E+01	1010	-1.034E+02
0	-8.551E-02	112	-1.138E+01	1010	-1.034E+02
138	-1.424E+01	558	-5.703E+01	1010	-1.034E+02
138	-1.417E+01	558	-5.702E+01	1010	-1.034E+02
138	-1.408E+01	558	-5.699E+01	2140	-2.193E+02
138	-1.415E+01	558	-5.696E+01	2140	-2.192E+02
138	-1.424E+01	558	-5.696E+01	2140	-2.190E+02
531	-5.448E+01	558	-5.695E+01	2140	-2.190E+02
531	-5.443E+01	558	-5.712E+01	3010	-3.082E+02
531	-5.448E+01	558	-5.698E+01	3010	-3.081E+02
531	-5.441E+01	558	-5.702E+01	3010	-3.082E+02
531	-5.445E+01	558	-5.704E+01	3010	-3.081E+02
531	-5.434E+01	558	-5.713E+01	3010	-3.082E+02
531	-5.446E+01	1045	-1.068E+02	4085	-4.182E+02
995	-1.020E+02	1045	-1.070E+02	4085	-4.181E+02
995	-1.019E+02	1045	-1.071E+02	4085	-4.181E+02
995	-1.018E+02	1045	-1.070E+02	4085	-4.182E+02
995	-1.020E+02	1045	-1.069E+02	5165	-5.288E+02
995	-1.019E+02	1045	-1.070E+02	5165	-5.288E+02
995	-1.019E+02	2232	-2.284E+02	5165	-5.290E+02
2194	-2.246E+02	2232	-2.283E+02	6190	-6.338E+02
2194	-2.246E+02	2232	-2.285E+02	6190	-6.339E+02
2194	-2.245E+02	2232	-2.284E+02	6190	-6.338E+02
2194	-2.246E+02	3135	-3.209E+02	6190	-6.339E+02
2194	-2.246E+02	3135	-3.209E+02	6190	-6.338E+02
3048	-3.120E+02	3135	-3.210E+02	7135	-7.305E+02
3048	-3.120E+02	3135	-3.209E+02	7135	-7.305E+02
3048	-3.121E+02	4505	-4.611E+02	7135	-7.306E+02
4011	-4.107E+02	4505	-4.612E+02	7135	-7.305E+02
4011	-4.107E+02	4505	-4.610E+02	8213	-8.407E+02
4011	-4.106E+02	4505	-4.612E+02	8213	-8.408E+02

4011	-4.106E+02	4505	-4.612E+02	8213	-8.408E+02
4011	-4.107E+02	5484	-5.615E+02	8213	-8.408E+02
5103	-5.225E+02	5484	-5.615E+02	8985	-9.197E+02
5103	-5.225E+02	5484	-5.613E+02	8985	-9.196E+02
5103	-5.224E+02	5484	-5.615E+02	8985	-9.195E+02
5103	-5.225E+02	6570	-6.727E+02	8985	-9.194E+02
5103	-5.226E+02	6570	-6.728E+02	8985	-9.197E+02
6371	-6.524E+02	6570	-6.727E+02		
6371	-6.523E+02	6570	-6.727E+02		
6371	-6.523E+02	7997	-8.189E+02		
6371	-6.524E+02	7997	-8.189E+02		
7157	-7.329E+02	7997	-8.188E+02		
7157	-7.329E+02	9005	-9.220E+02		
7157	-7.328E+02	9005	-9.220E+02		
7157	-7.330E+02	9005	-9.220E+02		
7164	-8.362E+02				
7164	-8.361E+02				
7164	-8.361E+02				
7164	-8.362E+02				
7164	-8.361E+02				
9250	-9.472E+02				
9250	-9.472E+02				
9250	-9.471E+02				
9250	-9.472E+02				

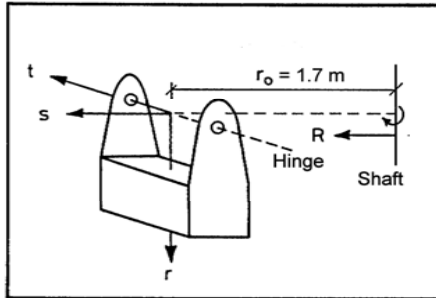
|

APPENDIX D.1 Calculation of centre of gravity

Project:VAZA

Name:Varvara Zania	24-03-2019	Approved: Varvara Zania
Distances in meter and weight in kg.		

Item Choice	Item Number	Items	Remarks	Distance to centre of gravity at hinge			Mass M	Moment		
				r	s	t		r x M	s x M	t x M
◀ ▶	20	Rectangular container with plate	from archive	0.626 m	0.013 m	0.000 m	868.3 kg	543.56 kgm	11.29 kgm	0.00 kgm
◀ ▶	21	Beam for PIV camera	From Solidworks	0.597 m	0.684 m	0.000 m	24.0 kg	14.33 kgm	16.42 kgm	0.00 kgm
◀ ▶	22	Retaining wall	From Solidworks	0.741 m	-0.045 m	0.000 m	46.0 kg	34.09 kgm	-2.07 kgm	0.00 kgm
◀ ▶	23	Motor with mounting plate	From Solidworks	0.130 m	-0.180 m	0.070 m	21.0 kg	2.73 kgm	-3.78 kgm	1.47 kgm
◀ ▶	14	Frequency converter	CTL note	-1.080 m	0.000 m	0.000 m	4.1 kg	-4.41 kgm	0.00 kgm	0.00 kgm
◀ ▶	24	Sand sample in rectangular container	0	0.795 m	0.125 m	0.000 m	89.1 kg	70.83 kgm	11.14 kgm	0.00 kgm
◀ ▶	1	-	-	0.000 m	0.000 m	0.000 m	0.0 kg	0.00 kgm	0.00 kgm	0.00 kgm
◀ ▶	1	-	-	0.000 m	0.000 m	0.000 m	0.0 kg	0.00 kgm	0.00 kgm	0.00 kgm
◀ ▶	1	-	-	0.000 m	0.000 m	0.000 m	0.0 kg	0.00 kgm	0.00 kgm	0.00 kgm
◀ ▶	1	-	-	0.000 m	0.000 m	0.000 m	0.0 kg	0.00 kgm	0.00 kgm	0.00 kgm
◀ ▶	1	-	-	0.000 m	0.000 m	0.000 m	0.0 kg	0.00 kgm	0.00 kgm	0.00 kgm
◀ ▶	1	-	-	0.000 m	0.000 m	0.000 m	0.0 kg	0.00 kgm	0.00 kgm	0.00 kgm
◀ ▶	1	-	-	0.000 m	0.000 m	0.000 m	0.0 kg	0.00 kgm	0.00 kgm	0.00 kgm
◀ ▶	1	-	-	0.000 m	0.000 m	0.000 m	0.0 kg	0.00 kgm	0.00 kgm	0.00 kgm
◀ ▶	1	-	-	0.000 m	0.000 m	0.000 m	0.0 kg	0.00 kgm	0.00 kgm	0.00 kgm



Summed values	r'	s'	t'	Mass	Moment 1	Moment 2	Moment 3
	0.628 m	0.031 m	0.001 m	1052.5 kg	661.1 kgm	32.99 kgm	1.47 kgm

Distance from shaft to hinge 1.700 m

Moment at shaft	Mass (total)	Distance $R_{ip} = r_o + r'$	Moment (total)
	1052.5 kg	2.328	2450.3 kgm

BEMÆRK: Iht "Betjeningsregler for BKF/DIAB centrifuge skal t x M < 30 kg m. Dvs ok her.

Counterweight (steel plates)	
Number of 10.1 mm plates:	27
Moment	2453.6 kgm
Difference (<50 kgm)	3.3 kgm

Useable steel plates	
Number of 30.3 mm plates:	9
Number of 10.1 mm plates:	0

APPENDIX E.1: Total displacement field (large images)

Soil displacements – $z_p/r_0 = 21$

Figure E.1.1/41a-g presents the total displacement field at 27.0 N, 44.1N, 63.8N, 78.5N, 107.9 N, 127.5N and 157.0N.

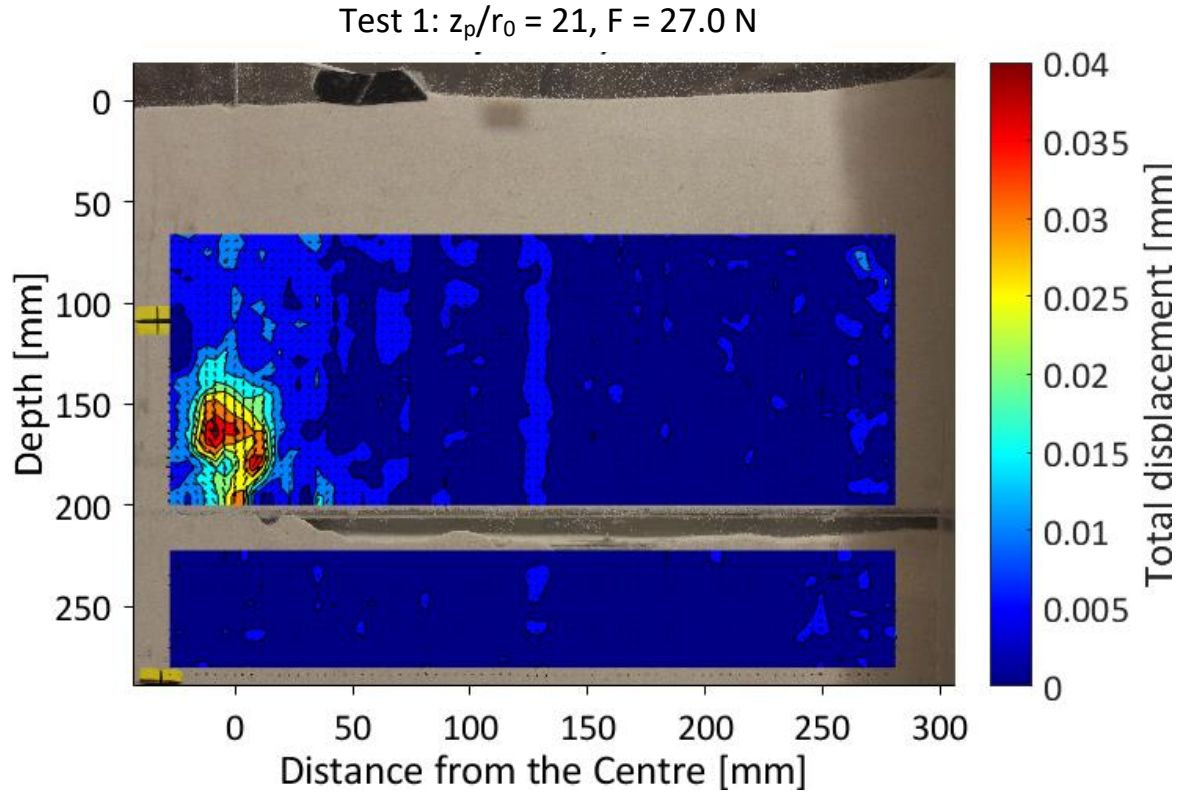


Figure E.1.1/41a: Contour plot of total displacement at 27.0 N

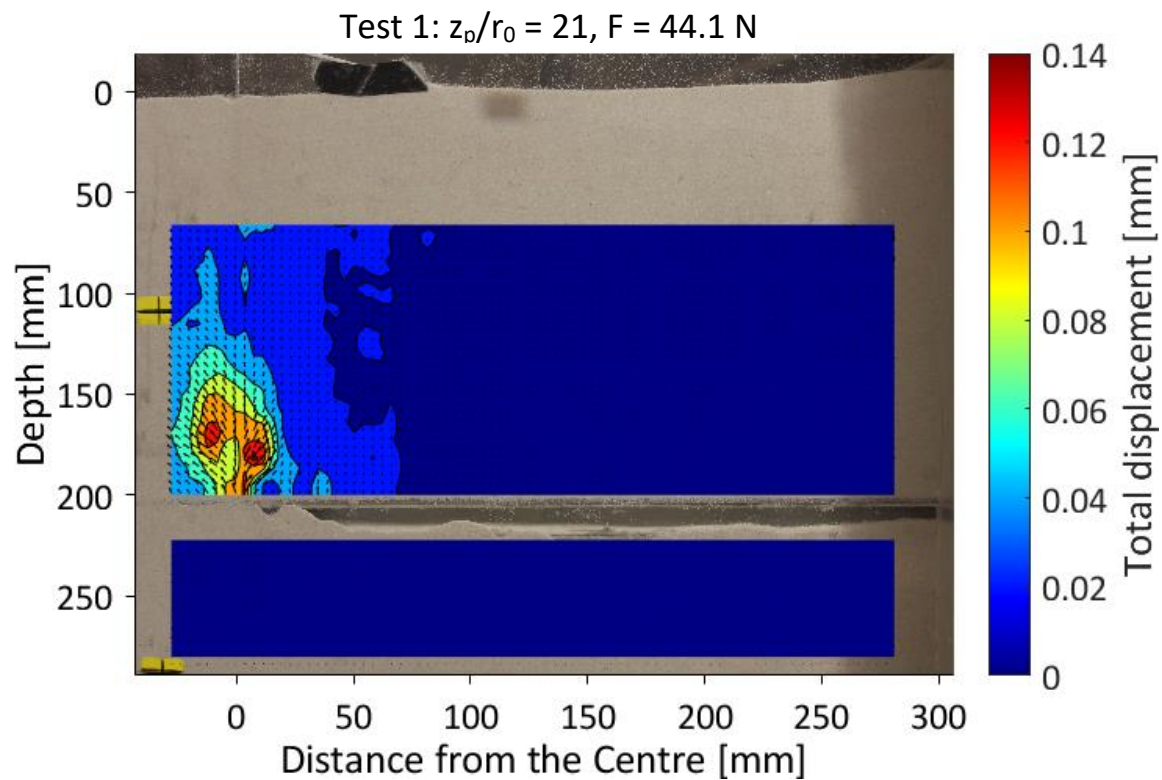


Figure E.1.1/41b: Contour plot of total displacement at 44.1 N

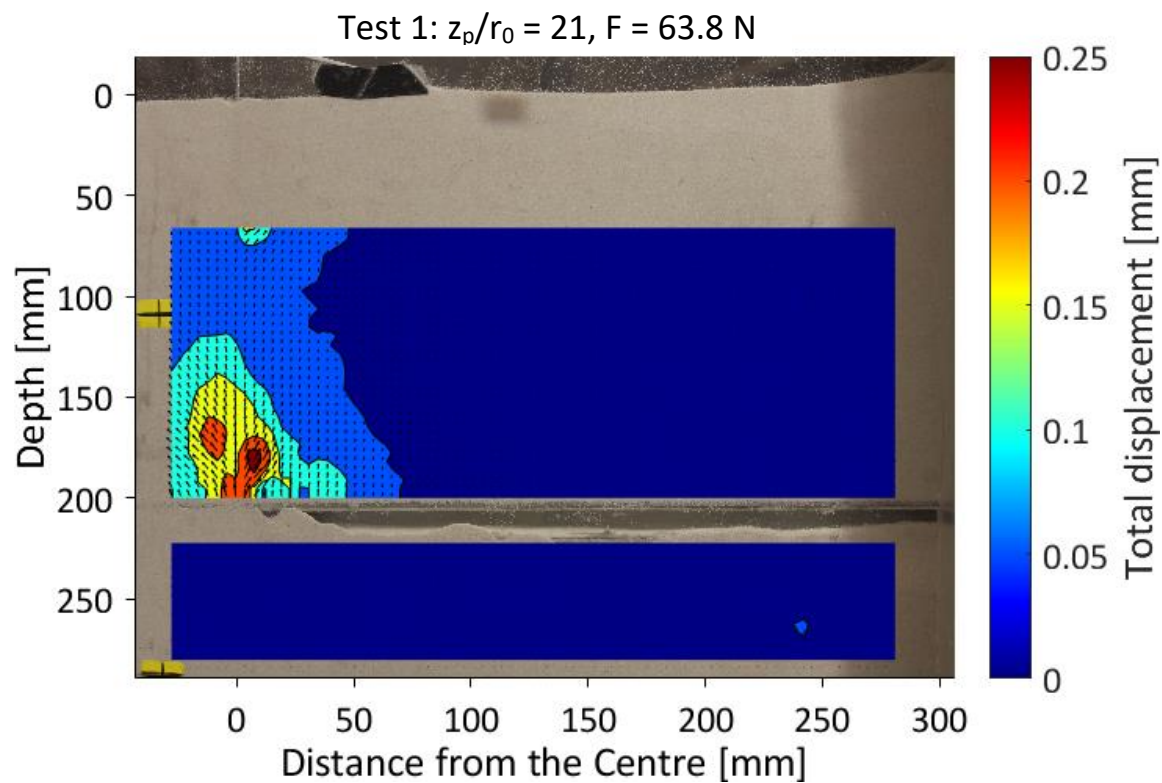


Figure E.1.1/41c: Contour plot of total displacement at 63.8 N

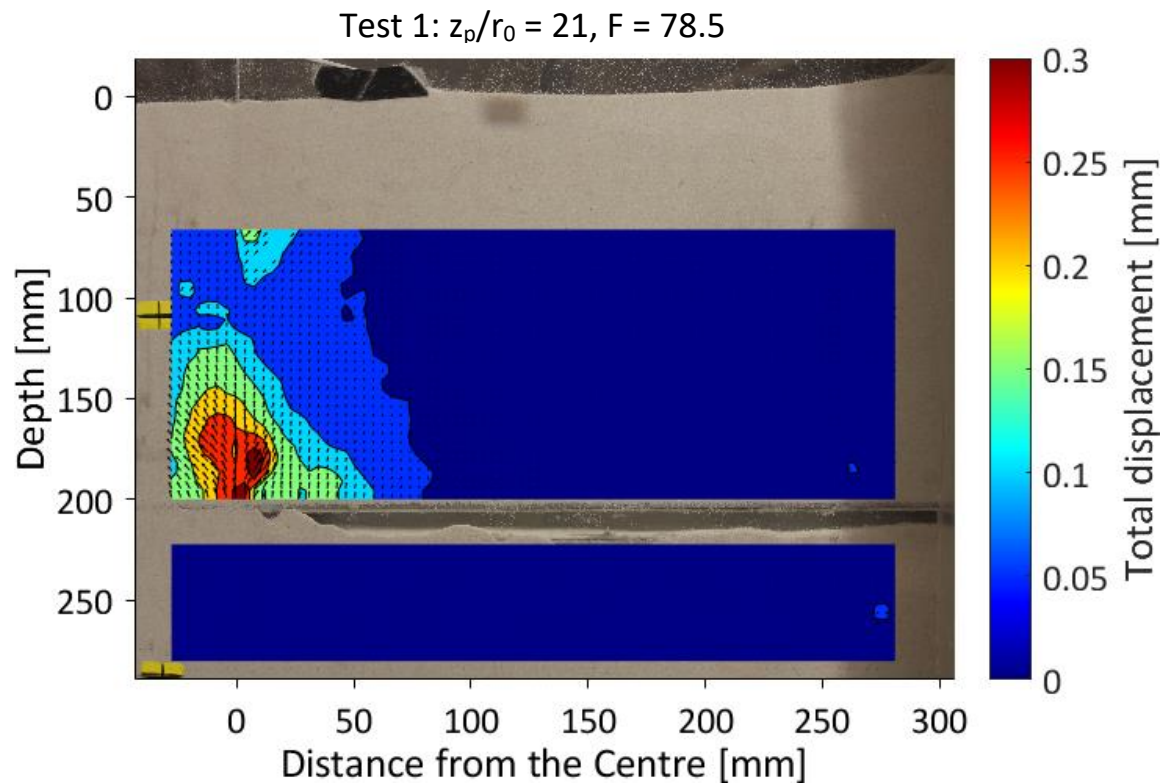


Figure E.1.1/41d: Contour plot of total displacement at 78.5 N (First time loaded to 78.5 N)

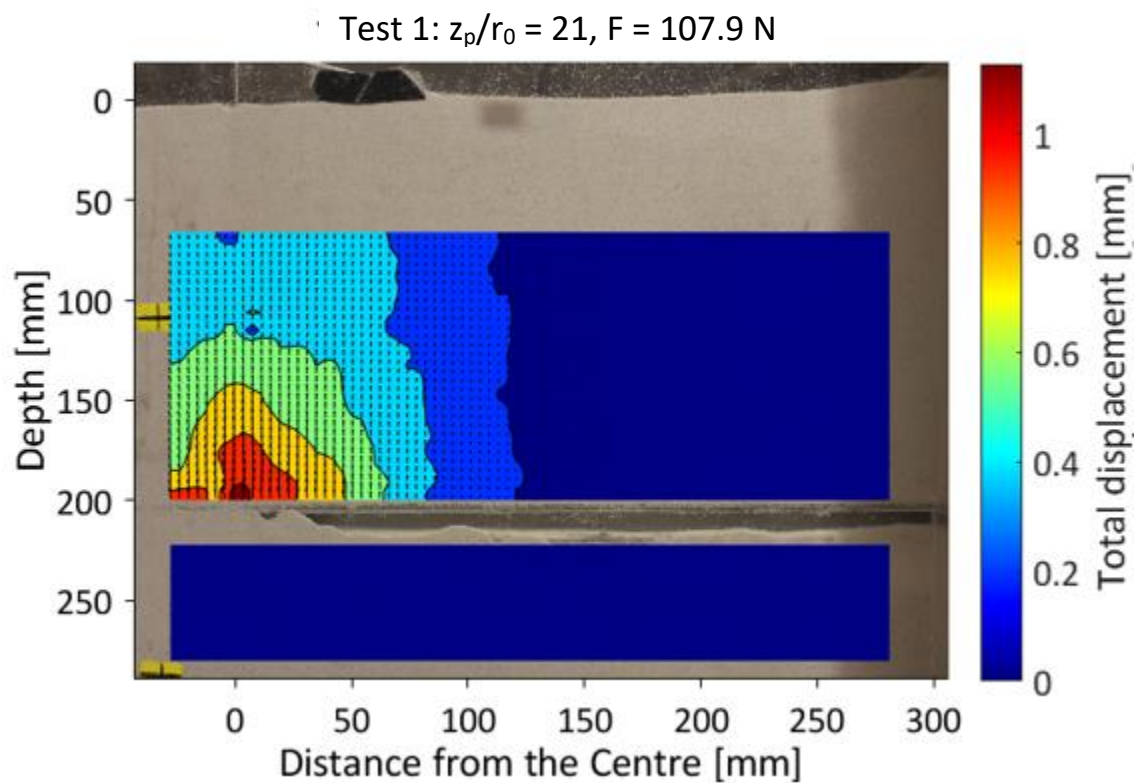


Figure E.1.1/41e: Contour plot of total displacement at 107.9 N

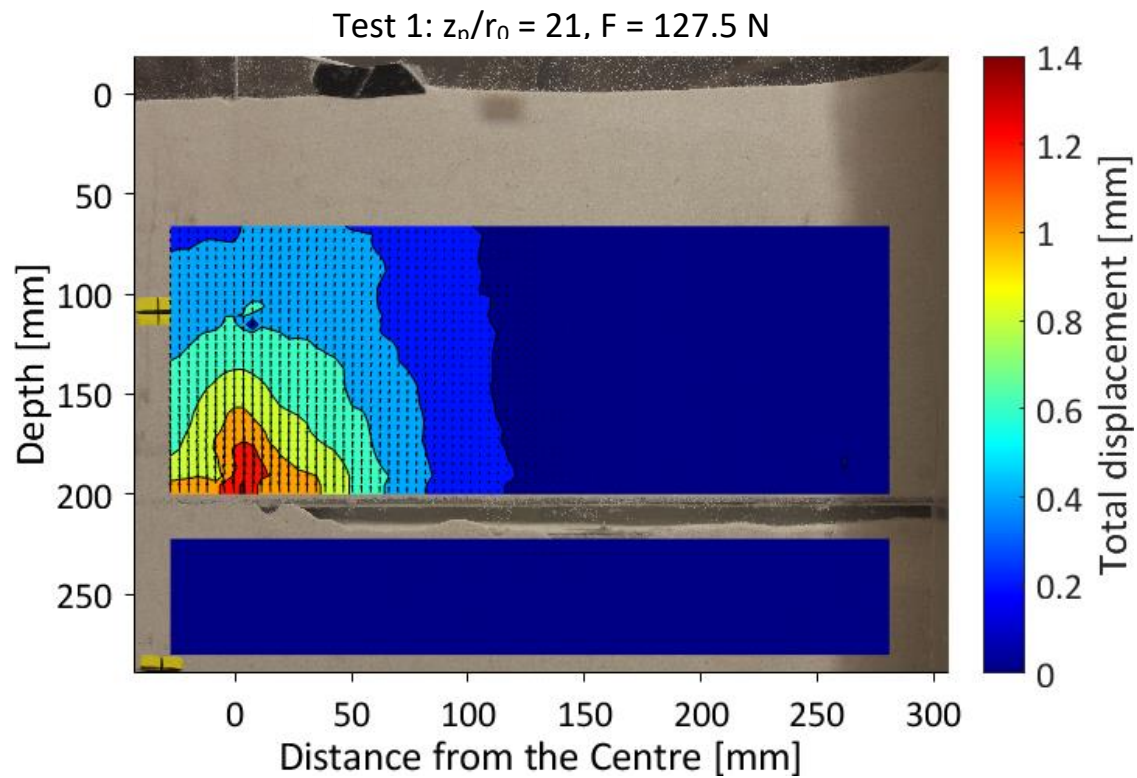


Figure E.1.1/41f: Contour plot of total displacement at 127.5 N

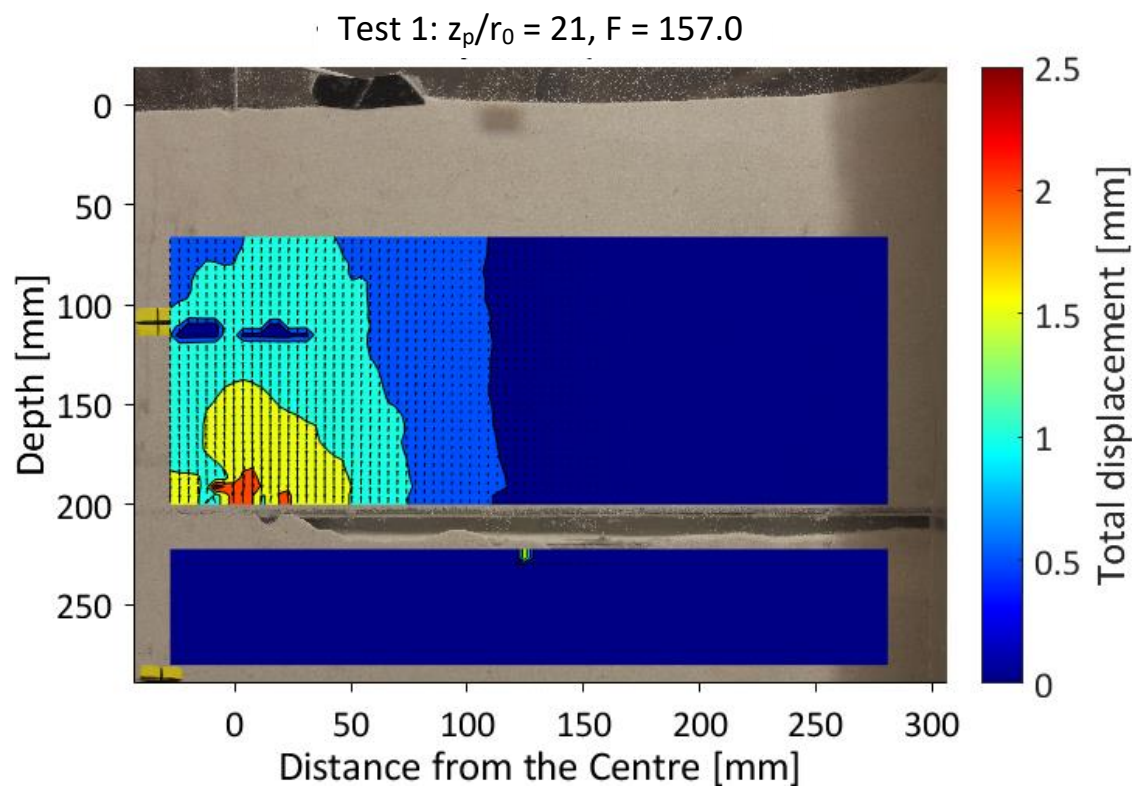


Figure E.1.1/41g: Contour plot of total displacement at 157.0 N

Soil displacements – $z_p/r_0 = 12$

Figure E.1.2/42 presents the total displacement field at 9.8 N, 19.6 N, 29.4 N, 43.2 N, 62.9 N and 82.5 N.

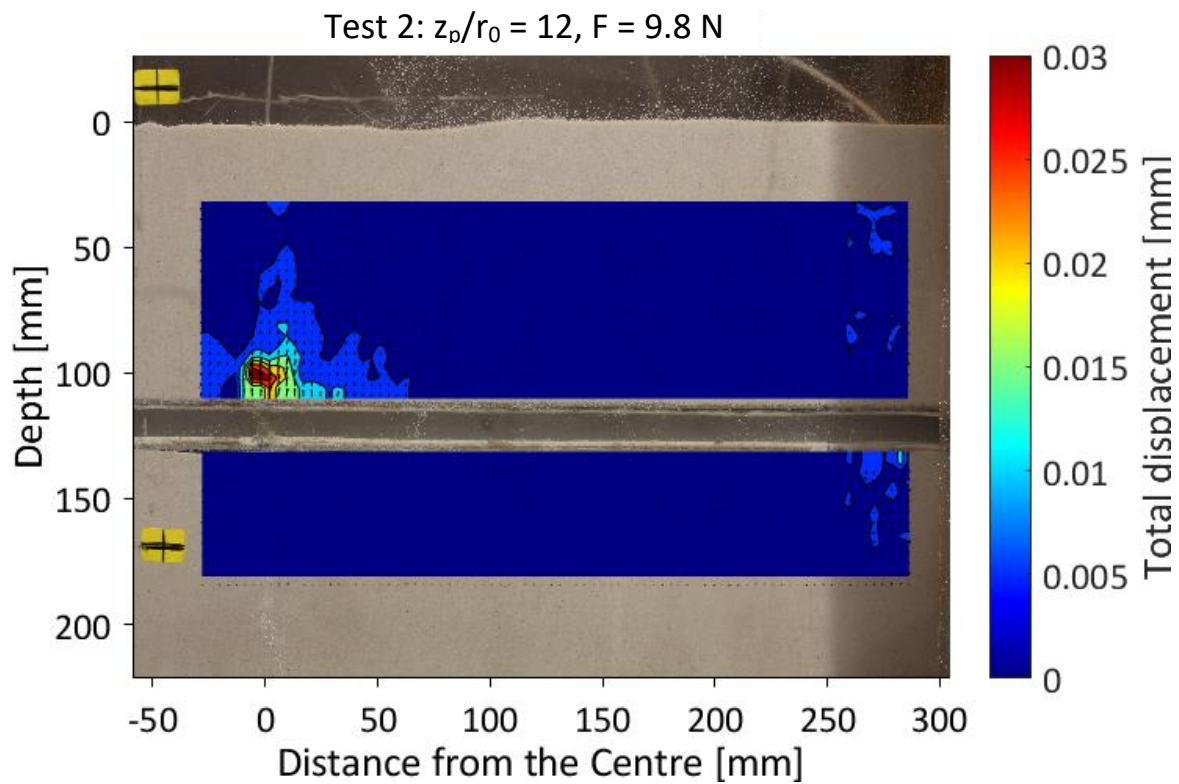


Figure E.1.2/42a: Contour plot of total displacement at 9.8 N (First time loaded to 9.8 N)

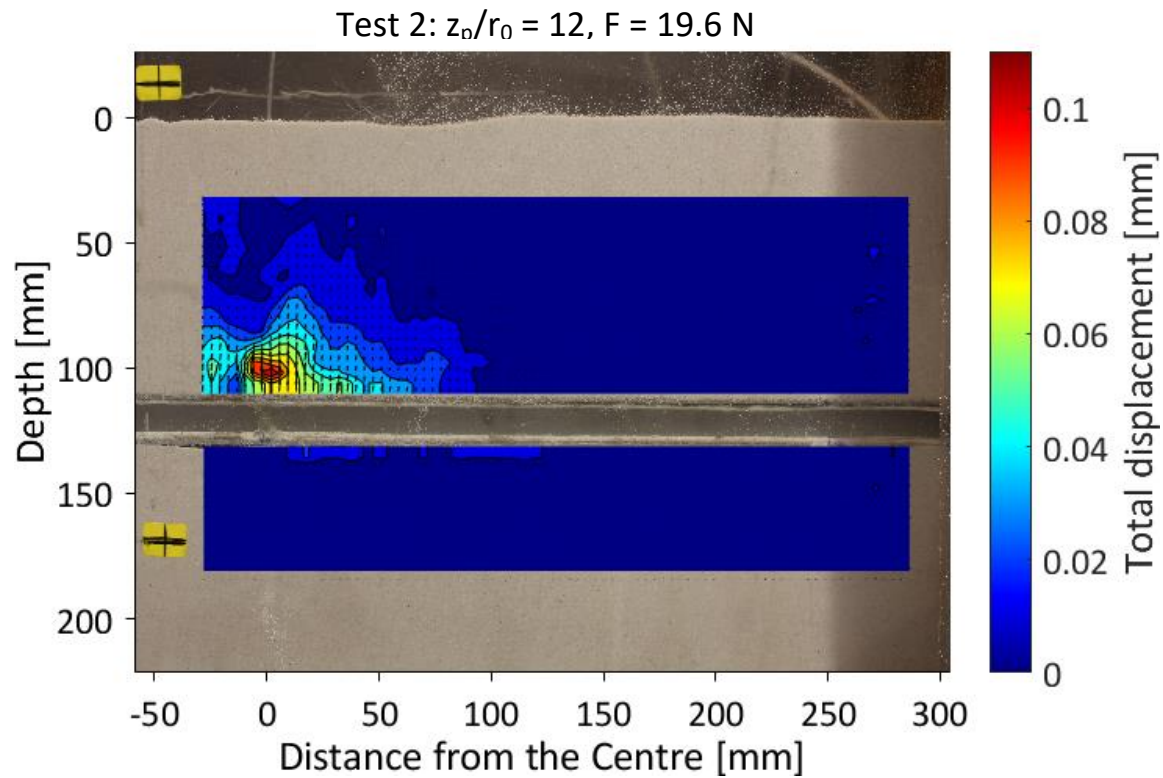


Figure E.1.2/42b: Contour plot of total displacement at 19.6 N (First time loaded to 19.6 N)

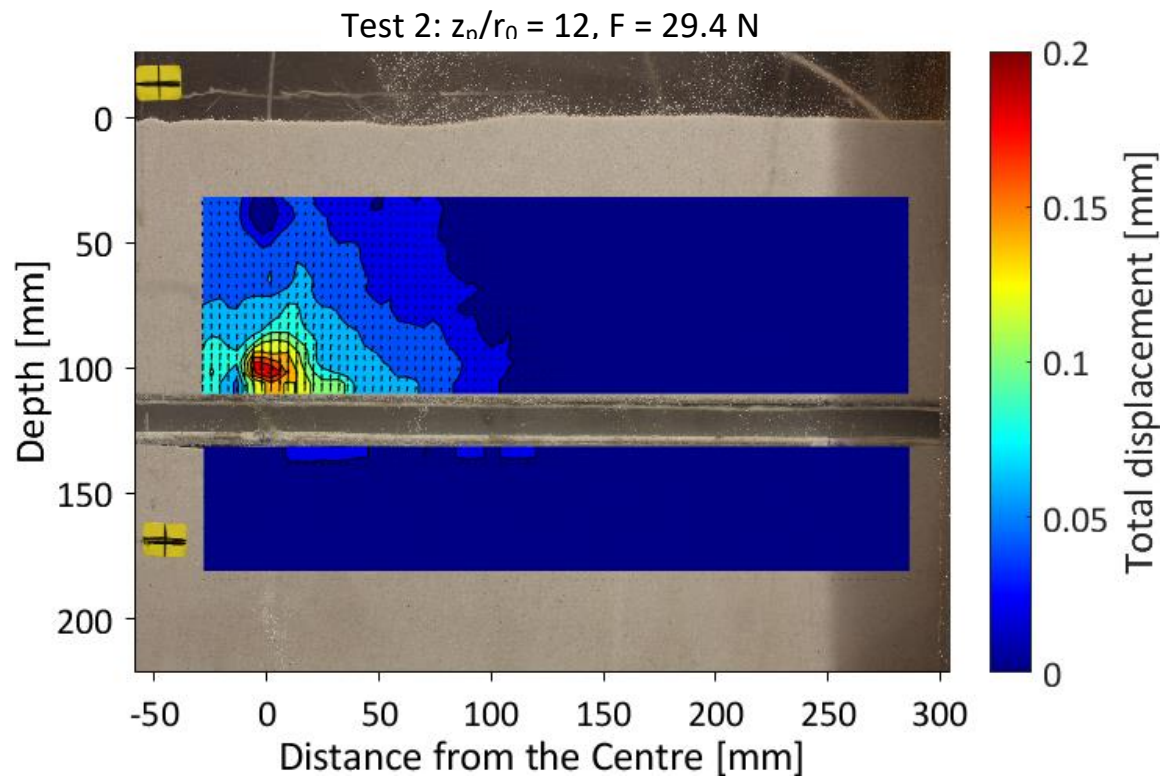


Figure E.1.2/42c: Contour plot of total displacement at 29.4 N (First time loaded to 29.4 N)

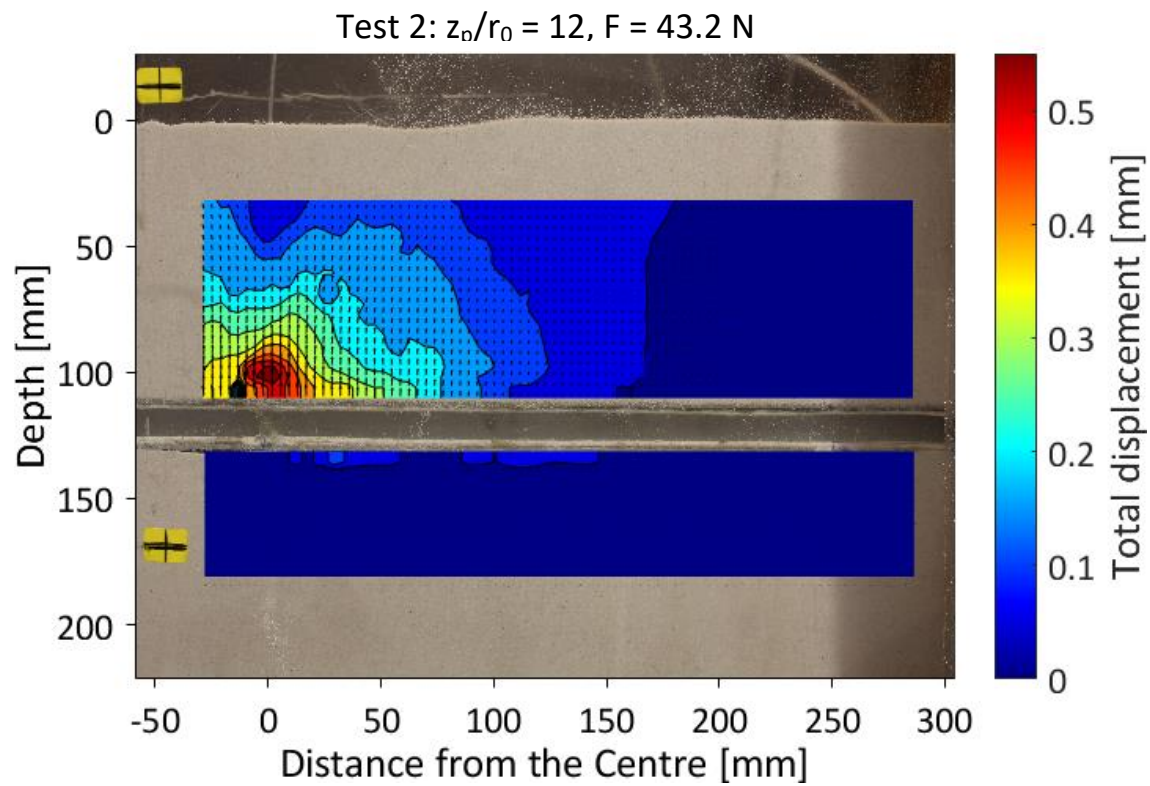


Figure E.1.2/42d: Contour plot of total displacement at 43.2 N

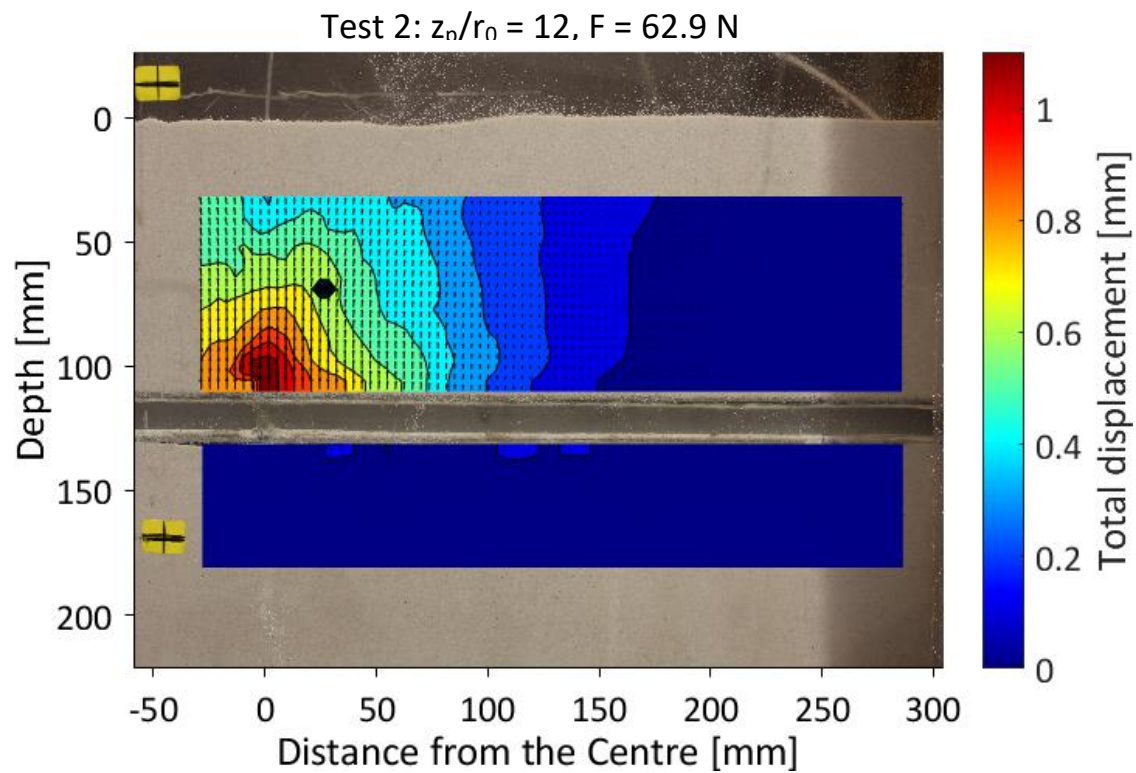


Figure E.1.2/42e: Contour plot of total displacement at 62.9 N

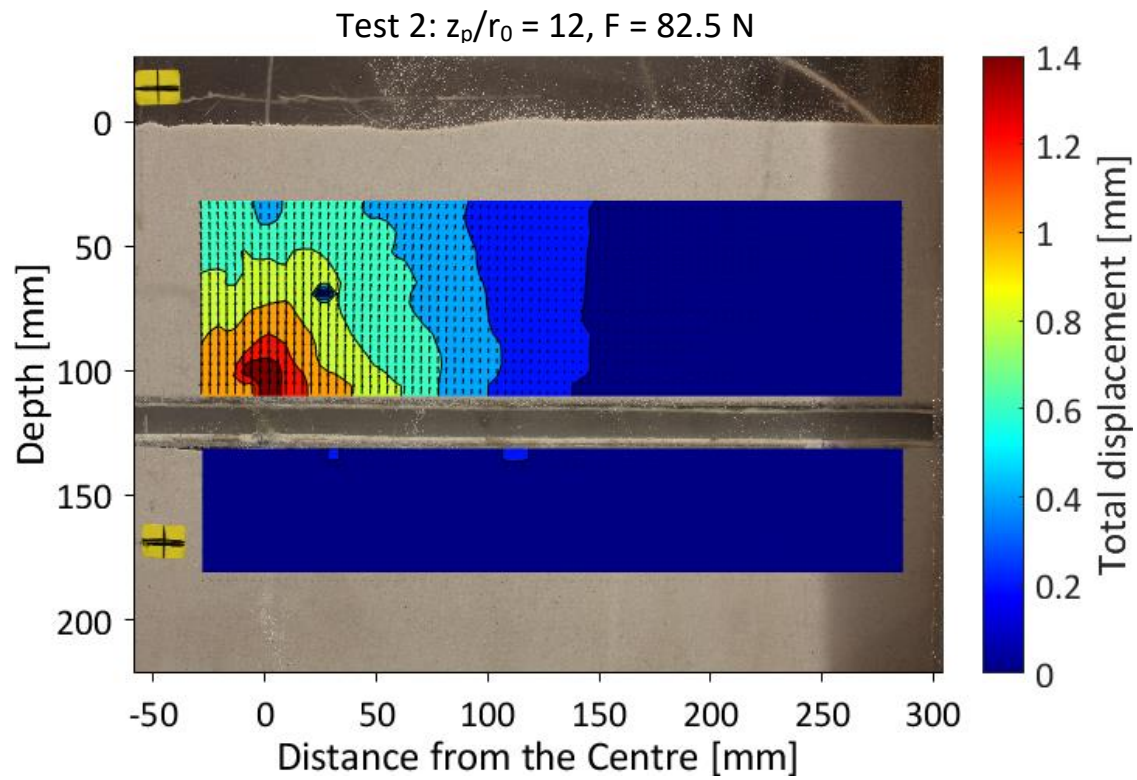


Figure E.1.2/42f: Contour plot of total displacement at 82.5 N

APPENDIX XX

Engineering strains – $z_p/r_0 = 21$

Figure 41a-g presents the engineering strain field above the pipe at 27.0 N, 44.1N, 63.8N, 78.5N, 107.9 N, 127.5N and 157.0N.

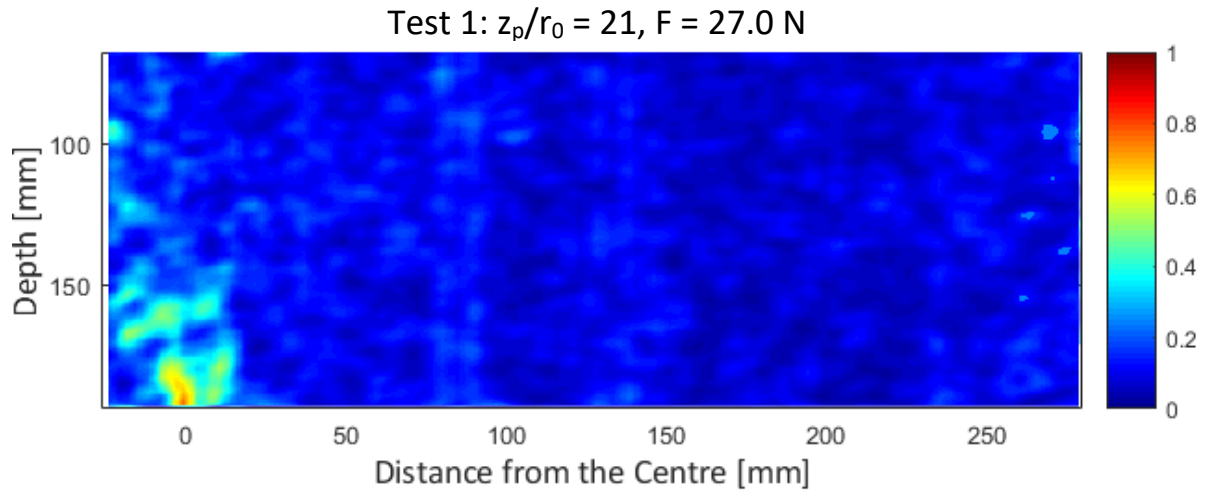


Figure 43a: Contour plot of engineering shear strain at 27.0 N

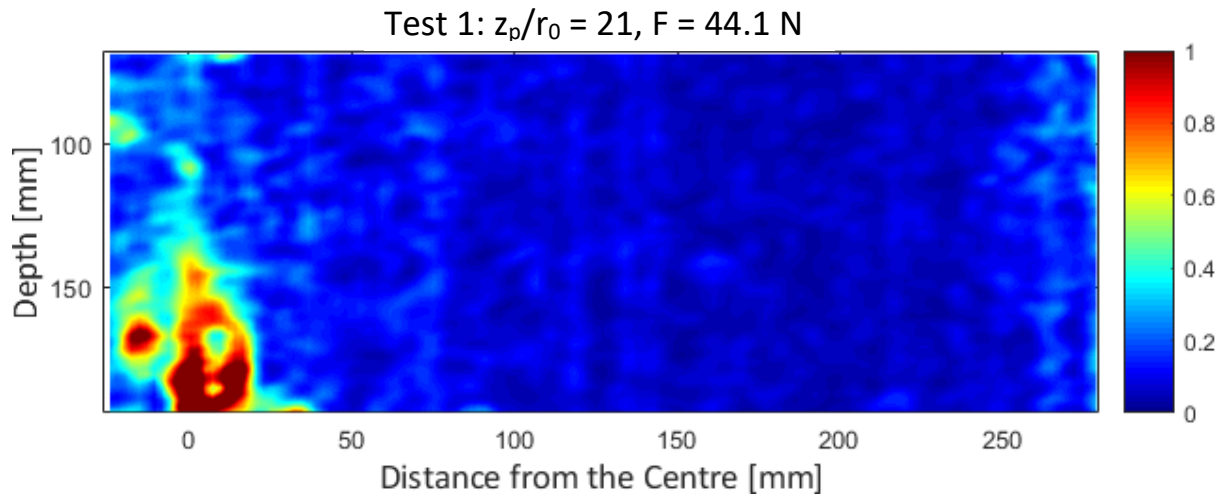


Figure 43b: Contour plot of engineering shear strain at 44.1 N

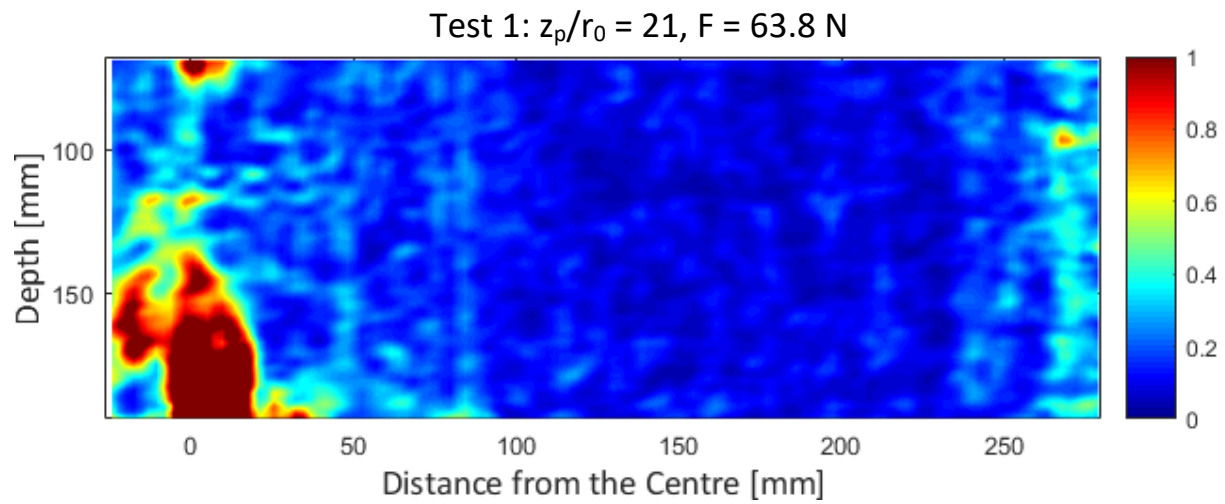


Figure 43c: Contour plot of engineering shear strain at 63.8 N

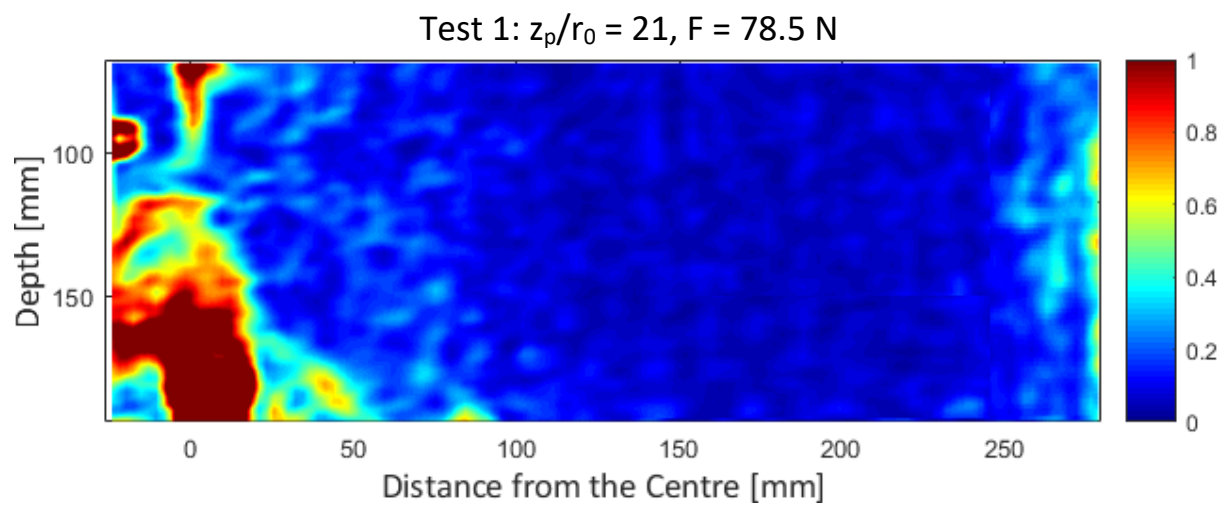


Figure 43d: Contour plot of engineering shear strain at 78 N (First time loaded to 78 N)

Test 1: $z_p/r_0 = 21$, $F = 107.9$ N

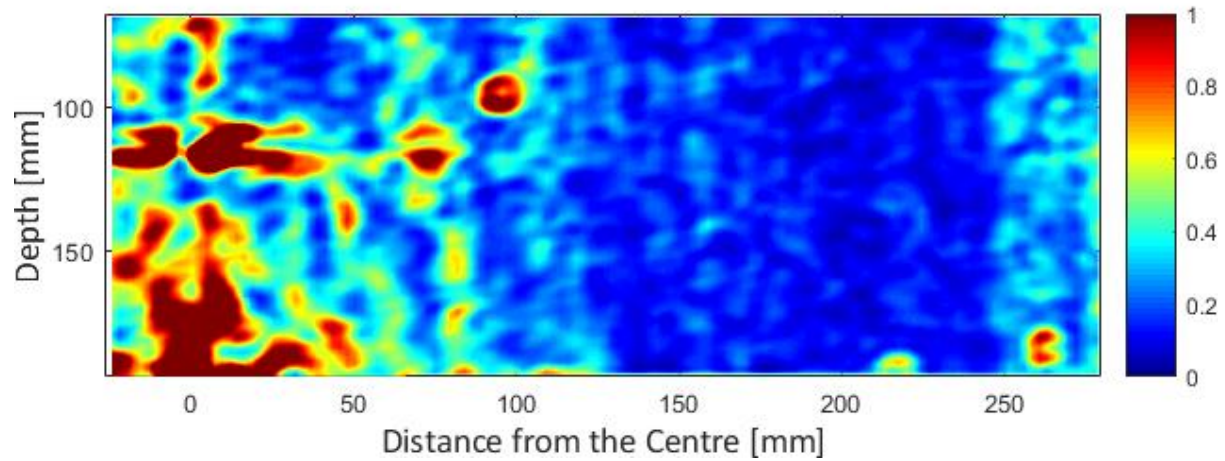


Figure 43e: Contour plot of engineering shear strain at 107.9 N

Test 1: $z_p/r_0 = 21$, $F = 127.5$ N

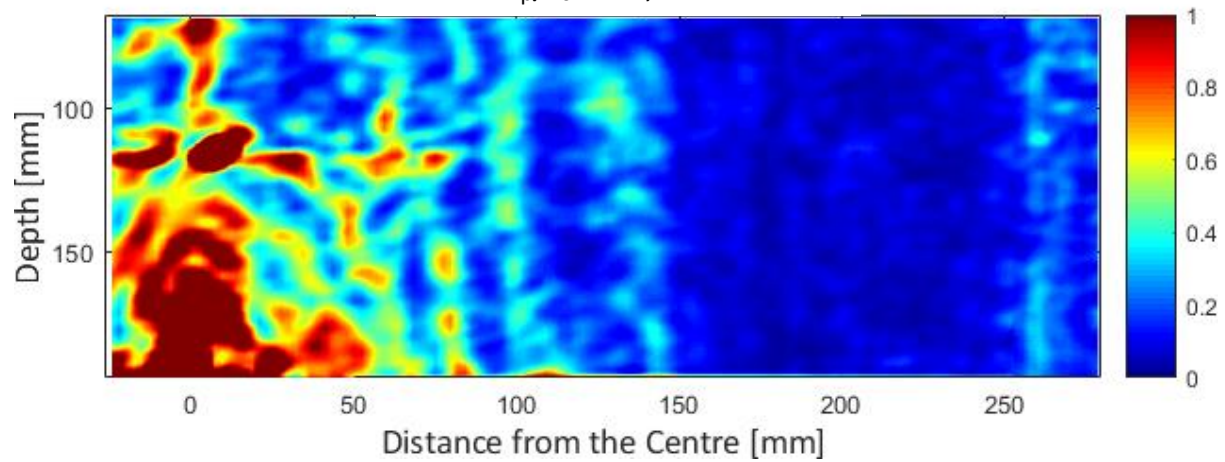


Figure 43f: Contour plot of engineering shear strain at 127.5 N

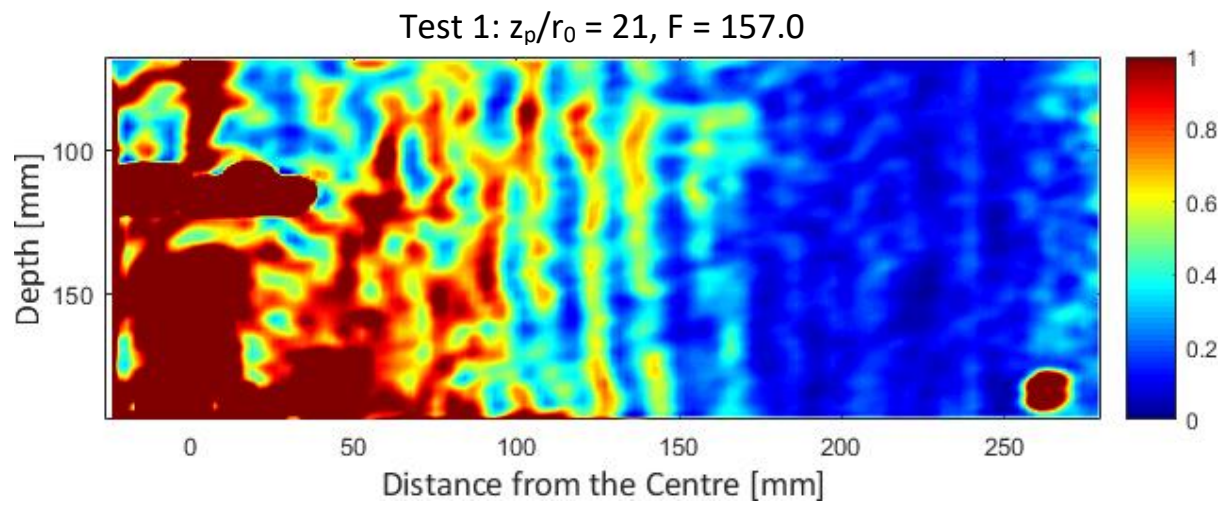


Figure 43f: Contour plot of engineering shear strain at 157.0 N

Engineering strains – $z_p/r_0 = 12$

Figure 42 presents the engineering strain field at 9.8 N, 19.6 N, 29.4 N, 43.2 N, 62.9 N and 82.5 N.

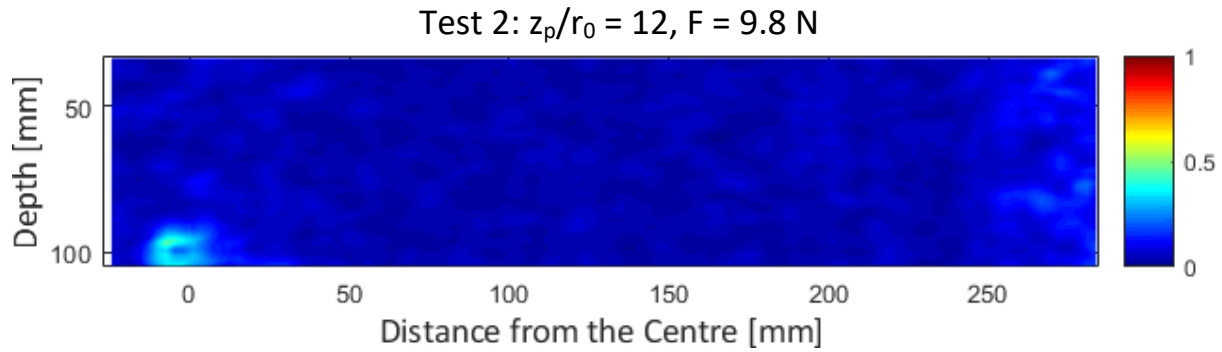


Figure 44a: Contour plot of engineering shear strain at 9.8 N (First time loaded to 9.8 N)

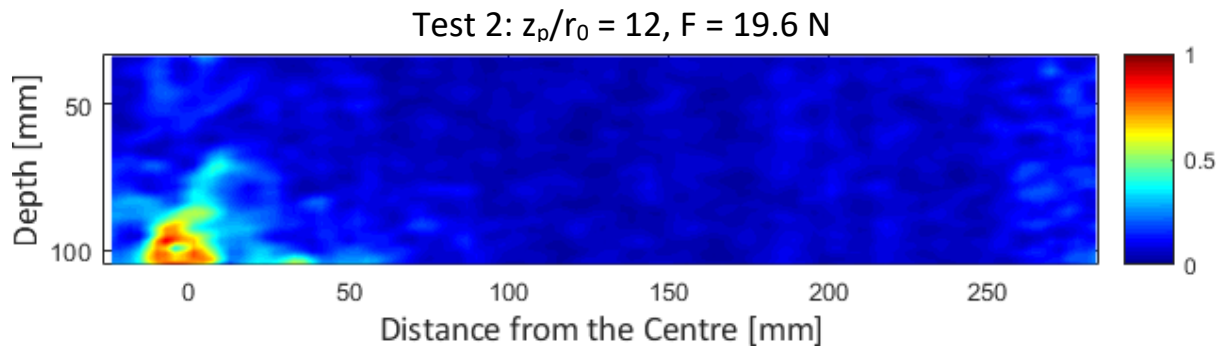


Figure 44b: Contour plot of engineering shear strain at 19.6 N (First time loaded to 19.6 N)

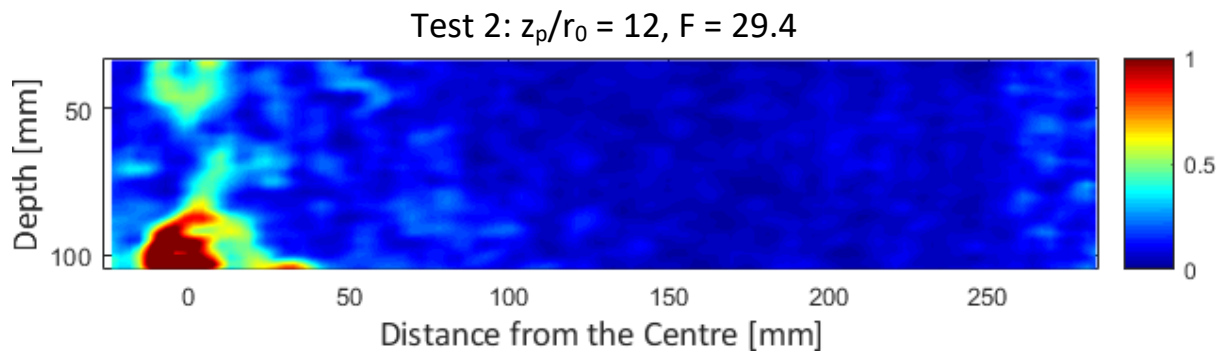


Figure 44c: Contour plot of engineering shear strain at 29.4 N (First time loaded to 29.4 N)

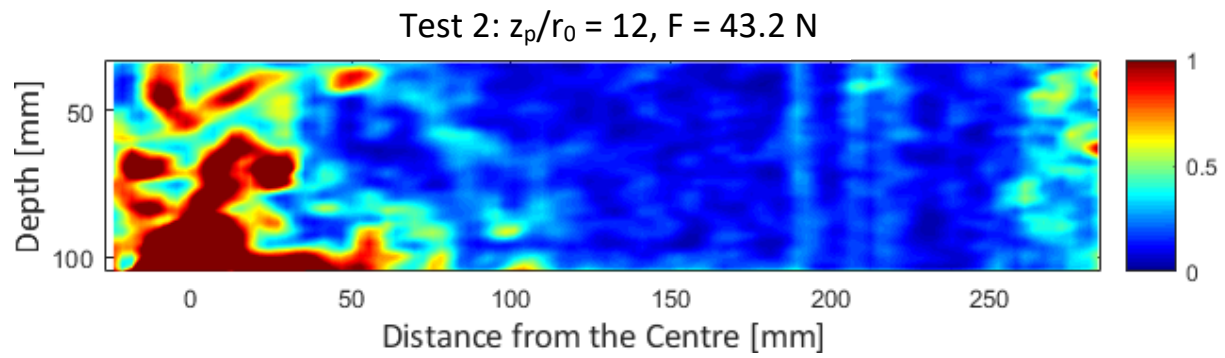


Figure 44d: Contour plot of engineering shear strain at 43.2 N

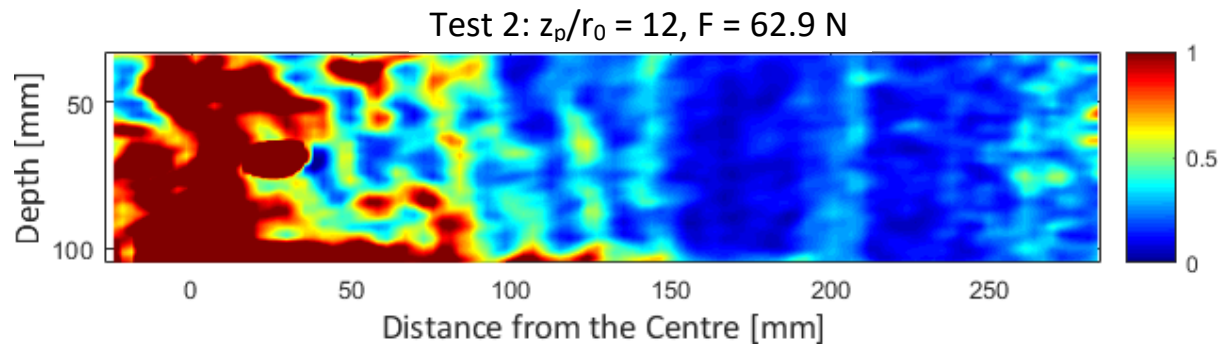


Figure 44e: Contour plot of engineering shear strain at 62.9 N

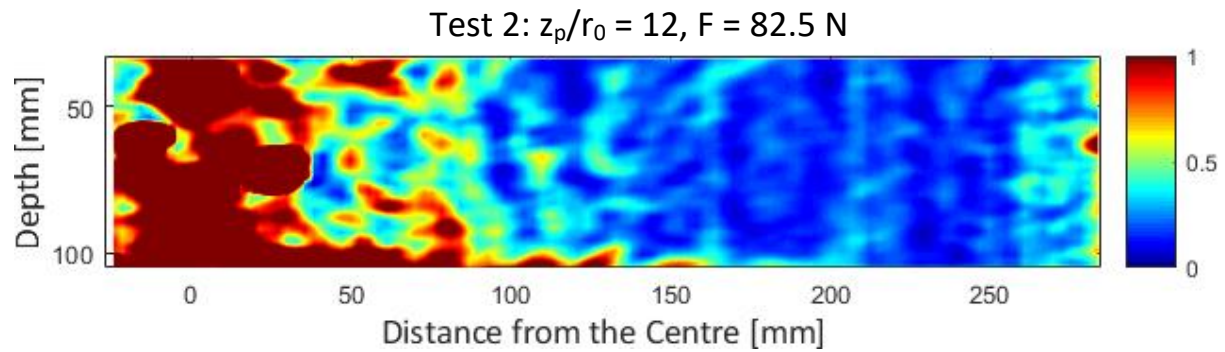


Figure 44f: Contour plot of engineering shear strain at 82.5 N

